

ABSTRACT

SOTORY, PETER ZSOLT. Biomimetic Nanostructures to Enhance Light Transmission Efficiency in Biomedical Optoelectronic Devices. (Under the direction of Dr. Alper Bozkurt and Dr. Michael Daniele).

Pulse Oximetry and photoplethysmography (PPG) are important tools for collecting vital measurements to gauge the healthiness of individuals. With recent developments in wearable sensing, more power efficient designs of these devices are of great interest. Two approaches were pursued in this work toward this goal.

The first was to make devices that are capable of bending and conformable to the human skin. By being in direct contact they should exhibit less light loss and signal noise. This work demonstrates a potential platform and methodology for making organic devices for PPG and pulse oximetry measurements that can be used towards this goal. The described approaches for the fabricated red light emitter OLED, green light emitter OLED, and the organic photodiode light detector establish a pathway to build even more advanced devices.

The second approach was to manufacture biomimetic nanostructures that aid in the transmission of light from LEDs to photodetectors, such as photodiodes and silicon photomultipliers (SiPM). This work fabricated nanostructures and transferred the patterns to the surface of LEDs, SiPMs and photodiodes that enhanced the in and out coupling of light. These devices modified with nanostructures were then shown to have improved coupling with the presence of the structures.

The conclusion of this work is that this approach of modifying the surfaces of a sensing system pair made of a light emitter and light detector for enhanced signal coupling is not only useful for biomedical devices, but is a promising method for the wider community of

applications that require a light source and detector for their sensing with interests in making their system more sensitive or power efficient.

© Copyright 2020 by Peter Zsolt Sotory

All Rights Reserved

Biomimetic Nanostructures to Enhance Light Transmission Efficiency
in Biomedical Optoelectronic Devices

by
Peter Zsolt Sotory

A dissertation submitted to the Graduate Faculty of
North Carolina State University in Raleigh and the
University of North Carolina at Chapel Hill
in partial fulfillment of the
requirements for the degree of
Doctor of Philosophy

Biomedical Engineering

Raleigh, North Carolina
2020

APPROVED BY:

Dr. Alper Bozkurt
Committee Co-Chair

Dr. Michael Daniele
Committee Co-Chair

Dr. Omer Oralkan

Dr. Tushar Ghosh

DEDICATION

To my family.

BIOGRAPHY

After undergraduate study, the author worked in research and development in industry. He was later accepted as a graduate student at the joint university Biomedical Graduate Program of North Carolina State University in Raleigh and the University of North Carolina at Chapel Hill where he earned a master's degree.

In 2012, out of 500 competitors, he won an honorary award in a nationwide contest sponsored by the NIEHS (National Institute of Environmental Health Sciences), EPA (Environmental Protection Agency), and Department of Health and Human Services (HHS) Office of the National Coordinator for Health Information Technology. In 2019, out of 466 papers, he won the third place poster award at an International IEEE Sensors Conference related to this thesis and was the lone graduate student author on the poster and associated paper. He also contributed to the work of an additional poster in 2019 that won a presentation award for work in ultrasound at the ABRCMS biomedical research conference.

ACKNOWLEDGMENTS

I would like to thank my parents, family and friends for their encouragement and support in this endeavor.

I would also like to sincerely thank my advisor Dr. Alper Bozkurt for his assistance, energy, and expertise that made this work possible. I would also like to thank Dr. Michael Daniele for his support, knowledge, access to his labs, and co-chairing the committee. Additionally, I would like to thank Dr. Oralkan, Dr. Ghosh and Dr. Chih-Hao Chang for beneficial discussions, lab access, students and putting the time and work into being on the committee.

I would also like to thank Vilma Berg for always being very helpful and knowledgeable with the procedures and steps needed to go forward in the department and university.

Thank you to the members of the iBionics, iMist, BioInterface, SMARTextiles and the NCSU Nanofabrication (NNF) labs for their assistance.

Additionally, I would like to thank the National Science Foundation (NSF) for funding the Engineering Research Center for the Advanced Self-Powered Systems of Integrated Sensors and Technologies (ASSIST) Center and the resources that the ASSIST Center contributed.

I would also like to thank Dr. H. Troy Nagle for helping to establish the joint Biomedical Program between North Carolina State University and the University of North Carolina Chapel Hill which merged the benefits of an engineering and medical school creating a unique graduate school program that has benefitted many students and faculty.

For this kind of academic journey, it is really not possible to thank everyone who contributed to all the incremental parts and background leading to its success without making a list as long as the dissertation itself. There are others who deserve my gratitude as well. Thank you to all.

TABLE OF CONTENTS

LIST OF TABLES.....	vii
LIST OF FIGURES	viii
Chapter 1: Introduction	1
1.1 Research Objectives and Contribution Summary	8
1.2 Organization of this Thesis	10
Chapter 2: Background for Pulse Oximetry and Organic Optoelectronic Devices	11
2.1 The Importance of Pulse Oximetry.....	11
2.2 Pulse Oximetry Equations and Absorption Curves	13
2.3 For Comparison – A Quick Review : Inorganic LED and Inorganic Photodiode Operation.....	17
2.4 Theory of Operation for Organic LEDs (OLEDs).....	19
2.5 Theory of Operation for Organic Photodiodes (OPDs)	23
2.6 Background for the Biomimetic Moth-Eye Nanostructure.....	29
Chapter 3: Organic Device for Pulse Oximeter and PPG Literature Review	34
3.1 Advantages to Organic Electronics for Pulse Oximetry	34
3.2 OLED and OPD Coupled Systems for Health Monitoring in Literature	36
Chapter 4: Organic Device Fabrication	66
4.1 Glass Substrate Fabrication and Green OLED on Glass Device Testing	66
4.2 Flexible Carrier Creation Header and Substrate Processing.....	79
4.3 Glovebox Metal Electrode Deposition Processing	85
4.4 Device Structure, Recipes and Design.....	88
4.4.1 Device layers, Energy Structure and Design	88
4.4.2 Device Spin Challenges.....	95
4.4.3 Calcium Deposition Issues	99
4.4.4 Device Storage.....	102
4.5 Flexible OLED and OPD Device Characterization	103
4.6 Interconnects for flexible devices	116
4.6.1 Z-Axis Tape Interconnect.....	116
4.6.2 Flexible silver epoxy Interconnect	119
4.6.3 Flexible conductive tape.....	125
4.7 OLED Human PPG Signal with Silicon Photomultiplier (SiPM)	129
4.8 Additional Encapsulation Trials	136

Chapter 5: Nanostructure Fabrication in Silicon	138
5.1 Introduction.....	138
5.2 Fabrication and Nanosphere Lithography.....	138
5.3 Transferring the Nanostructure from Silicon to Other Surfaces (Nanoimprint Lithography)	159
5.4 Patterning with Low Viscosity UV Curable Glue	175
5.5 Characterizing Nanostructures to Inorganic Devices	180
5.6 Biomimetic Nanostructure Fabrication to Increase Light Transmission Efficiency in Optoelectronic Devices	189
5.6.1 Polystyrene Mask on Silicon Substrate Preparation.....	189
5.6.2 Reactive Ion Etching, Mold Casting, and Pattern Transfer	191
5.6.3 Nanostructure Characterization	193
5.6.4 Electrical and Coupling Characterization.....	194
5.7 Results for Simulated and Actual PPG Measurements.....	196
5.7.1 Simulated PPG Measurement and Coupling	196
5.7.2 Human PPG Measurements.....	203
Chapter 6: Conclusion and Future Work	208
6.1 Future work.....	210
REFERENCES	212

LIST OF TABLES

Table 3-1: Electrical Power Parameters and Calculations for OLED/PLED Light Generation ..	63
Table 3-2: Electrical OPD Characteristics	64
Table 4-1: Summary of doped and undoped PEDOT:PSS green OLED devices.....	73
Table 4-2: Fabricated Green and Red OLED Characteristics.....	110
Table 5-1: Mold application technique and nanocone height.....	179
Table 5-2: Photodiode (PD) gain based on wavelength.....	183
Table 5-3: SiPM gain based on wavelength.	185
Table 5-4: Nanostructure measurements	195
Table 5-5: Coupling Results Under different Conditions	195
Table 5-6: LED – Photodiode Nanoamp (nA) Coupling for Simulated PPG.....	199
Table 5-7: LED – SiPM Coupling for Simulated PPG	202
Table 5-8: Unmodified LED with Unmodified Photodiode PPG Measurement Results	204
Table 5-9: Moth-Eye LED with Moth-Eye Photodiode PPG Measurement Results.....	205
Table 5-10: Coupling Gains Seen in Modified vs Unmodified LED/PD Device Pairs	205
Table 5-11: Top 2 Bare Pair vs ME Sets for LED/Photodiode.....	206
Table 5-12: Unmodified LED with unmodified SiPM Human PPG Measurement Results.....	206
Table 5-13: Moth-Eye LED with Moth-Eye SiPM PPG Measurement Results.....	207
Table 5-14: Coupling Gains Seen in Modified vs Unmodified LED/SiPM Device Pairs	207
Table 5-15: Comparison of Coupling Gains on LED/PD versus LED vs SiPM	207

LIST OF FIGURES

Figure 2-1: An illustration of several heart cycles of the absorbed and transmitted light in tissue showing the pulsating arterial blood, the non-pulsating arterial blood, venous blood and other tissue (adapted from [5]). The AC part of the signal comes from the pulsation of the arterial blood while the DC component is the non-pulsating arterial blood, the venous blood and blood in tissue [6][5]. The heart is contracting during the T_{Systolic} time and resting during $T_{\text{diastolic}}$. The transmitted light is lowest when the heart is pumping blood, and higher while the blood is less in volume while the heart rests [6][11]. Adapted/Translated by permission from Springer Nature Customer Service Centre GmbH: Springer Nature Nature Communications [5] (Lochner et al), © 2014.	13
Figure 2-2: Hemoglobin Molar Extinction Coefficient Curve [13]	15
Figure 2-3: Aligning the a) emissions of the OLEDs (adapted from [14] © 2015, Haigh et al. under CC-BY license 4.0: https://creativecommons.org/licenses/by/4.0), b) the hemoglobin absorptivity curve [13], and c) the organic photodiode response for this work [15]. Figure 2-3c) Reprinted (adapted) with permission from [15], © (2014) American Chemical Society	16
Figure 2-4: Silicon LED creating light by the recombination of electrons and holes at the p-n junction, © 2015 IEEE [16]	17
Figure 2-5: Radiative recombination and non-radiative recombination are possible, © 2015 IEEE [16]	18
Figure 2-6: When incident light has enough energy (greater than the 1.1 eV band gap of silicon), it has enough energy to create an electron-hole pair in the depletion region of a p-n junction of a photodiode or solar cell. Shown is a solar cell, but a photodiode would have the same result with the difference being that its circuit would reverse bias the photodiode to maximize sensitivity [18] [19]. Image © (2013) American Chemical Society, [19]	19
Figure 2-7: a) A rudimentary OLED and b) its energy diagram during operation [20], © 2009 IEEE	20
Figure 2-8: A multi-layered OLED with layers that enhance the device's functioning [16][20], © 2009 IEEE, © 2015 IEEE	21
Figure 2-9: Energy diagram where the HTL and EBL have been merged in function, as well as the ETL and HBL combined [25] . E1 and E2 are the electrodes with E1 being a high work function electrode and E2 a low work function electrode. The question marks were used by the original author to indicate possible shifts in energy levels at the interfaces. © IOP Publishing. Reproduced with permission. All rights reserved.	22

Figure 2-10: Factors that determine the EQE of an OLED. Adapted from Ref. [27] with permission from The Royal Society of Chemistry.	23
Figure 2-11: a) A basic organic photovoltaic where DL is the donor layer and AL is the acceptor layer , adapted from [28], © IEEE 2010.	24
Figure 2-12: The energy diagram of an OPD, showing the overall process [25][30][31]. Reprinted (adapted) with permission from "The future of organic photovoltaics", Ref. [31] , © 2015 The Royal Society of Chemistry, https://pubs.rsc.org/en/content/articlelanding/2015/CS/C4CS00227J	24
Figure 2-13: Additional diagrams showing the charge generation process. A bi-layer planar heterojunction (PHJ) a) has a straight plane interface between the donor and acceptor [29] (Reprinted by permission of John Wiley and Sons, Inc. © 2016 WILEY-VCH Verlag GmbH & Co. KGaA, Weinheim). In contrast, b) shows a bulk heterojunction (BHJ) for an OPD where the donor and acceptor have been mixed together [30] (Reprinted from Ref. [30] with permission from The Royal Society of Chemistry).	25
Figure 2-14: Visualization of the Fill Factor [31][34] (Adapted from Ref. [34] with permission from The Royal Society of Chemistry). The J-V (current density – voltage) curve of an OPD during light exposure (solid red line) has two points , the open circuit voltage (V_{oc}) and short circuit current (J_{sc}), that make a rectangle (diagonal lines). As shown by the formula in the figure, the Fill factor (FF) can be determined and seen as the ratio of the diagonal line square to the blue line dashed square. The red dashed line represents the device's characteristics during dark conditions.	27
Figure 2-15: A schematic showing the factors determining EQE for OPDs [31][35] (Image adapted from Ref. [35], © 2016 American Chemical Society).	29
Figure 2-16: COMSOL model showing the reflection and transmission of light (600 nm) with a flat surface ($n=1.539$). Light comes from the top, through air, down to the surface. At a normal (0 degree) angle, there is an approximate 4.64% reflection and 95.4% transmittance.....	31
Figure 2-17: COMSOL simulation with 300 nm tall biomimetic nanocones with a 200 nm period placed on the surface. In the image on the left, a) light (600 nm) again comes from the top, through air ($n=1$), down to the surface ($n=1.539$). For b) the reflection and transmission graph, the reflection has been minimized. At a normal (0 degree) angle, the reflection is a 0.04% and the transmission is 99.56%.	32
Figure 2-18: COMSOL simulation with 300 nm tall nanocones with a 200 nm period placed on the surface. In this situation, the light comes from below ($n=1.539$), to the surface where there are nanocones and then air ($n=1$). At a normal (0 degree) angle, there is 99.56% transmittance and 0.4% reflection.	33

- Figure 3-1: An acquired PPG signal using the OLEDs and OPD fabricated by Koetse et al (top) as compared to a commercial inorganic pulse oximeter by Nelcor [68]. Reproduced with permission from SPIE and Dr. F. Wierenga..... 37
- Figure 3-2: PPG signal from a commercial pulse-oximeter unit (top), an OLED and OPD fabricated coupled system (middle), and an ECG reference (bottom) [69]. Reprinted by permission from Springer Nature Customer Service Centre GmbH : Springer Nature, Springer eBook, Ref. [69], Wierenga et al, © 2008..... 38
- Figure 3-3: The a) OLED on glass substrate and the b) proposed design on a plastic (PET) substrate by Chuo et al [62], © 2010 IEEE..... 39
- Figure 3-4: a) Light output and current density of Chuo et al OLED on glass and PET substrates. b) The PET substrate OPD current density under 1SU illumination (blue) and dark current (red) [62], © 2010 IEEE..... 40
- Figure 3-5: a) Diagram showing how muscle contraction could be sensed with the light source and photodiode placement and b) the flex circuit board for the device [61] (Bansal et al. © 2014 under CC-BY license 4.0: <https://creativecommons.org/licenses/by/4.0>). The robot arm that was triggered from the detection is not shown..... 41
- Figure 3-6: Detected signals for a) isometric and b) isotonic contractions [61] (Bansal et al. © 2014 under CC-BY license 4.0: <https://creativecommons.org/licenses/by/4.0>)..... 42
- Figure 3-7: Bansal et al tissue oxygen sensor a) design and induced ischemia (cuff restricted blood flow) measurement results [61] (Bansal et al. © 2014 under CC-BY license 4.0: <https://creativecommons.org/licenses/by/4.0>)..... 43
- Figure 3-8: a) Diagram and b) implementation of the OLEDs and OPDs for the pulse oximetry system of Lochner et al [5]. Reprinted by permission from Springer Nature Customer Service Centre GmbH : Springer Nature, Nature Communications Ref. [5] (Lochner et al), © 2014..... 44
- Figure 3-9: The OLED irradiance and current density for Lochner et al [5]. Reprinted by permission from Springer Nature Customer Service Centre GmbH : Springer Nature, Nature Communications Ref. [5] (Lochner et al), © 2014. 45
- Figure 3-10: Lochner et al OPD's a) response curve (EQE) aligns with the red and green OLED emission spectra. The light and dark current responses are shown in b). For the light current measurement, the OPD was illuminated with a 640 nm source at an intensity of $355 \mu\text{W}/\text{cm}^2$. The dark current was attained by applying voltage to the device. Reprinted by permission from Springer Nature Customer Service Centre GmbH : Springer Nature, Nature Communications Ref. [5] (Lochner et al), © 2014..... 46

Figure 3-11: Red and green wavelength signals and derived heart rate (HR), red and green wavelength ratio (Ros), and blood oxygen saturation (SaO_2) interpretation [5]. Reprinted by permission from Springer Nature Customer Service Centre GmbH : Springer Nature, Nature Communications Ref. [5] (Lochner et al), © 2014.....	47
Figure 3-12: Device PPG signal degradation during 7 days [5]. [5]. Reprinted by permission from Springer Nature Customer Service Centre GmbH : Springer Nature, Nature Communications Ref. [5] (Lochner et al), © 2014.	48
Figure 3-13: Yokoto et al fabricated a a) reflection based pulse oximetry device that illuminated the tissue with red and green wavelengths [3]. The b) diagram, c) cross section, and d) actual device [3]. Yokota et al. © 2016 under CC BY-NC license 4.0: https://creativecommons.org/licenses/by-nc/4.0/legalcode	49
Figure 3-14: The a) J-V curves for red, green and blue PLEDs , and b) their EQEs as a function of current density, and (inset) luminance of the PLEDs made by Yokota et al [3]. Yokota et al. © 2016 under CC BY-NC license 4.0: https://creativecommons.org/licenses/by-nc/4.0/legalcode	50
Figure 3-15: Chart of the green PLED lifetime at 60% humidity and 20 °C operated at 12.5 mA/cm ² by Yokota et al [3]. The luminance operational half life was 29 hours with the 5 layer passivation. Yokota et al. © 2016 under CC BY-NC license 4.0: https://creativecommons.org/licenses/by-nc/4.0/legalcode	51
Figure 3-16: Luminance and current density characteristics and after the removal of the PLEDs from the supporting substrate [3]. Yokota et al. © 2016 under CC BY-NC license 4.0: https://creativecommons.org/licenses/by-nc/4.0/legalcode	52
Figure 3-17: Compression had a negligible effect on the green PLED luminance [3]. Yokota et al. © 2016 under CC BY-NC license 4.0: https://creativecommons.org/licenses/by-nc/4.0/legalcode	52
Figure 3-18: The OPD a) EQE spectral response to the PLED spectrums. The b) the current density and c) the Voc as a function of light intensity under a solar simulator of 1 sun and Air mass 1.5 Global filter [3]. Yokota et al. © 2016 under CC BY-NC license 4.0: https://creativecommons.org/licenses/by-nc/4.0/legalcode	54
Figure 3-19: OPD response as when a) illuminated by a green PLED and b) red PLED at two intensities [3]. The OPD c) open circuit voltage and the d) current density are plotted as a function for a series of green and red PLED intensities. Yokota et al. © 2016 under CC BY-NC license 4.0: https://creativecommons.org/licenses/by-nc/4.0/legalcode	55

Figure 3-20: OPD stretch experiments showing a) the open circuit voltage remain unaffected with compression up to 40%, and b) in a non-compressed state versus 37% compressed state, the dark (dashed line) and light (solid) current densities were the same when illuminated with a green laser [3]. c) Compressive cycling did not degrade the open circuit voltage, the current density and the light/dark current response [3]. Yokota et al. © 2016 under CC BY-NC license 4.0: https://creativecommons.org/licenses/by-nc/4.0/legalcode	56
Figure 3-21: The PPG signal from Yokota et al using the red PLED and OPD [3]. The device stability affected the signal quality over time. Yokota et al. © 2016 under CC BY-NC license 4.0: https://creativecommons.org/licenses/by-nc/4.0/legalcode	57
Figure 3-22: OPD signal for a) 99% blood oxygenation and b) for 90% blood oxygenation [3]. Yokota et al. © 2016 under CC BY-NC license 4.0: https://creativecommons.org/licenses/by-nc/4.0/legalcode	58
Figure 3-23: Han et al PLED and inorganic photodiode PPG and pulse oximeter for the wrist [1]. Han et al, © 2017 under CC BY license 3.0: https://creativecommons.org/licenses/by/3.0/	58
Figure 3-24: Green and red PLED characteristics on the PEN/ITO substrate [1]. Han et al, © 2017 under CC BY license 3.0: https://creativecommons.org/licenses/by/3.0/	59
Figure 3-25: An example of the red and green PPG signal by Han et al and how it translates to heart rate and blood oxygenation [1]. Han et al, © 2017 under CC BY license 3.0: https://creativecommons.org/licenses/by/3.0/	60
Figure 3-26: Khan et al made a flexible organic reflectance oximeter array [2]. © 2018, Khan et al, under CC-BY-ND license 4.0: https://creativecommons.org/licenses/by-nd/4.0/	61
Figure 3-27: Lee et al developed a red and green OLED patch [4]. Copyright 2018, Lee et al, under CC-BY-NC license 4.0: http://creativecommons.org/licenses/by-nc/4.0/legalcode	62
Figure 4-1: Using vinyl tape to pattern ITO covered glass surfaces. First the glass is covered in a) and then the tape is cut b) with a razor to cover those areas where the ITO will be preserved as an electrode	66
Figure 4-2: Patterning of the ITO glass substrate with hydrochloric acid (HCL). First, a) the taped patterned ITO glass is put into a bowl and then some zinc powder is sprinkled on its surface b). Hydrochloric acid is then introduced and the competition reaction is quickly quenched with water and the pieces rinsed c). The glass is then left with patterned ITO that will become the electrode for the OLED or OPD.....	68

Figure 4-3: Initial attempts of spinning PEDOT on substrates were not uniform. These were done on PET before the glass substrate was attempted.....	69
Figure 4-4: The polymer a) F8BT used for the green OLED came from the manufacturer as b) lightweight yellow strands. As F8BT is measured to create a solution, the dry strands would be difficult to handle due to the static charge and it was helpful to use c) a static gun and grounded tweezers to handle the polymer strands especially when weighing with plastic.	70
Figure 4-5: The first fabricated green OLEDs looked dim as illustrated in a) in the lower right corner. An enhanced photo b) shows the same scene as a) but lightened to better show the green OLED In the lower right corner. The red light source in the upper left of both photos is the power switch lamp of a power strip and the more elongated light in the upper right is a reflection of the switch lamp.	71
Figure 4-6: Sorbitol doping increases the conductivity of PEDOT:PSS [70].	72
Figure 4-7: The current density and electroluminescence favorably shifts for doped and undoped PEDOT:PSS [71].	72
Figure 4-8: Power consumption characteristics of undoped and doped PEDOT:PSS green OLEDs.	74
Figure 4-9: Pinhole formation was more prevalent in undoped PEDOT:PSS. The defect formation typically started with a) lightening of an area of the device, b) become brighter and have a small area left that illuminates or the whole device burn out.....	75
Figure 4-10: With doped PEDOT:PSS OLEDs there was illumination in regions outside the electrode overlap area. The a) overlap zone is where the where the illumination was expected to be limited, as seen with the undoped PEDOT:PSS devices of Table 4-1. In b) and c) the device's illumination can be seen in room lighting and dark conditions.	76
Figure 4-11: Here moving the alligator clip connection is moved from the ITO electrode location from a) one device to the ITO electrode of a b) second device. The first OLED stays illuminated because the electrical circuit in the second configuration allows for the current to flow through the doped PEDOT:PSS layer.....	77
Figure 4-12: When producing a) multiple substrates, many pieces of patterning tape were meticulously applied and then b) carefully removed. By using doped PEDOT:PSS, the need to apply and remove these small piece of tape, as well as the acid etching step, could be avoided and the substrate fabrication process be simplified since the device would be defined and patterned by the area of metal electrode deposition.	78

Figure 4-13: Making carriers for processing the flexible substrates by a)-c) pouring the silicone onto a one inch square aluminum until the surface is covered and then spinning it. Carriers are then d) put aside and left to cure overnight.....	80
Figure 4-14: The ITO covered PET plastic substrate was laser cut into one inch squares as the substrates for the OLEDs and OPDs.	81
Figure 4-15: The a) ITO coated PET came with a protective layer that was removed to expose the ITO coated side of the plastic. The substrate then had kapton tape placed on its edges and b) placed on top of a prepared carrier. There the substrate c) adhered to the silicone coated surface of the aluminum square. Next, doped PEDOT:PSS was used to flood the surface, the substrate was spun, and what was resulted was e) a spincoated layer of PEDOT:PSS on the substrate. The coated substrates were then f) put on a hotplate for annealing.	82
Figure 4-16: Post annealed substrates were put in individual petri dishes and stored until there was an opportunity to put OLED or OPD polymer on them in the glovebox.....	83
Figure 4-17: Temperature could affect the PET surface by introducing deformations randomly. However, some substrates remained unaffected.....	83
Figure 4-18: Glass carriers were also attempted to see if they would function better than metal carriers.....	84
Figure 4-19: Glass carriers with PET substrate after PEDOT:PSS annealing step have warping from the heat process.	84
Figure 4-20: PET/ITO thermal heat treatment results [73]. For this current OLED work, the PET/ITO was processed at a maximum temperature of 120 deg C, well below the melting temperature of the PET substrate. As the picture shows, heating PET beyond its glass transition temperature (T_g) causes deformations. © 2011, Zardetto et al, under CC-BY license 3.0: https://creativecommons.org/licenses/by/3.0/	85
Figure 4-21: A laser cutter was used a) to cut the mask. Once cut, the mask was attached to the mask holder. The substrates covered in F8BT polymer were then loaded into the mask holder and were then ready to have metal electrodes deposited to become green OLEDs.....	86
Figure 4-22: The mask holder and substrates were a) put into the evaporator chamber and attached to the rotating plate at the top of the chamber. Metal was loaded into b) the appropriate thermal evaporator boats. The current driven through the boat evaporated the metal which was c) deposited on the substrates to make electrodes for the OLEDs.	87

Figure 4-23: The a)-b) OLED and c) OPD layer structure. The completed devices they were encapsulated with polyimide (kapton) tape or a combination of kapton and a top layer of PET.....	88
Figure 4-24: Chemical structure of the components for OLEDs and the conducting layer, PEDOT:PSS. MDMO-PPV and F8BT were the red and green emissive layers respectively.....	90
Figure 4-25: Chemical structures of the active layer organic compounds for the OPD. P3HT functioned as the electron donor and ICBA as the electron receptor [76].....	90
Figure 4-26: The green OLED stack and energy structure. The values for aluminum, calcium and ITO were sourced from by Hasan et al [77], PEDOT:PSS by Lochner et al [5], and F8BT from Ossila.....	91
Figure 4-27: The red OLED stack and energy structure. The values for aluminum, calcium and ITO were sourced from Hasan et al [77], PEDOT:PSS by Lochner et al [5], and MDMO-PPV by MilliporeSigma.....	92
Figure 4-28: The OPD stack and energy structure. The values for aluminum, calcium and ITO were sourced from Hasan et al [77] and PEDOT:PSS by Lochner et al [5]. The values for P3HT and ICBA were sourced from An et al [78].....	92
Figure 4-29: An alignment is required for the system to work for pulse oximetry. The a) emissions of the OLEDs must correspond with the b) hemoglobin absorptivity curve [13], and the c) photodiode response has to be active in the spectrum of the OLEDs. The OLED spectra is from Reference [14] and the OPD absorption is from reference [76]. (Figure 4-29a adapted from [14] © 2015, Haigh et al. under CC-BY license 4.0: https://creativecommons.org/licenses/by/4.0/ , Figure 4-29c) Reprinted (adapted) with permission from [15], © (2014) American Chemical Society.)	94
Figure 4-30: Spincoating varied with the polymer. F8BT dissolved well and could be a) spun on uniformly but required an additional step not mentioned in literature of filtering. MDMO-PPV had a high viscosity and b) initially would not spin on uniformly and required the development of a spin recipe to overcome this issue. If left to sit in a bottle, a portion of MDMO-PPV will c) gel on the bottom of the container as can be seen in this bottle put on its side. MDMO-PPV needs to be mixed with a stirrer for hours before use. The photodiode solution was sensitive to speed conditions and the difference can be seen in d) and e) which only vary in 3 seconds of spin. The photodiode solution needed to be stirred for hours as well.	96
Figure 4-31: MDMO-PPV can be sensitive to slight changes in concentration, as shown by Mendez-Pinzon et al [80].....	97

Figure 4-32: Testing showed that some spinning speeds and annealing temperatures can make a device prone to developing pinholes. A pinhole has developed in a) and b) is shown in regular lighting conditions. The other examples are additional devices that suddenly developed pinholes.	98
Figure 4-33: Spinning recipes and techniques were developed that eventually produced polymer coats that were more uniform.	98
Figure 4-34: Calcium came a) packed in mineral oil. When in the b) evaporation chamber, the current of the evaporation boat needed to be carefully adjusted. If the current was changed too quickly, the temperature of the boat could correspondingly increase too quickly, causing the calcium pellet to explode and send debris and dust into the chamber. In c) the pellet in the center exploded because the temperature either changed too rapidly or became too hot.	100
Figure 4-35: The initial attempts of using calcium were problematic because the calcium came packaged in mineral oil. The mineral oil's carbon became a contaminant in the metal electrode deposition process. Carbon was easily noticeable as a black color on a)-b) some calcium pellets following the thermal evaporation. The c) first devices made with calcium had carbon contamination, causing their electrodes to be turned black in regions. From left to right in c) is a contaminated green OLED, a glass slide coated for evaluation purposes, and a contaminated red OLED. The carbon affected the device by interfering with illumination in the regions where the carbon was present. The activated d)-e) OLEDs illustrate how the illumination was more in the regions that had less carbon and more metal.	101
Figure 4-36: Blank substrates of different materials were used to experiment which method best diminished carbon contamination.....	102
Figure 4-37: The calcium evaporation technique was refined until little or no carbon contamination were visible either on the a) PET side or b) the deposited metal electrode side.....	102
Figure 4-38: Storage conditions in glove box sometimes introduced dots of unknown origin, but the devices still worked.	103
Figure 4-39: Initial Red OLED IV curves. Instability seen. Later they became more stable with better spinning technique.....	104
Figure 4-40: Red OLED IV Curve.....	105
Figure 4-41: Red OLED current density.....	105
Figure 4-42: A time series showing the red OLED on flex substrate cycled to 12V.	106

Figure 4-43: The green OLED IV Curve was more stable after device fabrication improvement.....	107
Figure 4-44: Green OLED current density.....	108
Figure 4-45: A time series showing the green OLED on flex substrate cycled to 12V.....	109
Figure 4-46: A side by side comparison of the final frames in the time elapsed photos of the red and green OLEDs lighting up from Figure 4-44 and Figure 4-47.....	110
Figure 4-47: The organic photodiode responded to a flashing green inorganic LED which had an intensity greater than that of the green OLED. This test at least proved that the organic photodiode can respond to green wavelengths and the selection of chemicals were responsive if the intensity was high enough.....	111
Figure 4-48: Direct measurement of current for OPD responding to a red inorganic LED flashing. The response indicates the selection of chemicals for the organic photodiode can respond to red wavelengths as long as the intensity is high enough.....	112
Figure 4-49: Organic photodiode could also be made to respond to the fluorescent lights of both the room and the glovebox.....	113
Figure 4-52: The dark and light current measurement was taken as a function of applied voltage for the organic photodiode response curve. The short circuit current was 8×10^{-7} A (0V intercept) and the open circuit voltage was 0.029V (0 Current intercept).	114
Figure 4-51: The larger sized devices were tested for coupling with the a) green OLED and b) red OLED mounted with the organic photodiode.....	115
Figure 4-54: The larger green OLED response in the organic photodiode OPD could be seen, but had noise in it.....	115
Figure 4-53: Z-axis tape used to create a flexible interconnect to the green OLED with a copper coated polyimide lead (in black, above red alligator clip).	117
Figure 4-54: Green OLED IV curve before and after Z-axis interconnect. Before interconnect OLED was lighting up, but afterwards b)-e) it did not light up. A light press was done for c) but that did not produce illumination in c) through e). The conclusion was that Z-axis tape requiring a pressure resulted in malfunctioning devices.	118
Figure 4-55: This is the OLED neighbor to the Z-axis device interconnected in Figure 4-55. Even though this device was not connected with the Z-axis tape, it was affected by the pressure put on nearby region of the flexible substrate and consequently fractured. This is the device being touched by the curving	

red wire in Figure 4-55. The metal electrode didn't seem to have any marks that matched up with the fractures observed during illumination.....	119
Figure 4-56: Stencil used for first silver epoxy application attempts.....	120
Figure 4-57: Silver epoxy interconnect attempted with green OLED. A stencil a) was laser cut out of a transparency, which allowed the silver epoxy to be b) patterned. When the leads were attached, the epoxy would smear and the leads could detach from the polymer surface, sometimes taking parts of the polymer layer with it.....	121
Figure 4-58: Silver epoxy interconnect attempted with red OLED. The device was patterned with silver epoxy on the a) deposited electrode side. The other side of device in a) is seen in b) and the silver interconnect pathway can be seen through the plastic substrate.....	121
Figure 4-59: Red OLED IV curves a) after fabrication, b) after excising from the substrate and c) after the second type of silver epoxy interconnect application.....	123
Figure 4-60: A third silver epoxy was attempted, this one with a 2 day working time and suitable for medical applications. The patterned epoxy can be seen in a) on the deposited electrode and b) reverse sides, respectively. The IV curve of the OLED resembles a normal diode curve after it was removed from the fabrication substrate and had silver epoxy applied and cured. However, these devices did not turn on and illuminate.....	124
Figure 4-61: Devices made with extra aluminum being deposited on the metal electrode for the fourth variation of silver epoxy interconnects.....	125
Figure 4-62: Pinholes formed where the arrows are indicating for the devices from Figure 4-63.....	125
Figure 4-63: Fabricated red OLED with conductive tape.....	126
Figure 4-64: This measurement was the proof of concept that conductive tape could work to connect an OLED, as shown by IV curve of devices. Illumination was seen.....	126
Figure 4-65: OPD testing before and after conductive tape application. The response was essentially identical.....	127
Figure 4-66: Green OLED testing with the conductive tape and mounting.....	128
Figure 4-67: Device pairs that were fabricated on the same substrate were separated by cutting and then kapton tape and conductive tape were applied. Pairs of device are shown here that were made on the substrate with one of the pair had the kapton tape added and ready for testing.....	128

Figure 4-68: A solder oven a) was used to attach the SiPM to a printed circuit board and then b) black tape was put around it to minimize reflection from the circuit board. The circuit board section that is visible was covered as well.....	129
Figure 4-69: The a) green OLED and b) red OLED mounted with the SiPM to measure response.....	130
Figure 4-70: The SiPM response curve to the green OLED being driven with a 10Hz, 50% duty cycle signal at different voltages. The peak luminosity of the green OLED was reached at 0.05s at 11V, 0.03s at 12V and 0.01s at 12.5 V. The 12.5V case reached the maximum current setting.....	131
Figure 4-71: The SiPM response curve to the red OLED being driven with a 10Hz, 50% duty cycle signal at different voltages.....	132
Figure 4-74: Leads were a) attached to the green OLED and it was encapsulated with b) kapton tape and could be made to c) illuminate. Encapsulation with tape sometimes introduced momentary d) shorts during initial IV curve measurements, but after the momentary short, the OLED could be made to operate normally and also have a normal IV curve.....	133
Figure 4-73: The green OLED was encapsulated and a) attached to leads and the 3D printed holder and b) could be made to activate.....	134
Figure 4-74: The human PPG was obtained with the OLED mounted on a 3D printed plastic plate OLED that was hinged with a second plate that had the SiPM mounted.....	134
Figure 4-75: Two PPG's obtained with the OLED and SiPM within 10 minutes of glovebox withdrawal of the OLED.....	135
Figure 4-76: The encapsulation with kapton tape worked and additional PPGs could be obtained even at a) 1 hour 9 minutes outside the glovebox and, b) 1 hour 40 minutes.....	136
Figure 4-77: Out of 4 devices made with another encapsulation method, 1 did not work, a) had a defect from the process, while b) and c) did illuminate properly.	137
Figure 5-1: Some necessary tools for nanosphere lithography include beakers, pipettes, pipettors, glass bowls, solvents like ethanol, solutions of different SDS concentrations, a solution of nanospheres, b) a sonicator and c) a UVO cleaner.....	139
Figure 5-2: SEM image of the monodisperse polystyrene nanospheres used in this work on an aluminum surface in a non-compact distribution.....	140
Figure 5-3: Early methods for nanosphere colloidal crystal deposition.	141

Figure 5-4: Spinning on the nanospheres to a glass slide was also attempted but did not produce consistent nor uniform results.....	142
Figure 5-5: Attempted deposition techniques. The use of small silicon samples allowed for many pieces to be coated simultaneously, helping to provide the number of samples needed to explore the parameter space of the plasma etcher.....	144
Figure 5-6: The initial samples had unexpected features large scale where a) elliptical patterns or b) sparse coverage.....	145
Figure 5-7: Close resolution of one of the first attempts at etching silicon with a nanosphere mask lacked any distinct indication of correct patterning or what step to take next. Features in this SEM image range from nanometers to microns.....	146
Figure 5-8: Images showing the results of different silicon etch conditions.....	147
Figure 5-9: Results of the application of the nanosphere suspension to the DI water surface hinted at the next procedure to attempt.....	148
Figure 5-10: The diagram a) shows convective assembly drives self-assembly of the colloidal crystal [87][88]. Here 'h' is the particle layer that develops as water is evaporating from a surface with a meniscus. In b) a simplified version is illustrated. The concept for a dropping water level with a colloidal crystal on its surface is similar to both a) and b). Images reprinted from "Advances in Colloid and Interface Science", vol. 246, Lotito et al, "Approaches to self-assembly of colloidal monolayers: A guide for nanotechnologists", pp. 217–274, Copyright (2017), with permission from Elsevier.	150
Figure 5-11: The improved setup included the bowl, sample, sample holder and most importantly, the syringe pump. Metal weights were put on the pump too to make it more secure.....	151
Figure 5-12: A sideways view of the setup showing how the metal strips were put in place defining where the reduced area for the nanospheres dispersal would be.....	151
Figure 5-13: An aluminum foil barrier was added to the metal bars to create a smaller channel and limit the water's surface area. The nanospheres suspension was then introduced creating a greater amount of yellow areas.....	152
Figure 5-14: By adding a solution of SDS a compacted layer of monodisperse nanospheres was created. The silicon was hoisted through this layer and SDS was continually applied to maintain the pressure.....	152
Figure 5-15: When viewed from another angle, the same colloidal monolayer of nanobeads from the prior figure was not visible.....	153

Figure 5-16: Even up close, the monolayer cannot be seen from the incorrect angle.....	153
Figure 5-17: A time series of the deposition of the self-assembled nanosphere colloidal crystal on silicon that is slowly hoisted upwards from underneath the water with the monolayer on it.....	154
Figure 5-18: With the adjustments in experiments features become large enough to see and start becoming areas measured in square millimeters. The silicon piece here is about 2 cm long in height. In a) the substrate can be seen after nanosphere deposition and before reactive ion etching (RIE). In b) the same substrate can be seen when it is removed from the blue holder of the previous picture, dried, and still before RIE. In c) the substrate is shown after RIE. The dark areas indicate where the moth-eye features have formed on a large scale.....	155
Figure 5-19: The results of concentrations and rate of movement were compared too. The concentration of samples 3 and 4 are double of 1 and 2. Samples 3 and 4 also were withdrawn from the water at 1/3 the speed of samples 1 and 2. The concentration of sample 5 is also double the concentration of samples 1 and 2, but the speed was reduced even further to be 1/10 the speed of samples 1 and 2. Higher concentration and slower movement seemed to help make a larger nanosphere crystal deposit. Under the right lighting conditions, the blueish tint areas can be seen where the nanospheres were deposited as a colloidal crystal and the moth-eye biomimetic nanostructures with long range order would appear after etching. The patches of monolayer crystals here are approaching centimeter scales.....	156
Figure 5-20: An excellent compacted monolayer crystal ready to be transferred to a silicon piece.....	157
Figure 5-21: Compaction could sometimes lead to fracturing of the crystal from the pressure of the SDS.....	157
Figure 5-22: Before and after plasma etching of silicon samples coated with the colloidal nanosphere mask. In b) the biomimetic nanostructures have been fabricated, causing light to be absorbed and the surface to turn black. The samples here are approximately 1.5 cm by 2 cm in size.....	158
Figure 5-23: Samples that were now on the centimeter scale could be made with a refined colloidal crystal deposition process and appropriate plasma etching parameters. These samples are approximately 1.5 cm by 2 cm long and much larger than the samples of the Figure 5-5 setup that only produced microscopic sized dense coverage moth-eye patterns on one silicon sample.....	159
Figure 5-24: A patterned silicon substrate that was used to create a PDMS stamp to pattern heat cured glue, UV cured glue, standard epoxies and medical epoxy. The specifics of fabricating the PDMS stamp are diagrammed later in this chapter.....	160

Figure 5-25: The features of Figure 5-24 were close packed as seen in this SEM image from above.	161
Figure 5-26: Time series showing the hydrophobic surface of the silanized nanostructured silicon substrate.	161
Figure 5-27: The nanostructured silicon surface was treated with a silane to produce a hydrophobic surface. The contact angle of a water droplet was found to be 135 degrees.	162
Figure 5-28: The nanostructures transferred to glue were sputtered with gold-palladium to be observable in the SEM.	163
Figure 5-29: The first transfer attempts had feature collapse and possible static effects. When enlarging the images of a) and c), the contact and leaning of the features are easily seen in b) and d) respectively.	164
Figure 5-30: A different silicon sample with more etch done and more space between the cones became the next candidate for PDMS mold and stamp fabrication.	165
Figure 5-31: The spacing differences of the nanostructured silicon from Figure 5-24 and Figure 5-30 are best seen when comparing the samples from above.	166
Figure 5-32: Small variation in process can change feature outcome. In this image the parameters that produced Figure 5-30 and Figure 5-31 were slightly adjusted, producing sharper features.	167
Figure 5-33: One variety of heat cured glue patterning produced results that were incorrectly shaped. This glue had a high viscosity and was not pursued further.	168
Figure 5-34: The next heat cured glue results. Some moth-eye like nanostructures are visible, but the pattern is small.	169
Figure 5-35: Large scale of heat cured glue showed good uniformity.	169
Figure 5-36: Different heat cure sample. This PDMS stamp did not have slight slope in the stamp as previous.	170
Figure 5-37: UV cure glue results were again not in the desired size range. Both a) and b) are the same image, but b) has measurements.	171
Figure 5-38: Large scale UV glue showed good uniformity.	172
Figure 5-39: The scanning electron beam can wear down the epoxy samples over time if the beam is focused too long on a single area.	173
Figure 5-40: Medical epoxy nanostructure patterning were short as well.	173

Figure 5-41: The medical epoxy large scale nanostructure patterning was uniform as seen with a tilt	174
Figure 5-42: A closer look at the medical epoxy from above without a tilt shows nice feature spacing.	174
Figure 5-43: Large scale hole pattern in the PDMS stamp looked normal upon inspection.	175
Figure 5-44: Results of UV glue that was heated before the mold was applied.	176
Figure 5-45: Results of UV glue applied in a vacuum. Long term b) ordering looked good , here seen at the edge of a sample where the sample was warped from the cutting pressure of a razor.....	177
Figure 5-46: Samples of UV glue being pushed for 1 minute by the mold showed good feature form and long range order.	178
Figure 5-47: Modifying the mold making technique was advantageous for creating taller features.....	179
Figure 5-48: The taller structures were also close packed with good long range order.	180
Figure 5-49: Cutting the molds for nanoimprint lithography required the mold to be cut to be approximately 1.5 mm thicker. If it was much thicker, there was a chance the UV glue would not cure since the PDMS could absorb some of the light.	181
Figure 5-50: Xenon lamp source, Digikrom monochromator and platform for characterizing the photodiode and SiPM detectors.....	182
Figure 5-51: Photodiode response with and without nanostructures from 450 nm to 650 nm.	183
Figure 5-52: Photodiode response with and without nanostructures from 400 nm to 800 nm.	184
Figure 5-53: SiPM response with and without nanostructures from 450 nm to 650 nm.	185
Figure 5-54: SiPM response with and without nanostructures from 400 nm to 800 nm.	186
Figure 5-55: A StellarNet integrating sphere setup with ASEQ spectrometer for LED characterization.....	187
Figure 5-56: LED output with and without nanostructures.	188
Figure 5-57: A schematic illustration showing the syringe pump with the cantilever arm slowly lifting the silicon substrate out of the water with the polystyrene nanosphere monolayer. d) The nanospheres are initially distributed across the water surface in an unordered monolayer. e) A dropper introduces a 5%	

solution of sodium dodecyl sulfate (SDS) that compacts the monolayer to form a highly ordered colloidal crystal that is deposited on the silicon while it is withdrawn from the water. f) The silicon becomes covered with the polystyrene nanosphere monolayer and set aside to dry.....	191
Figure 5-58: Steps to fabricate the moth-eye like structure include a polystyrene (PS) mask deposition on silicon, reactive ion etching (RIE), mold making, and stamping the pattern into UV curable adhesive on an optoelectronic device.	192
Figure 5-59: Examples of the a) biomimetic moth-eye nanostructures (scale bar 100 nm) and b) their long range order (scale bar 1 micron) as fabricated in optical adhesive.....	195
Figure 5-60: During the course of this work, it was found that fingerprint residue can have an effect and as a result, the non-contact holders were designed and 3D printed [92]. Reprinted with permission from "Nanostructured Stealth Surfaces for Visible and Near-Infrared Light", Ref [92], retrieved from https://pubs.acs.org/doi/abs/10.1021/acs.nanolett.6b03308 , © 2016 American Chemical Society. Further permissions related to this excerpted material should be directed to the American Chemical Society.	197
Figure 5-61: The patterned and unpatterned a) devices were each mounted in their individual 3D printed holders. The b) phantom finger placed between two device holders inside of an enclosure. The device holders held the LED and photodiode. An c) illustration showing how the device holders held the devices.....	198
Figure 5-62: Comparison of LED-PD (photodiode) coupling produced from combinations of moth-eye (ME) patterned and unpatterned (bare) LED and PD.	199
Figure 5-63: A normalized photodiode current response from a simulated PPG for patterned and bare LED/PD combinations scaled to the results from Table 5-6.	200
Figure 5-64: Comparison of LED-SiPM coupling produced from combinations of moth-eye (ME) patterned and unpatterned (bare) LED and SiPM.	201
Figure 5-65: A normalized photodiode current response from a simulated PPG for patterned and bare LED/SiPM combinations scaled according to the results of Table 5-7.....	202
Figure 5-66: An illustration showing how the pairs of patterned and unpatterned LEDs, photodiodes and SiPM were held with a holder to take the human PPG measurement a few millimeters away from the skin.	203
Figure 5-67: Example of a collected human PPG signal using the LED at constant voltage and photodiode. Signal height was measured peak to peak.	204

Chapter 1: Introduction

In recent years, there have been greater efforts to make photoplethysmography and pulse oximeter devices more wearable through the use of flexible technologies instead of rigid silicon devices. Flexible devices are less noticeable to the wearer and allow the devices to be used more often and universally. Groups have pursued this goal because pulse oximetry is a standard tool for assessing the well-being of an individual by examining the important health indicators of heart rate and blood oxygenation.

These kinds of measurements are done by probing tissue with light in either a reflective or transmissive mode. As a result, it is advantageous to find ways to make that light transmission more effective. The pliability of flexible devices allow the light emitter to be close to the skin which increases the signal to noise ratio by increasing the light coupling with the skin [1]. The advantages of conformal contact have been used to probe both large areas with arrays of devices [2] or on the millimeter scale [3][4].

This approach helped define one of the research goals of this dissertation to generate a potential design for flexible devices capable of PPG or pulse oximetry. This implementation achievement required identifying readily available components starting with the polymers. This needed to be accomplished because several of the current examples of related work did not reveal their exact chemical compositions for their solution processable active layers [1][2][3]. In another recent example, the authors did the opposite and were detailed in their selection of active layer materials, however, they used thermally evaporated organic layers, which could not be done with the local facilities [5]. Additionally, some of the prior work included processes such as screen printing and blade coating which were not available locally as well [1][2][5].

The challenge of this dissertation was to make a product with similar PPG or pulse oximetry function but with different resources than in literature. These challenges and constraints helped frame where the contributions of this work would be defined. The first contribution was locating active layer polymers from commercially available varieties. The light producing polymers were selected for emitting biologically relevant wavelengths of light for two different organic light emitting diode devices. The light detecting chemicals were picked since they were reactive in that spectrum range for creating the third device, a photodiode.

Simultaneously, another effort was underway with addressing the challenge of creating a repeatable uniform spincoats of PEDOT:PSS (Poly(3,4-ethylenedioxythiophene)-poly(styrenesulfonate)). To overcome this situation, a fluorosurfactant was attempted as an additive, which produced the desired even coating of the conducting polymer. It was an achievement that succeeded without having prior knowledge or an example indicating that the surfactant compound would function with the chosen manufacture variety of PEDOT:PSS.

The next contribution came from identifying a method to improve the intensity of light emissions since the initial light production was weak. A search was conducted for viable resolutions to this challenge. From this endeavor, a chemical doping process was found that enhanced the conductivity of the PEDOT:PSS layer. Its introduction led to the consequent achievement of more luminous devices without the need to alter the original active layer polymer selection that was already well suited for biologically relevant wavelengths.

However, in order to accomplish this contribution of more luminous devices, different spin recipes needed to be first identified for the various polymers that were layered on the PEDOT:PSS. These were discovered through iterative experimentation as literature was not

rich with proper spincoating instructions. Additionally, even if there had been detailed instructions available, they probably would have needed modification and specific tailoring to the local spinner and substrate selection.

The doping of the PEDOT:PSS led to other beneficial outcomes. Prior to the use of a dopant, the substrates needed multiple steps to have the ITO (Indium Tin Oxide) layer patterned. This began with meticulous application of small strips of tape to preserve a region of ITO that would become an electrode when the ITO covered substrate was exposed to acid. After the acid exposure was completed, the tape pieces would then need to also be removed cautiously with tweezers to avoid scratching the underlying ITO. With every substrate having multiple pieces of tape, this led to an extended processing time. The enhanced conductivity of the doped PEDOT:PSS allowed for this lengthy and hazardous manual procedure to be avoided. The patterning of the device could then be controlled with one single step, which was the thermal evaporation and deposition of the metal electrode. This single step of device patterning replaced separate steps across different labs. This achievement was a contribution in streamlining the fabrication process.

The doping of the PEDOT:PSS was also useful in transitioning the device fabrication from rigid glass substrates onto a flexible substrate. The acid patterning of the ITO layer required the protective tape to have good adherence to the substrate. However, the removal of this protective tape pulled on the substrate upon removal. For a flexible substrate this presented a problem because the action could warp or deform the substrate. The elimination of the acid ITO patterning process was a contribution that allowed the flexible substrate to be patterned without this added stress on the substrate being a variable. Another contribution that was closely related to this step was creating a unique carrier to support the fabrication steps of the

flexible substrate. An aluminum square coated with silicone rubber spun onto it, provided a stable platform that adhered well to the flexible PET plastic substrate of the devices and allowed for easy detachment later.

Interconnects to the devices and encapsulations were identified and developed as well, yielding further contributions different than what had been done in prior work. The interconnects were needed to connect the thermally evaporated metalized top electrode of the devices and ITO electrode to their respective leads and circuit connections. The contribution in this case was to locate a flexible conductive tape that could attach to the devices without impacting their operation or degrading them as had some of the silver epoxy traces that were used first. A number of conductive flexible tape options were explored before finding a solution that performed better than the others. The encapsulation also presented a challenge because when it was observed that the silver epoxies can degrade the devices, it was determined that it would be better to avoid the typical encapsulation method that usually involved epoxies. This was because their unknown solvents could have the potential detrimental property of penetrating the aluminized electrode and polymer underlayers as had the silver epoxies. Another solution explored was to demonstrate that polyimide tape could be carefully applied to encapsulate the organic device for the duration of a PPG test.

In addition to the polyimide tape encapsulation, the aforementioned leads were a contribution as well, since they needed to be selected with several properties. They needed to be several inches long and pliable enough to bend with the flexible substrate. The search included different kinds of wires with solid cores of different diameters as well as multistranded wires with varied amounts of strands. The final selection was not a wire, but custom cut lengths of polyimide coated copper cut from sheets of the material. These adhered the best with

the conductive flexible tape and could bend with the substrate without detaching. The successful use of these was a contribution that has not been seen in other examples of similar work.

Collectively, all these contributions led to the successful creation of subsequent OLEDs, which then led to the contribution of attaining a PPG and characterizing the OLEDs with the SiPM. Also, the PPG measurement was made possible by increasing the green OLED device size to approximately 0.49 cm^2 from the original 10 mm^2 . This final device surface area was larger than earlier designs made by an earlier group [5] and similar to the size of more recent devices [1][2]. When compared to one of the earlier devices of another group [5], the green OLED of this work used less power, 49 mW , when operated at 10V , than that group, which operated at 117 mW at 9V . When adjusted for device surface area, the green OLED of this work operated at 0.0998 W/cm^2 , which is close to Han et al (0.08 W/cm^2), but much less than Lochner et al (2.925 W/cm^2).

Another goal of this current work was to improve the light coupling for biomedical devices involved with photoplethysmography and pulse oximetry. A different approach was used than prior work, where they relied on conformal contact. Here, the light coupling enhancement came from biomimetic nanostructures inspired from features found on moth eyes. These structures help provide a smooth index of refraction change from one medium to the other, minimizing reflection losses. The nanostructures are placed on the surfaces of the optoelectronic devices. For the light emitters, the structures help channel the light out of the device and for the light detectors, they help channel additional light into the device. The concept takes into account that skin is not a perfectly smooth surface, and there can be air under a device or that certain optoelectronic devices may be designed to have air gaps under them.

The air introduces an index of refraction change that can be mitigated by the presence of these nanostructure features.

In the larger scope, this work shows conceptually that having biomimetic nanostructures on a light emitter and light detector sensing pair is beneficial for coupling the signal from one device to the other. From this it can be concluded that the presence of these structures can be beneficial at either reducing power levels without losing sensitivity or increasing sensitivity without needing additional power. This sensor configuration and design concept is what was submitted as a paper to an international IEEE Sensors Conference in 2019. Upon recognition of the concept's contribution, the paper was awarded a poster prize out of 466 competing papers with typically many more graduate student authors, while the paper related to the prize and this thesis had just one. An abridged version of the submitted paper that the poster was based upon can be found in Section 5.6 of this dissertation. There it is shown that when the air gap separated LED and photodiode pair were both patterned with the biomimetic nanostructures, there was a noticeable improvement in the operation of the system. For the same LED voltage and current settings as an unpatterned LED, the biomimetic patterned pair of light emitter and light detector devices saw a 21% increase in the photodiode current from approximately 15.9 nA to 19.3 nA. This signal increase came without needing to input more power into the LED or amplifying the photodiode output, and was accomplished by merely modifying the surfaces of the devices.

The recognition of the work's contribution from the IEEE Sensors community prompted further efforts to pattern devices and determine if a PPG measurement could be enhanced with the presence of the nanostructures on similar devices. As a result, patterned versus unpatterned pairs of light emitter and light detector devices were compared. LEDs and two kinds of

photodetectors, SiPMs (silicon photomultipliers) and photodiodes, were utilized with patterned versus unpatterned pairs being compared.

This additional contribution began with a phantom finger and a simulated PPG. For this scenario, the unpatterned pair produced an approximate 3.65 nA peak to peak signal, while the patterned pair produced 4.3 nA. This corresponded to the patterned LED and photodiode pairs showing an increase of 18% for the maximum photodiode current versus an unpatterned pair. When the experiment was modified to be done with patterned LED and SiPM pairs, there was also an increase. There was a 16.9% increase of peak to peak current for the patterned versus the unpatterned pairs. This corresponded to an approximate 2.07 mA versus 1.77 mA, respectively.

It was estimated that the percent increase performance of the LED-photodiode pair was more than the LED-SiPM pair because the index of refraction for the UV optical resin that composed the biomimetic features was more closely matched to that of the photodiode than the SiPM. The UV optical resin had an index of refraction of 1.56, while the SiPM's top glass layer was 1.5 and the photodiode's top layer was 1.57.

The next step was to then investigate the measurement of a human PPG on a finger. Here too an enhancement was seen with the patterned devices versus the unpatterned devices. For the LED-photodiode pairs, the measured peak to peak current was averaged to be 1.631 nA to 1.732 nA for the unpatterned device pairs. With the patterned device pairs of LED and photodiodes, there was an increase to 2.054 nA, which represented a 18% to 26% increase in photodiode current with the presence of the structures, without the need to put extra power into the system.

An increase was also shown with the LED-SiPM pair response for patterned devices versus unpatterned devices. In this case, unpatterned devices had a 9.021 mV peak to peak response (0.177 mA peak to peak) for the SiPM, while the patterned pair of devices had an 11.018 mV peak to peak response (0.216 mA peak to peak). This was a 22% larger peak to peak signal response for the patterned devices than the unpatterned devices at the same settings.

For both the LED-photodiode and LED-SiPM pairs, the increases in coupling, as defined by the increased signal response for the patterned pair of devices versus the unpatterned pairs, are clearly another contribution for this work.

As can be seen, this project touched upon many topics and had a wide foundation, resulting in many contributions relating to the work that was done.

1.1 Research Objectives and Contribution Summary

This section lists the hypotheses and research objectives for this dissertation. Some of these contributions were described in more detail in the prior section.

The two main hypotheses were as follows.

- LEDs and photodiodes can be fabricated on flexible substrates for the purposes of being used for PPG with the eventual goal of pulse oximetry.
- The patterning of the surfaces of light emitting and light detecting devices such as LEDs and photodiodes used for PPG or pulse oximetry can improve the coupling of the sensing system providing a greater signal strength.

These two research hypotheses required satisfying numerous research objectives because the work necessary was across a wide array of topics from chemistry, to physics, to material science, to circuits, to software, instrumentation, physical processes, plasma etching, etc. In doing so, the work to examine these hypotheses also required a fair amount of logistics

since the effort took place across 4 buildings, in 13 labs and rooms, which was a non-technical factor, but an element that needed to be considered throughout the project.

The principal goals required to demonstrate and test the hypotheses are summarized below, and reflect some of the contributions mentioned in the prior section:

- The successful selection of commercially available polymers with suitable spectrum, chemistry and other properties to work for PPG and eventually pulse oximetry devices.
- Fabricate devices with an active area of at least 10 mm².
- Create an optoelectronic device fabrication process that allows for device size to increase for experimental modification.
- Development of the optoelectronic device fabrication process on stiff substrates and successfully transitioning the process to flexible substrates, modifying it where necessary.
- Use nanosphere lithography to create an etching mask for silicon with nanospheres.
- Plasma etching silicon with different gasses and a nanosphere colloidal crystal mask to create biomimetic nanostructures in silicon.
- Develop method to create large scale coverage of silicon in biomimetic structures.
- Nanostructure mold creation, fabrication and testing.
- Nanoimprint lithography to transfer structures to surfaces for validation in SEM.
- Selection of UV resin with properties that help optimize structures.
- Transfer nanostructures to optoelectronic devices (LED, PD, SiPM).

- Test device coupling with a modified light emitter and a light detector.
- Use devices to attempt to take a physiological measurement like PPG.
- Observation and testing of improved signal coupling with modified devices for PPG.

1.2 Organization of this Thesis

Chapter 1 presents a brief summary of the project with the hypotheses, the project goals and contributions.

Chapter 2 explains the background information for this project, including the principles for photoplethysmography and pulse oximetry.

Chapter 3 is a review of existing work in photoplethysmography (PPG) and pulse oximetry.

Chapter 4 discusses the organic LEDs and photodiodes, in terms of how their materials were selected, how the devices were fabricated and processed, how interconnects were developed, device testing and a human PPG result.

Chapter 5 describes the fabrication of the biomimetic nanostructure in silicon with nanosphere lithography, along with the characterization of the nanocones. It is also discussed how the transfer of the nanopatterns were done with a dual layer mold to other surfaces, the characterization of the features on the secondary surface, the successful pattern transfer to LEDs, photodiodes and silicon photomultipliers allowing for signal measurement. The signal improvement was tested with a square wave, an artificial PPG signal and a human PPG result as well.

Chapter 6 mentions conclusions and suggestions for future work.

Chapter 2: Background for Pulse Oximetry and Organic Optoelectronic Devices

2.1 The Importance of Pulse Oximetry

Oxygen is needed for life, and having a way to measure its delivery is a useful method to help evaluate a patient's health [6]. Pulse oximetry is a technique that can do this in a non-invasive way by using different wavelengths of light. By evaluating the absorption of light, pulse rate and blood oxygenation can be elicited. This measurement can be done quickly and continuously which are both beneficial features since vital organs can be permanently damaged without adequate oxygen in a short time [6]. For the cerebral cortex of the brain, this irreparable harm happens the quickest in just mere minutes [6].

The detection of low arterial oxygenation can mean a variety of health problems, especially when there are issues with the lungs. It could be indicative of poor lung compliance, where pneumonia, fibrosis, acute respiratory distress (ADRS), pulmonary embolus or emphysema, which could reduce the lung's ability to stretch and expand [6][7]. A reduced arterial oxygenation level could also be a sign that there is airway resistance from illnesses such as cystic fibrosis, chronic bronchitis, or asthma [6][7]. Physical problems can also cause a drop in blood oxygenation from issues like choking, secretions from intubations, pus or obstructive sleep apnea. In some cases, low oxygenation can also mean damage to the phrenic nerve via lead poisoning or even congenital heart disease [6].

Pulse oximetry is often used during the anesthesia process for surgery. The anesthesiologist will apply the pulse oximeter for surgery and keep it on the patient for approximately an hour following the surgery [6]. Blood oxygenation is carefully measured under these circumstances because the administered anesthetic narcotics suppress the nervous system, while muscle relaxants stop a patient's natural respiration and allow airways to close [6]. In these situations, the patient's pulmonary control is compromised and the only way a

patient breathes at this time is through the oversight of the physicians, who maintain the life-giving blood oxygen concentration through intubation and artificial respiration [6].

When monitoring oxygenation, pulse oximetry is better than other methods because it is a leading indicator. This means that of the various parameters and variables that can be checked for oxygenation, pulse oximetry is among the technique where a change in oxygenation can be first detected. For instance, blood pressure lags behind a drop in blood oxygenation [6]. Despite the ability to monitor the heart's pulse with an electrocardiogram (ECG), the ECG indicates blood oxygenation problems even later than blood pressure changes. The other methods available are not much better. Checking for cyanosis can be done, but does not have the immediacy of pulse oximetry either because it may take time for the skin, fingertips or other body parts to turn a blueish hue indicating a lack of oxygen. Some last options available to the anesthesiologist would be to take oxygen, carbon dioxide and pH gas blood samples, but these can take several minutes to do [6].

The helpfulness and importance of pulse oximetry is perhaps best described by it being referred to as "the fifth vital sign" [7][8][9][10]. The additional four vital signs are pulse and respiratory rate, blood pressure, and temperature [7].

Considering the widespread acceptance and significance of pulse oximetry, it would be valuable to explore ways to enhance the technology. A way to accomplish this is to fabricate a pulse oximeter that aims toward increasing the efficiency of the device. This can be explored by utilizing organic electronics and having the benefit of other healthcare centric features, such as being flexible, easier to manufacture or disposable.

2.2 Pulse Oximetry Equations and Absorption Curves

Pulse oximetry measures the oxygenation level in the blood of the arteries and arterioles, referred to as arterial oxygen saturation [6]. In the body's circulatory system, this is the blood being pumped away from the heart. The rhythmic cycles of this pulsation are shown in Figure 2-1.

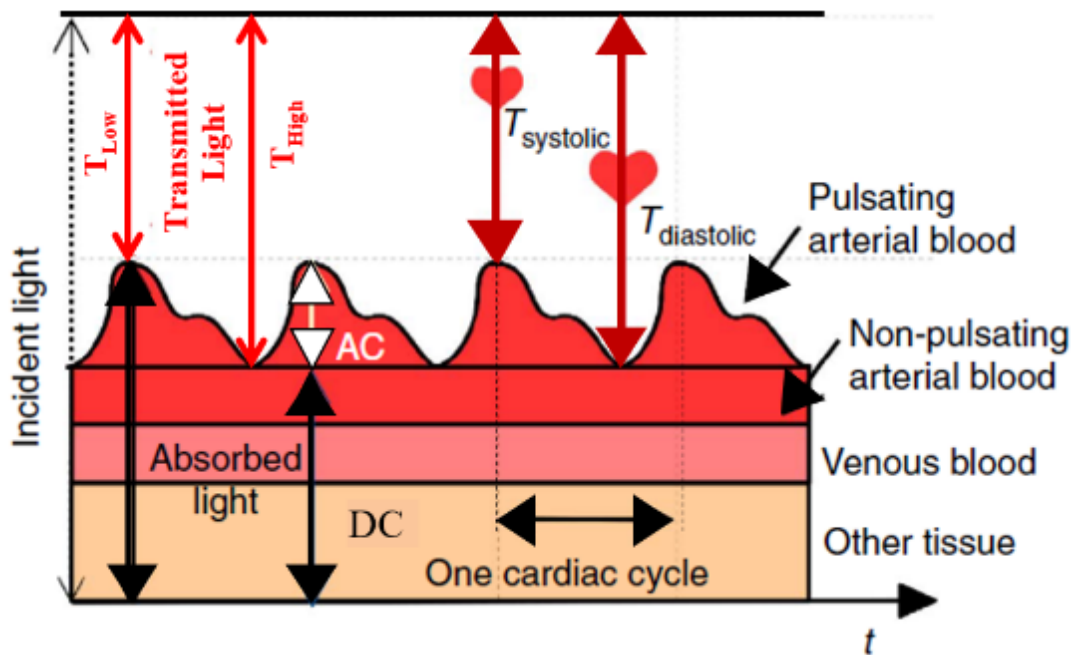


Figure 2-1: An illustration of several heart cycles of the absorbed and transmitted light in tissue showing the pulsating arterial blood, the non-pulsating arterial blood, venous blood and other tissue (adapted from [5]). The AC part of the signal comes from the pulsation of the arterial blood while the DC component is the non-pulsating arterial blood, the venous blood and blood in tissue [6][5]. The heart is contracting during the T_{systolic} time and resting during $T_{\text{diastolic}}$. The transmitted light is lowest when the heart is pumping blood, and higher while the blood is less in volume while the heart rests [6][11]. Adapted/Translated by permission from Springer Nature Customer Service Centre GmbH: Springer Nature Nature Communications [5] (Lochner et al), © 2014.

Blood oxygen saturation, SO_2 , is the ratio of oxygenated hemoglobin, C_{HbO_2} as compared to the total concentrations of oxygenated and reduced hemoglobin ($\text{C}_{\text{HbO}_2} + \text{C}_{\text{Hb}}$) as shown in equation 1 below [5][12].

$$SO_2 = \frac{C_{HbO_2}}{C_{HbO_2} + C_{Hb}} \quad (1)$$

Equation 2 defines the Ros , the so-called “ratio of ratios”, where the absorbance red light, A_{rd} , and green light, A_{gr} are compared. This ratio is then related to the transmittance [5][12].

$$R_{OS} = \frac{A_{rd}}{A_{gr}} = \frac{\ln (T_{n,rd})}{\ln (T_{n,gr})} \quad (2)$$

By combining the concepts of equation 1 and 2 , equation 3 can be derived to give a formula for arterial oxygen concentration, S_aO_2 , as shown below [5].

$$S_aO_2(R_{OS}) = \frac{\varepsilon_{\lambda 1,Hb} - \varepsilon_{\lambda 2,Hb} R_{OS}}{(\varepsilon_{\lambda 1,Hb} - \varepsilon_{\lambda 1,HbO_2}) + (\varepsilon_{\lambda 2,HbO_2} - \varepsilon_{\lambda 2,Hb}) R_{OS}} \quad (3)$$

In equation 3, $\varepsilon_{\lambda 1,Hb}$ is the absorptivity of reduced hemoglobin and $\varepsilon_{\lambda 1,HbO_2}$ is the absorptivity of oxygenated hemoglobin, measured at λ_1 (595 nm). Similarly, $\varepsilon_{\lambda 2,Hb}$ and $\varepsilon_{\lambda 2,HbO_2}$ are the absorptivities of reduced hemoglobin, and oxygenated hemoglobin respectively, but measured at λ_2 (535 nm). The wavelength values mentioned for λ_1 and λ_2 are chosen for this work specifically.

The selection of the wavelengths are done based upon the reduced and oxygenated hemoglobin states, as indicated in Figure 2-2.

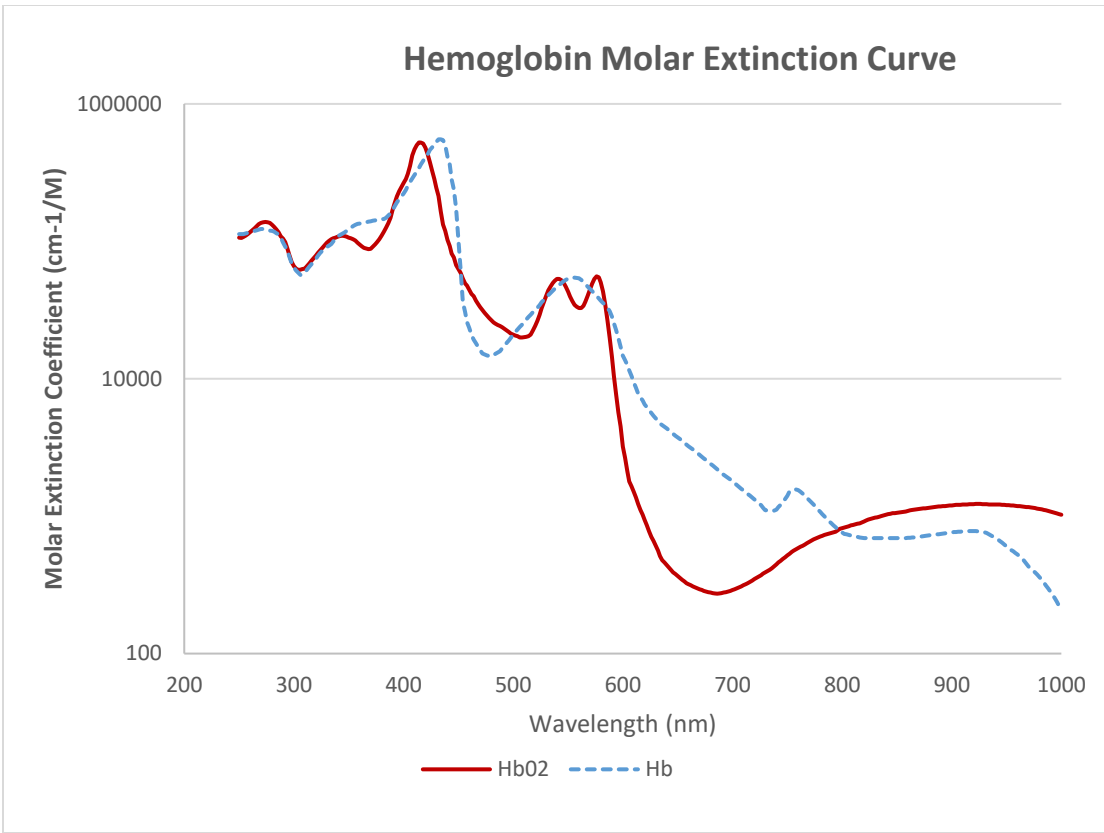


Figure 2-2: Hemoglobin Molar Extinction Coefficient Curve [13].

The places where the curves cross are called isobestic points and are where the light absorption is the same for the oxygenated and reduced forms of hemoglobin.

The differences in the oxygenated and the reduced hemoglobin absorption spectra are what pulse oximeters utilize to collect pulse rate and blood oxygenation information. Typically a red wavelength approximately 660 nm and near infrared approximately 900 nm are used. Other wavelengths can be used as well.

Figure 2-3 shows the kind of alignment that must occur for a pulse oximeter system to work. The emission spectra of the light emitters (OLED) must correspond to biologically relevant wavelengths of the hemoglobin extinction curve, with the photodiode response lining up with both the OLED and photodiode materials.

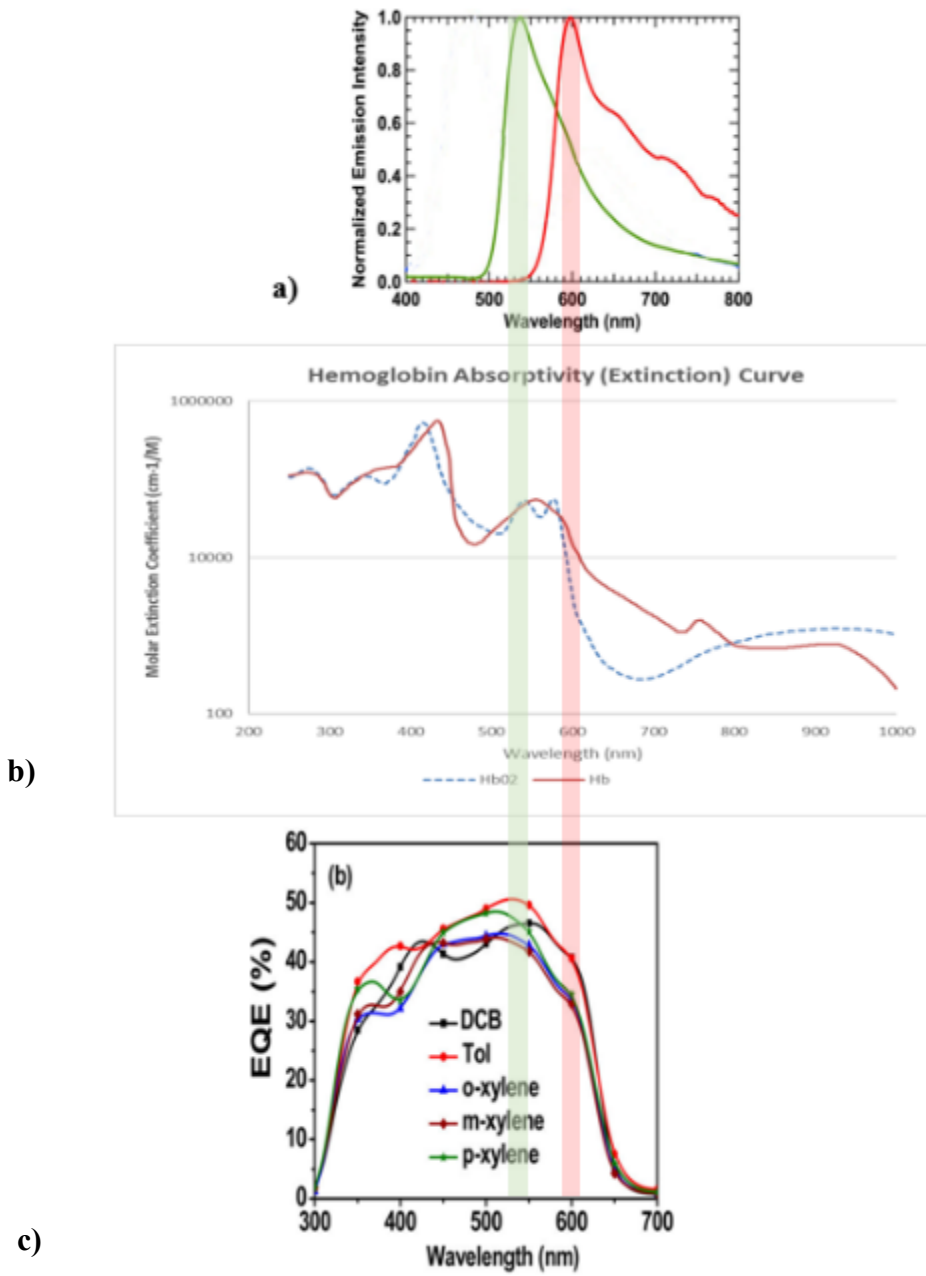


Figure 2-3: Aligning the a) emissions of the OLEDs (adapted from [14] © 2015, Haigh et al. under CC-BY license 4.0: <https://creativecommons.org/licenses/by/4.0>), b) the hemoglobin absorptivity curve [13], and c) the organic photodiode response for this work [15]. Figure 2-3c) Reprinted (adapted) with permission from [15], © (2014) American Chemical Society.

2.3 For Comparison – A Quick Review : Inorganic LED and Inorganic Photodiode Operation

Since inorganic LEDs and photodiodes are more widely known, it is useful to review how these more common devices work as a comparison with the organic devices.

An inorganic LED is typically made of P-type and N-type silicon pieces joined together forming a junction of the two materials. Under forward bias, the holes injected from the P-type silicon can combine with the electrons injected from the N-type silicon to emit light in a process referred to as radiative recombination [16][17]. The band gap will determine the energy of the photon emitted from the meeting of the electron and hole [16]. Figure 2-4 illustrates the light emission process of a silicon LED.

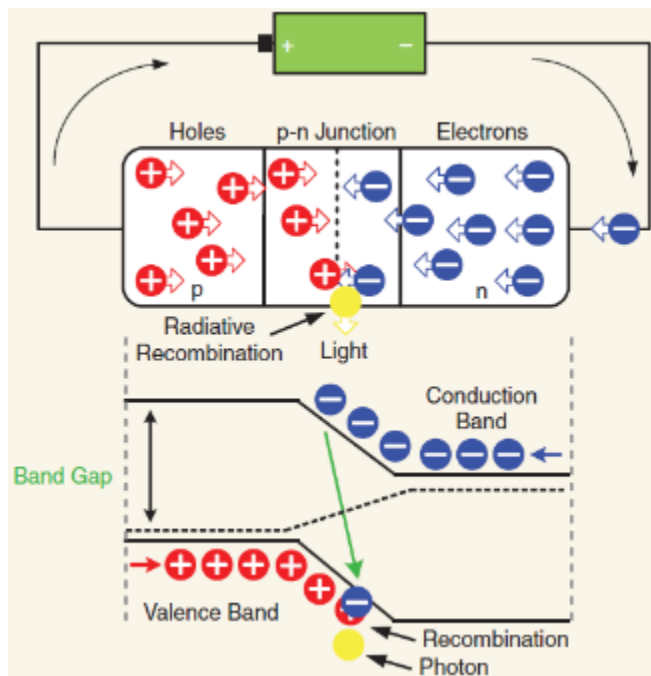


Figure 2-4: Silicon LED creating light by the recombination of electrons and holes at the p-n junction, © 2015 IEEE [16].

Figure 2-5 illustrates how the radiative recombination process would schematically occur in a lattice. The same figure also shows how non-radiative recombination is possible as

well, where the electron energy does not result in a photon, but instead becomes phonons, vibrations in the atomic lattice [16].

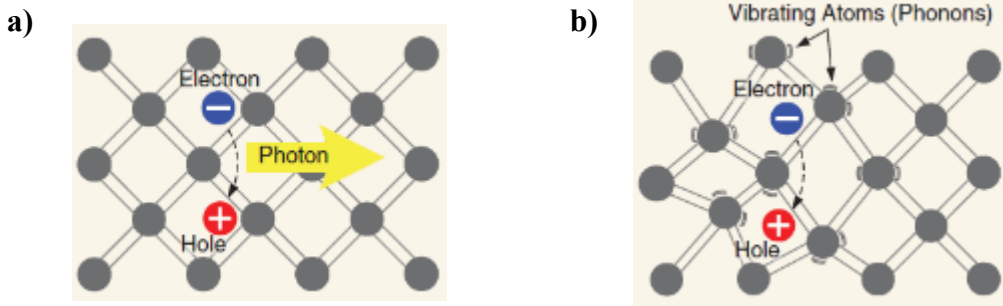


Figure 2-5: Radiative recombination and non-radiative recombination are possible, © 2015 IEEE [16].

Silicon based photodiodes and photovoltaics have the opposite function of LEDs. Instead of using electricity to generate light, they use light to generate current. If light with an energy greater than the band gap of silicon, 1.1 eV, then it can create an electron-hole pair in the depletion region of a photodiode. The internal electric field of the depletion region ushers the electron to the N-side of the p-n junction and the hole goes toward the P-side [18][19].

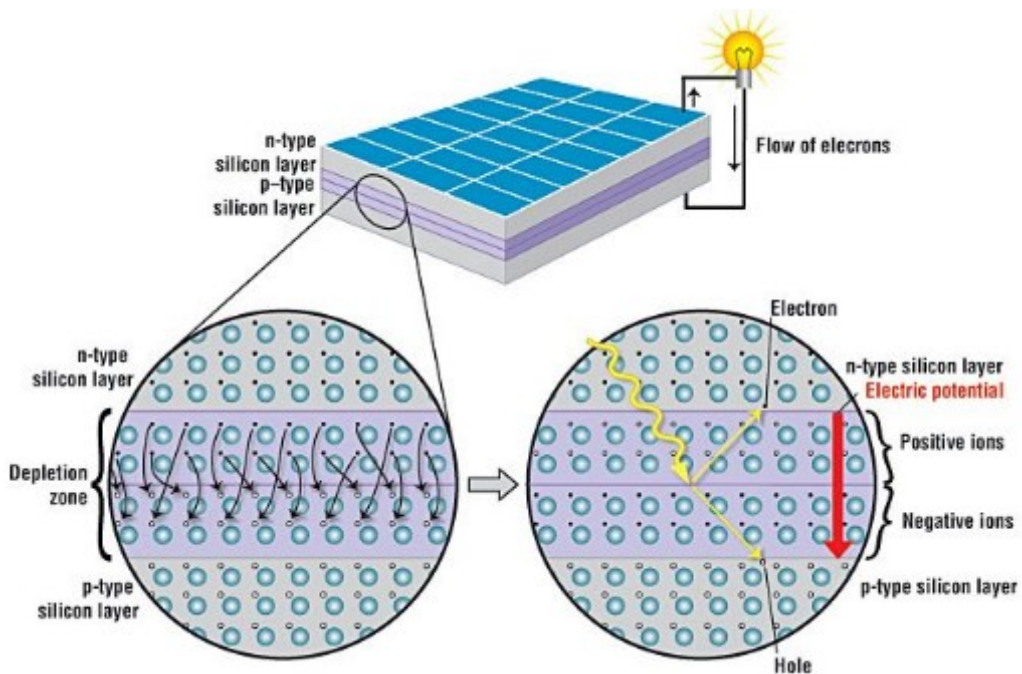


Figure 2-6: When incident light has enough energy (greater than the 1.1 eV band gap of silicon), it has enough energy to create an electron-hole pair in the depletion region of a p-n junction of a photodiode or solar cell. Shown is a solar cell, but a photodiode would have the same result with the difference being that its circuit would reverse bias the photodiode to maximize sensitivity [18] [19]. Image © (2013) American Chemical Society, [19].

2.4 Theory of Operation for Organic LEDs (OLEDs)

The most basic OLED construction of an OLED is a conducting organic layer sandwiched between an anode and a cathode [16][20]. The anode can be made of a transparent conducting material, such as indium tin oxide (ITO) deposited on a substrate, which allows the light to exit [20][16]. This rudimentary kind of OLED design is seen in Figure 2-7a with a substrate of glass and reflective metal cathode [16][20]. Figure 2-7b shows the energy diagram of such a single layer OLED when a voltage is applied and an electric field established [16] [20][21]. Electrons are injected from the cathode side into the organic layer, and holes are injected from the anode on the opposite side [20][21]. These two charge carriers then move across the organic layer towards the electrodes of the opposite charge[21][22]. The holes hop from molecule to molecule along the highest occupied molecular orbitals (HOMO), while the

electrons travel in lowest unoccupied molecular orbitals (LUMO) moving in the opposing direction [16] [20][22]. If the electrons and holes are on the same molecule, they may combine to create an exciton, a bound electron-hole pair [22][23][24]. Some of the excitons may then relax into their ground state and in the process, emit light [20][21][22].

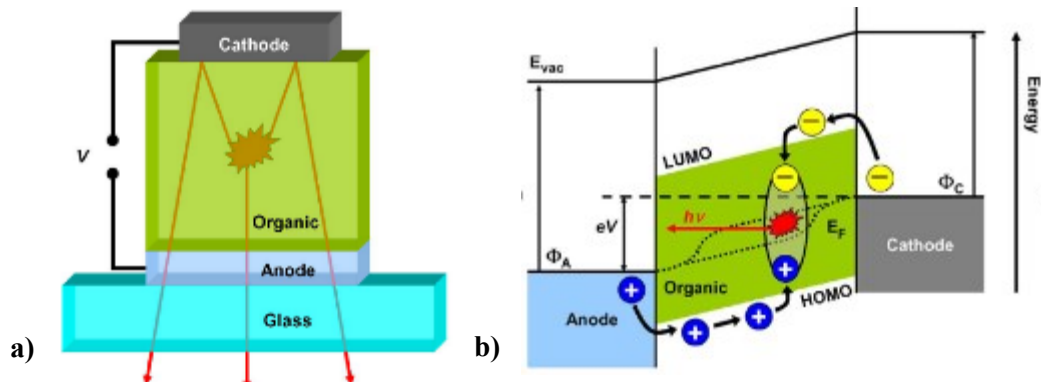


Figure 2-7: a) A rudimentary OLED and b) its energy diagram during operation [20], © 2009 IEEE.

As mentioned earlier, Figure 2-7 is a basic example of an OLED with only one layer. Figure 2-8 shows an example of an OLED where several layers with different functions are included to enhance device performance [16][20]. The hole transport layers (HTL) and electron transport layers (ETL) promote charge injection from the anode and cathode, respectively. The right selections of these materials can increase the device's power efficiency and lower the operational voltage [20]. The electron blocking layer (EBL) and hole blocking layer (HBL) function to restrict the movement of the charge carriers out of the organic emissive layer (EML) after their arrival [20]. This helps with balancing the charges and increases their chances of encountering each other to generate light via the exciton and recombination process [20].

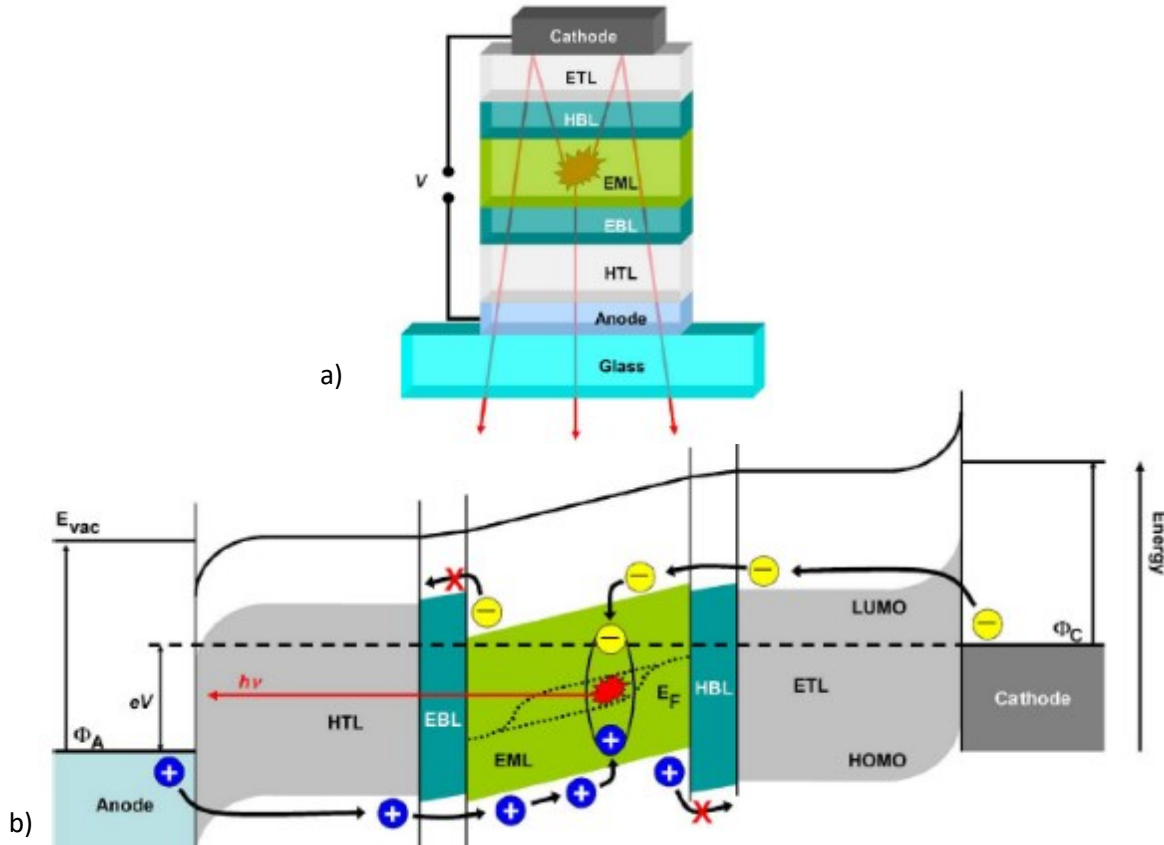


Figure 2-8: A multi-layered OLED with layers that enhance the device's functioning [16][20], © 2009 IEEE, © 2015 IEEE.

There can be some combining of these layers to reduce the total number of layers present in a device. With the proper material choice, the HTL and EBL could be merged into a single layer and serve the purpose of both layers. A material could be selected also to be a HBL and ETL, making that a single layer as well. A diagram showing this is seen in Figure 2-9.

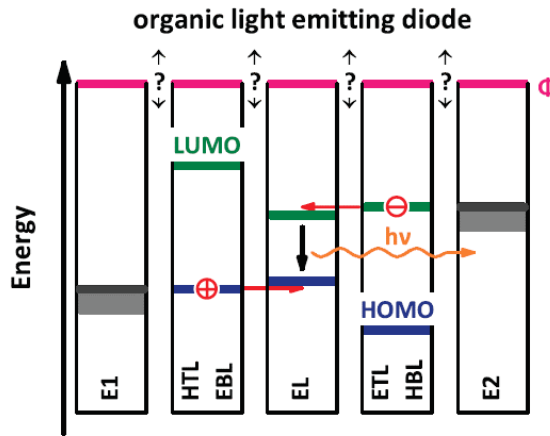


Figure 2-9: Energy diagram where the HTL and EBL have been merged in function, as well as the ETL and HBL combined [25]. E1 and E2 are the electrodes with E1 being a high work function electrode and E2 a low work function electrode. The question marks were used by the original author to indicate possible shifts in energy levels at the interfaces. © IOP Publishing. Reproduced with permission. All rights reserved.

The efficiency of OLEDs is measured by its external quantum efficiency (EQE), η_q , describing the ratio of photons that are emitted to the number of electrons injected into the device [20][26].

$$EQE = \eta_q = \frac{Photons}{Injected\ Charge} = \gamma \chi \eta_r \xi = \eta_i \xi \quad (4)$$

Here, γ is the charge carrier balance and defines the probability that an electron will meet a hole, combining to create an exciton [20][21]. χ is the exciton spin factor [20]. For fluorescent emitters, χ is 0.25, while for phosphorescent and thermally activated delayed fluorescent (TADF) emitters it can be 1 [20][26]. η_r describes how efficient the radiative decay of the emitter substance is, given by the ratio of emitted photons to generated excitons [20]. The remaining term, ξ , is a factor representing the fraction of light delivered out of the device and available to be used [26]. The first three terms can be combined to be referred to as the η_i , the internal quantum efficiency [20].

A visualization of the EQE factors which makes the concept clearer is shown in Figure 2-10.

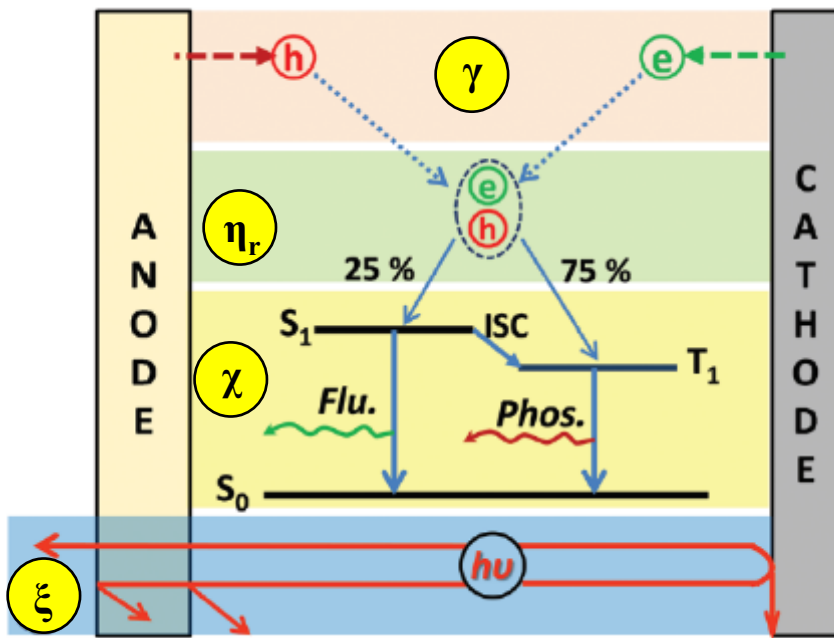


Figure 2-10: Factors that determine the EQE of an OLED. Adapted from Ref. [27] with permission from The Royal Society of Chemistry.

2.5 Theory of Operation for Organic Photodiodes (OPDs)

Organic photovoltaic are layered devices like OLEDs. The simplest construction would be two electrodes attached to the outside of an organic acceptor (A) and donor (D) layer in planar contact with one another as shown in Figure 2-11a [28].

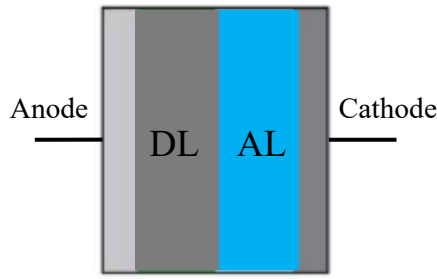


Figure 2-11: a) A basic organic photovoltaic where DL is the donor layer and AL is the acceptor layer , adapted from [28], © IEEE 2010.

The process for organic photovoltaics operation is shown in Figure 2-12. It begins when there is an absorption of light which generates excitons [25][28][29]. The resulting exciton diffuses to the donor-acceptor interface where the excitons disassociate into charge carriers [25] [28][29][30]. The charge carriers can then be collected at the electrodes [28].

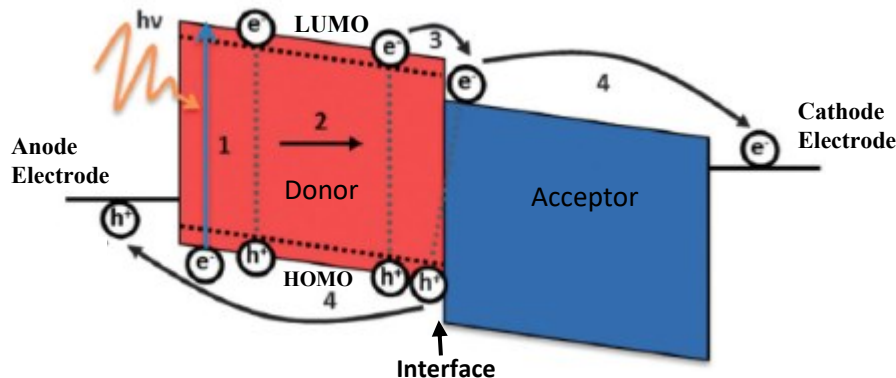


Figure 2-12: The energy diagram of an OPD, showing the overall process [25][30][31]. Reprinted (adapted) with permission from "The future of organic photovoltaics", Ref. [31] , © 2015 The Royal Society of Chemistry, <https://pubs.rsc.org/en/content/articlelanding/2015/CS/C4CS00227J> .

Others diagram of this same process are given in Figure 2-13 without energy levels to give a way of visualizing the charge generation process concept in OPDs at a molecular interface level.

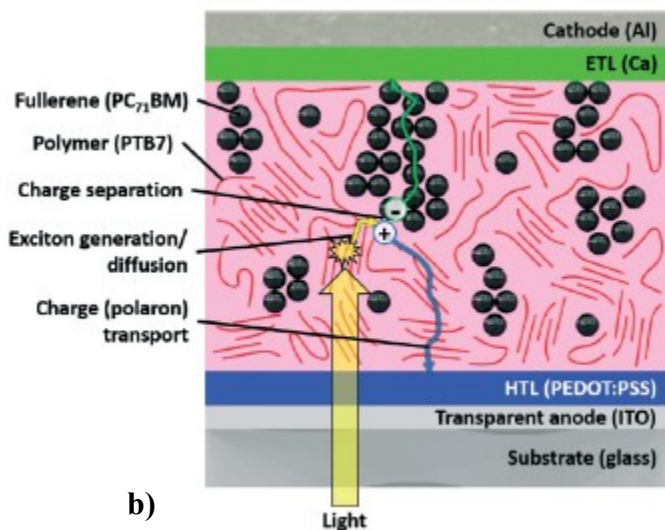
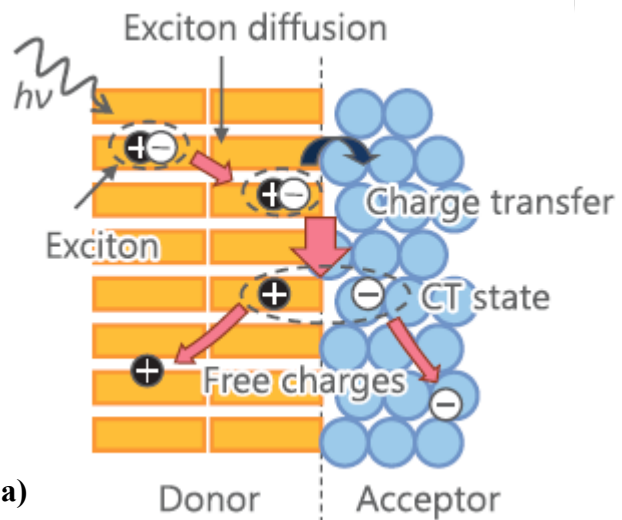


Figure 2-13: Additional diagrams showing the charge generation process. A bi-layer planar heterojunction (PHJ) a) has a straight plane interface between the donor and acceptor [29] (Reprinted by permission of John Wiley and Sons, Inc. © 2016 WILEY-VCH Verlag GmbH & Co. KGaA, Weinheim). In contrast, b) shows a bulk heterojunction (BHJ) for an OPD where the donor and acceptor have been mixed together [30] (Reprinted from Ref. [30] with permission from The Royal Society of Chemistry).

Power conversion efficiency (PCE), η_e , is how an OPD can be rated. This is a ratio of the maximum amount of electrical power that can be created by the OPD to the amount of light incident light on the device. It is given by the following equation [31][32][33].

$$\begin{aligned}
\text{PCE} = \eta_e &= \frac{P_m}{P_{in}} \times 100\% = \frac{J_m \times V_m}{P_{in}} \times 100\% \\
&= \frac{V_{oc} \times J_{sc} \times FF}{P_{in}} \times 100\%
\end{aligned} \tag{5}$$

Where P_m is the maximum electrical power, P_{in} is the total incident light power, V_{oc} is the open circuit voltage, and FF is the fill factor. The fill factor, FF , is given by [31]:

$$FF = \frac{J_{MP} \times V_M}{J_{SC} \times V_{OC}}$$

J_{MP} is the current density at the device's maximum power point, M_{pp} , while V_M is the voltage at the same point [31][34]. J_{SC} is the current density during short circuit and V_{OC} is the open circuit voltage [31][34]. If the OPD could deliver maximum current (J_{SC}) and maximum voltage (V_{OC}), then the resulting power would be the product of $J_{SC} \times V_{OC}$. This can be visualized by the dashed blue box in

Figure 2-14.

The product of $J_{MP} \times V_{MP}$ can be seen as the box made by the solid red solid line. The comparison of the two boxes is what the FF represents. The FF is regarded as the “squareness” of the J-V curve and how readily charges can be extracted from the photovoltaic device [31][34].

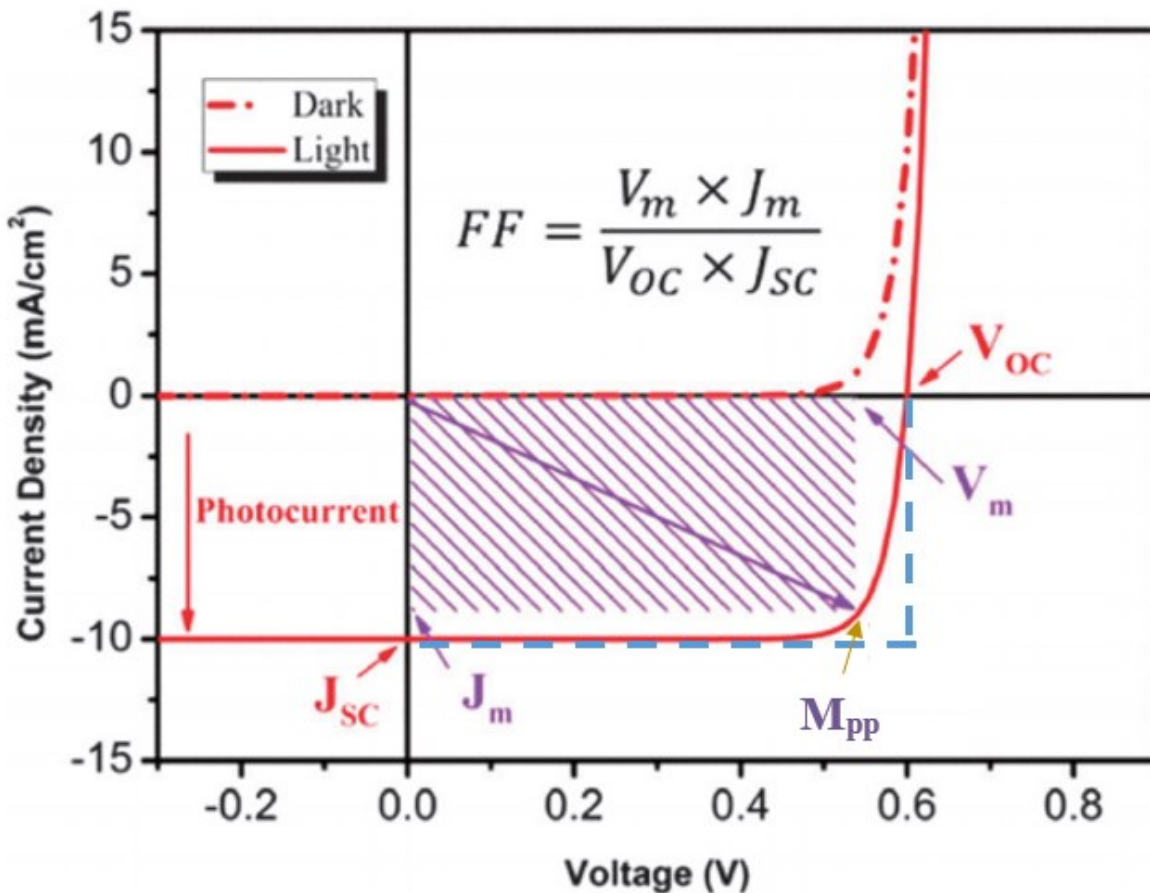


Figure 2-14: Visualization of the Fill Factor [31][34] (Adapted from Ref. [34] with permission from The Royal Society of Chemistry). The J-V (current density – voltage) curve of an OPD during light exposure (solid red line) has two points , the open circuit voltage (V_{oc}) and short circuit current (J_{sc}), that make a rectangle (diagonal lines). As shown by the formula in the figure, the Fill factor (FF) can be determined and seen as the ratio of the diagonal line square to the blue line dashed square. The red dashed line represents the device’s characteristics during dark conditions.

Figure 2-14 shows that the best possible value for the fill factor would be when the two rectangles entirely overlap [34]. However, with even a small voltage deviation from V_{oc} , the current density can change to its largest value, J_{sc} and remain steady at that value when there is applied voltage from the open circuit voltage to zero or even when a substantial large reverse bias is applied [34]. Actually, the fill factor has not attained 100% for either organic or inorganic devices [34]. For organic photovoltaics, the fill factor tends to vary around 50 to 70% [34]. In the more conventional inorganic photovoltaics, the best fill factor reported has been

90% [34]. The FF can be modified by numerous factors which are complexly interconnected [34].

Another indication of an organic photovoltaic's performance is given by the external quantum efficiency (EQE) [31]. This is the overall efficiency of an OPD for a given wavelength, as given by the equation below [31].

$$\text{EQE}(\lambda) = \eta_{\text{abs}(\lambda)} \times \eta_{\text{diff}(\lambda)} \times \eta_{\text{CT}(\lambda)} \times \eta_{\text{coll}(\lambda)} \quad (6)$$

Equation 6 brings together the chief factors of absorption, exciton diffusion, charge separation and charge collection by their efficiency terms [31]. The photoabsorption efficiency and exciton diffusion efficiency are given by $\eta_{\text{abs}(\lambda)}$ and $\eta_{\text{diff}(\lambda)}$, respectively [31]. While the exciton diffusion efficiency to the donor/acceptance junction is given by $\eta_{\text{CT}(\lambda)}$ and the charge collection efficiency is given by η_{coll} [31].

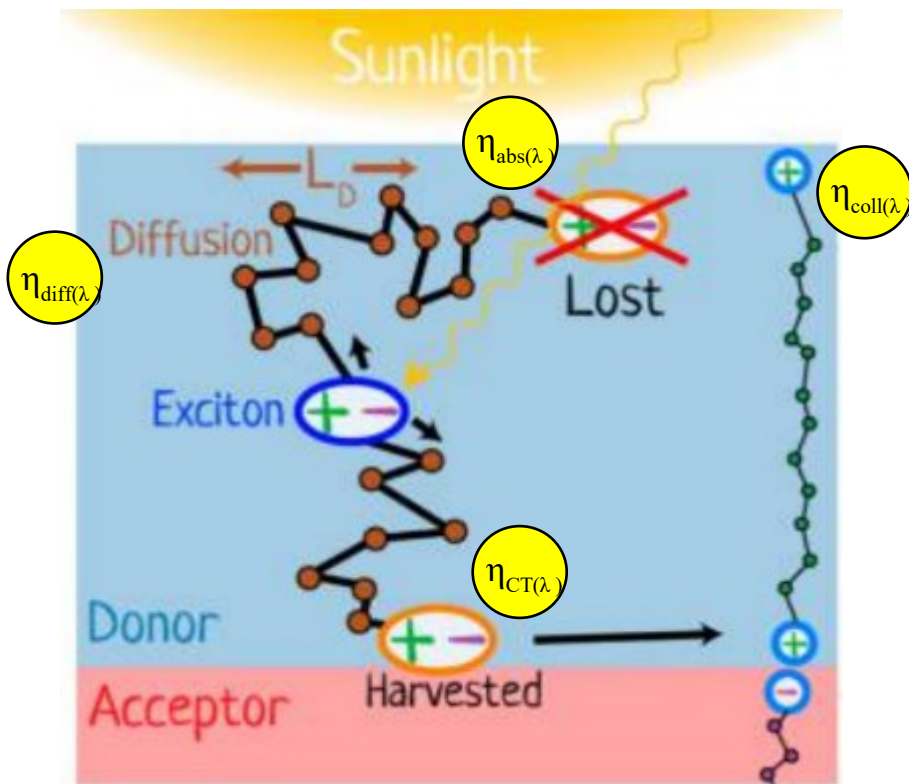


Figure 2-15: A schematic showing the factors determining EQE for OPDs [31][35] (Image adapted from Ref. [35], © 2016 American Chemical Society).

The efficiency of an OPD can also be improved by increasing the surface area of interaction of the donor and acceptor layers [25]. Two such ways are to interdigitate donor/acceptor layers or intermix donor/acceptor materials [25].

Furthermore, fullerenes and chemicals based on them have been the best acceptor molecule candidates due to their electron affinity and high charge mobility [36].

2.6 Background for the Biomimetic Moth-Eye Nanostructure

The biomimetic moth-eye nanostructures referred to this work are features smaller than the wavelength of light and channel light from one medium to the other by introducing a smooth change in the index of refraction. When the nanostructures are put on the light emitters, they help light escape into the air from the device, and when put on a photodetector, they help light to couple into the device.

This solution is of interest for light emitters because up to 30% of the light is lost at the glass and air interface, and for flexible OLEDs, only about 18% of light is coupled out [37][38]. As for light absorbers, such as solar cells, reflection loss from the top surface must be overcome to bring in as much light into the device as possible [39].

Due to their beneficial properties for optical devices, the nanostructures have since been used on organic light emitting diodes OLEDs, LEDs, solar cells and organic photodiodes for improving the device performance [40][41][42][43][44][45][46].

The nanostructures work by suppressing the Fresnel reflection that occurs when light goes from one material to another [47][48]. This is done by making their dimensions sufficiently small so they do not scatter light in the ray optics regime where features are much larger than the wavelength of light [49]. Instead, the nanostructures have a feature size below that of visible light wavelengths and interact with light as a bulk material with a varying index of refraction defined by the weighted volume average of one substrate in relation to the other.

The other requirement for these structures to function is that they should be regular in arrangement and size to be considered a zero order diffraction grating [39]. This will avoid diffraction grating scattering effects [37]. For this condition to be met, the period of the structures should be less than the light wavelength divided by the substrate's index of refraction [37][50]. The final criteria is that the height of the structures should be larger than approximately half the wavelength to reduce reflection to under 0.5% [50]. A second reference also gave the relation that the period should be less than the wavelength and it should be less than 2.5 times the height in order to have a reflection under 0.5% [51]. The above mentioned conditions were used as guidelines for this present work.

For this work, COMSOL models were also created to demonstrate the concept using the nanostructures to couple light in and out of surfaces. The first model shows a flat surface with light shining on it and reflection results without any nanostructures being present. It has a reflection of 4.64%

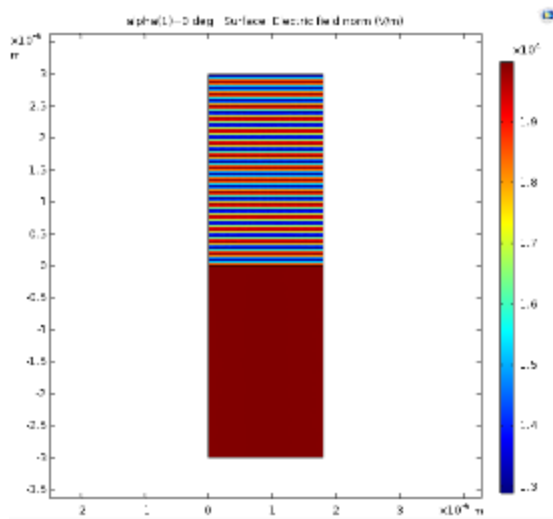


Figure 2-16: COMSOL model showing the reflection and transmission of light (600 nm) with a flat surface ($n=1.539$). Light comes from the top, through air, down to the surface. At a normal (0 degree) angle, there is an approximate 4.64% reflection and 95.4% transmittance.

The next model introduces nanostructures that are 300 nm tall and have a 200 nm period. The reflection for 600 nm light now drops to be 0.04% with a transmission of 99.56%, as detailed in Figure 2-17.

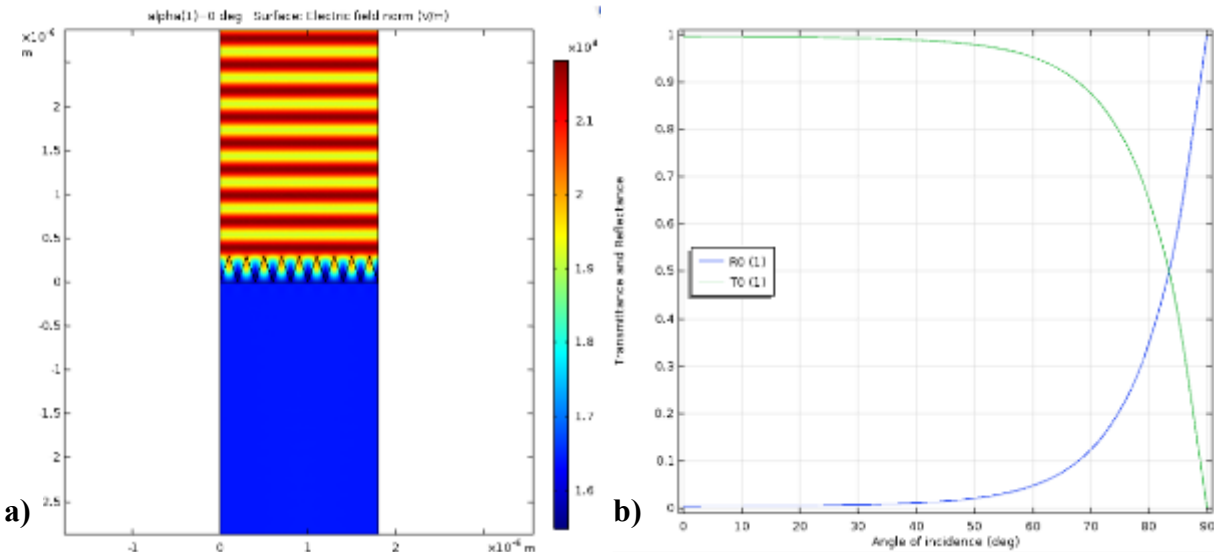


Figure 2-17: COMSOL simulation with 300 nm tall biomimetic nanocones with a 200 nm period placed on the surface. In the image on the left, a) light (600 nm) again comes from the top, through air ($n=1$), down to the surface ($n=1.539$). For b) the reflection and transmission graph, the reflection has been minimized. At a normal (0 degree) angle, the reflection is a 0.04% and the transmission is 99.56%.

In the last simulation, light is generated inside the solid on the bottom of the model and then propagated upwards to where the 300 nm tall nanocones are with a 200 nm period. The smooth change in the gradient of refraction makes the transmission to be 99.56% and the reflection to be 0.4%. This is detailed in Figure 2-18.

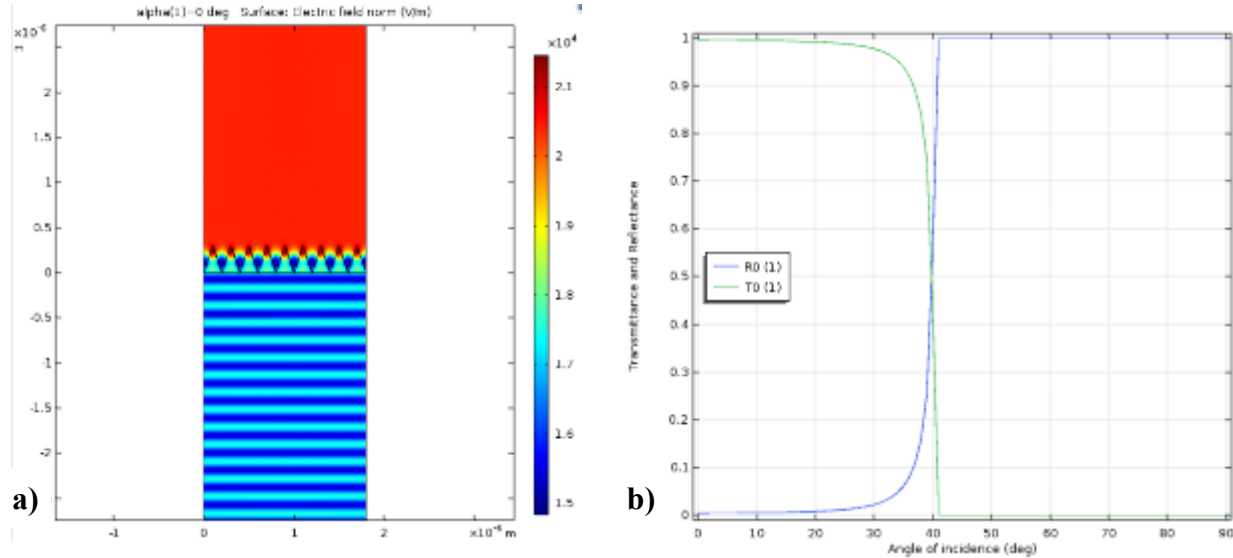


Figure 2-18: COMSOL simulation with 300 nm tall nanocones with a 200 nm period placed on the surface. In this situation, the light comes from below ($n=1.539$), to the surface where there are nanocones and then air ($n=1$). At a normal (0 degree) angle, there is 99.56% transmittance and 0.4% reflection.

The index of refraction for the materials of this work indicate why the nanocones can be useful. The index of refraction of skin (epidermis) has an approximate value $n = 1.4$ for the wavelengths of this work [52]. Air has a value of $n=1$, for PET plastic $n=1.58$ and for the glass or epoxy found on inorganic LEDs and other devices, $n=1.5$. The corresponding values of normal incidence reflection between air to glass is 4%, glass/epoxy to skin 0.06%, PET to skin is 0.25% and air to PET plastic is 5.1%. When there is an air gap either intentionally designed under a device or there is unintentionally air there within the ridges, folds and imperfections of skin, the nanocones can help increase light transmission and improve signal coupling between light emitter and light detecting sensors.

Chapter 3: Organic Device for Pulse Oximeter and PPG Literature Review

3.1 Advantages to Organic Electronics for Pulse Oximetry

Organic electronics are a compelling option for optical devices like a pulse oximeter because this technology can manufacture inexpensive, flexible devices and sensors that be fabricated at low or room temperatures without the high temperatures used in inorganic device manufacturing [53][54][55]. This allows thin filmed organic devices to be constructed directly onto flexible plastic, organic substrates and other wearable substrates that would not otherwise withstand the inorganic device harsh fabrication procedures [55].

Examples of using organic electronics span a number of applications. They have been used in the opto-microfluidic devices for hormone, pathogen and water borne illness detection [56][57][58][59][60]. For health related devices, organic electronics have been used for observing overall blood flow dynamics, muscle contractions and pulse oximetry [3][5][61][62].

Important for pulse oximeters are the light emitter photonic organic devices which are usually referred to as organic light emitting diodes (OLEDs) or sometimes polymer light emitting diodes (PLEDs) if their active layer is a polymer. Light absorbing organic photonic devices are also key for pulse oximeters. In literature, organic light absorber devices can be referred to as organic photodiodes (OPDs), organic solar cells (OSCs), or organic photovoltaics (OPVs).

Another attractive reason for pursuing organic optoelectronics is the potential to use methods that lower manufacturing such as roll-to-roll printing and solution processing [5] [55][61][62]. This can in turn benefit consumers and hospitals by providing, low cost, imperceptible and disposable medical devices [5][55][62]. The flexibility, lower costs of processing, and scalability also offer the opportunity to make new kinds of medical sensors of novel dimensions and shapes that increase the locations on the body where sensors can be

utilized, ways to non-invasively monitor life signs and altogether provide additional health diagnostics about the wearer [1][3][5].

More specifically, in traditional pulse oximetry the location for the measurements are usually done on the heads, hands or feet [63]. The reason for this is because there is low variability in these zones between subjects, the areas are easy to access and there is excellent perfusion of the face, ears, fingers and palms [63]. However, there are cases where these places are not available. For instance, a fingertip sensor would interfere with the regular activities of the day [64]. Very similarly, in the case of soldiers, they require heads, hands and feet for their tasks [63]. The same could be argued for race car drivers, performance athletes and pilots. In all these cases and more, it would be better if the pulse oximeter or PPG device could be placed somewhere else out of the way. By using flexible organic electronics, it becomes possible to accomplish this goal.

In terms of health devices, a flexible organic electronic device has the additional advantage of being able to follow the skin contour closely and be placed on the body which is a moving, dynamic surface. Unlike a stiff and rigid silicon based electronic device that may shift on the surface during body movement, an organic electronic remain in contact with the attachment area even when the skin is stretching or moving [65][66].

This capability of organic electronics to be conformal offers several advantages over the rigid silicon electronics. By being conformal and not shifting during movement, the organic electronic devices could have a better signal to noise ratio due to the decreased introduction of motion artifacts [65][66]. Device conformality also means greater comfort to the wearer of the device, whether it be a patient, an athlete or an average individual interested in monitoring their own health [5]. Comfort to the user also means they are more likely to wear the device for

longer lengths of time and in hospital settings this may help shorten hospital stays and costs [5] [6].

3.2 OLED and OPD Coupled Systems for Health Monitoring in Literature

Coupled OLEDs and OPDs have been shown in literature to be used in personal health sensing devices for photoplethysmography (PPG) and pulse oximetry systems. In both implementations, light is used to non-invasively probe blood or tissue. For PPG, one wavelength of light is sufficient to detect the blood volume changes. In pulse oximetry, the oxygenation level of the sample is determined with two wavelengths of light.

With either PPG or pulse oximetry, the emitted light comes from the OLED(s) and is scattered through the biological medium. The detection of the emerging light can be done on the opposite side of the sample if it is sufficiently thin. Another design is to have the OLED(s) and the OPD on the same plane, but separated by a distance. In this situation, the OPD detects light that has scattered into the biological medium, emerging back at the surface after following a curved “banana-like” shaped path through the sample.

To date, there have been a small group of organic optoelectronic PPG and pulse oximeter devices.

The earliest implementation appears to be by Koetse et al in 2008 who fabricated an OLED and OPD coupled system as a proof-of-principle for a “smart bandage” device that could detect PPG [68]. (In this isolated case, their acronym for the OPD stood for “organic photo detector”.) They fabricated a glass substrate device with two red OLEDs and one photodiode based on poly(3-hexylthiophene) (P3HT) and [6,6]-phenyl C₆₁butyric acid methyl ester (PCBM).

The authors report the OLEDs had low efficiency which caused a heating issue, making the device quickly heat up to 60 °C and be unusable for prolonged contact with the skin. They switched from a red emitting polymer with a 0.45 cd/A efficiency to a yellow emitting polymer with a 10 cd/A efficiency. With this change of polymer, the device could operate at a lower current density and voltage and maintained a working temperature below 35 °C .

Koetse et al suggest that a PPG was possible because there was a part of the yellow polymer emission that was in the red wavelengths typically used for PPG. The authors report that with their organic optoelectronic system, they could acquire a PPG signal from the fingers, wrist and forehead. An example of their signal detection as compared to a commercial pulse-oximeter can be seen in Figure 3-1.

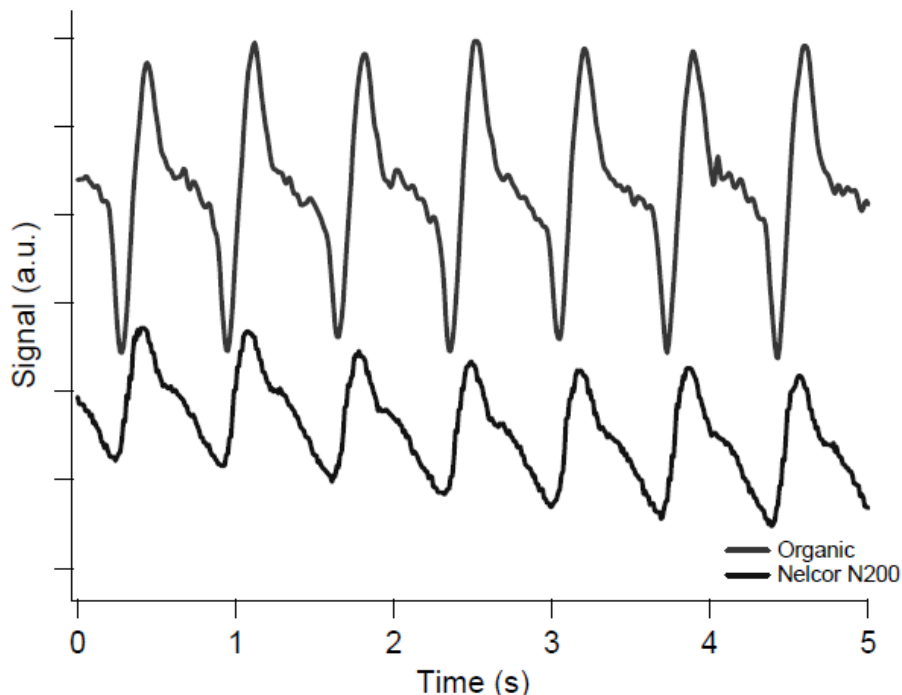


Figure 3-1: An acquired PPG signal using the OLEDs and OPD fabricated by Koetse et al (top) as compared to a commercial inorganic pulse oximeter by Nelcor [68]. Reproduced with permission from SPIE and Dr. F. Wieringa.

A coauthor of the Koetse et al work and a member at the same institution, Wierenga et al also mentioned the same “smart bandage” as part of on-going work and produced a similar graph as Figure 3-1 but also included an ECG reference as shown in Figure 3-2 [69].

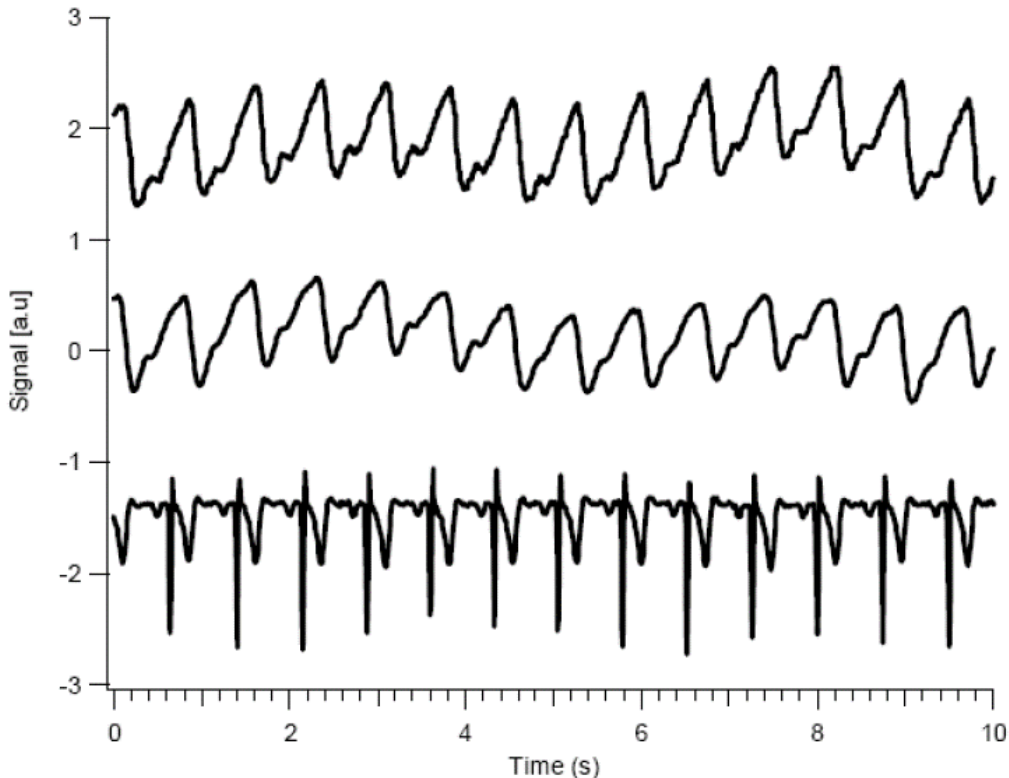


Figure 3-2: PPG signal from a commercial pulse-oximeter unit (top), an OLED and OPD fabricated coupled system (middle), and an ECG reference (bottom) [69]. Reprinted by permission from Springer Nature Customer Service Centre GmbH : Springer Nature, Springer eBook, Ref. [69], Wierenga et al, © 2008.

Another early example is a 2010 conference paper by Chuo et al in 2010 where they proposed a design and showed its feasibility by fabricating the basics of a pulse oximeter platform [62]. However, as the definition of pulse oximetry requires two wavelengths, the device did not meet this criteria despite the title of the paper indicating otherwise. The authors did create a working PPG system since only one wavelength was used with one detector. If the device had included a second OLED at a biologically relevant different wavelength it could have been considered as pulse oximeter.

Chuo et al acknowledged that 600 nm to 1000 nm are the mostly used for determining blood oxygenation level, but for the purposes of their work they used a blue emitting polymer light source, explaining that the polymer could be swapped out for another polymer that emit in the red and infrared wavelengths. The fabrication Chuo et al employed was a method that allowed an OLED and OPD to be patterned and constructed in parallel on the same piece of substrate.

The authors did their work on two kinds of substrate, glass and polyethylene terephthalate (PET). Their OLED had the structure of substrate/PEDOT:PSS/emissive polymer/Al where the emissive polymer was Poly(9,9-di-n-dodecylfluorenyl-2,7-diyl) (PDDF). The layers of their OPD were substrate/PEDOT:PSS/P3HT:PCBM/Al, where P3HT is poly(3-hexylthiophene) and PCBM is phenyl-C61-butyric acid methyl ester. The devices were encapsulated in a resin.

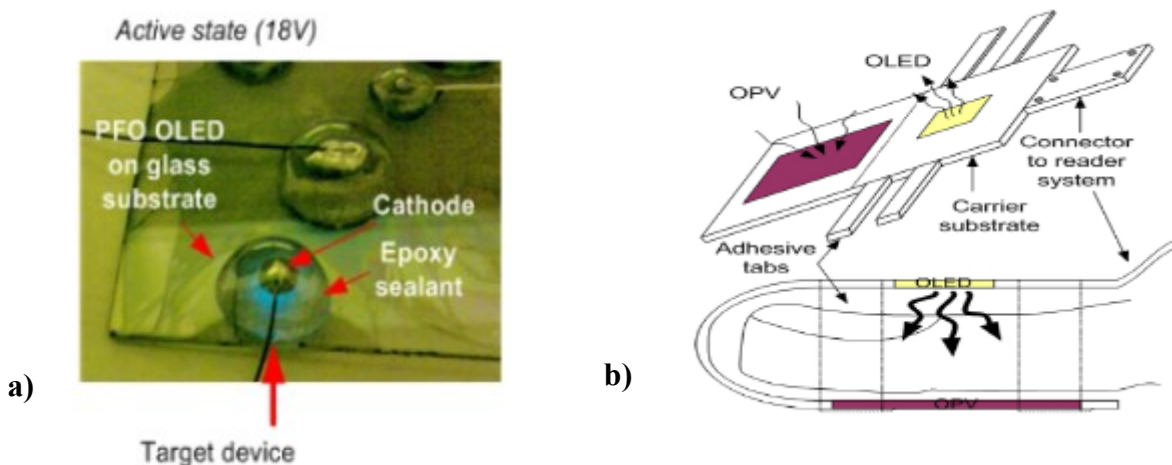


Figure 3-3: The a) OLED on glass substrate and the b) proposed design on a plastic (PET) substrate by Chuo et al [62], © 2010 IEEE.

In terms of performance, the OLEDs fabricated on a glass substrate had larger current density and light output than those fabricated on PET as seen in Figure 3-4. When the OLED on glass was operated at 18V, it had a current density of 125 mA/cm^2 , and a light output of 0.52

$\mu\text{W}/\text{cm}^2$. The OLED made on PET had a current density of $40 \text{ mA}/\text{cm}^2$ and produced just under $0.1 \mu\text{W}/\text{cm}^2$. From these values the electrical power can be approximated for the glass and PET substrate OLED as $2.25 \text{ W}/\text{cm}^2$ and $0.72 \text{ W}/\text{cm}^2$, respectively.

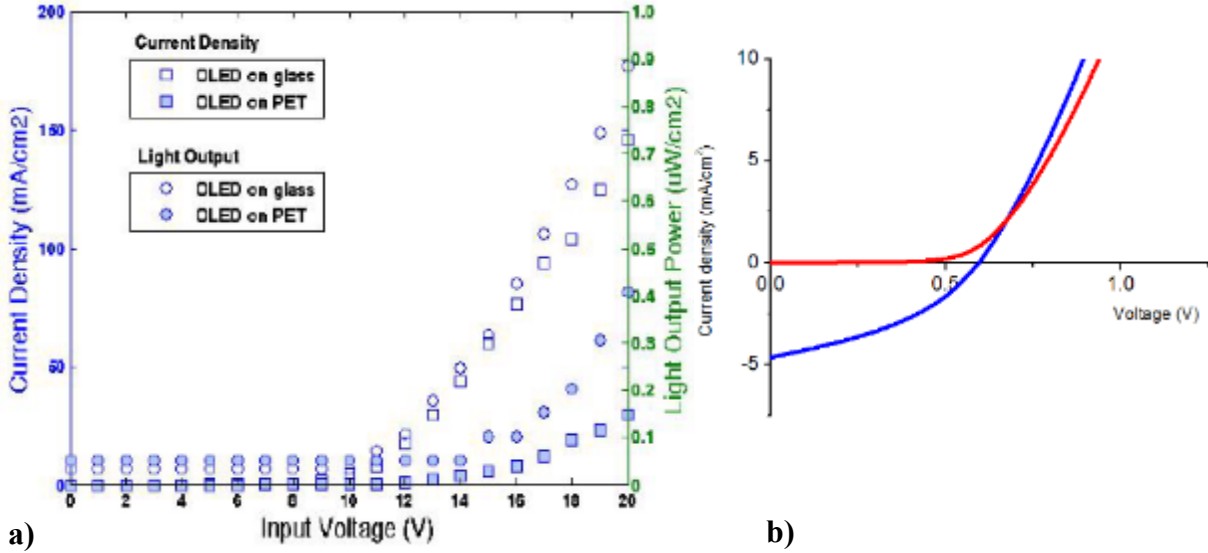


Figure 3-4: a) Light output and current density of Chuo et al OLED on glass and PET substrates. b) The PET substrate OPD current density under 1SU illumination (blue) and dark current (red) [62], © 2010 IEEE.

The authors report that the sealed OLED was exposed to the atmosphere for over 6 months and maintained its level light output, but did not include any irradiance measurements.

The OPD devices were made only on a PET substrate. Under a solar simulator of 1SU, the OPD had an approximate open-circuit voltage of 0.6V with a short circuit current, J_{sc} , of $4.8 \text{ mA}/\text{cm}^2$.

The next example of a coupled OLED and OPD systems for health applications were developed by Bansal et al in 2014 who published about two kinds of devices [61]. The first device could sense the contraction of muscles. That detection was then used to activate a robot arm. Their second kind of device could measure tissue oxygenation.

The muscle contraction sensor was placed on a human bicep and the wearer was asked to perform either isometric or isotonic contractions. For isometric contractions, the muscle length does not change with actions such as rotating the arm or pushing against a wall. Isotonic contractions are the more familiar kind of contractions where the muscle length is shortened by doing an action like lifting a weight.

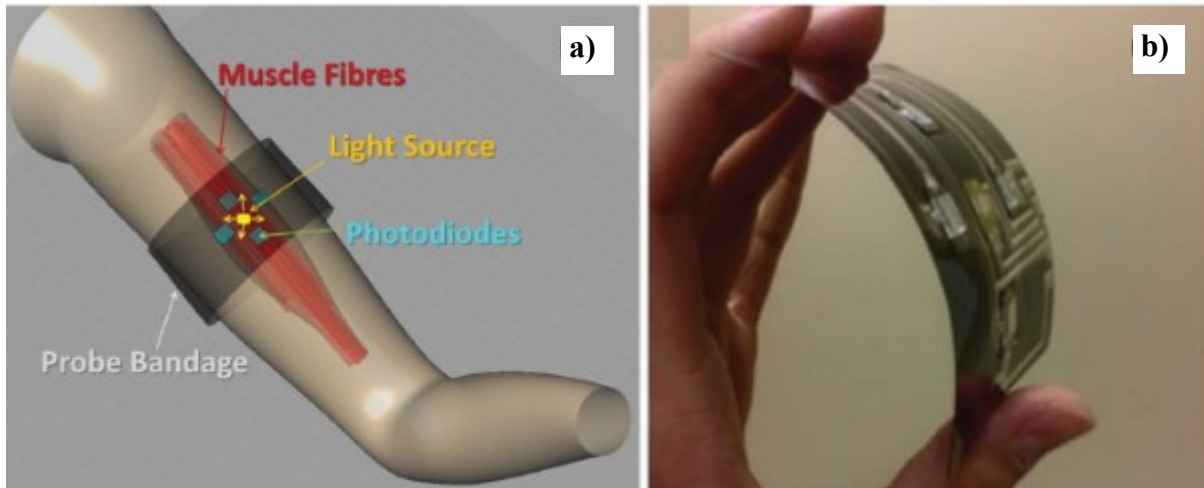


Figure 3-5: a) Diagram showing how muscle contraction could be sensed with the light source and photodiode placement and b) the flex circuit board for the device [61] (Bansal et al. © 2014 under CC-BY license 4.0: <https://creativecommons.org/licenses/by/4.0>). The robot arm that was triggered from the detection is not shown.

The detected signal could indicate which muscle activity was being performed as shown in Figure 3-6. The signals represent the flow of blood in the muscle and the unequal scattering of light across the width and length of the muscle fibers during action, relaxation and steady-state. The authors explain that a benefit of their design is that unlike electromyography (EMG), it can differentiate between isotonic and isometric contractions which is a capability electromyography (EMG) does not do.

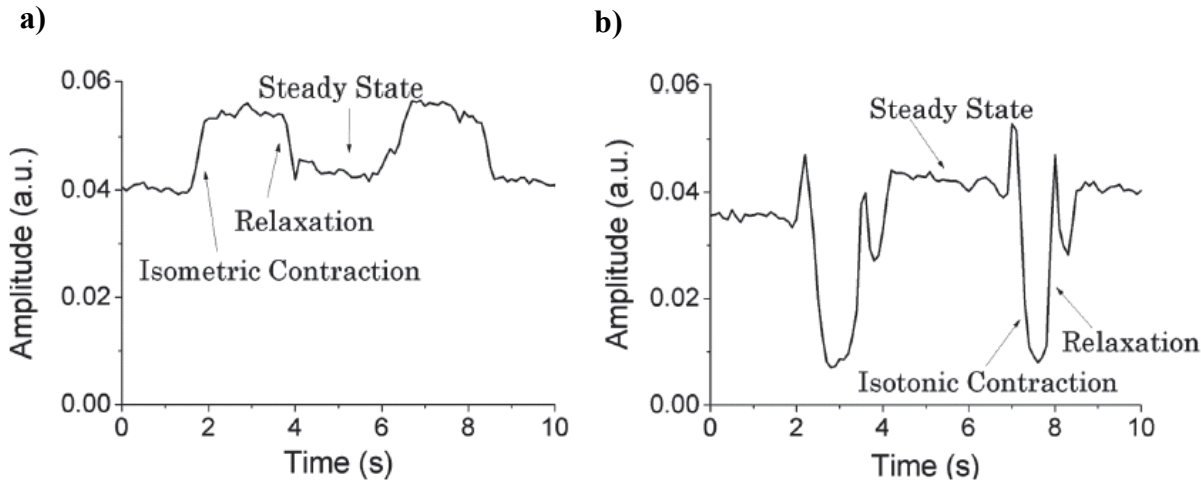


Figure 3-6: Detected signals for a) isometric and b) isotonic contractions [61] (Bansal et al. © 2014 under CC-BY license 4.0: <https://creativecommons.org/licenses/by/4.0>).

The OLED of the device was 3 mm by 3 mm. Its layers were ITO-covered-PET/PEDOT:PSS/Super Yellow polymer/Ca/Al. The OPD was fabricated with the layers of ITO-covered-PET/PEDOT:PSS/PTB7:PC70BM/Ca/Al with the device being 6 mm x 6 mm.

The OLED had an illumination of 100 cd/m² and an external quantum efficiency (EQE) of 2.3%. For comparison, the authors created the same OLED design on a piece of glass where the EQE was slight larger at 2.9%.

The OPD was prepared on PET and glass as well. On plastic, they had an EQE of 50% and on glass 65%. The authors state the EQE difference for both plastic and glass substrate OLEDs and OPDs are not substantial and indicate that the plastic PET is adequate to serve as a substrate for the sensor. There is no mention of power amounts of the OLEDs or OPDs.

The second kind of device created by the authors had the different purpose of measuring tissue oxygenation. It consisted of a broadly emitting OLED and 2 photodiodes, with each photodiode specifically detecting either red or near infrared wavelengths. This arrangement is not quite a PPG system since it does not measure the heart or breathing rate, but it is close to being a PPG system since it could measure the change in oxygenated and deoxygenated

hemoglobin. The design of the device and collected data of induced ischemia measurements showing the steady reduction in tissue oxygenation in the arm can be seen in Figure 3-7.

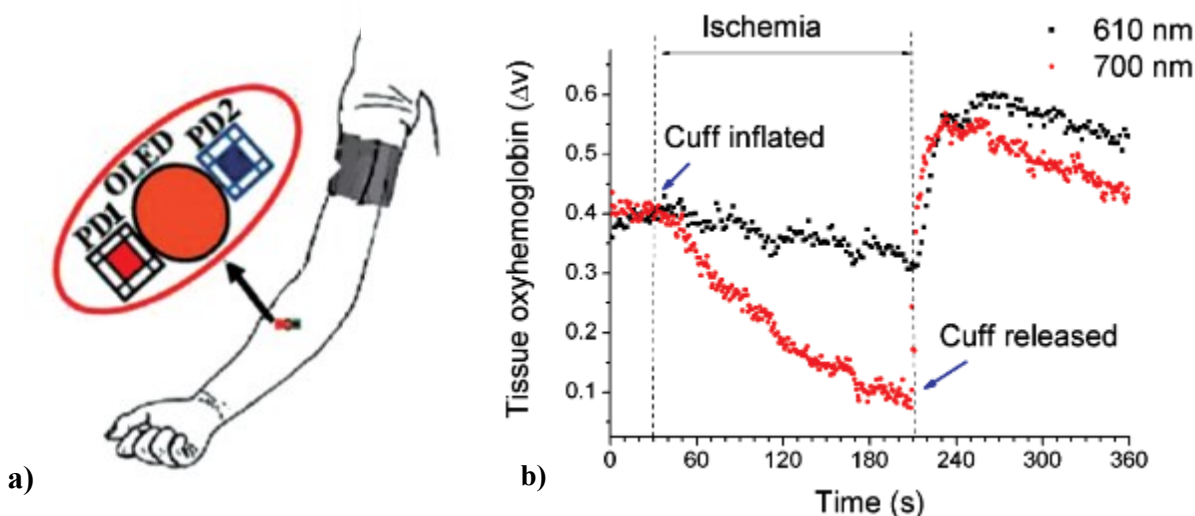


Figure 3-7: Bansal et al tissue oxygen sensor a) design and induced ischemia (cuff restricted blood flow) measurement results [61] (Bansal et al. © 2014 under CC-BY license 4.0: <https://creativecommons.org/licenses/by/4.0>).

Here the OLED was circular, 2 cm in diameter, had a current of 80 mA and used the emissive polymer OC₁C₁₀-PPV. The fabrication of the OPD was as described earlier for the author's muscle contraction project.

Bansal et al did not mention a lifetime or stability for either their muscle contraction detection or tissue oxygenation device.

A true organic optoelectronic pulse oximetry system was developed by Lochner et al in 2014 [5]. The assembled combination of OLEDs and OPD for the pulse oximetry is seen in Figure 3-8. The arrangement makes this device a transmission pulse oximetry implementation because the light shines through the finger to be detected by the OPD on the other side of the finger.

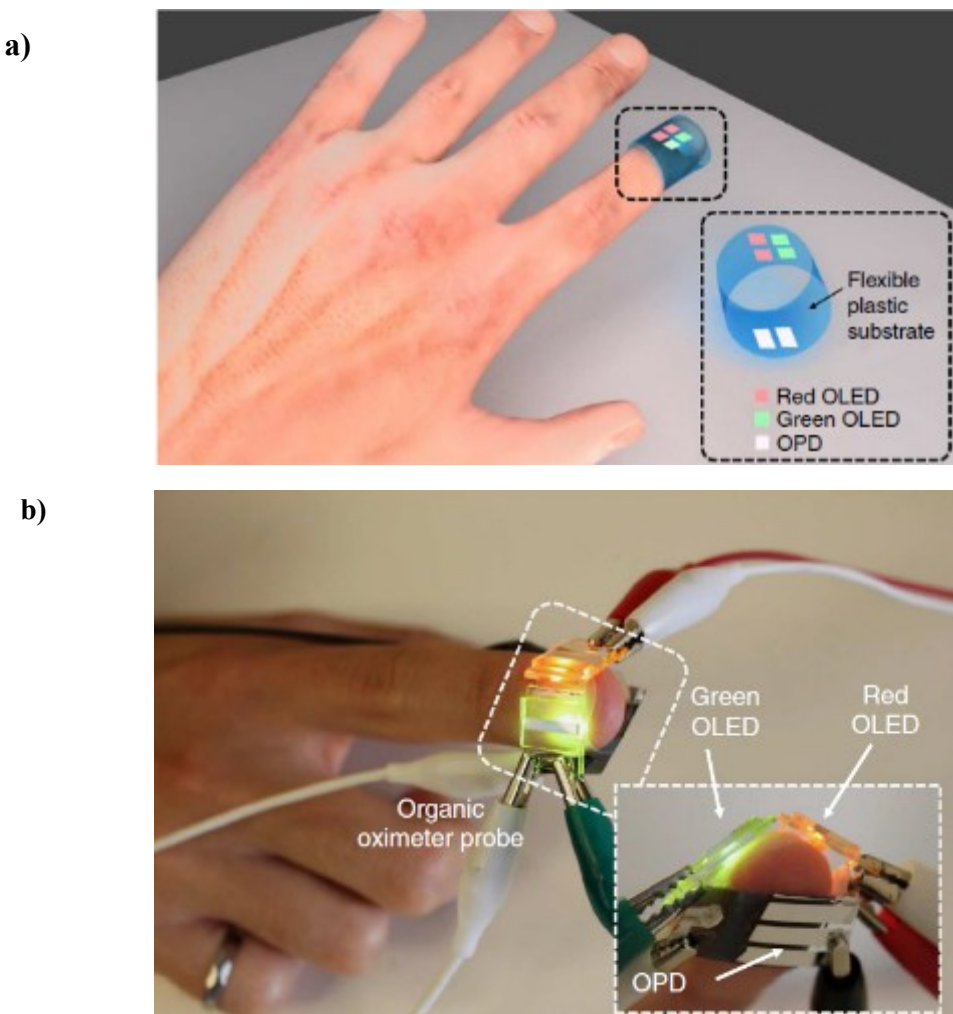


Figure 3-8: a) Diagram and b) implementation of the OLEDs and OPDs for the pulse oximetry system of Lochner et al [5]. Reprinted by permission from Springer Nature Customer Service Centre GmbH : Springer Nature, Nature Communications Ref. [5] (Lochner et al), © 2014.

Lochner et al chose to use red and green wavelengths for measuring blood oxygenation level unlike the more conventional red and infrared wavelengths. They explained that they chose green light because near-infrared materials exhibit lower efficiencies and are unstable in air. They further justified their selection by explaining how the difference between oxygenated and deoxygenated hemoglobin absorptivity in the green wavelength is similar to the difference observed in the near-infrared spectrum region.

The authors state that the most significant factor for determining an OLED's performance is its irradiance. They cite that as irradiance of a device rises, the efficiency will be reduced. Their OLED data illustrates this when the irradiance curve slopes are compared to the current density slopes as the applied voltage is increased. As can be seen in Figure 3-9, the irradiance curve slopes become lessened with higher voltage, while in contrast the current densities slope do not show diminishment.

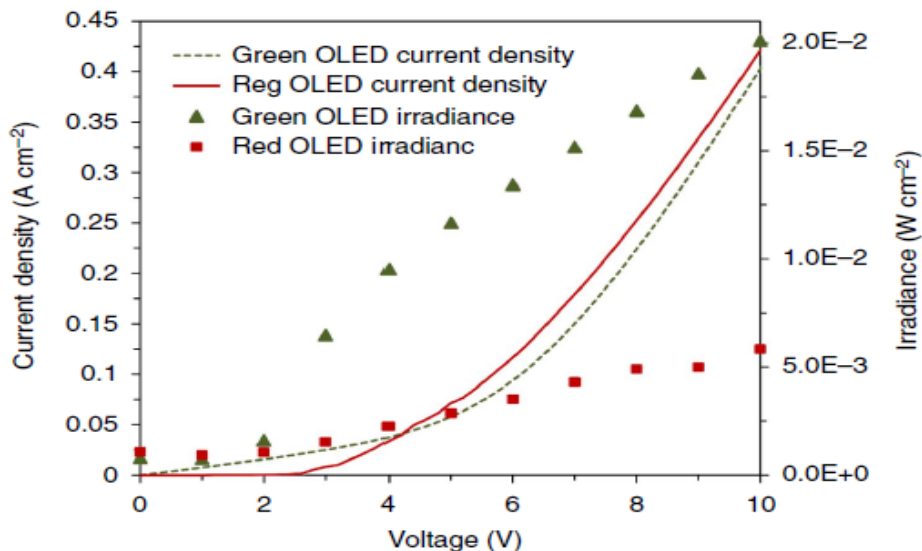


Figure 3-9: The OLED irradiance and current density for Lochner et al [5]. Reprinted by permission from Springer Nature Customer Service Centre GmbH : Springer Nature, Nature Communications Ref. [5] (Lochner et al), © 2014.

The OLEDs were constructed on an ITO coated glass substrate. The full layering scheme was ITO-coated-glass/PEDOT:PSS/TFB/emissive layer/LiF/Al. For green, the emissive layer was blend of TFB to F8BT in a 1:9 ratio where TFB was poly(9,9-dioctylfluorene-co-n-(4-butylphenyl)-diphenylamine) and F8BT was poly((9,9-dioctylfluorene-2,7-diyl)-alt-(2,1,3-benzothiadiazole-4, 8-diyl)). The red emissive layer was a 25:70:5 ratio mix of TFB, F8BT and TBT , where TBT was poly((9,9-dioctylfluorene-2,7-diyl)-alt-(4,7-bis(3-hexylthiophene-5-yl)-2,1,3-benzothiadiazole)-20,20-diyl).

When operated at 9V, the light output of the green OLED was 20.1 mW/cm^2 and the red was 5.83 mW/cm^2 . From Figure 3-9, the electrical power of the devices at this same applied voltage can be calculated. The green and red OLED operated approximately at 3.6 W/cm^2 and 0.9 W/cm^2 , respectively. Both OLED types were 4 mm^2 in area and encapsulated with a piece of epoxied quartz glass.

For the OPD, the authors indicate the most significant performance factor is a high EQE. This helps generate the largest achievable short circuit current to determine the pulse rate and oxygenation level. The EQE of their device is plotted in Figure 3-10a showing how the OPD is responsive to the light output of the red and green wavelengths selected to probe the tissue. The EQE at the peak of the green (532 nm) and red (626 nm) is 38% and 47%, respectively.

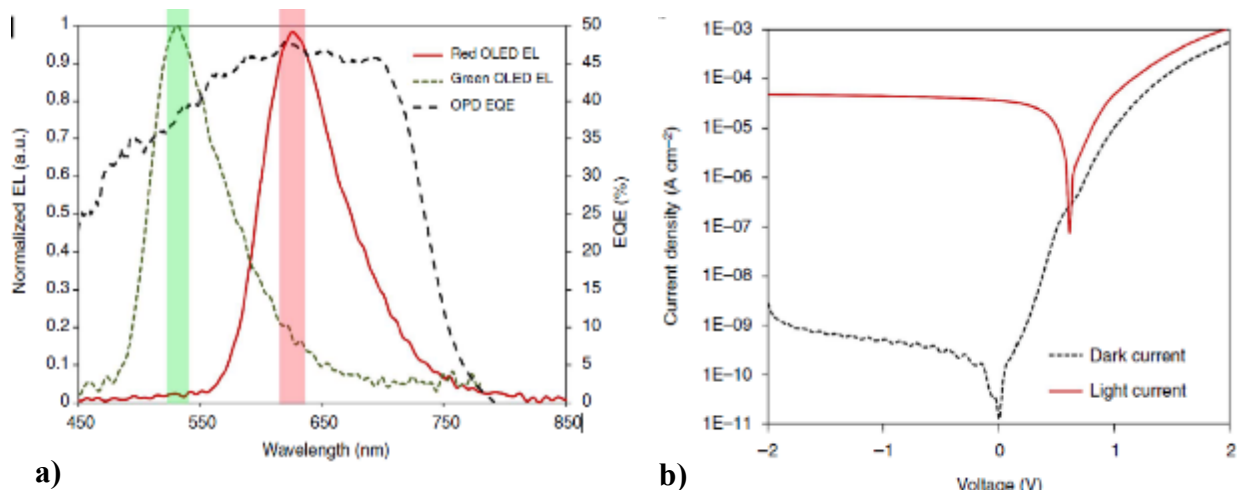


Figure 3-10: Lochner et al OPD's a) response curve (EQE) aligns with the red and green OLED emission spectra. The light and dark current responses are shown in b). For the light current measurement, the OPD was illuminated with a 640 nm source at an intensity of $355 \mu\text{W/cm}^2$. The dark current was attained by applying voltage to the device. Reprinted by permission from Springer Nature Customer Service Centre GmbH : Springer Nature, *Nature Communications* Ref. [5] (Lochner et al), © 2014.

The OPD was built on a polyethylene naphthalate (PEN) substrate. The layering of the device was PEN/PEDOT:PSS (conductive)/PEDOT:PSS (hole blocking)/PTB7:PC₇₀BM/Al,

with the PTB7: PC₇₀BM in a 1:1 ratio. The OPD was also encapsulated in epoxy and a thin plastic film. At the peak of the red spectrum, 626 nm, the device had an EQE of 47% while for the green spectrum peak, 532 nm, the EQE was 38%. The device had an active area of 21 mm².

The authors reported an example of their detected signal and how their system translated that into heart rate and blood oxygen saturation as seen in Figure 3-11.

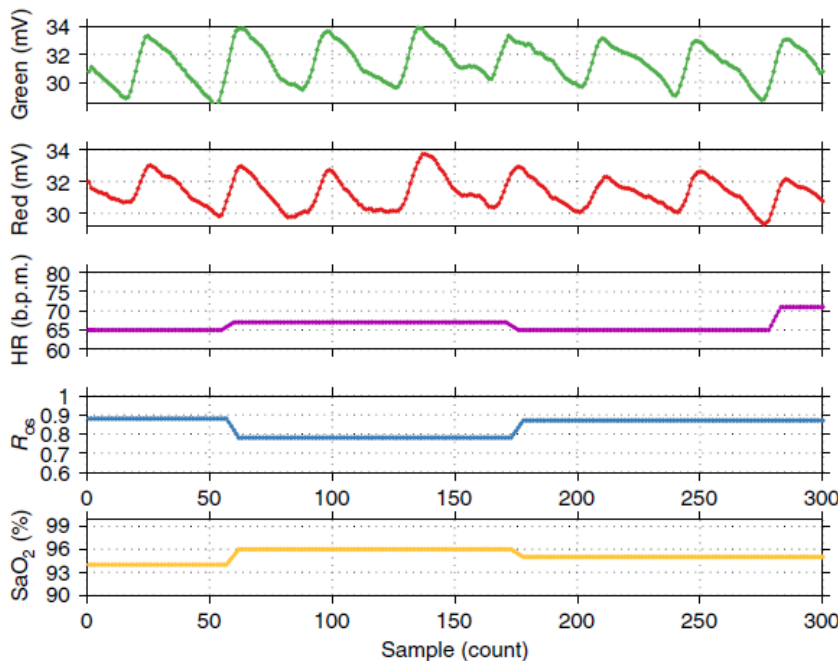


Figure 3-11: Red and green wavelength signals and derived heart rate (HR), red and green wavelength ratio (R_{os}), and blood oxygen saturation (SaO_2) interpretation [5]. Reprinted by permission from Springer Nature Customer Service Centre GmbH : Springer Nature, Nature Communications Ref. [5] (Lochner et al), © 2014.

As with many organic devices there are challenges with the device lifetime. The intensity of the green OLED PPG signal was reduced by 24% over the course of seven days, while the red OLED PPG signal experienced a 54% decrease as shown in Figure 3-12.

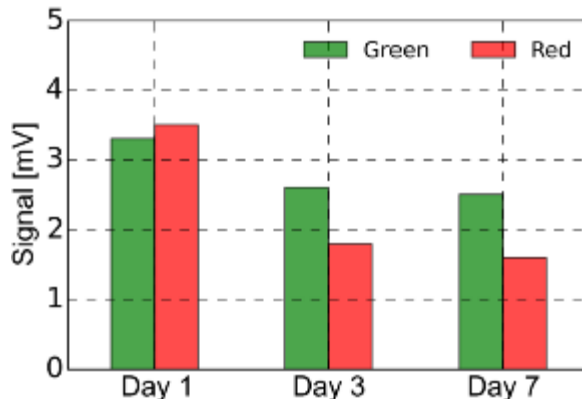


Figure 3-12: Device PPG signal degradation during 7 days [5]. [5]. Reprinted by permission from Springer Nature Customer Service Centre GmbH : Springer Nature, Nature Communications Ref. [5] (Lochner et al), © 2014.

The next implementation of an organic optoelectronic health monitor was developed in 2016 by Yokota et al. in the form of a finger pulse oximeter [3]. The authors worked with polymers and referred to their OLEDs as polymer light emitting diodes, or PLEDs. They worked with red, green and blue wavelengths. The red and green wavelengths were the biologically relevant wavelengths that were used in the pulse oximetry work.

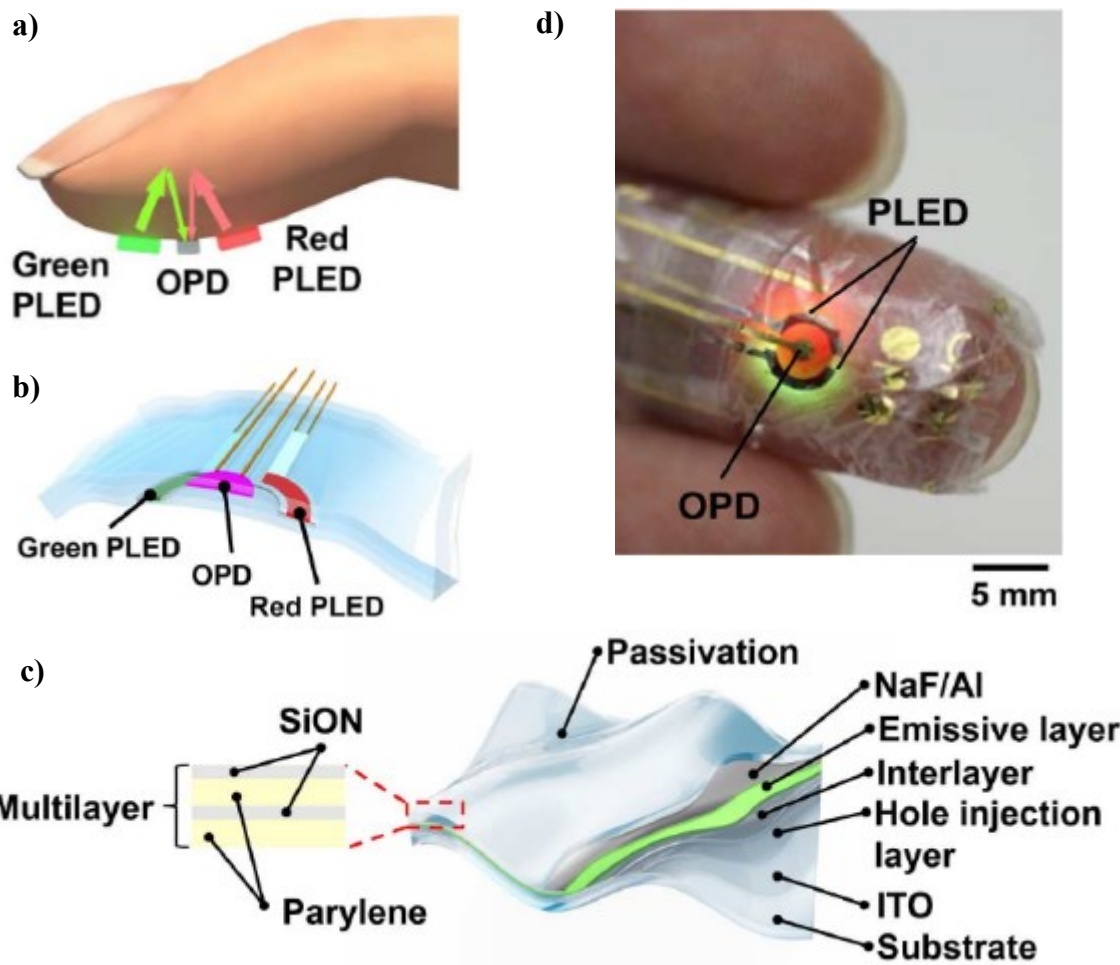


Figure 3-13: Yokoto et al fabricated a a) reflection based pulse oximetry device that illuminated the tissue with red and green wavelengths [3]. The b) diagram, c) cross section, and d) actual device [3]. Yokota et al. © 2016 under CC BY-NC license 4.0: <https://creativecommons.org/licenses/by-nc/4.0/legalcode>.

Their PLEDs had excellent flexibility with the capability of withstanding being crumpled or subjected to a bending radius of 100 μm on the edge of a razor. Additional compressive experiments and data suggest the bending radius can be even less than 100 μm .

At 5.8V and a current density of 10 mA/cm², the EQE for red was 12.4% with an irradiance of 2100 cd/m². For the green PLED at the same current density, it operated at 8.1 V with an EQE of 13.9% and a luminance of 4900 cd/m². In terms of electrical power at these parameters, the red was functioning at 0.081 W/cm² and the green was at 0.058 W/cm². The

full J-V (current density vs voltage) curves of the PLED devices, the EQE as a function of current density, and luminance per applied voltage can be seen in Figure 3-14.

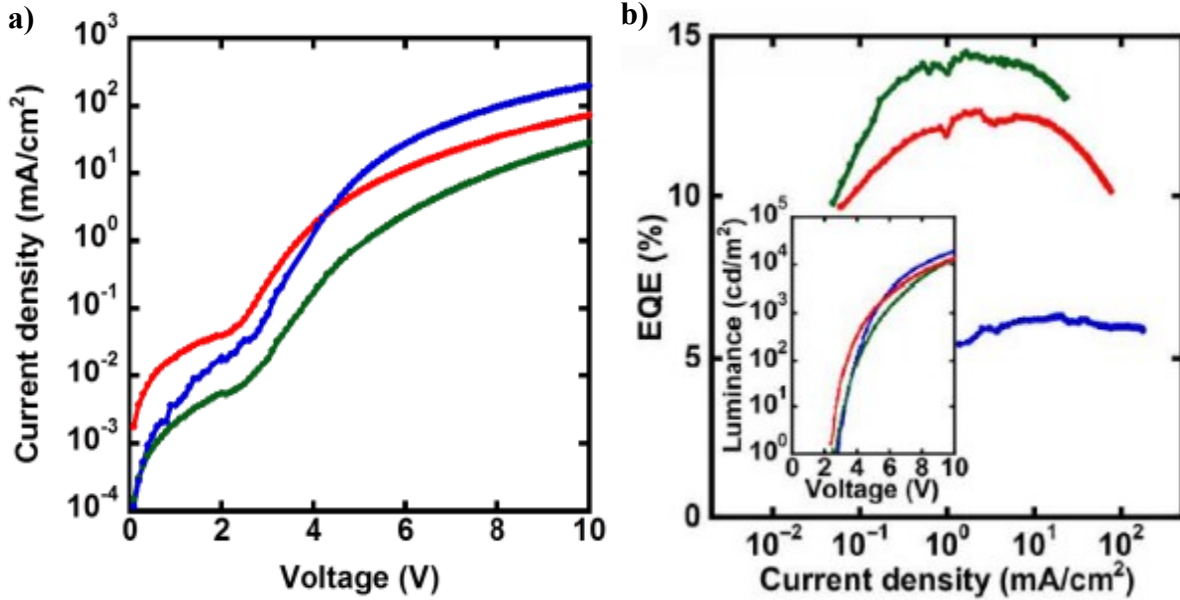


Figure 3-14: The a) J-V curves for red, green and blue PLEDs , and b) their EQEs as a function of current density, and (inset) luminance of the PLEDs made by Yokota et al [3].
Yokota et al. © 2016 under CC BY-NC license 4.0: <https://creativecommons.org/licenses/by-nc/4.0/legalcode>.

The structure of the PLED was parylene/polyimide/ITO/HIL/Interlayer/Active Layer/NaF/Al/passivation. The authors do not detail their HIL (hole injection layer), nor the active layers (for red and green), but did explain their passivation layers was five alternating layers of SiON and parylene. Yokota et al report that this passivation layer scheme helped increase the irradiance operational half life of their device from 2 to 29 hours as shown in Figure 3-15.

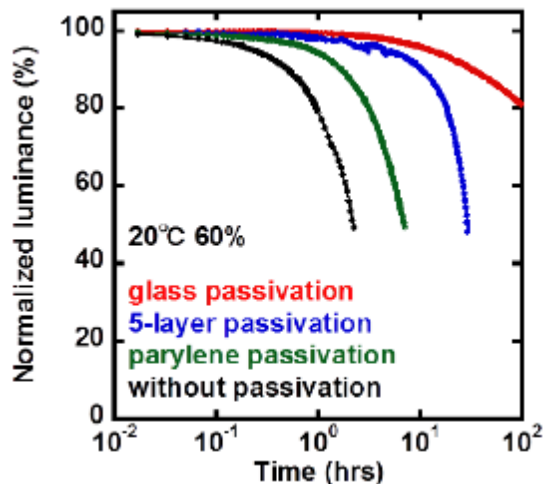


Figure 3-15: Chart of the green PLED lifetime at 60% humidity and 20 °C operated at 12.5 mA/cm² by Yokota et al [3]. The luminance operational half life was 29 hours with the 5 layer passivation. Yokota et al. © 2016 under CC BY-NC license 4.0: <https://creativecommons.org/licenses/by-nc/4.0/legalcode>.

Yokota et al fabricated their PLEDs on glass and plastic substrates to compare their characteristics. They found the substrate type did not influence the PLED and the PLEDs on either substrate possessed almost an identical current-density (J-V) and luminance-voltage (L-V) curve. Devices were also compared before and after peeling from the supporting substrate to see if there was any harm caused in the delamination procedure. Except for a slight increase in leakage current, the J-V and L-V performance were nearly identical before and after peeling.

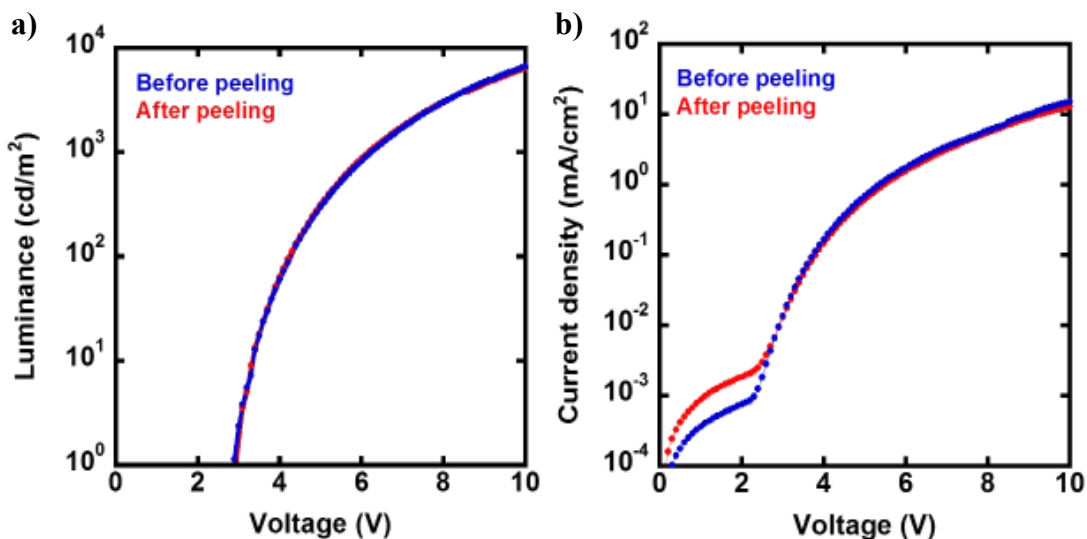


Figure 3-16: Luminance and current density characteristics and after the removal of the PLEDs from the supporting substrate [3]. Yokota et al. © 2016 under CC BY-NC license 4.0: <https://creativecommons.org/licenses/by-nc/4.0/legalcode>.

Yokota et al also showed that the green PLED luminance could be compressed from 0% to 67% and maintain their luminance even after 1000 cycles without much change as seen in Figure 3-17.

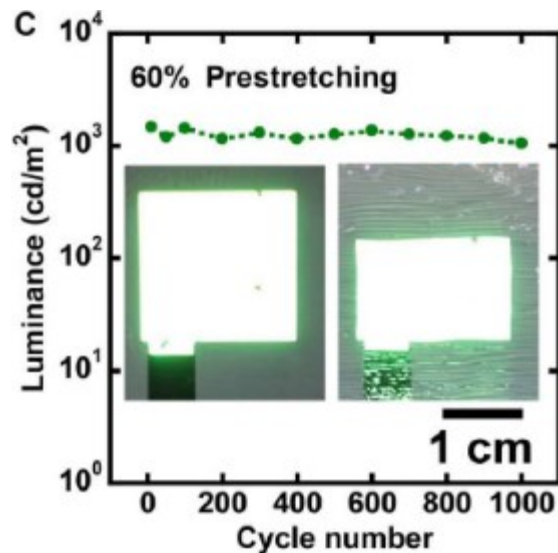


Figure 3-17: Compression had a negligible effect on the green PLED luminance [3]. Yokota et al. © 2016 under CC BY-NC license 4.0: <https://creativecommons.org/licenses/by-nc/4.0/legalcode>.

To be able to detect the light emitted from the PLED, the team also constructed an OPD. It had a similar layering as the PLED with the principal difference being the active layer was a mixture of P3HT and PCBM. A solar simulator was used at 1 sun with an AirMass 1.5 Global filter. This experimental setup yielded a V_{oc} (open-circuit voltage) of 0.52 V, a J_{sc} (short circuit current) of -56 A/m^2 , a fill factor of 0.5 and a power conversion efficiency was 1.46%.

Figure 3-18a shows the OPD spectral response corresponded well to the emitted spectrum of the PLEDs. The current density was dependent on the light intensity as indicated by Figure 3-18b, where a range of intensities was used from 99 W/m^2 to 1000 W/m^2 , including the dark condition 0 W/m^2 . The V_{oc} , open circuit voltage, is also a function of light intensity as indicated in Figure 3-18c.

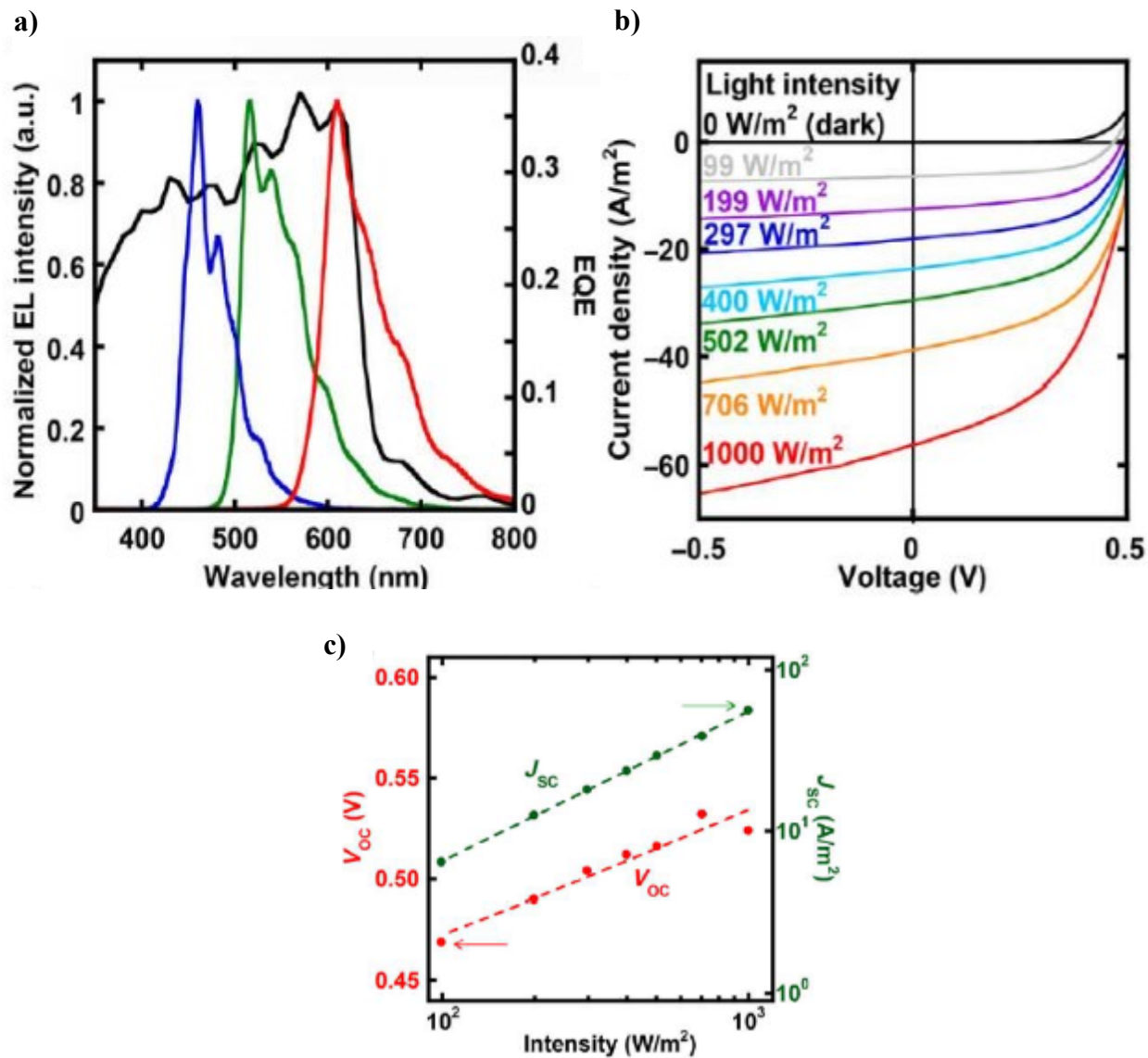


Figure 3-18: The OPD a) EQE spectral response to the PLED spectrums. The b) the current density and c) the Voc as a function of light intensity under a solar simulator of 1 sun and Air mass 1.5 Global filter [3]. Yokota et al. © 2016 under CC BY-NC license 4.0: <https://creativecommons.org/licenses/by-nc/4.0/legalcode>.

A further analysis of the OPD was done to measure how the device responds to excitation from the green and red PLED used in their pulse oximetry device. Different intensities of the red and green wavelengths were used and the resulting luminance-current densities are seen in Figure 3-19.

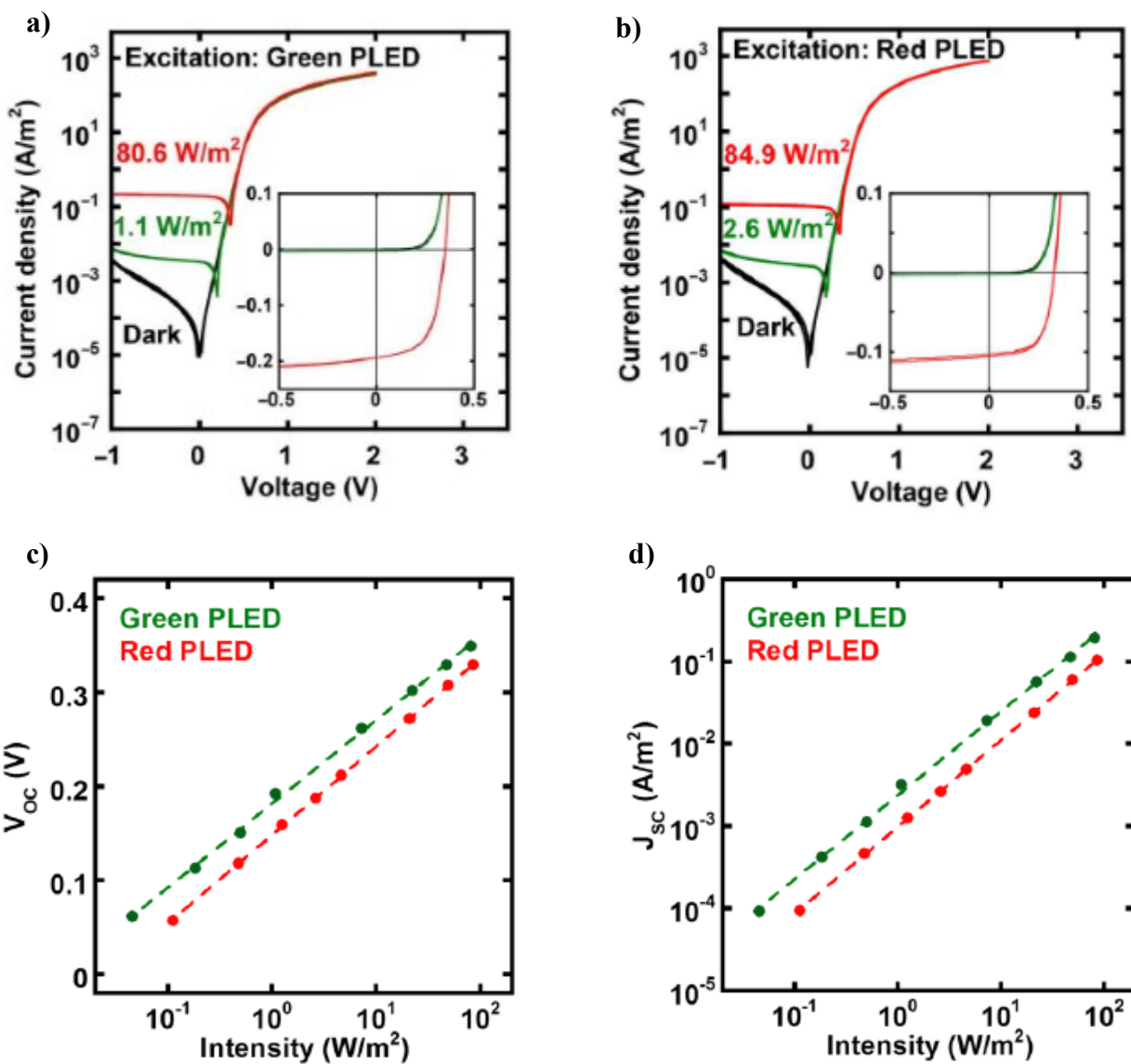


Figure 3-19: OPD response as when a) illuminated by a green PLED and b) red PLED at two intensities [3]. The OPD c) open circuit voltage and the d) current density are plotted as a function for a series of green and red PLED intensities. Yokota et al. © 2016 under CC BY-NC license 4.0: <https://creativecommons.org/licenses/by-nc/4.0/legalcode>.

As with the PLEDs, Yokota et al did compression testing and determined the OPDs had very little open circuit voltage change when compressed up to 40% and similarly the current density for the light/dark current did not vary compression as shown in Figure 3-20a-b. Even after going through 300 stretching cycles, the characteristics of the OPD did not change (Figure 3-20c).

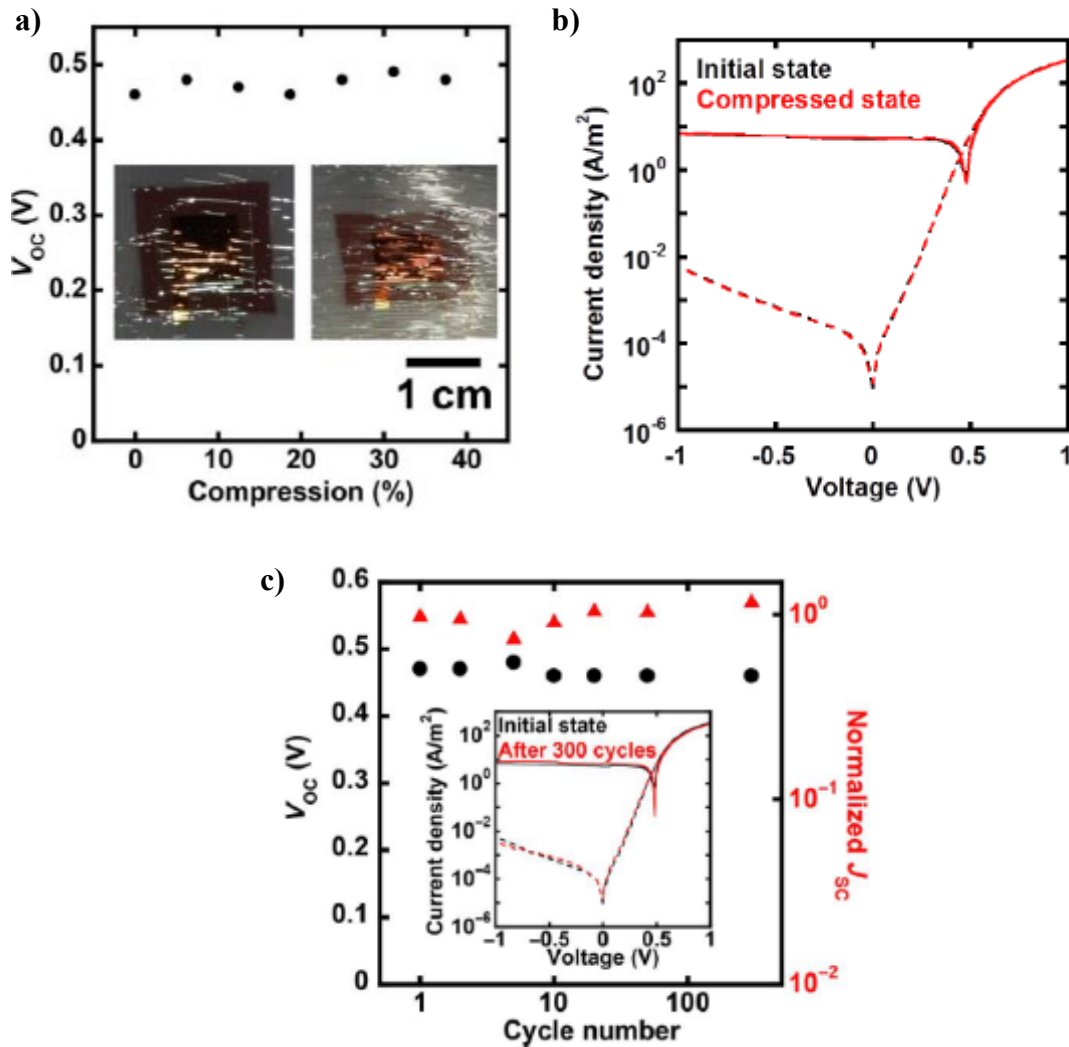


Figure 3-20: OPD stretch experiments showing a) the open circuit voltage remain unaffected with compression up to 40%, and b) in a non-compressed state versus 37% compressed state, the dark (dashed line) and light (solid) current densities were the same when illuminated with a green laser [3]. c) Compressive cycling did not degrade the open circuit voltage, the current density and the light/dark current response [3]. Yokota et al. © 2016 under CC BY-NC license 4.0: <https://creativecommons.org/licenses/by-nc/4.0/legalcode>.

An example of the attainable PPG signal with the red PLED and OPD can be seen in Figure 3-21. As mentioned earlier, the devices had a stability which affected the signal over time.

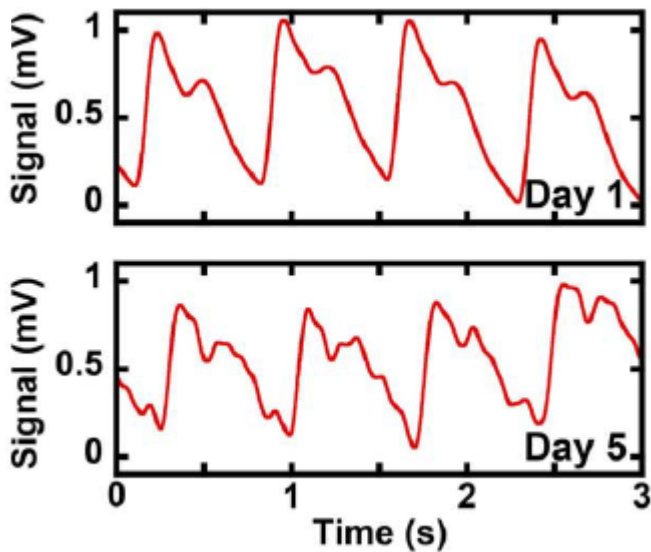


Figure 3-21: The PPG signal from Yokota et al using the red PLED and OPD [3]. The device stability affected the signal quality over time. Yokota et al. © 2016 under CC BY-NC license 4.0: <https://creativecommons.org/licenses/by-nc/4.0/legalcode>.

During pulse oximetry operation, the device was taped on a finger and the PLEDS were driven at 6 V and alternatively turned on and off for 5 seconds. The authors report that the OPD could detect the PPG signal reliably and they credited that to the good adhesion of the device. The signals for 99% and 90% blood oxygenation can be seen in Figure 3-22. With less blood oxygenation, the signal amplitude became reduced.

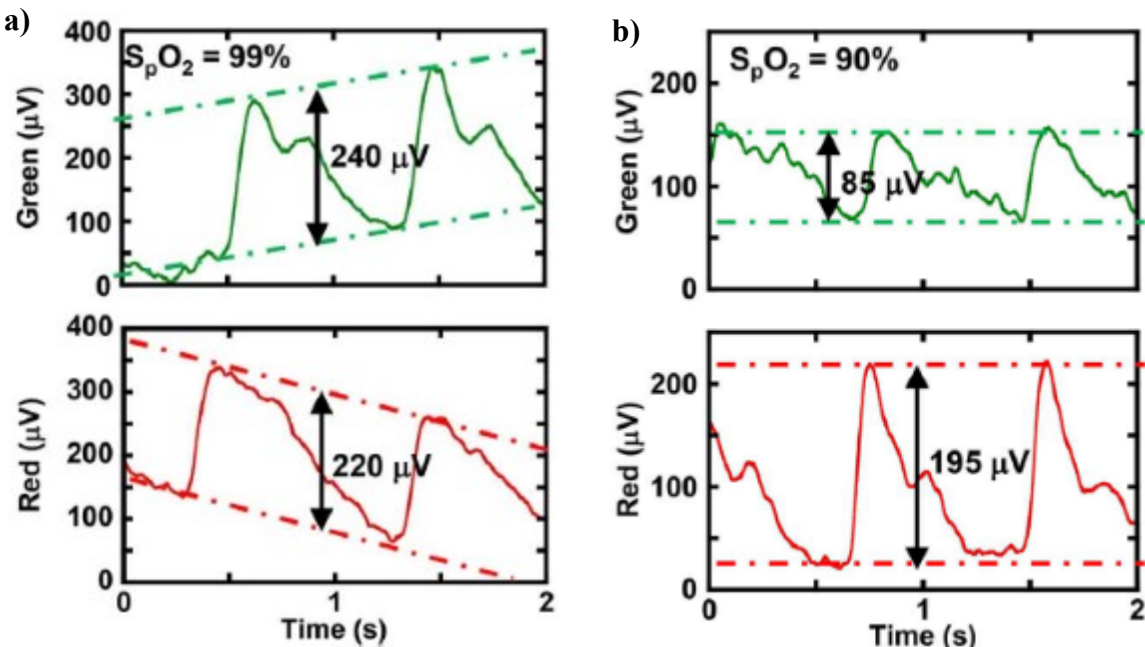


Figure 3-22: OPD signal for a) 99% blood oxygenation and b) for 90% blood oxygenation [3]. Yokota et al. © 2016 under CC BY-NC license 4.0: <https://creativecommons.org/licenses/by-nc/4.0/legalcode>.

One of the more recent organic optoelectronics for health monitoring was created by Han et al who used a blade coating method to fabricate a reflection-mode pulse oximetry mode device on a PEN-ITO substrate for the wrist.

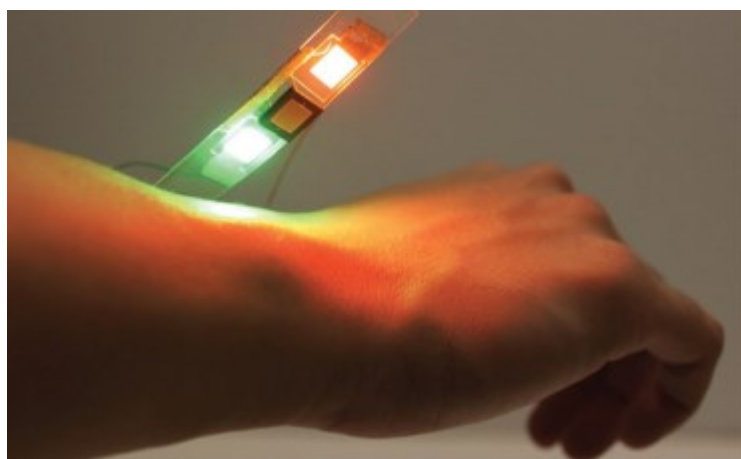


Figure 3-23: Han et al PLED and inorganic photodiode PPG and pulse oximeter for the wrist [1]. Han et al, © 2017 under CC BY license 3.0: <https://creativecommons.org/licenses/by/3.0/>.

The authors report each PLED device was 0.49 cm^2 ($0.7 \text{ cm} \times 0.7 \text{ cm}$). To collect a light signal they used an inorganic photodiode adjacent to the PLED on the wrist. They

established that red, green and NIR PLEDs could acquire PPG signals and report that 10 mA/cm^2 created reproducible results. They could apply an algorithm to determine the heart rate.

From Figure 3-24a it is possible to approximate the voltage for the 10 mA/cm^2 current density for the green PLED as 7V and the red as 8V. This means a 0.08 W/cm^2 and 0.07 W/cm^2 for the green and red PLED, respectively. Since the area of the devices are 0.49 cm^2 , the actual wattage of the devices can be approximated as well, yielding 0.04 W for the green and 0.03 W for the red PLED.

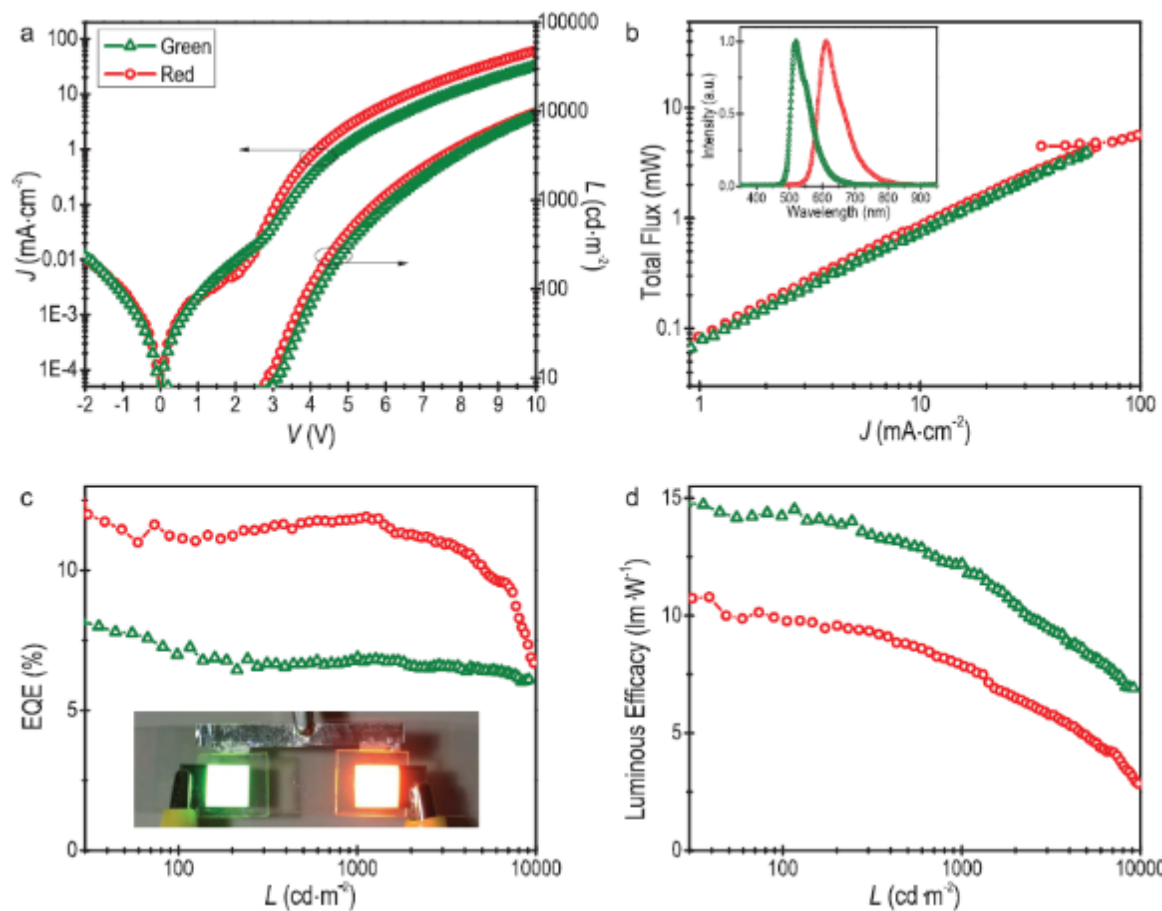


Figure 3-24: Green and red PLED characteristics on the PEN/ITO substrate [1]. Han et al, © 2017 under CC BY license 3.0: <https://creativecommons.org/licenses/by/3.0/>

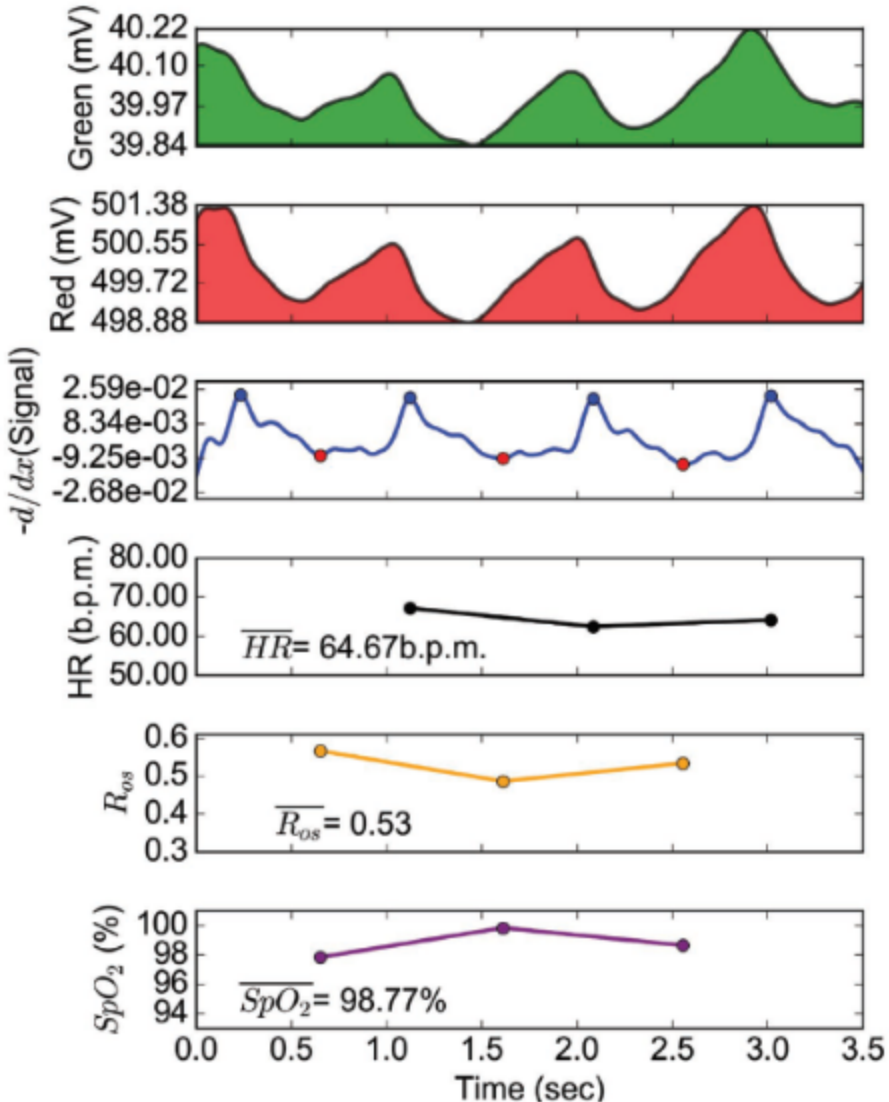


Figure 3-25: An example of the red and green PPG signal by Han et al and how it translates to heart rate and blood oxygenation [1]. Han et al, © 2017 under CC BY license 3.0: <https://creativecommons.org/licenses/by/3.0/>

Han et al did not mention a lifetime for their device and gave examples of what structural layers their device could have used, but were non-specific in the PLED active layer components.

The next related project was done by Khan et al of the same group as the previous project and was titled “Flexible Organic Reflectance Oximeter Array”. Their device can be seen in Figure 3-26.

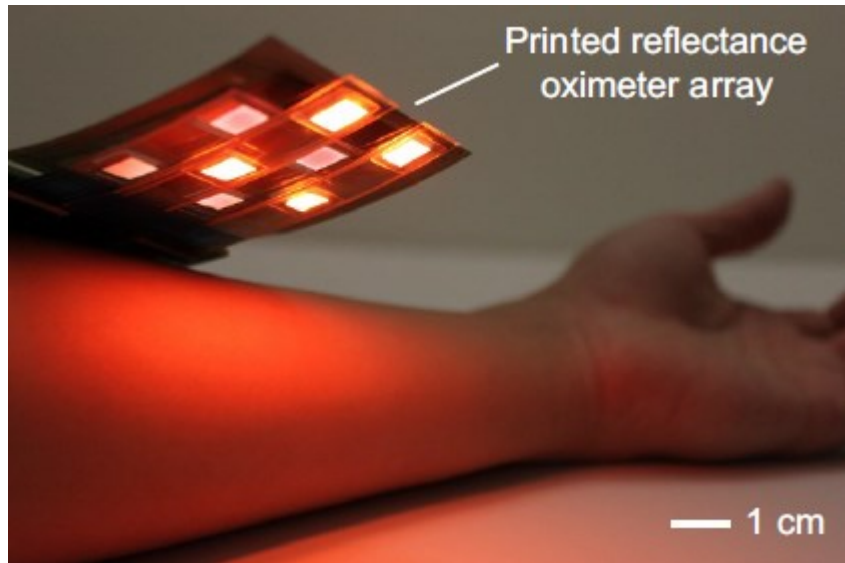


Figure 3-26: Khan et al made a flexible organic reflectance oximeter array [2]. © 2018, Khan et al, under CC-BY-ND license 4.0: <https://creativecommons.org/licenses/by-nd/4.0/>.

They used a Red, Green and NIR devices. The OLEDs were fabricated on a PEN/ITO substrate, spun on with 70 nm PEDOT:PSS, OLED active matrix (AM), Ca, and aluminum, encapsulated with epoxy and a piece of plastic. The OLED AM was supplied from Cambridge Display Technologies. The OPD was also made on PEN, without ITO, followed by the OPD active matrix (AM) and then aluminum.

Lee et al developed a red and green OLED patch , along with OPD. Their device was on a PET and Indium Zinc Oxide (IZO) substrate. The radius of the OLEDs were 0.4 mm and they were encircled by the OPDs as shown in Figure 3-27.

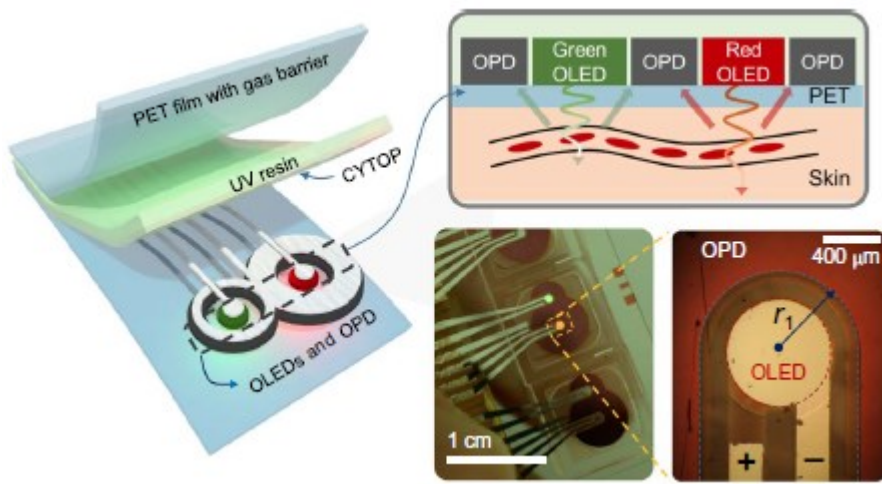


Figure 3-27: Lee et al developed a red and green OLED patch [4]. Copyright 2018, Lee et al, under CC-BY-NC license 4.0: <http://creativecommons.org/licenses/by-nc/4.0/legalcode>.

According to the authors, their power usage is the lowest for reported pulse oximetry.

The electrical power characteristics of the device mentioned in this chapter are summarized in Table 3-1 for the OLEDs. A selection was chosen for the OPDs in Table 3-2.

Table 3-1: Electrical Power Parameters and Calculations for OLED/PLED Light Generation

OLED or PLED color	Voltage (V)	Current Density (mA/cm ²)	Electrical Power (W/cm ²)	Device Size	Power per device (W)	Light Output	Ref
Red	8V	70	0.84	8 mm ²	0.0672	320 cd/m ²	[68]
Blue	18	125	2.25	Unknown	Unknown	0.52 μW/cm ²	[62]
Blue	18	40	0.72	Unknown	Unknown	0.1 μW/cm ²	[62]
Green	9	~325	2.925	4 mm ²	0.117	20.1 mW/cm ²	[5]
Red	9	~350	3.15	4 mm ²	0.126	5.83 mW/cm ²	[5]
Green	8.1	10	0.081	4 mm ²	0.00324	4900 cd / m ²	*[3]
Red	5.8	10	0.058	4 mm ²	0.00232	2100 cd / m ²	*[3]
Green	~8	10	0.08	0.49 cm ²	0.0392	~20000 cd/m ²	[1]
Red	~7	10	0.08	0.49 cm ²	0.0343	~20000 cd/m ²	[1]
NIR	~6	10	0.06	0.49 cm ²	0.0294	0.2 mW	[1]
Red	~7	10	0.07	0.49 cm ²	0.0343	0.9 mW	[2]
Infrared	~6.7	10	0.067	0.49 cm ²	0.0328	0.2 mW	[2]
Red	3.3	~5	0.0165	0.004 cm ²	**31uW /125 uW	~4 cd/m ²	[4]
Green	5	~5	0.025	0.004 cm ²	**17 uW /68uW	~4 cd/m ²	[4]

* = For pulse oximetry operation the authors used 6V for the red and green PLED and did not provide the associated current density values. Shown in the tables are voltage and current density values for general operation for the PLEDs provided by the authors.

** = 25% / 100% duty cycle

Table 3-2: Electrical OPD Characteristics

OPD material	Voltage open circuit (Voc)	J _{sc} short circuit current density (mA/cm ²)	Device Size	Reference
P3HT:PC ₆₁ BM	0.58	10	1 mm ²	[68]
PTB7:PC ₇₀ BM	~1V	~0.0145	21 mm ²	[5]
P3HT:PC ₆₁ BM	0.52	-5.62	~25 mm ² *	[3]
Inorganic photodiode Hamamatsu S2387-66R	Not given	24 uA @100 lux	33.64 mm ²	[1]
1:2 CDT Donor:PC ₇₁ BM	Not given	Not given	0.49 cm ²	[2]
Small Molecule Mix	Not given	Not given	2 rings: OPD for red: inner radius 0.6 mm and ring width 3.6 mm (39.5 mm ²) OPD for green: inner radius 0.6 mm and ring width 2.8 mm (23.5 mm ²)	[4]

* = The working OPD (for pulse oximetry) dimensions were not supplied by the authors. Estimated size is from the picture of the square OPD in the author's figures that was not directly used in the pulse oximetry device.

As can be seen from the limited family of organic electronic pulse oximeter show there are certain challenge that must be met with the creation of these kinds of devices. Polymer materials need to be selected in order to produce the correct wavelengths of light. The substrates need to be selected from flexible and transparent materials. Encapsulation needs to be done in order to protect the devices and try to extend their lifetime. These factors and

others are brought together to create a conformal organic electronic device capable of photoplethysmography or pulse oximetry device.

Chapter 4: Organic Device Fabrication

4.1 Glass Substrate Fabrication and Green OLED on Glass Device Testing

The creation of the organic devices began with glass substrates coated with ITO. The reasoning here was that the issues and fabrication methods would first be worked out on stiff substrates before moving on to flexible substrates. This was also done because some early attempts were made with flexible substrates initially, but the PEDOT:PSS (MilliporeSigma) coverage was an issue as seen in Figure 4-3.

The one inch squares of glass covered with Indium Tin Oxide (ITO) were purchased (Sigma) and patterned with vinyl tape. The tape would cover portions of the device side that had the ITO layer. Where the tape was placed, the ITO would be preserved as part of the device's layers.

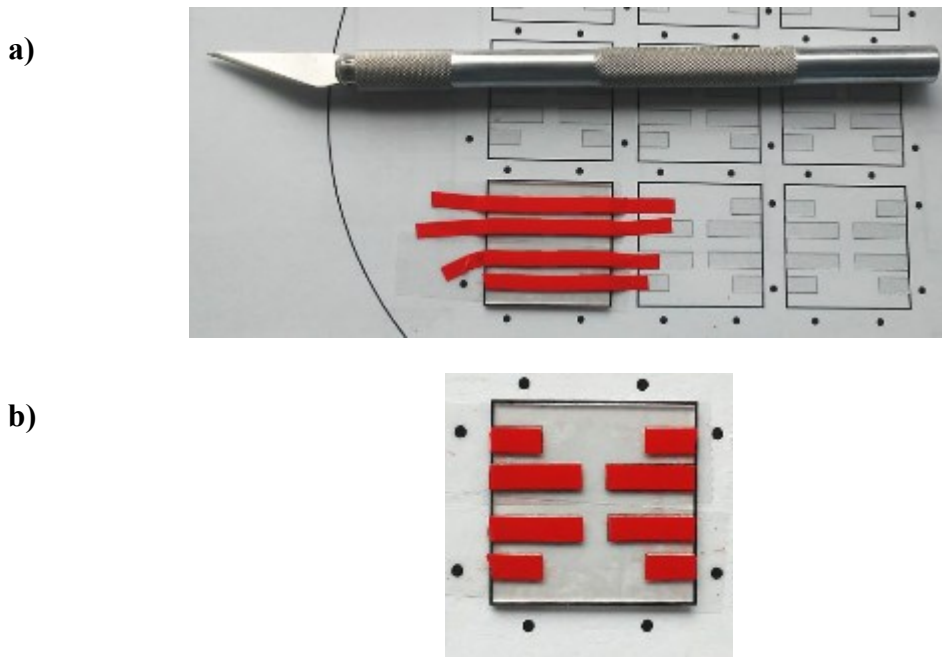


Figure 4-1: Using vinyl tape to pattern ITO covered glass surfaces. First the glass is covered in a) and then the tape is cut b) with a razor to cover those areas where the ITO will be preserved as an electrode.

The patterned substrates were then placed in a bowl. A tiny amount of zinc powder, enough to cover a small spatula, was then scooped. The zinc from the spatula was placed on the exposed ITO areas of the ITO glass and spread out evenly with the spatula.

A small volume (~1-3 ml) of 12.1M fuming hydrochloric acid (Carolina Biological) was then dispensed via a transfer pipette onto the zinc powder that was on the 1" by 1" ITO covered glass. The reaction etched off the ITO from the glass substrate where the tape was not covering the ITO. All the Zn powder was reacted with HCl. This took only a few seconds and the reaction was halted with excess DI water to neutralize all materials. The reaction created a small amount of hydrogen gas and some resultant ZnCl₂ that was disposed of with other aqueous metal salt waste in disposal bottles

Some isopropyl alcohol and acetone were then used on a cleanroom napkin to wipe away any adhesive left from the tape.

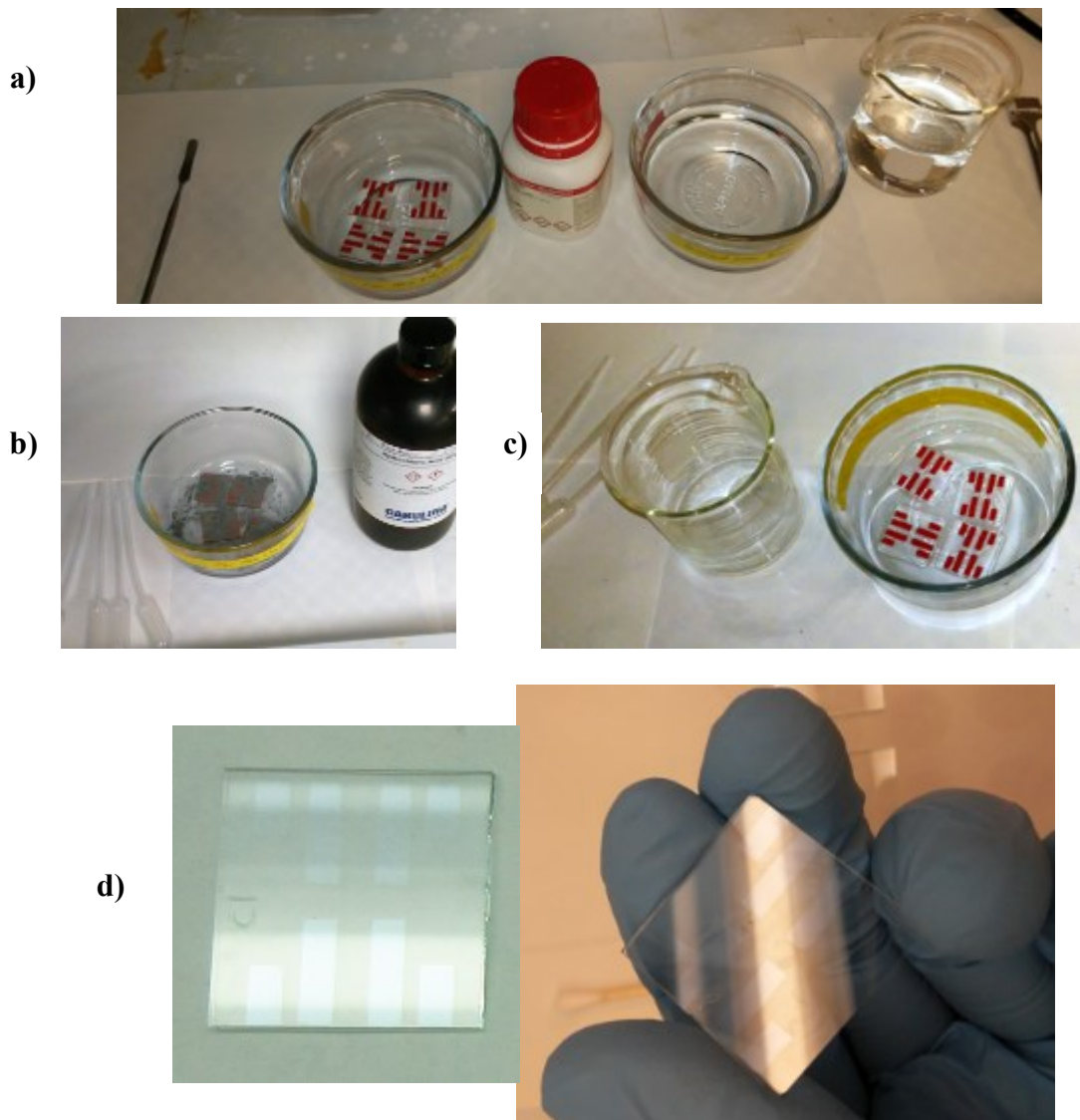


Figure 4-2: Patterning of the ITO glass substrate with hydrochloric acid (HCl). First, a) the taped patterned ITO glass is put into a bowl and then some zinc powder is sprinkled on its surface b). Hydrochloric acid is then introduced and the competition reaction is quickly quenched with water and the pieces rinsed c). The glass is then left with patterned ITO that will become the electrode for the OLED or OPD.

The patterned ITO substrate was then cleaned by ultrasonication in successive bathes of deionized water, detergent, acetone, isopropyl alcohol and deionized water. Then the substrates were taken for plasma cleaning where they were plasma treated for 10 minutes.

Next, PEDOT:PSS (Sigma) was spun on the substrate after being filtered through a 0.45 um filter. The first attempts at this did not produce the intended results and some of the results can be seen in Figure 4-3.

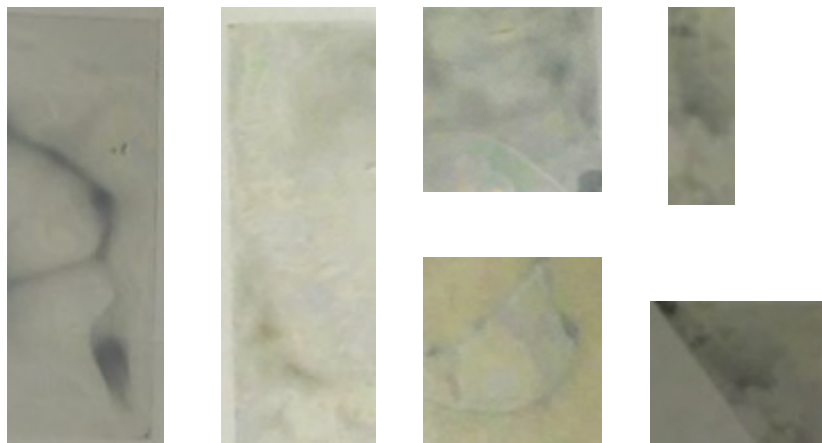
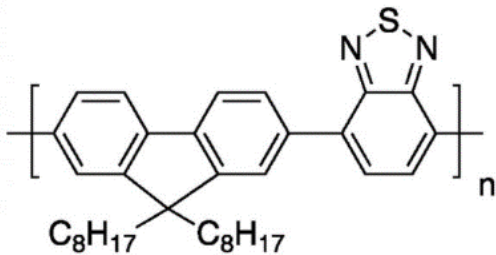


Figure 4-3: Initial attempts of spinning PEDOT on substrates were not uniform. These were done on PET before the glass substrate was attempted.

To improve the deposition of PEDOT:PSS, a different product was selected (pH1000 Heraeus), a surfactant was added at a 0.1% concentration of the total volume. This helped created a uniform PEDOT:PSS film on top of the ITO. Afterwards, the substrates were annealed for 30 minutes at 120 degrees Celsius on a hotplate.

The next step in OLED fabrication was the creation of the solution that would become the active layer that produces the light. The green OLED used the polymer Poly[(9,9-dioctylfluorenyl-2,7-diyl)-alt-co-(1,4-benzo-{2,1',3}- thiadiazole)] , often referred to as F8BT (Solaris Chem). For F8BT, a 20 mg/ml solution was made, dissolved in p-xylene. To increase the rate of dissolving, the mixture was sonicated.



a)



b)



c)

Figure 4-4: The polymer a) F8BT used for the green OLED came from the manufacturer as b) lightweight yellow strands. As F8BT is measured to create a solution, the dry strands would be difficult to handle due to the static charge and it was helpful to use c) a static gun and tweezers to handle the polymer strands, especially when weighing with plastic.

The solutions and PEDOT:PSS coated substrates were then taken and put into the glovebox. The glass substrates were baked for 120 degrees for 10 minutes. They then had the green polymer spun on at 2000 rpm. This was followed by having them placed in an evaporator. A thin metal mask was used to pattern the samples with a deposited aluminum electrode. Approximately 200 nm of aluminum was deposited in a 10^{-6} Torr vacuum in a thermal evaporator. In both OLED architectures, the active area is defined by the overlap of the top and the bottom electrodes, an area approximately 10 mm^2 .

Following this process produced green OLEDs that were viable, but also very dim as illustrated in Figure 4-5.

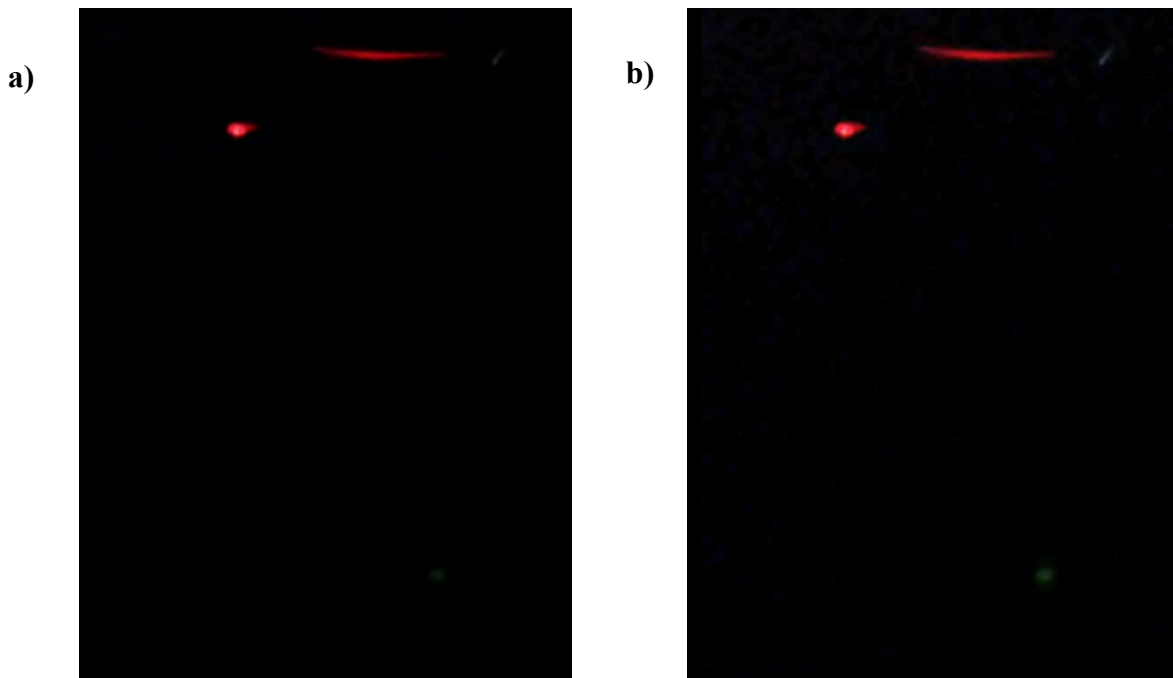


Figure 4-5: The first fabricated green OLEDs looked dim as illustrated in a) in the lower right corner. An enhanced photo b) shows the same scene as a) but lightened to better show the green OLED In the lower right corner. The red light source in the upper left of both photos is the power switch lamp of a power strip and the more elongated light in the upper right is a reflection of the switch lamp.

Efforts to increase the light output were done with two approaches. First, varying the thickness of the PEDOT:PSS through different spin rates was attempted. Second, the composition of the PEDOT:PSS layer was modified. Changing the spin rate would adjust the thickness of the layer, which directly affects its conductivity. A layer of 70-80 nm is considered optimal according to some references. Altering the chemical composition of the PEDOT:PSS with doping can also increase conductivity, current density and increase electroluminescence as shown in Figure 4-6 and Figure 4-7. Based on Figure 4-6, this current work chose to make a PEDOT:PSS with 5% sorbitol doping.

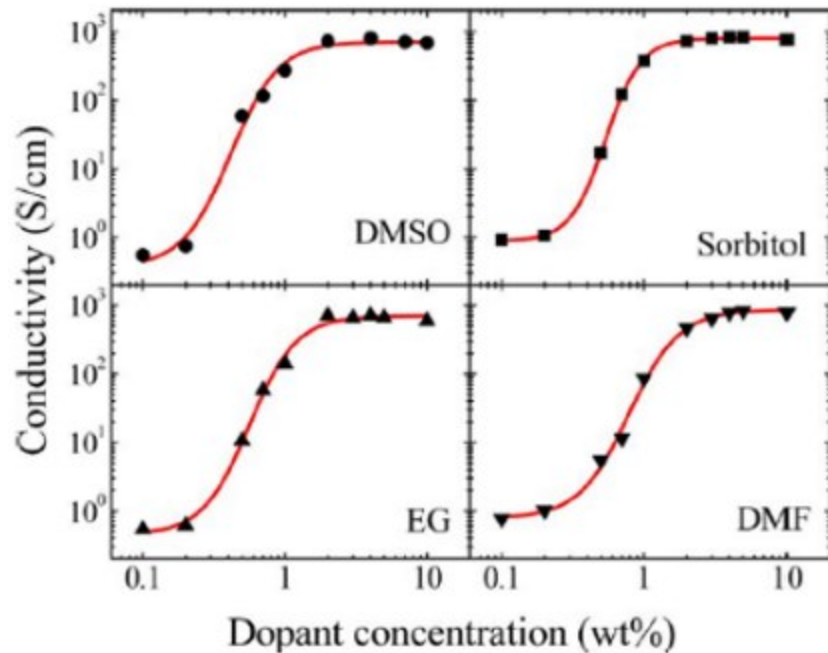


Figure 4-6: Sorbitol doping increases the conductivity of PEDOT:PSS [70].

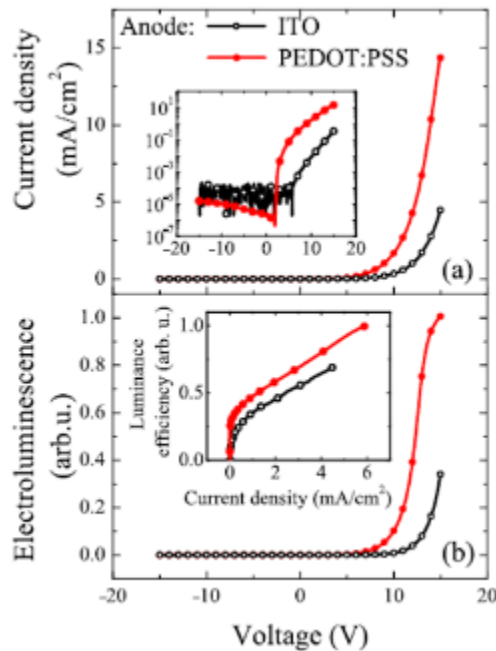


Figure 4-7: The current density and electroluminescence favorably shifts for doped and undoped PEDOT:PSS [71].

The result of some of these experiments can be seen in Table 4-1.

As the values in Table 4-1 show, the doped PEDOT:PSS OLEDs operated with lower voltage, lower current and greater light output than the undoped PEDOT:PSS OLEDs.

Table 4-1: Summary of doped and undoped PEDOT:PSS green OLED devices.

OLED Device Name	PEDOT:PSS Undoped/ Doped	PEDOT:PSS RPM	Operating Voltage	Operating Current	Power (mW)	Image of OLED
C4-6	Undoped	2000	~16 V	~9 mA	144	
			~17 V	~11 mA	187	
C5-7	Undoped	3500	~19 V	13 mA	247	
C5-3	Undoped	3500	~18 V	11 mA	198	
C6-6	Undoped	5000	~18 V	6 mA (dim)	108	
C6-3	Undoped	5000	~18 V	8 mA	144	
C1-6	Doped	2000	~13.7 V	~2.3 mA	32	
C1-7	Doped	2000	~13.52	~2.4 mA	32	

Table 4-1 indicates how the operating current of undoped PEDOT:PSS devices were 3.3 times (8 mA vs 2.4 mA) to 5.4 times (13 mA vs 2.4 mA) that of doped PEDOT:PSS devices with less electroluminescence produced. The undoped PEDOT:PSS devices also operated at a higher voltage than the doped devices. This meant the power parameters were higher for the undoped devices, ranging from 108 mW to 247 mW, while the doped ones were 32 mW. Since the operating parameters of the doped PEDOT:PSS were better in terms of lower power usage and greater light produced, it became apparent doped PEDOT:PSS should be used in the devices.

The IV (current-voltage) characteristics for these devices and others were also measured and charted in terms of power consumption. Some device results are shown in Figure 4-8.

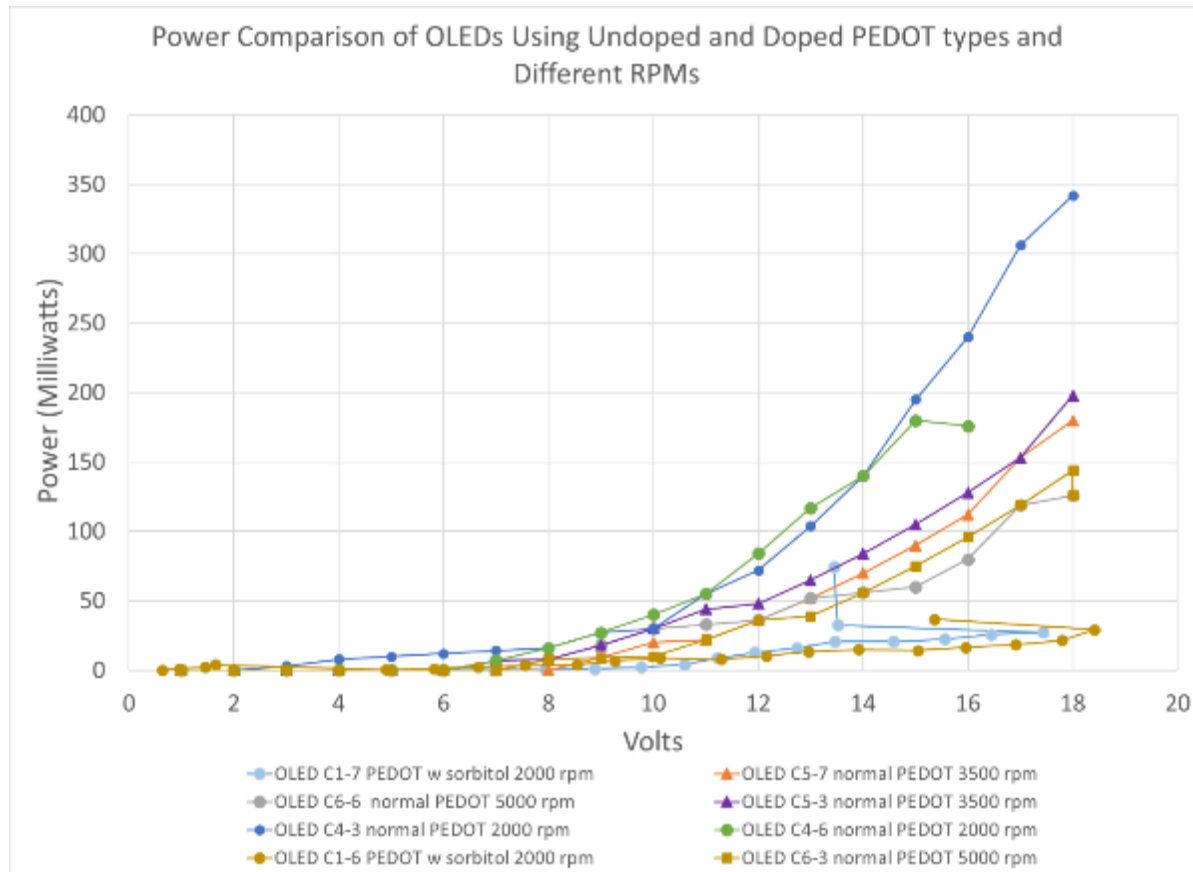


Figure 4-8: Power consumption characteristics of undoped and doped PEDOT:PSS green OLEDs.

It is clear in Figure 4-8 that the doped PEDOT:PSS devices have lower curves than the undoped devices. What is not immediately clear from the graph is why the curves unusually jump from higher voltages to lower voltage toward the end of their curves. At these points the OLED was being would begin drifting with its IV characteristics. Despite being brighter with less power than the undoped PEDOT:PSS devices, the doped devices exhibited an electrical instability for an unknown reason at the time. However, the beneficial outcome that could not be illustrated with Table 4-1 and Figure 4-8 was that the doped PEDOT:PSS were less prone to pinholes and burning out than the undoped PEDOT:PSS devices. A sequence showing pinhole formation is shown in Figure 4-9.

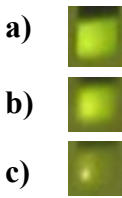


Figure 4-9: Pinhole formation was more prevalent in undoped PEDOT:PSS. The defect formation typically started with a) lightening of an area of the device, b) become brighter and have a small area left that illuminates or the whole device burn out.

Two important observations were also made at this point. The first was that when doped PEDOT:PSS were used in OLEDs, the location of the illumination was no longer limited to be at the overlap of the fabricated device's anode and cathode. This is the 3 mm by 3 mm region at the tip of the metallized electrode. This is shown in Figure 4-10a where the dashed red boxes illustrate how the ITO electrode and aluminum electrode overlap.

The second observation was that the doped PEDOT:PSS was made much more conductive than the undoped PEDOT:PSS. This higher conductivity allowed the PEDOT:PSS film to conduct across the entire surface where it was deposited. This new outcome allowed an OLED to activate and illuminate as long as there was a circuit which included the doped PEDOT:PSS layer. Figure 4-11 illustrates this by moving the alligator clip connection from the ITO electrode location from one device to the ITO electrode of a second device. The first OLED stays illuminated because the electrical circuit in the second configuration allows for the current to flow through the doped PEDOT:PSS layer.

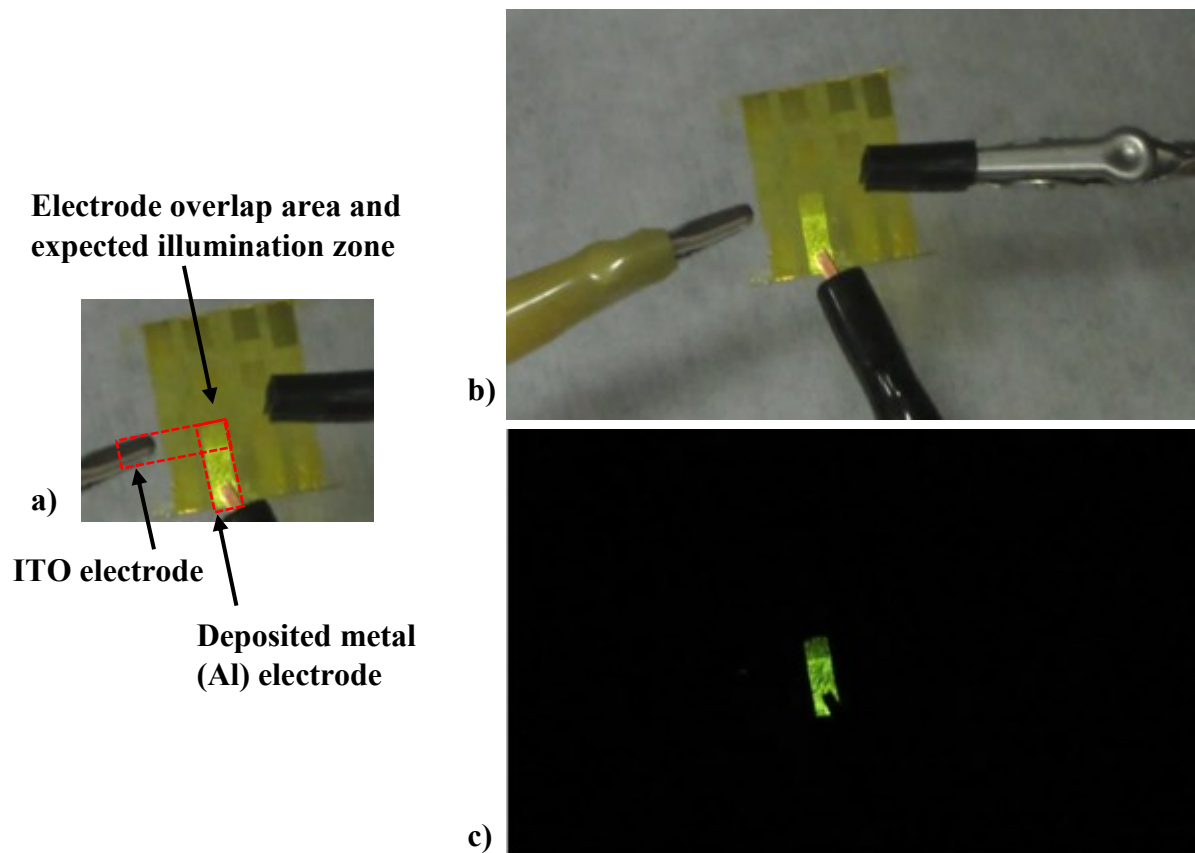


Figure 4-10: With doped PEDOT:PSS OLEDs there was illumination in regions outside the electrode overlap area. The a) overlap zone is where the where the illumination was expected to be limited, as seen with the undoped PEDOT:PSS devices of Table 4-1. In b) and c) the device's illumination can be seen in room lighting and dark conditions.

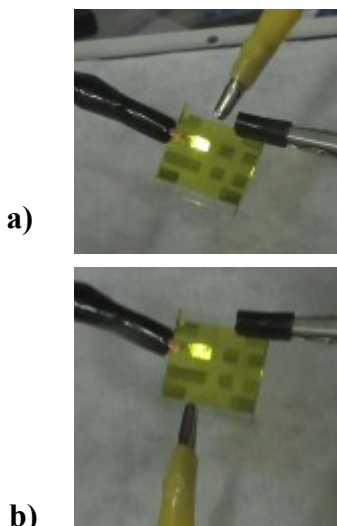


Figure 4-11: Here moving the alligator clip connection is moved from the ITO electrode location from a) one device to the ITO electrode of a b) second device. The first OLED stays illuminated because the electrical circuit in the second configuration allows for the current to flow through the doped PEDOT:PSS layer.

There was a third benefit from this higher conductivity of PEDOT:PSS with doping.

It was no longer necessary to take the acid etching step to pattern the ITO electrode for creating the OLED. Instead it was enough to deposit the metal electrode with thermal evaporation because the OLED would illuminate where the metal was deposited as long as there was an electrical circuit to the metal electrode and ITO layer. This was beneficial because the fuming HCl acid was very strong at 12.1M (36%) and required extra precautions. Also, when there were many substrates as in Figure 4-12a there were numerous pieces of tape that needed to be meticulously applied and then carefully removed as seen in Figure 4-12b. The tape also presented a problem for the future because when the eventual move to a flexible substrate would come, the tape's removal could ruin the smoothness of substrate by deforming the flexible plastic during the removal process. Several tapes were investigated and the issue seemed unavoidable. However, the use of the doped PEDOT:PSS allowed for the total

circumvention of patterning, avoiding the tape removal deformation problem and was the fourth benefit of using the doped PEDOT:PSS.

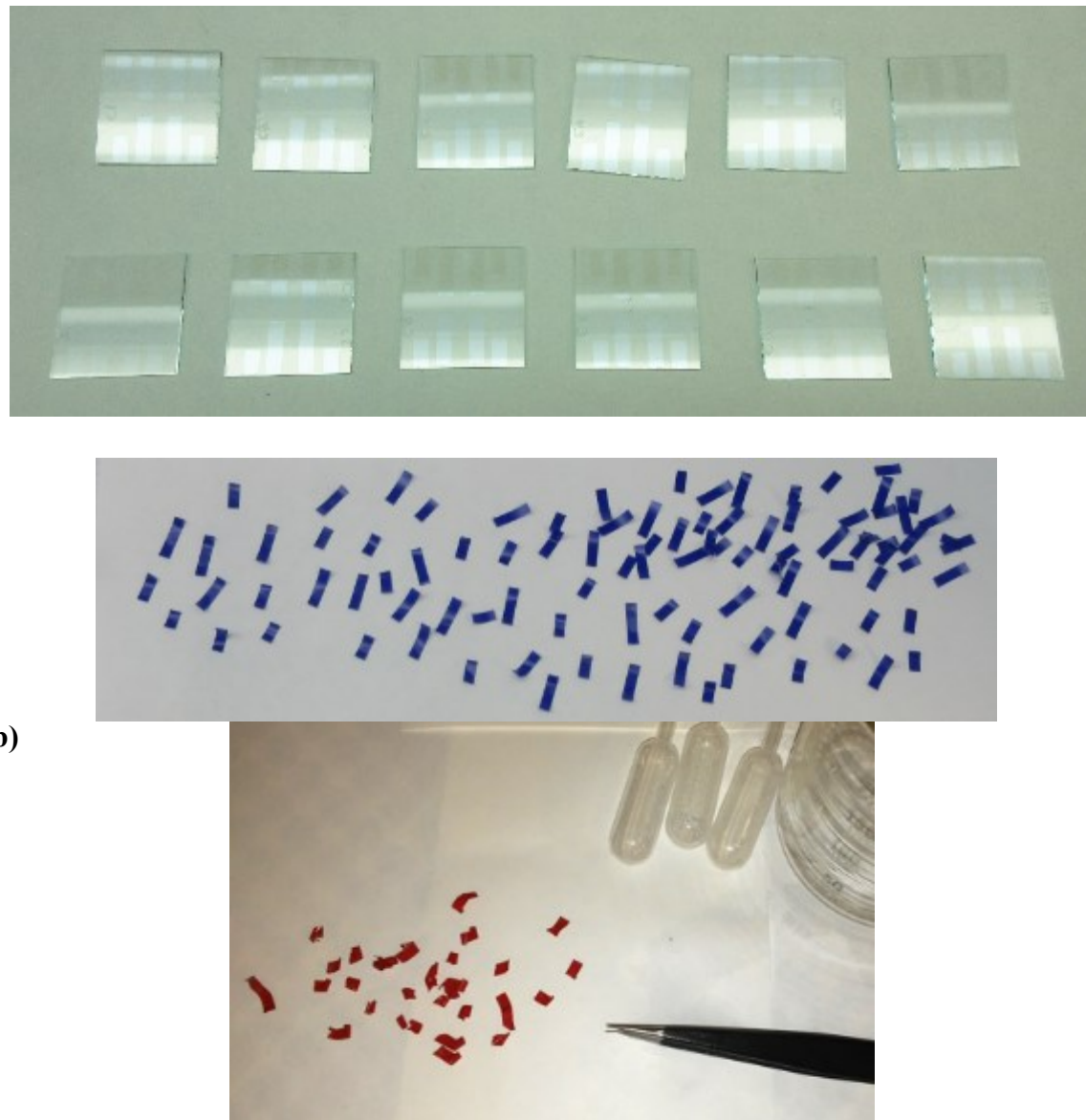


Figure 4-12: When producing a) multiple substrates, many pieces of patterning tape were meticulously applied and then b) carefully removed. By using doped PEDOT:PSS, the need to apply and remove these small piece of tape, as well as the acid etching step, could be avoided and the substrate fabrication process be simplified since the device would be defined and patterned by the area of metal electrode deposition.

4.2 Flexible Carrier Creation Header and Substrate Processing

In order to move from stiff glass substrates for the OLEDs to flexible substrates, a way to hold the flexible devices needed to be used. Two spinners were used in this project in separate labs and would have each required different chucks from the manufacturers to hold flexible substrates. An alternative approach was used which allowed a device to be processed on the two spinners in two labs without the need for specialized chucks from both of different manufacturers. This solution was use one inch aluminum squares with rounded corners and process their surface to make them adhere to plastic substrates. Prior work had made similar carriers with cut glass squares [72].

Several methods were attempted with making the carriers. All involved using a kind of silicone on the surface. One method was mixing PDMS with hexane and spinning it on [72]. Another was using Gel-Pak commercial silicone pieces, and the third was using a commercial two part silicone blend from Smooth-On. Figure 4-13 shows the third method. Here the aluminum square was coated with the silicone mixture and spun at 1000 rpm for 60 seconds and the carriers were then left alone to cure, usually overnight. Of these methods, the two-part silicone blend yielded the best results in terms of creating the carrier and in adhering to the PET substrate.

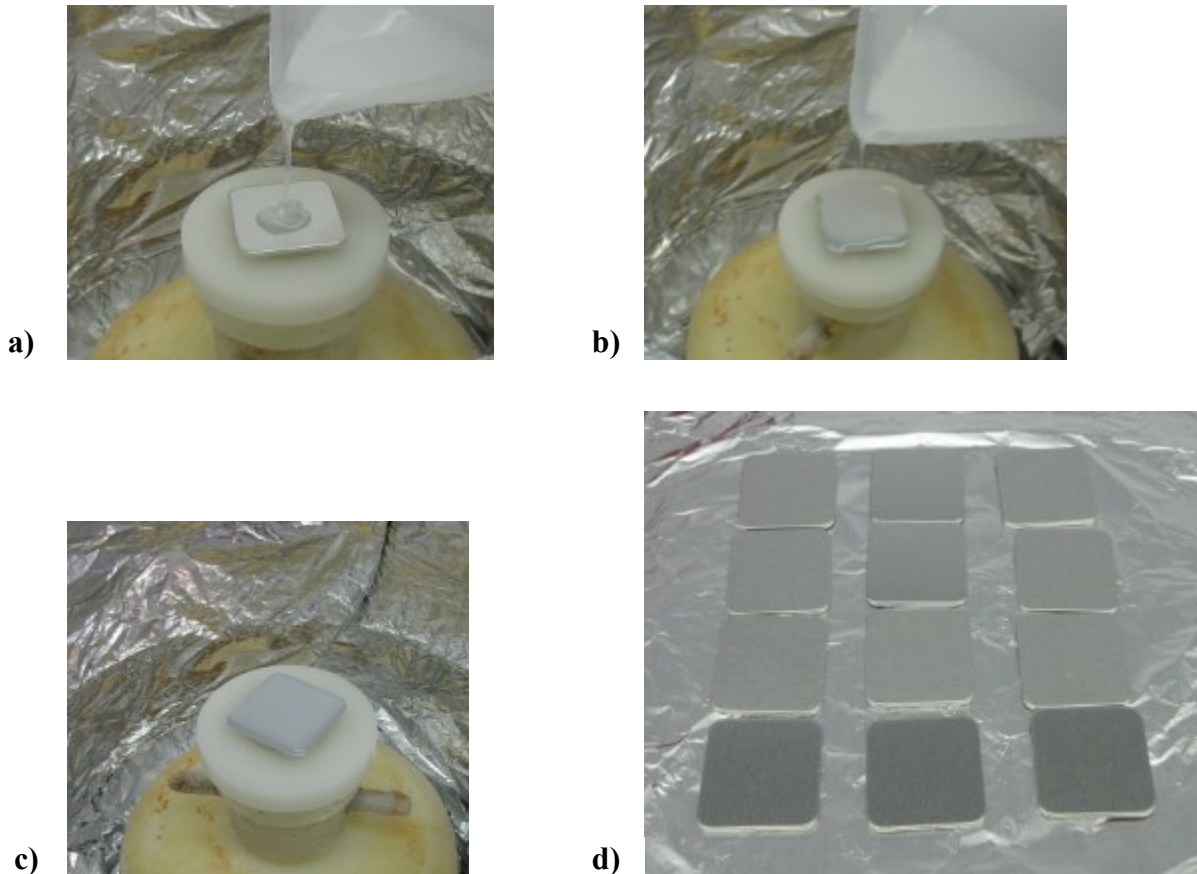


Figure 4-13: Making carriers for processing the flexible substrates by a)-c) pouring the silicone onto a one inch square aluminum until the surface is covered and then spinning it. Carriers are then d) put aside and left to cure overnight.

The next step after making the carriers was to start working on the actual substrate. In this case the selected PET substrate (MilliporeSigma) had an ITO layer 130 nm thick, a radius of curvature of 75 mm, a sheet resistance of $60 \Omega/\text{sq}$, and overall thickness of 127 um. It was taken to a laser cutter and cut into 1 inch square pieces as shown in Figure 4-14. Identification numbers were rastered onto the surface of each square to keep track of the devices through processing and device fabrication.

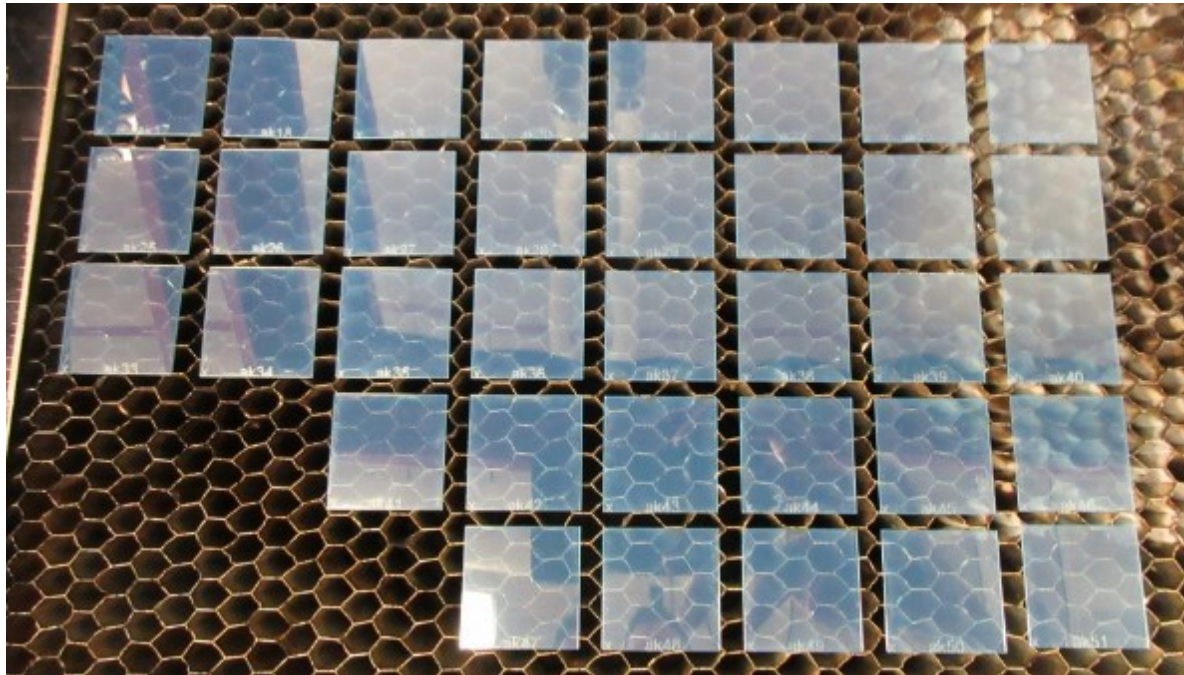


Figure 4-14: The ITO covered PET plastic substrate was laser cut into one inch squares as the substrates for the OLEDs and OPDs.

The start of the substrate processing is shown in Figure 4-15. Here the protective layer on the PET substrate was removed, the PET attached to a carrier, PEDOT:PSS spun on and the substrate baked on a hot plate.

After the substrates were coated and baked, they were put away individually in petri dishes as shown in Figure 4-16 and stored in the dry conditions of the glovebox until needed for device fabrication.

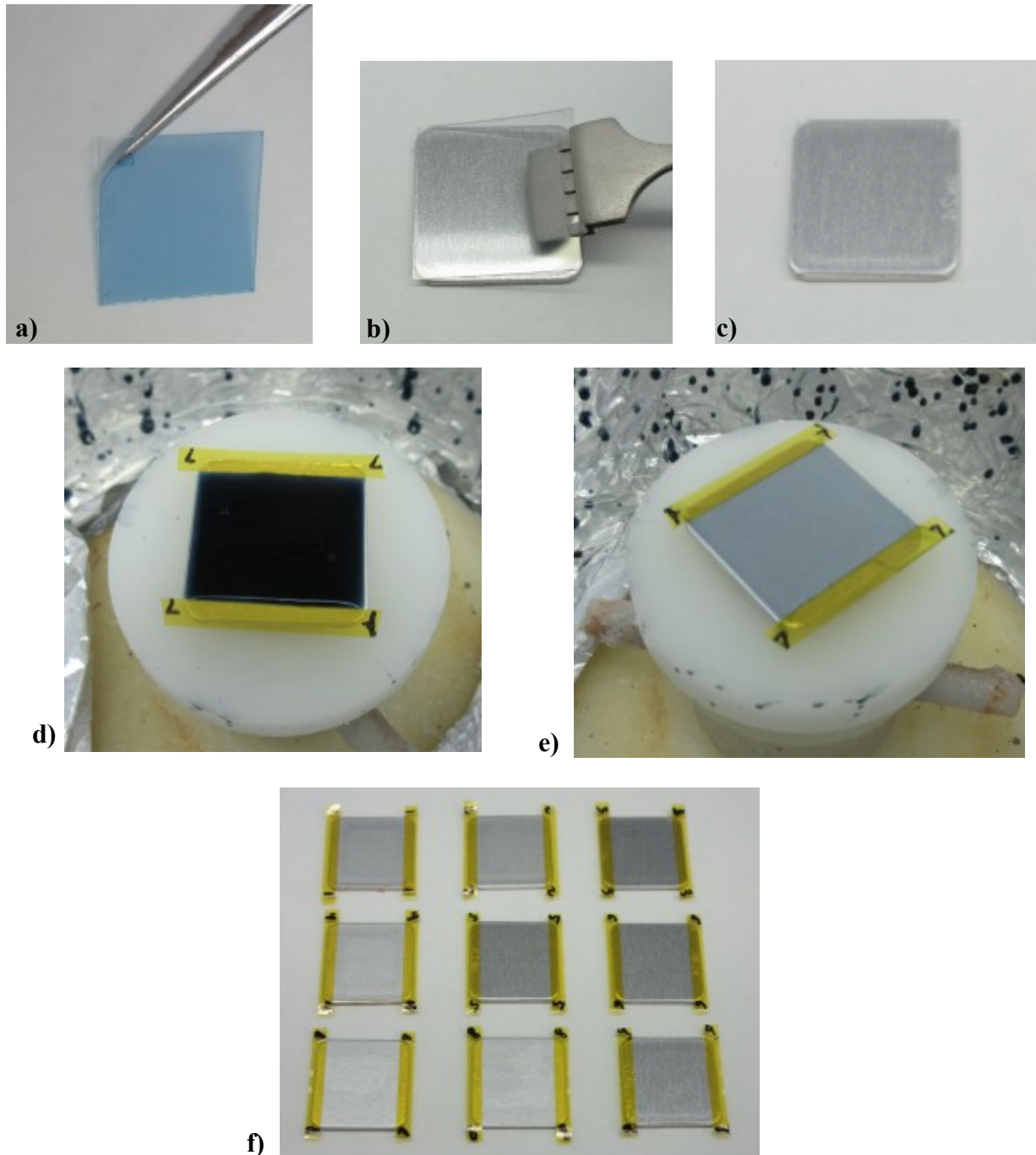


Figure 4-15: The a) ITO coated PET came with a protective layer that was removed to expose the ITO coated side of the plastic. The substrate then had kapton tape placed on its edges and b) placed on top of a prepared carrier. There the substrate c) adhered to the silicone coated surface of the aluminum square. Next, doped PEDOT:PSS was used to flood the surface, the substrate was spun, and what was resulted was e) a spincoated layer of PEDOT:PSS on the substrate. The coated substrates were then f) put on a hotplate for annealing.

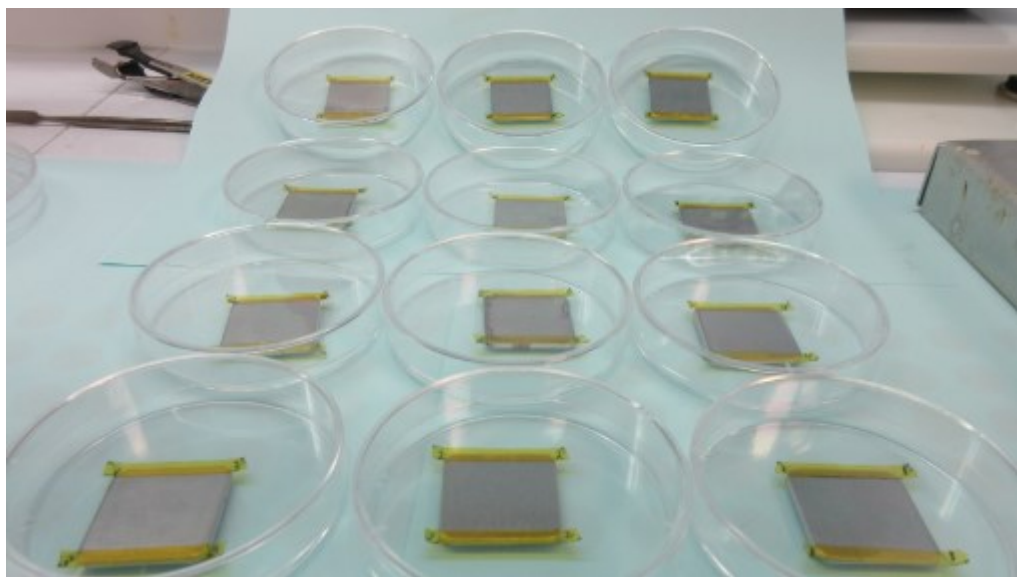


Figure 4-16: Post annealed substrates were put in individual petri dishes and stored until there was an opportunity to put OLED or OPD polymer on them in the glovebox.

The processing of the substrates was over one hundred degrees, less than the melting temperature of PET of 250 deg C. However, randomly some of the substrates would warp as shown in Figure 4-17, but some would not change. Other groups that had used PET did not report any similar observation, but they used a thinner sheet of 1.5 um.



Figure 4-17: Temperature could affect the PET surface by introducing deformations randomly. However, some substrates remained unaffected.

It was also investigated if glass carriers could reduce the sample bump formation or warping during PEDOT:PSS annealing and silicone rubber was applied to them at different spin speeds and allowed to cure , as indicated in Figure 4-18.



Figure 4-18: Glass carriers were also attempted to see if they would function better than metal carriers.

Four of the best results of the silicone-glass carrier and went through the process of putting the PET substrate on the silicone covered glass carrier and annealing the PEDOT:PSS.

Three out of the four PET substrates developed distortions, while one substrate was unaffected and remained planar. The silicone glass carrier seemed to be worse than metal that had been used. As a result, it was decided to not switch from metal to glass carriers.

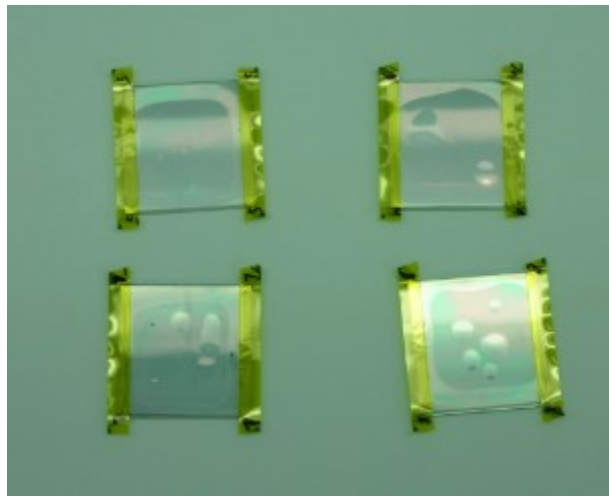


Figure 4-19: Glass carriers with PET substrate after PEDOT:PSS annealing step have warping from the heat process.

Even though the annealing process temperature was approximately 130 degrees C under the melting temperature of the PET, PET has a characteristic that when it is heated beyond the

glass transition temperature (T_g) , it can undergo thermal deformation [73]. The T_g for PET can be between 67 and 81 deg C, depending on the amorphous or crystalline nature of the PET [74].

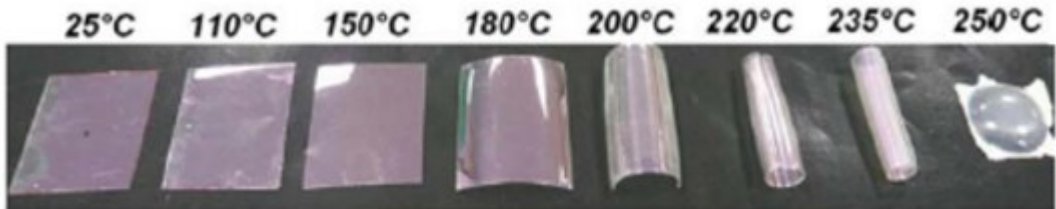


Figure 4-20: PET/ITO thermal heat treatment results [73]. For this current OLED work, the PET/ITO was processed at a maximum temperature of 120 deg C, well below the melting temperature of the PET substrate. As the picture shows, heating PET beyond its glass transition temperature (T_g) causes deformations. © 2011, Zardetto et al, under CC-BY license 3.0: <https://creativecommons.org/licenses/by/3.0/>.

Prior OLED work has taken place on PET/ITO substrate, but the authors had a much thinner substrate of 1.5 microns and did not report any deformations with their thinner material [3][72].

More recent OLED work has used a PEN (polyethylene napthalate) substrate [2]. PEN was likely chosen because it has both a higher melting temperature and glass transition temperature than PET. The glass transition temperature is about 40 degrees higher than PET at approximately 120 deg C [75]. Vendors sell sheets of PEN for several times the cost of the PET/ITO purchased for this work.

4.3 Glovebox Metal Electrode Deposition Processing

At the glovebox, the PEDOT:PSS covered PET substrates would be coated with the polymer needed for the function of the flexible device. For the green OLED this meant F8BT, the red OLED this was MDMO-PPV and for the OPD this was a mixture of ICBA and P3HT.

First a deposition mask was designed for the metal electrode patterning of the devices in the glovebox's thermal evaporation chamber. Initially this mask was made of thin steel, but it was found later that the device size needed to be adjusted. This led to experiments of using

heavy paper or multiple sheets of paper to create a mask. These could be cut locally on the laser cutter instead of relying on a vendor for the metal cutting. The laser cutting of the mask can be seen in Figure 4-21a.

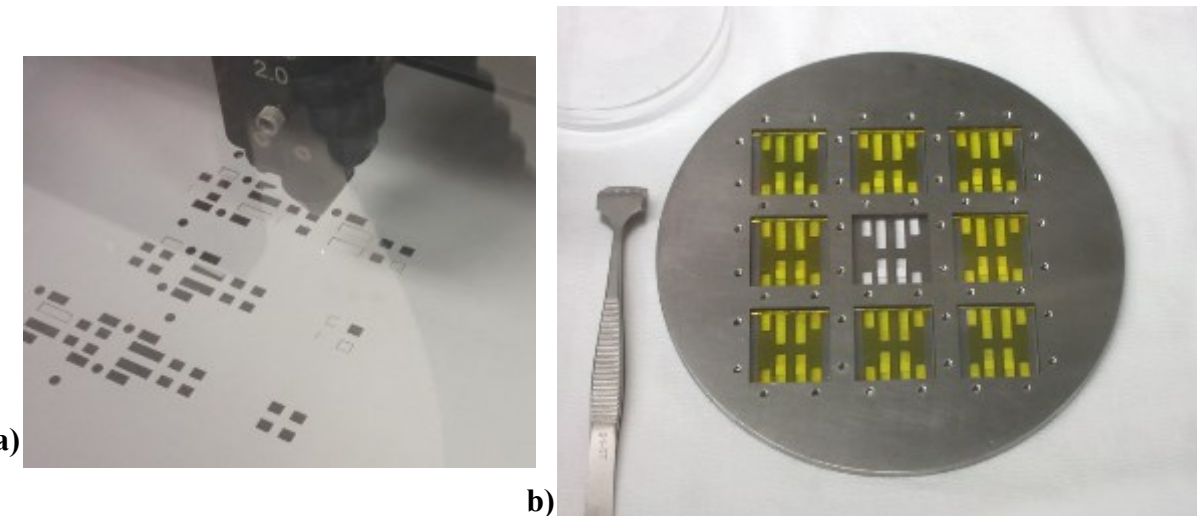
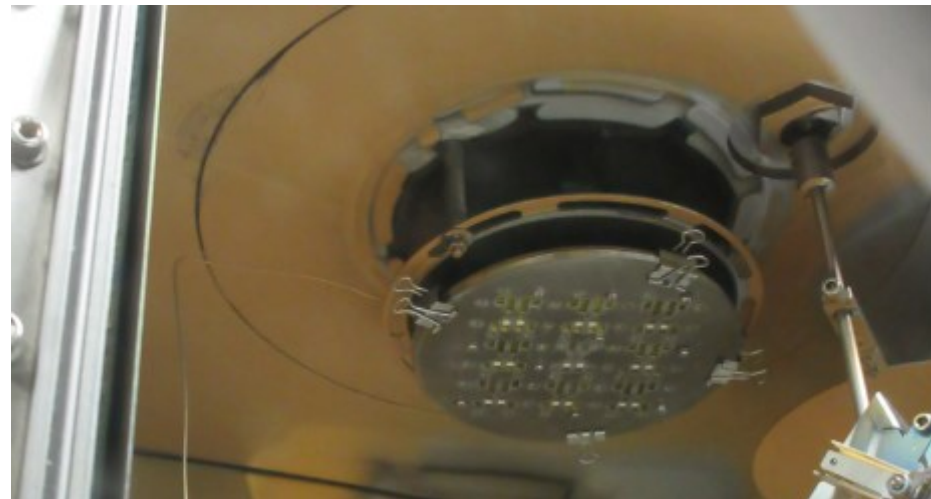


Figure 4-21: A laser cutter was used a) to cut the mask. Once cut, the mask was attached to the mask holder. The substrates covered in F8BT polymer were then loaded into the mask holder and were then ready to have metal electrodes deposited to become green OLEDs

The mask was fitted to the 6 inch sample holder that could hold 8 samples at a time. The central position was not used since the uniformity of the device may be affected by it not rotating around the center like the other positions of the substrate holder.

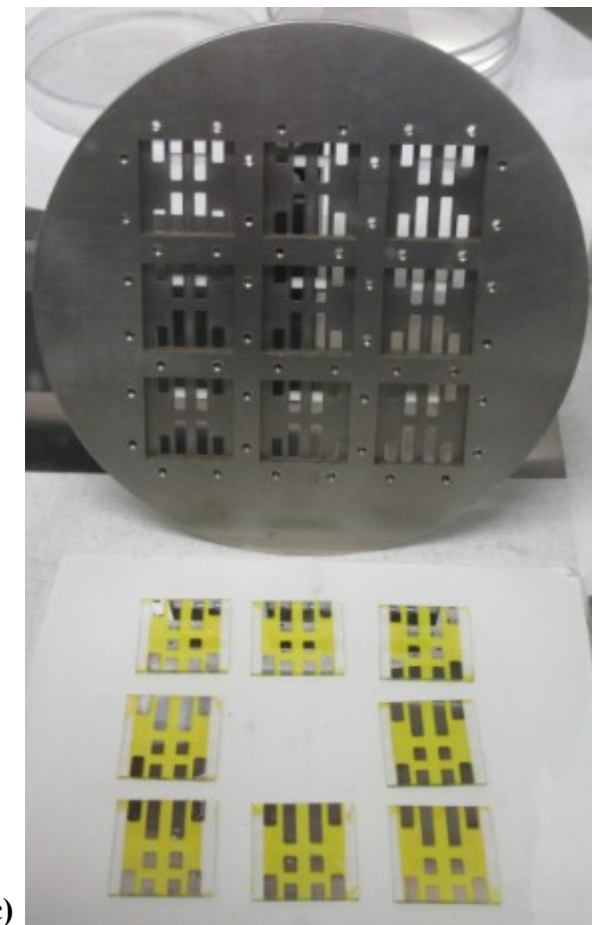
The substrates were then spincoated as detailed in later sections of this chapter. Following this, the newly coated substrates were put into the sample holder with the mask as shown in Figure 4-21b. They were then mounted to the top of the chamber as in Figure 4-22a, and the metal of choice was loaded in the thermal evaporation boats, Figure 4-22b. After the evaporation process was completed, the samples now had a metal electrode patterned on them as the picture in Figure 4-22c shows.



a)



b)



c)

Figure 4-22: The mask holder and substrates were a) put into the evaporator chamber and attached to the rotating plate at the top of the chamber. Metal was loaded into b) the appropriate thermal evaporator boats. The current driven through the boat evaporated the metal which was c) deposited on the substrates to make electrodes for the OLEDs.

4.4 Device Structure, Recipes and Design

4.4.1 Device layers, Energy Structure and Design

The structure of the device layers can be seen in Figure 4-23.

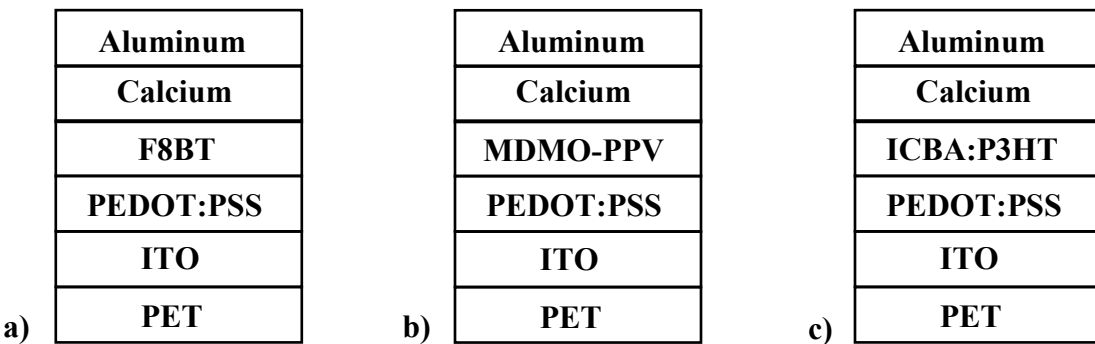


Figure 4-23: The a)-b) OLED and c) OPD layer structure. The completed devices they were encapsulated with polyimide (kapton) tape or a combination of kapton and a top layer of PET.

All the final devices were on an ITO covered PET substrate. The PET was 127 micron (5 mil) thick (Sigma) and the ITO was 130 nm thick.

First, a layer of PEDOT:PSS was spun on to the substrate. The PEDOT:PSS layer was done the same for every device. It had two additives put into it. The first was the FS-31 fluorosurfactant (Chemours) at 0.1%. The second additive was sorbitol at 5% to dope the PEDOT:PSS and make it more conductive. This solution was filtered with a 0.2 um PTFE membrane filter, and flooded on a the PEDOT:PSS surface and spun for 60 seconds. It was then annealed at 120 deg C for 10 minutes and the resulting PEDOT:PSS thickness is estimated to be 200 nm based on prior work [72]. The devices were then taken to the glovebox and stored there until ready for polymer application.

The green OLED emissive layer was poly[(9,9-di-noctylfluorenyl- 2,7-diyl)-alt-(benzo[2,1,3]thiadiazol-4,8-diyl)] (F8BT, Solaris Chem) with an Mw of 60 kDa. The layer was deposited via spin-coating from an approximate 20 mg/mL solution in p-xylene. The

spincoating was done at 2000 rpm for 60 seconds, and it was then annealed at 120 deg C for 10 minutes.

The red OLED emissive layer was be poly [2-methoxy-5-(3',7'-dimethyloctyloxy)-1,4-phenylenevinylene] (MDMO-PPV, Sigma Aldrich) with an Mn of ~120,000 g/mol deposited via spincoating from an approximate 8 mg/mL solution in toluene. The viscosity of this solution required it to be stirred overnight at 300 rpm before use. The solution was filtered with a 0.2 micron PTFE filter, and it was spun on with 500 rpm for 10 seconds, followed by 1500 rpm for 45 seconds. This was followed by annealing at 120 deg C for 10 minutes. Based on previous work, it is estimated the film thickness was approximately 225 nm [72].

The OPD was made of two components of 1:1 mixture of poly(3-hexylthiophene-2,5-diyl):indene-C60 bis-adduct (ICBA:P3HT, Solaris Chem) that was 17 mg/ml. The P3HT had a weight of Mw 55 kDa. This solution was filtered with a 0.2 um PTFE filter and then spun on at 800 rpm for 30 seconds. It was annealed at 120 deg C for 10 minutes. The film was estimated to be about 100 nm thick based upon prior work [15].

After coated with the emissive layer, the organic devices were taken to an evaporation chamber and a calcium layer (~25 nm) was deposited. This was followed by an aluminum evaporated layer, approximately 200 nm thick.

Figure 4-24 shows the chemical structure for the red emissive layer (MDMO-PPV), the green emissive layer (F8BT) and PEDOT:PSS.

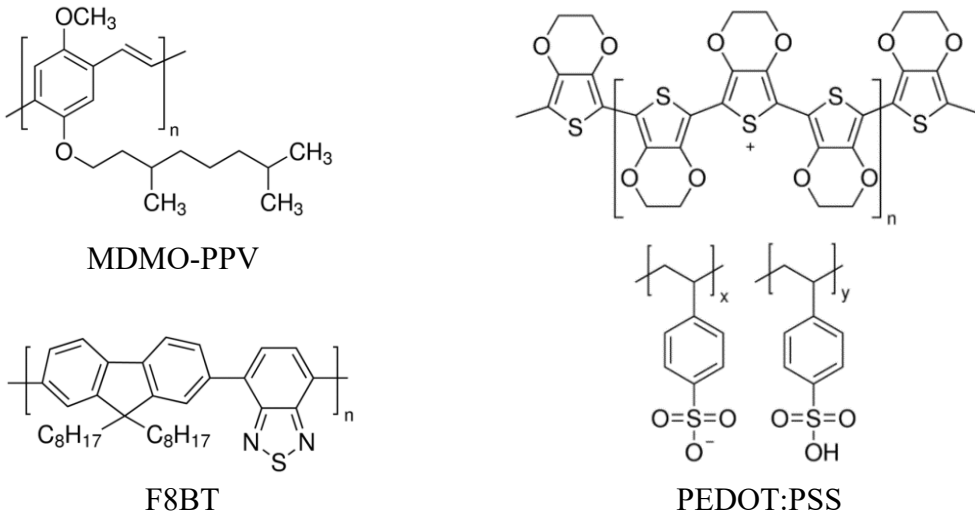


Figure 4-24: Chemical structure of the components for OLEDs and the conducting layer, PEDOT:PSS. MDMO-PPV and F8BT were the red and green emissive layers respectively.

The OPDs had different active layer compounds as mentioned earlier. They were P3HT and ICBA. These two compounds were mixed with a 1:1 w/w ratio.

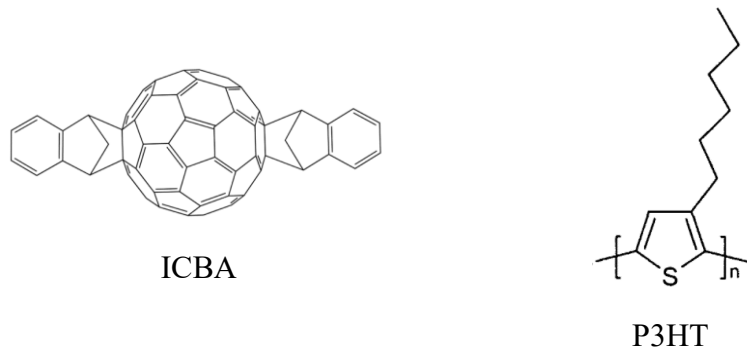


Figure 4-25: Chemical structures of the active layer organic compounds for the OPD. P3HT functioned as the electron donor and ICBA as the electron receptor [76].

The energy structures of the green and red OLEDs are similar, but not the same due to their emissive layers being different. Figure 4-26 shows the green OLED energy structure.

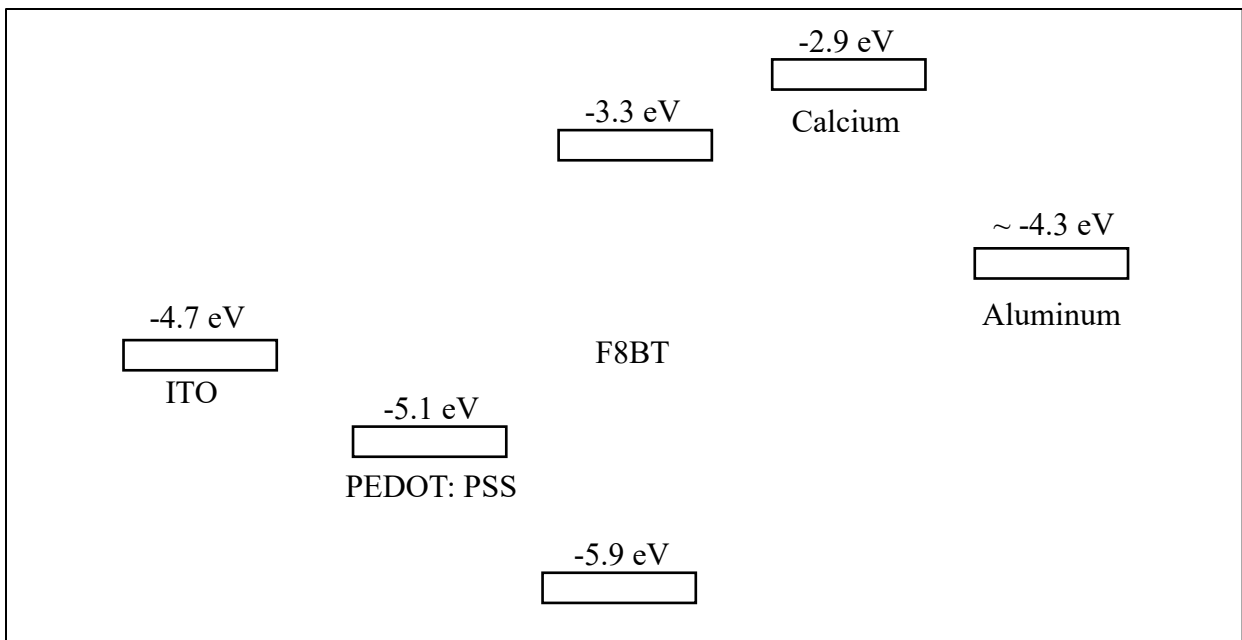


Figure 4-26: The green OLED stack and energy structure. The values for aluminum, calcium and ITO were sourced from by Hasan et al [77], PEDOT:PSS by Lochner et al [5], and F8BT from Ossila.

As mentioned above, the red OLED differs by the emissive layer with respect to the green OLED. That is reflected in the red OLED energy structure that is shown in Figure 4-27.

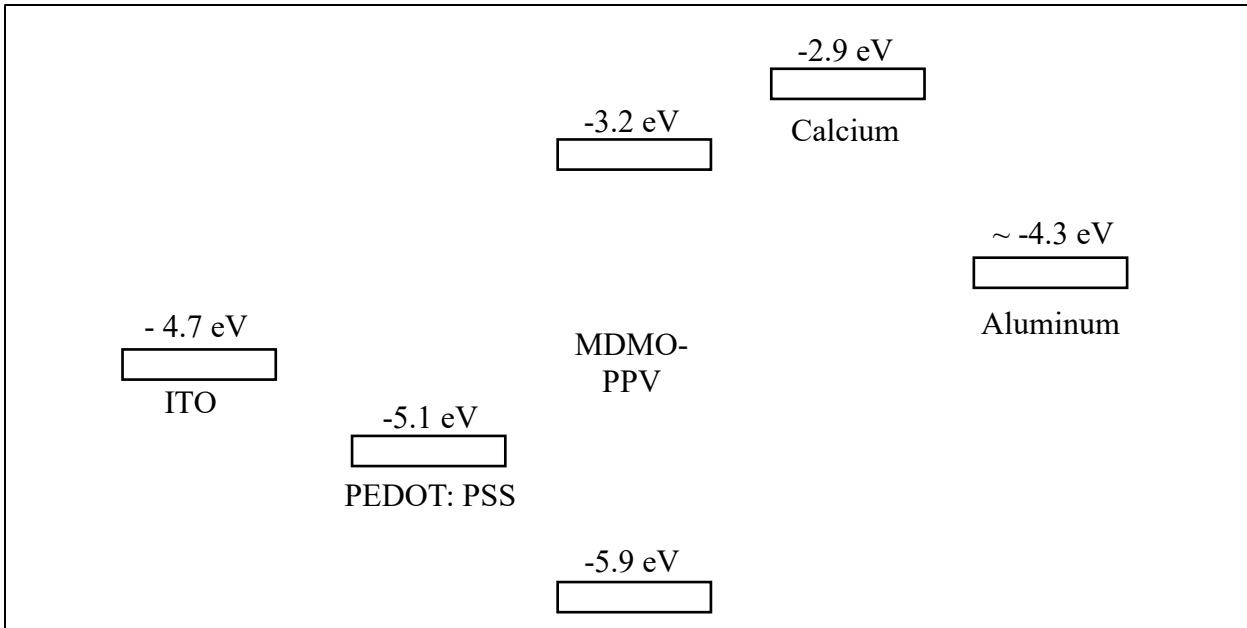


Figure 4-27: The red OLED stack and energy structure. The values for aluminum, calcium and ITO were sourced from Hasan et al [77], PEDOT:PSS by Lochner et al [5], and MDMO-PPV by MilliporeSigma.

The detection of the light that was refracted through the tissue was planned to be done by an OPD, had the energy structure as shown in Figure 4-28.

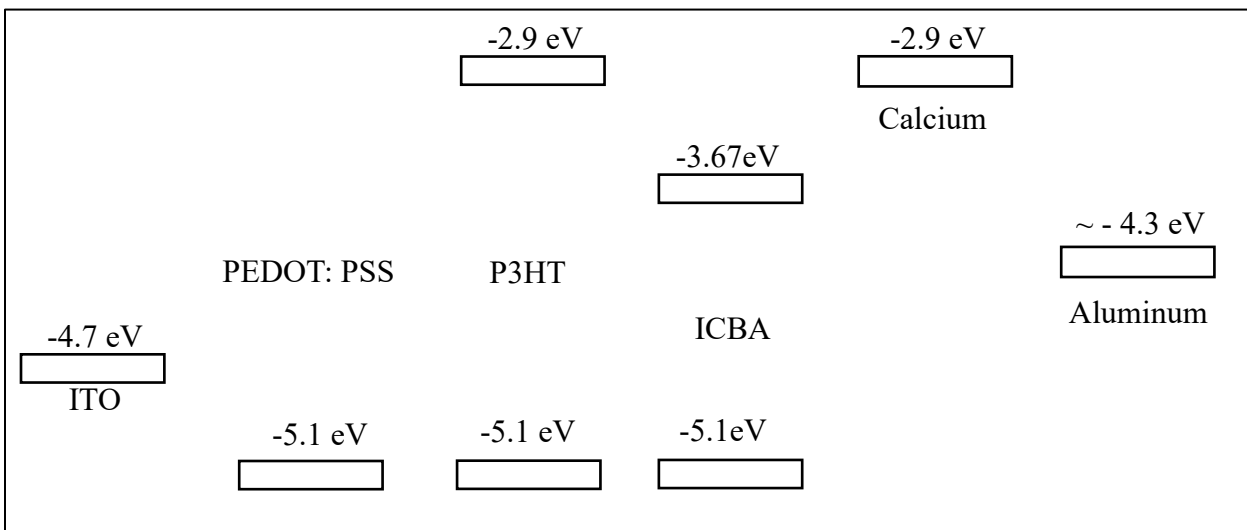


Figure 4-28: The OPD stack and energy structure. The values for aluminum, calcium and ITO were sourced from Hasan et al [77] and PEDOT:PSS by Lochner et al [5]. The values for P3HT and ICBA were sourced from An et al [78].

There are a number of reasons as to why these materials were good options for this work.

First, the emission spectrum of the red and green OLEDs coincide with the absorption spectrum of the OPD. The emission and absorption of these devices are shown in Figure 4-29.

More importantly, the emission spectra of the OLED and the absorption spectra also align with biologically relevant wavelengths for the absorption spectra of oxygenated and deoxygenated hemoglobin. To illustrate this arrangement, the peaks of the red and green OLED emission curve have been highlighted across the emission spectra, the oxy- and deoxy-hemoglobin curve, and the OPD absorption spectra in Figure 4-29.

Some added benefits include the green OLED having an active layer known that belongs to the polyfluorene family, known for its stability and relative higher efficiencies [5]. The OPD has the benefit of an active layer with P3HT as a component, which has been well characterized and is reasonably priced. Additionally, the other active layer component of the OPD is the fullerene ICBA, that when mixed with P3HT creates a high open circuit voltage and good efficiency [79].

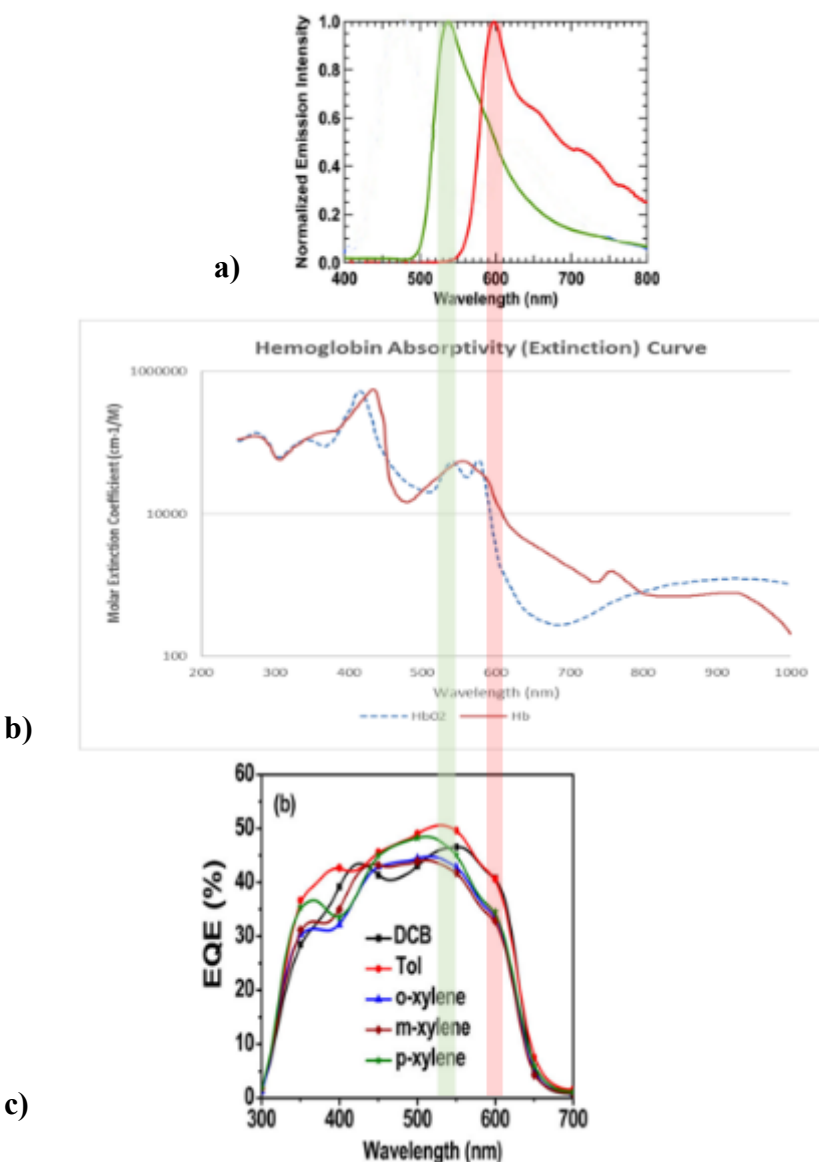


Figure 4-29: An alignment is required for the system to work for pulse oximetry. The a) emissions of the OLEDs must correspond with the b) hemoglobin absorptivity curve [13], and the c) photodiode response has to be active in the spectrum of the OLEDs. The OLED spectra is from Reference [14] and the OPD absorption is from reference [76]. (Figure 4-29a adapted from [14] © 2015, Haigh et al. under CC-BY license 4.0: <https://creativecommons.org/licenses/by/4.0/>, Figure 4-29c) Reprinted (adapted) with permission from [15], © (2014) American Chemical Society.)

4.4.2 Device Spin Challenges

All of the polymers selected in this work were commercially available and had been used in prior work. However, this did not mean their recipes were complete. For the local equipment and settings, the further refinement was done to develop these recipes.

The work began with the green OLED and in the beginning devices were made on glass. When the transition came from creating devices on rigid substrates on glass to flexible substrates on the PET, there was an immediate first issue with spinning change. The devices did not illuminate as before. It turned out that the PEDOT:PSS application rpm needed to be reduced for the flexible substrate because the water based adhered differently to the plastic. The speed had to be reduced from 2000 rpm to 1000 rpm.

Initially it appeared that there weren't issues with the green polymer since it dissolved in the solvent over time. However, there could be some inconsistent graininess with the device's illumination. Initially it was thought to be the underlying doped PEDOT:PSS. However, a change in protocol of filtering the green OLED solution through a 0.2 um PTFE filter made the device more uniform when it illuminated. This indicates there must have been some particles inside the F8BT. However, whether the F8BT is filtered or not, it looks very uniform as shown in Figure 4-30a.

The MDMO-PPV had issues with dissolving. Various attempts to make it dissolve were tried. Sonicating it in a bath for 3 hours did not work. Other methods were then attempted of giving it 24 hours to dissolve and trying different solvents such as p-xylene and dichlorobenzene did not work either. Then the three vials with the three solvents and MDMO-PPV were attached to foam floats and put in the sonicator directly without a bath to be sonicated. This was unsuccessful too. Finally a 7 mm stir bar was put into the 4 mL vial and let spin for a few hours and the MDMO-PPV finally dissolved in the toluene.

The viscosity of the MDMO-PPV solution became an issue in the spincoating onto the PET substrate. Despite being filtered and applied with a spin speed found in literature, the spincoating recipe needed to be adjusted to create a uniform film, otherwise what resulted was a heavily streaked coating as shown in Figure 4-30b. If left to stand and not stirred, MDMO-PPV in toluene will gel at the bottom of the bottle as shown in Figure 4-30c.

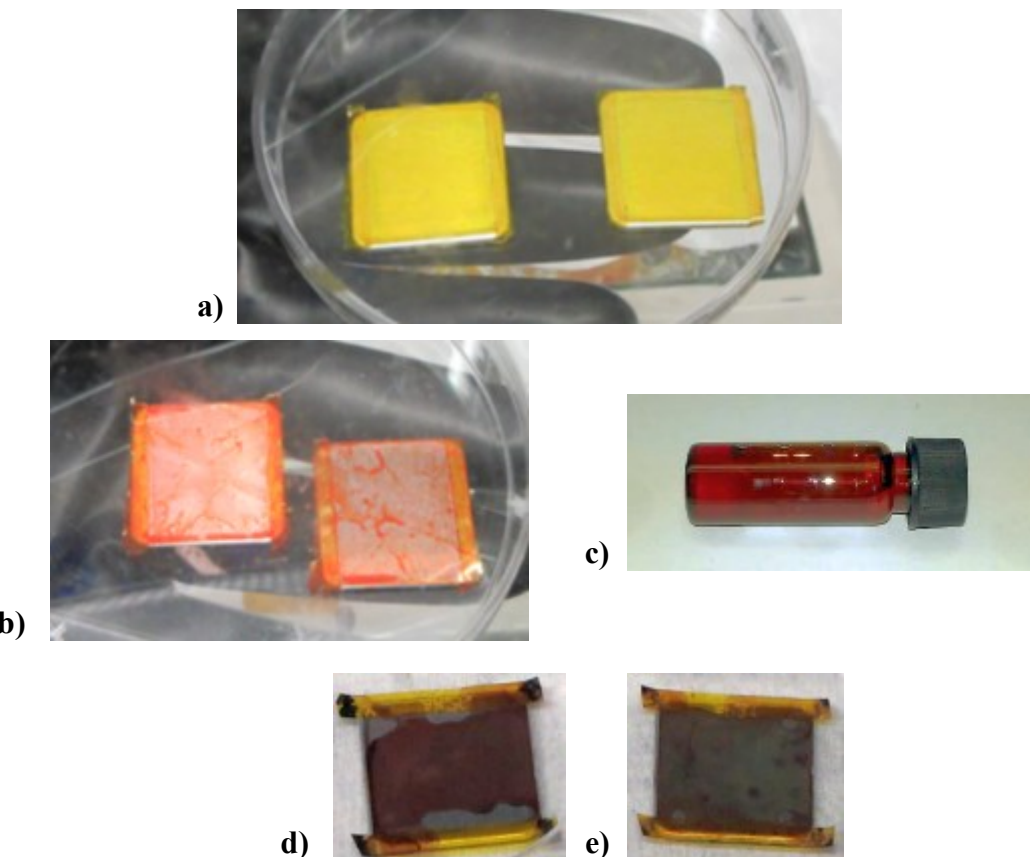


Figure 4-30: Spincoating varied with the polymer. F8BT dissolved well and could be a) spun on uniformly but required an additional step not mentioned in literature of filtering. MDMO-PPV had a high viscosity and b) initially would not spin on uniformly and required the development of a spin recipe to overcome this issue. If left to sit in a bottle, a portion of MDMO-PPV will c) gel on the bottom of the container as can be seen in this bottle put on its side. MDMO-PPV needs to be mixed with a stirrer for hours before use. The photodiode solution was sensitive to speed conditions and the difference can be seen in d) and e) which only vary in 3 seconds of spin. The photodiode solution needed to be stirred for hours as well.

While working with the red OLEDs make them brighter another issue surfaced with MDMO-PPV. This can be seen in Figure 4-31 and indicates the measurements of the volume of solvent and mass of MDMO-PPV to be used should be measured as accurately as possible.

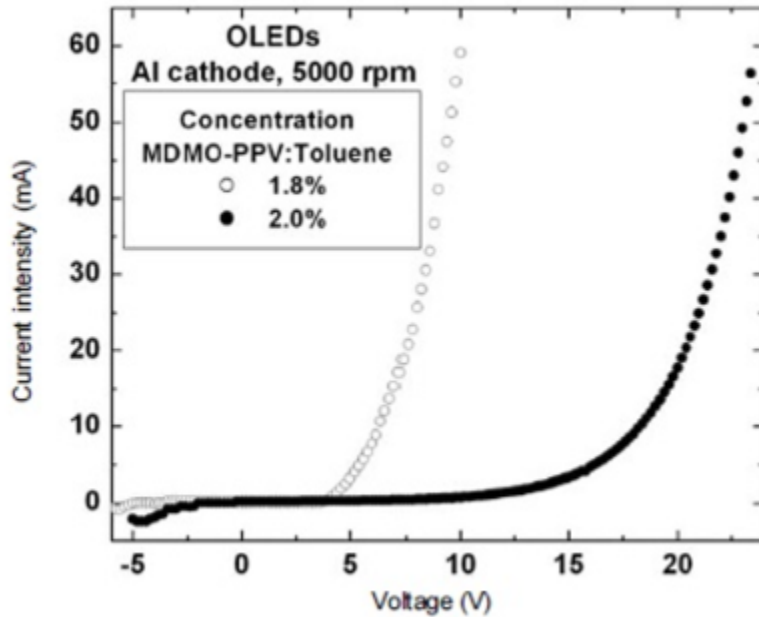


Figure 4-31: MDMO-PPV can be sensitive to slight changes in concentration, as shown by Mendez-Pinzon et al [80].

The photodiode solution was not without issues and the spinning of the solution needed to be carefully calibrated. The spin shown in Figure 4-30e is just three seconds longer than Figure 4-30d. The spin result in Figure 4-30e has more inconsistency in the center of the square than Figure 4-30d. The spin recipe for Figure 4-30d was more uniform in the area where the devices would be fabricated. Since the devices became larger over time, the spin for Figure 4-30d was chosen.

Red polymer devices were also susceptible to pinholes at various speeds and annealing temperatures other than the final parameters used. Figure 4-32 shows examples of this issue.

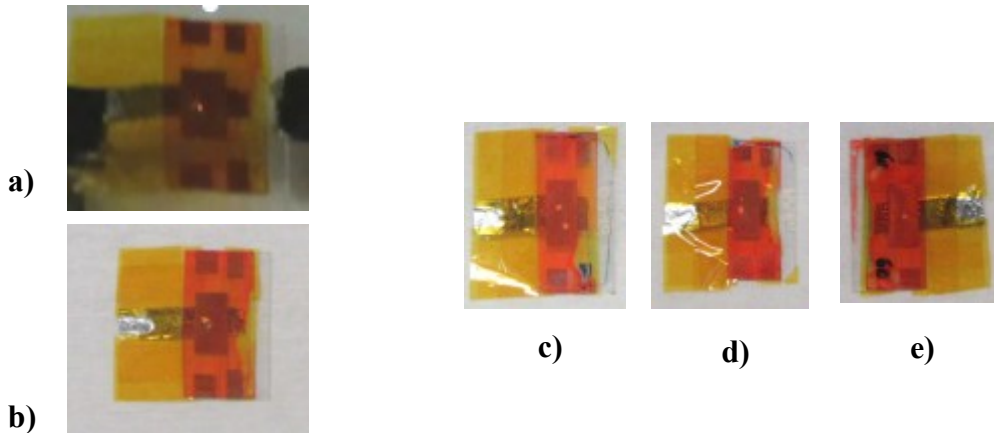


Figure 4-32: Testing showed that some spinning speeds and annealing temperatures can make a device prone to developing pinholes. A pinhole has developed in a) and b) is shown in regular lighting conditions. The other examples are additional devices that suddenly developed pinholes.

Eventually the spinning issues were overcome to create substrates with uniform coatings as shown in Figure 4-33.

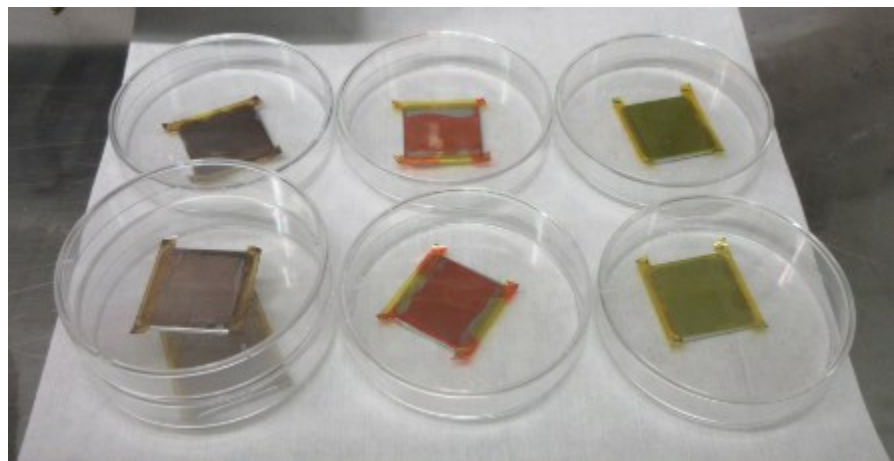


Figure 4-33: Spinning recipes and techniques were developed that eventually produced polymer coats that were more uniform.

4.4.3 Calcium Deposition Issues

Calcium came from the manufacturer packaged with mineral oil (Figure 4-34a) that protected it from oxidation but caused contamination issues with deposition. An additional issue was that calcium sublimates instead of melting. This means that while thermal heating (Figure 4-34b) is ongoing, both mineral oil and calcium gas are coming off the mineral pellets. Experiments were conducted that varied the rate of thermal heating to separate the evaporation of carbon from the calcium before deposition. The internal pressure of the sublimating calcium can become so large that it can explode (Figure 4-34c). Sometimes the gas pressure was so large during heating that the calcium could be seen to move in the chamber in the thermal heating step shown in Figure 4-34b.

The vendor's instructions that required hexane to be removed which could not be done with this glovebox.

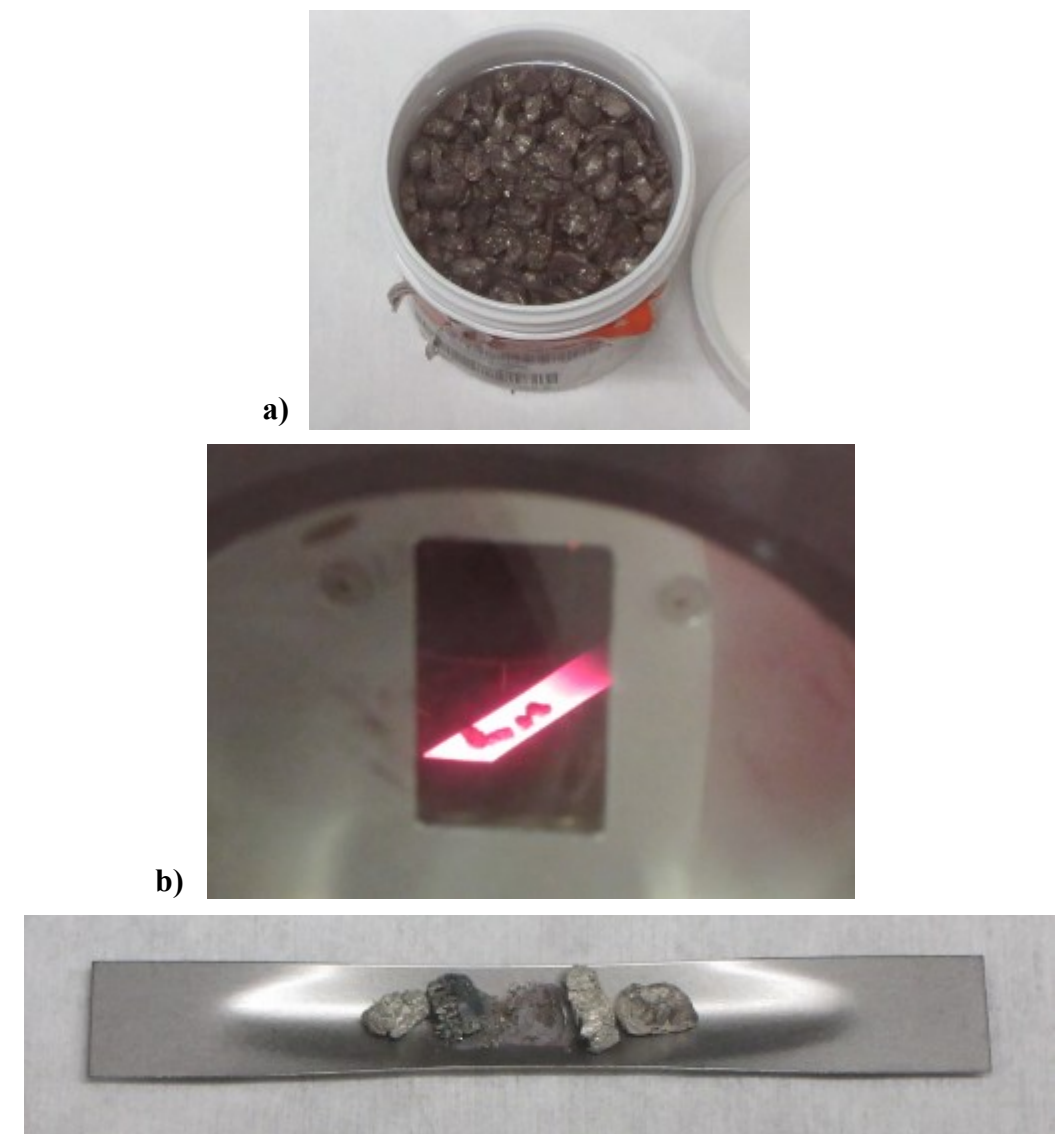


Figure 4-34: Calcium came a) packed in mineral oil. When in the b) evaporation chamber, the current of the evaporation boat needed to be carefully adjusted. If the current was changed too quickly, the temperature of the boat could correspondingly increase too quickly, causing the calcium pellet to explode and send debris and dust into the chamber. In c) the pellet in the center exploded because the temperature either changed too rapidly or became too hot.

A picture of a heated calcium pellet illustrates the carbon in Figure 4-35a)-b). The results of the carbon contamination can be seen in Figure 4-35c)-e).

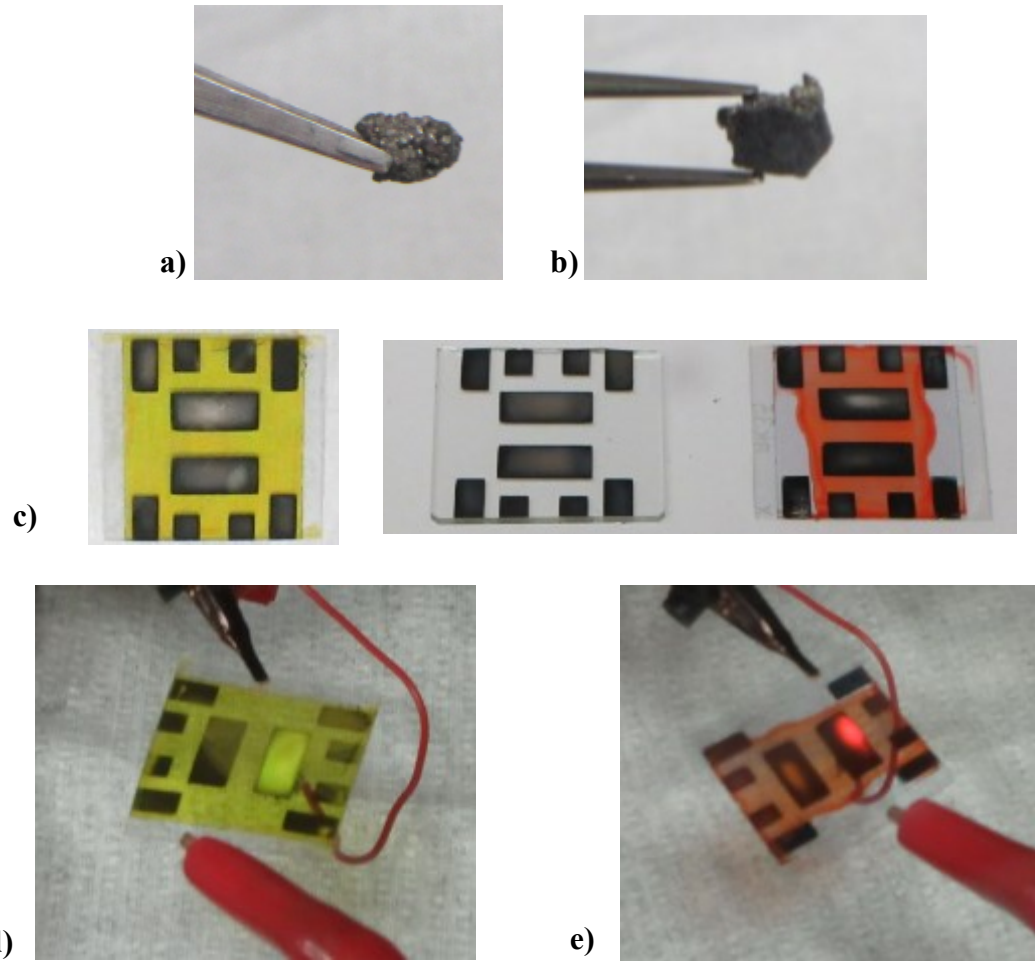


Figure 4-35: The initial attempts of using calcium were problematic because the calcium came packaged in mineral oil. The mineral oil's carbon became a contaminant in the metal electrode deposition process. Carbon was easily noticeable as a black color on a)-b) some calcium pellets following the thermal evaporation. The c) first devices made with calcium had carbon contamination, causing their electrodes to be turned black in regions. From left to right in c) is a contaminated green OLED, a glass slide coated for evaluation purposes, and a contaminated red OLED. The carbon affected the device by interfering with illumination in the regions where the carbon was present. The activated d)-e) OLEDs illustrate how the illumination was more in the regions that had less carbon and more metal.

Iterative experimenting was done on a blank substrates that were not PEDOT coated or ready to be made into devices. Their function was just to discover which method or process refinement deposited less carbon. Some of these blanks can be seen in Figure 4-36.

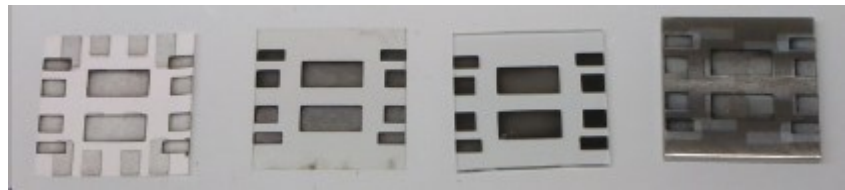


Figure 4-36: Blank substrates of different materials were used to experiment which method best diminished carbon contamination.

Eventually an evaporation recipe was developed that solved the challenges of the carbon contamination and the devices shown in Figure 4-37 and in the next sections show that the carbon was either much reduced or not present in later devices.

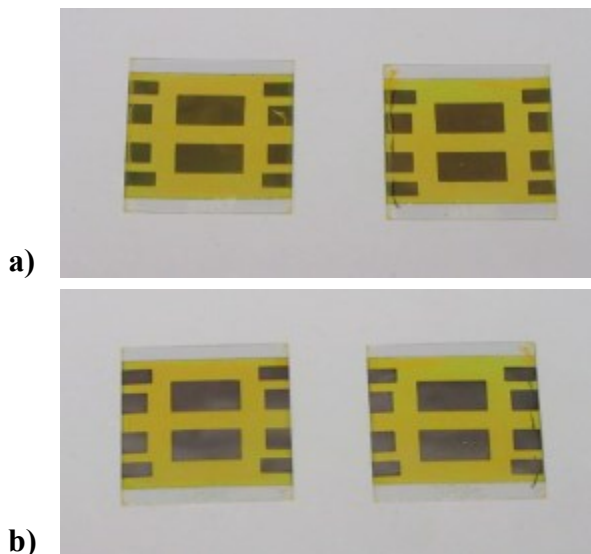


Figure 4-37: The calcium evaporation technique was refined until little or no carbon contamination were visible either on the a) PET side or b) the deposited metal electrode side.

4.4.4 Device Storage

Sometimes the PEDOT:PSS covered PET substrates would develop spots while in storage inside the glovebox. It was uncertain what caused these features. They can be seen in Figure 4-38.

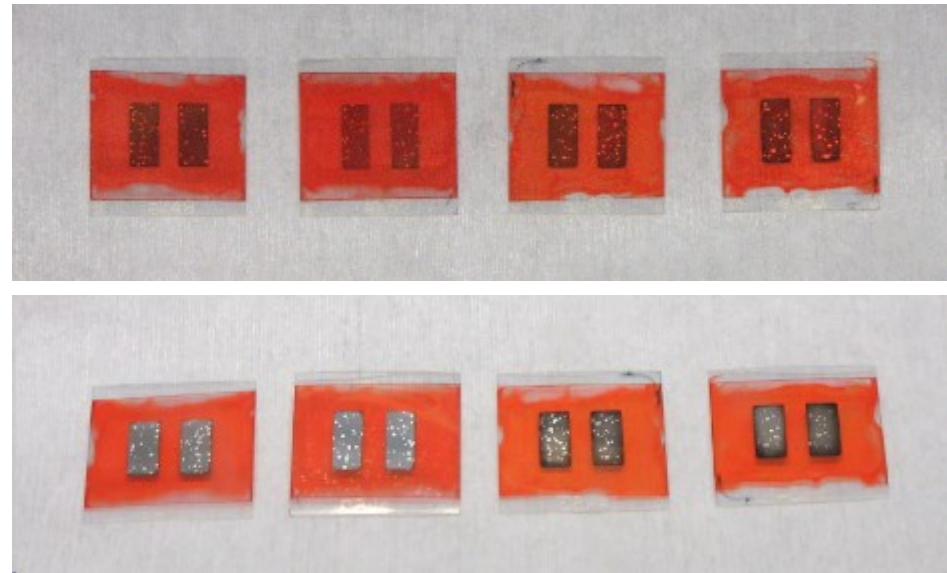


Figure 4-38: Storage conditions in glove box sometimes introduced dots of unknown origin, but the devices still worked.

4.5 Flexible OLED and OPD Device Characterization

As mentioned in the earlier section on spinning, the red polymer was a challenge to spin on evenly and required trials to get the polymer coat on the PEDOT:PSS to be more uniform. Figure 4-39 shows how various attempts were made to at different spin speeds to fabricate the red OLED. The initial results were unstable devices.

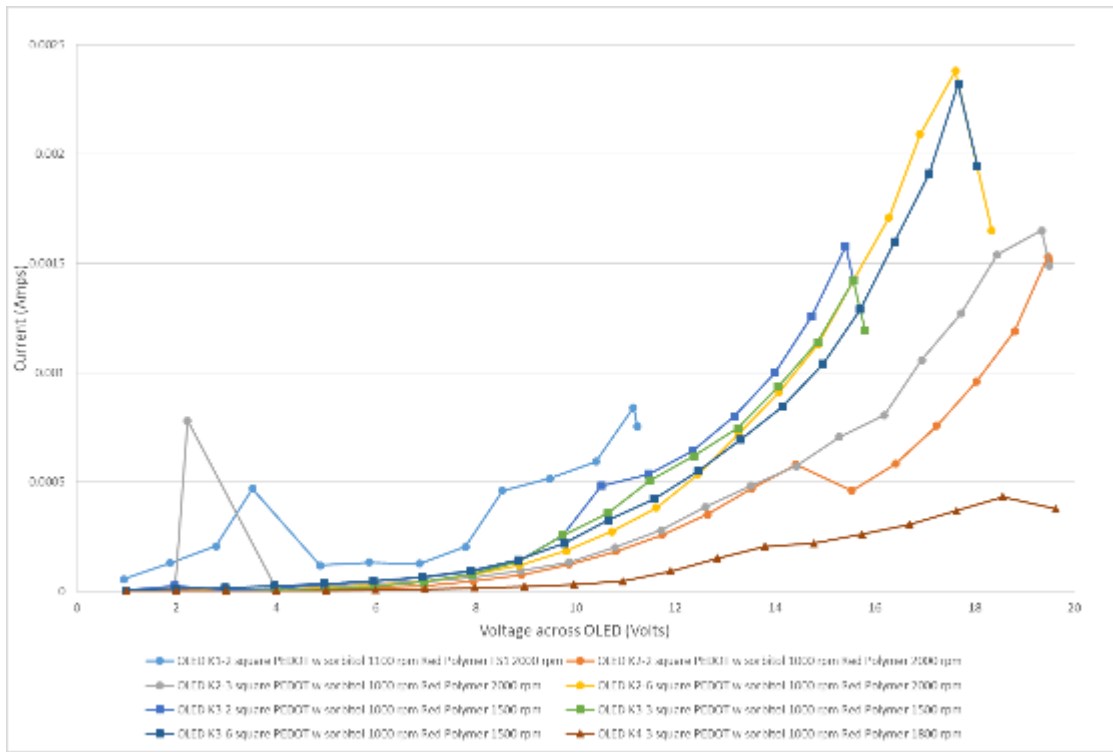


Figure 4-39: Initial Red OLED IV curves. Instability seen. Later they became more stable with better spinning technique.

Eventually a spin recipe was discovered that could make the red polymer go on more uniformly and the red OLED IV curve was seen to become more stable and repeatable. The red OLED IV curve is shown in Figure 4-40.

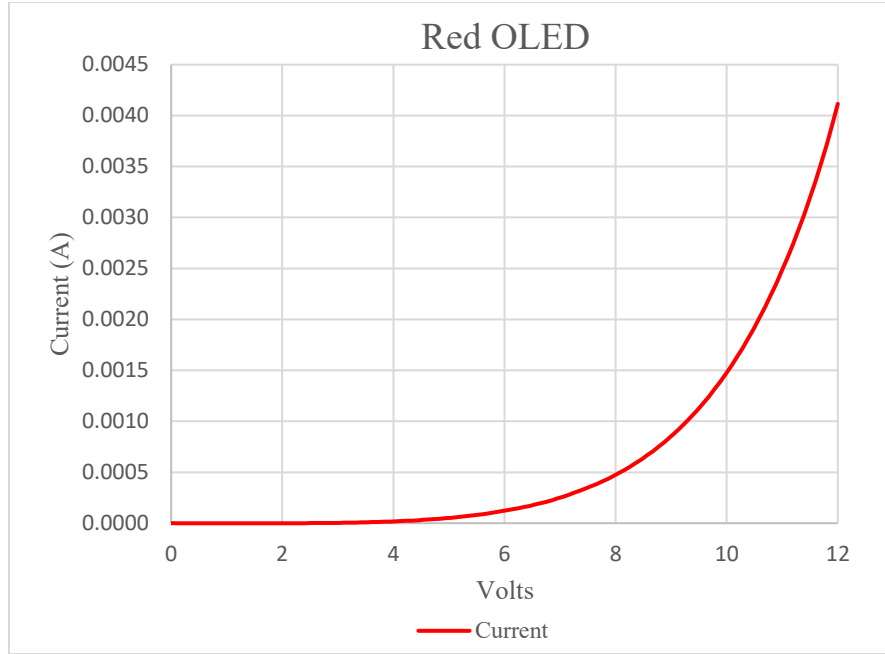


Figure 4-40: Red OLED IV Curve

From knowing the approximate surface area of the device, 0.49 cm^2 , the current density per driving voltage was calculated in Figure 4-41.

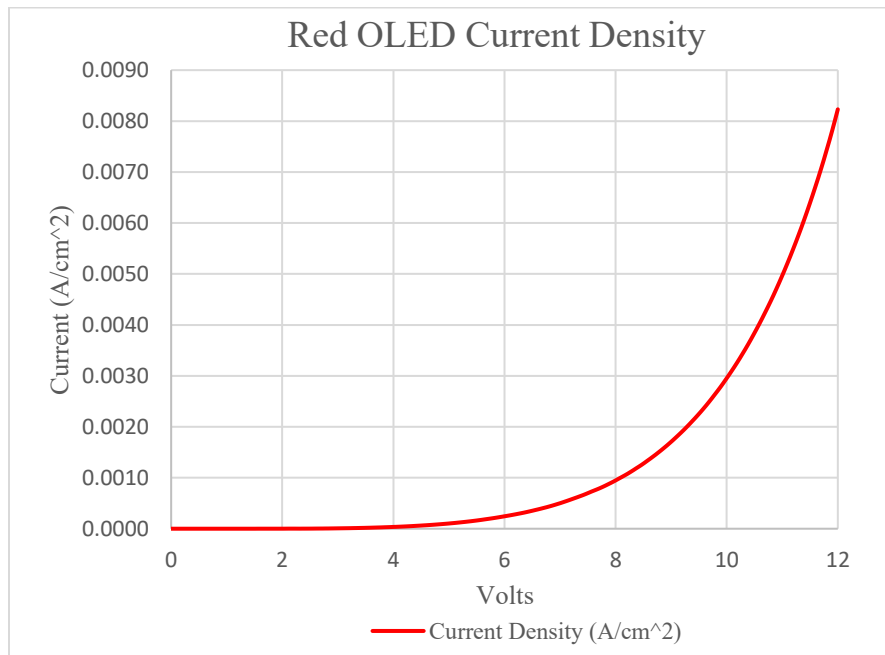


Figure 4-41: Red OLED current density.

A set of time lapse photos was taken as the red OLED was reaching full illumination and they are shown in Figure 4-42.

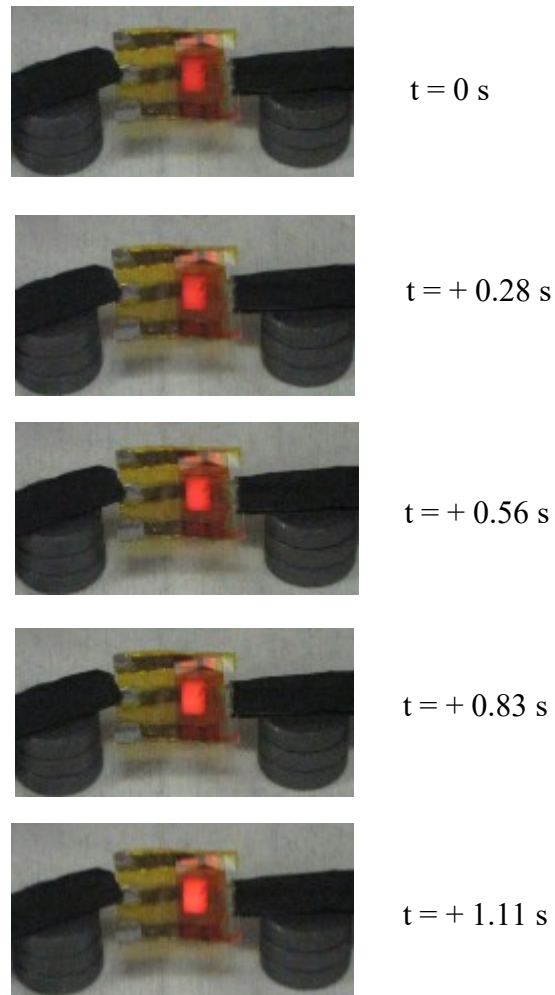


Figure 4-42: A time series showing the red OLED on flex substrate cycled to 12V.

The green OLED IV curve is shown in Figure 4-43.

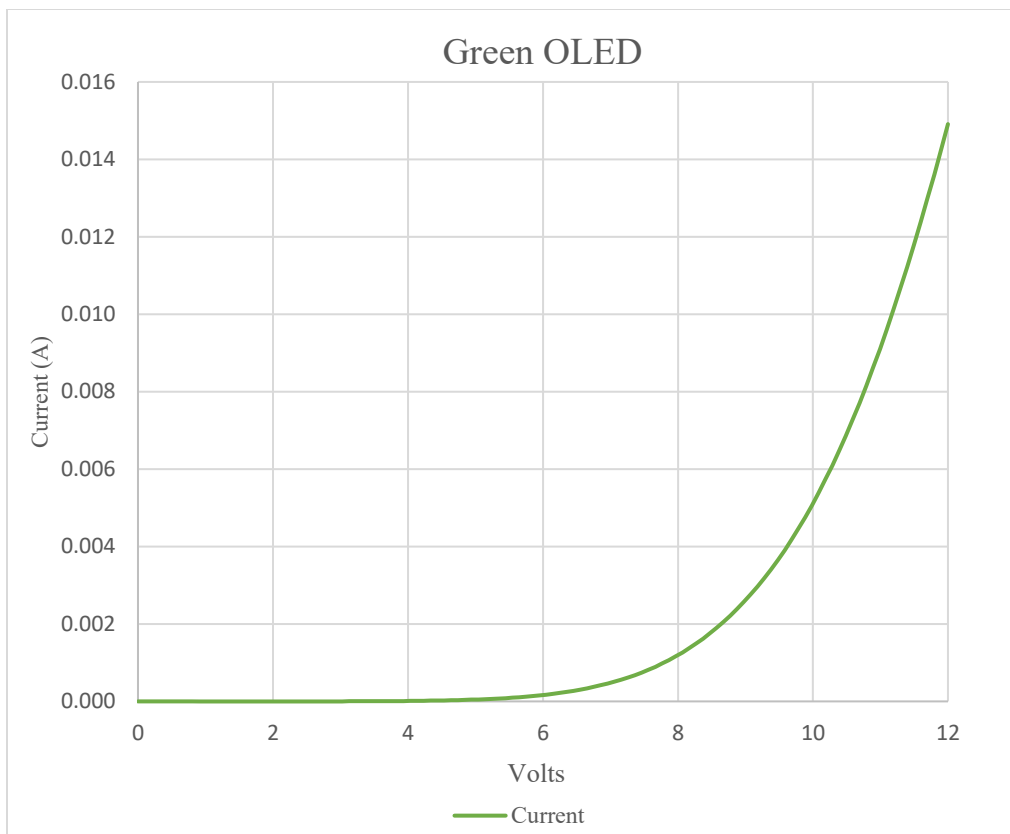


Figure 4-43: The green OLED IV Curve was more stable after device fabrication improvement.

The current density per driving voltage was calculated for the green OLED in Figure 4-44. The device area was approximately 0.49 cm^2 .

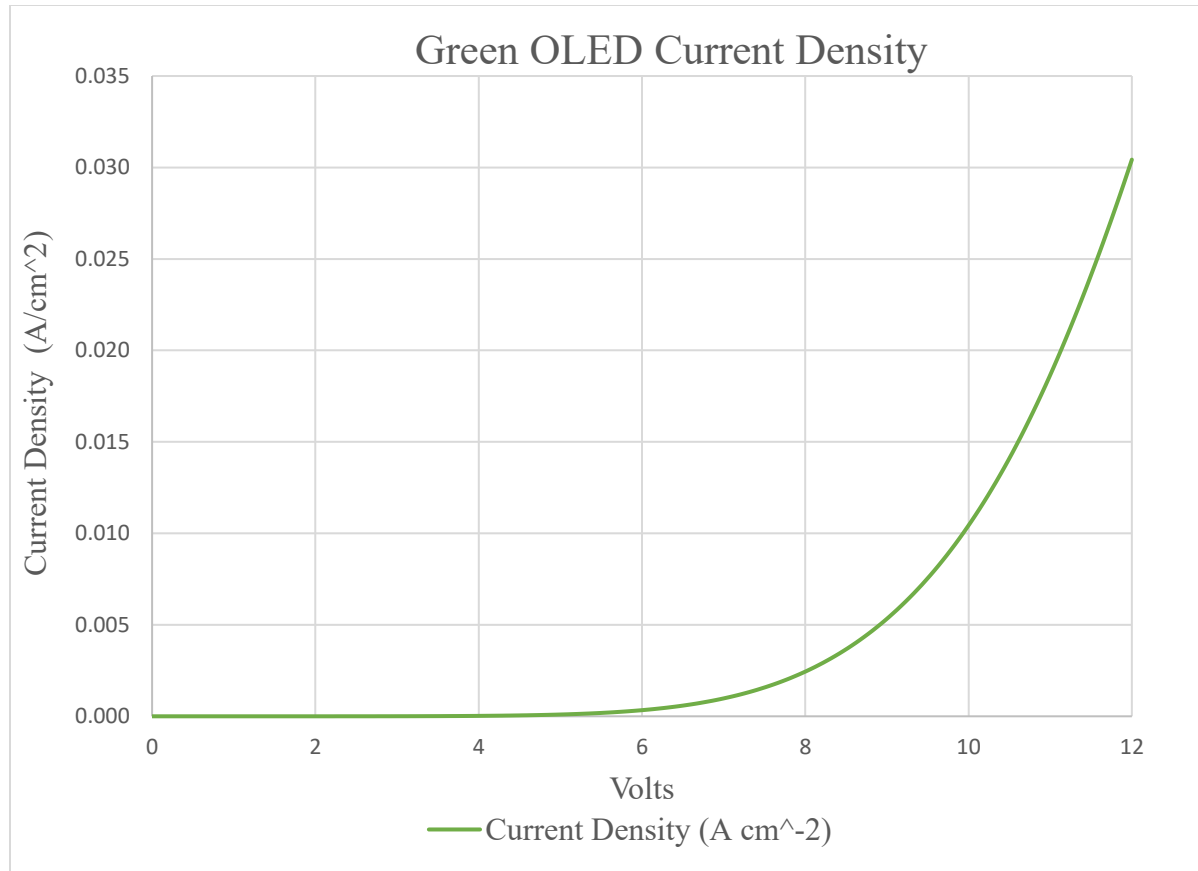


Figure 4-44: Green OLED current density.

A set of time lapse photos was taken as the green OLED was reaching full illumination and they are shown in Figure 4-45.

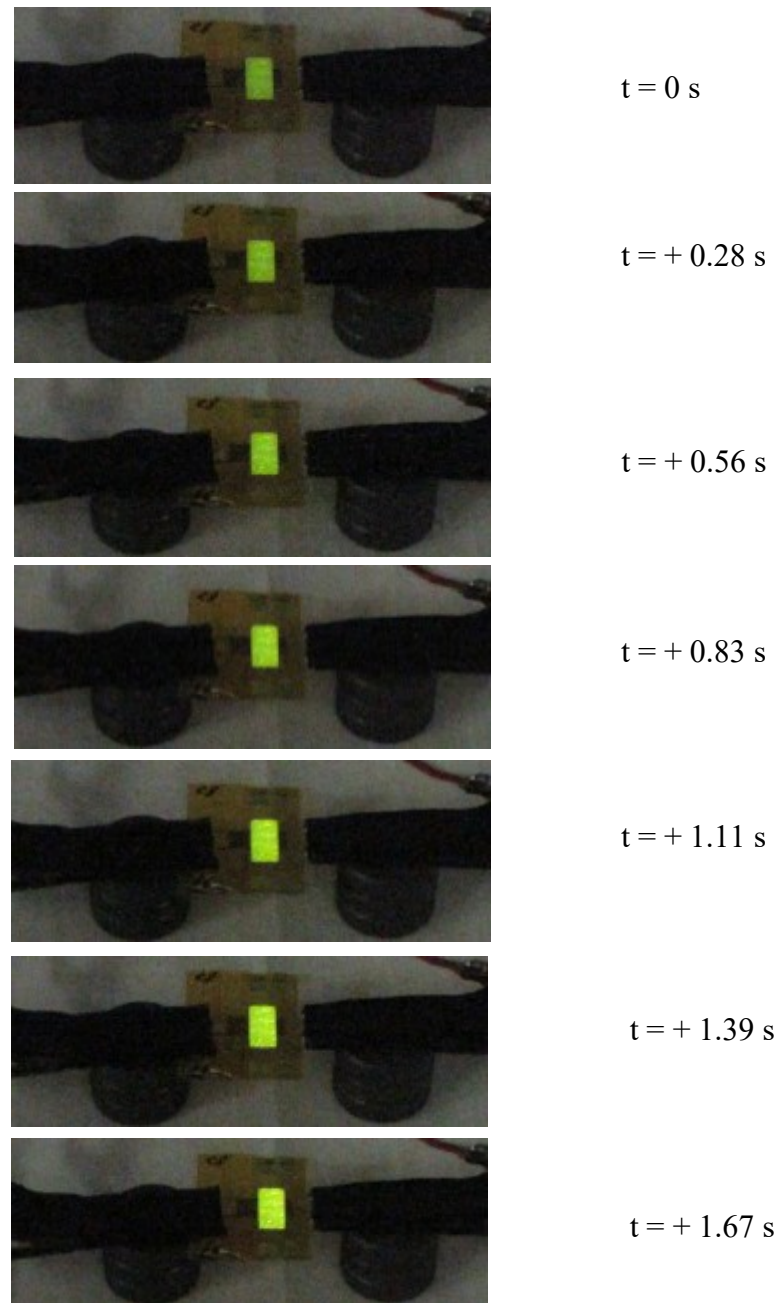


Figure 4-45: A time series showing the green OLED on flex substrate cycled to 12V.

The final frame of the two time series are shown below in Figure 4-46 for comparison.

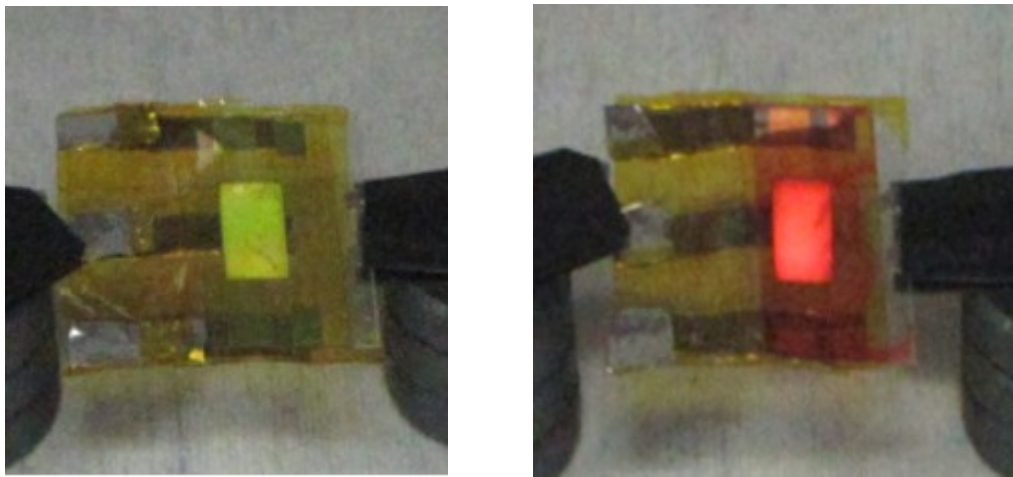


Figure 4-46: A side by side comparison of the final frames in the time elapsed photos of the red and green OLEDs lighting up from Figure 4-42 and Figure 4-45.

A summary of the electrical characteristics and some power calculations for the red and green OLEDs are given in Table 4-2.

Table 4-2: Fabricated Green and Red OLED Characteristics

OLED	Voltage (V)	Current Density (mA/cm ²)	Electrical Power (W/cm ²)	Device Size	Power per device (W)
Red OLED	12	8.23	0.101	0.49 cm ²	0.049
Green OLED	12	30.4	0.365	0.49 cm ²	0.179
Green OLED at 10 mA/cm ²	9.98	10	0.0998	0.49 cm ²	0.0489

The organic photodiode was fabricated and then tested for responsiveness by putting a fabricated OLED flash at 10 Hz approximately 5 mm away. No coupling was seen at 10 Hz, so the frequency was changed to one Hz in case the organic photodiode needed a longer exposure time to react.

This did not work either, so then the organic photodiode was then checked to see if it would respond to green wavelengths by taking an inorganic green LED and flashing it. The intensity of the inorganic LED was bright enough that the photodiode did respond as shown in Figure 4-47.

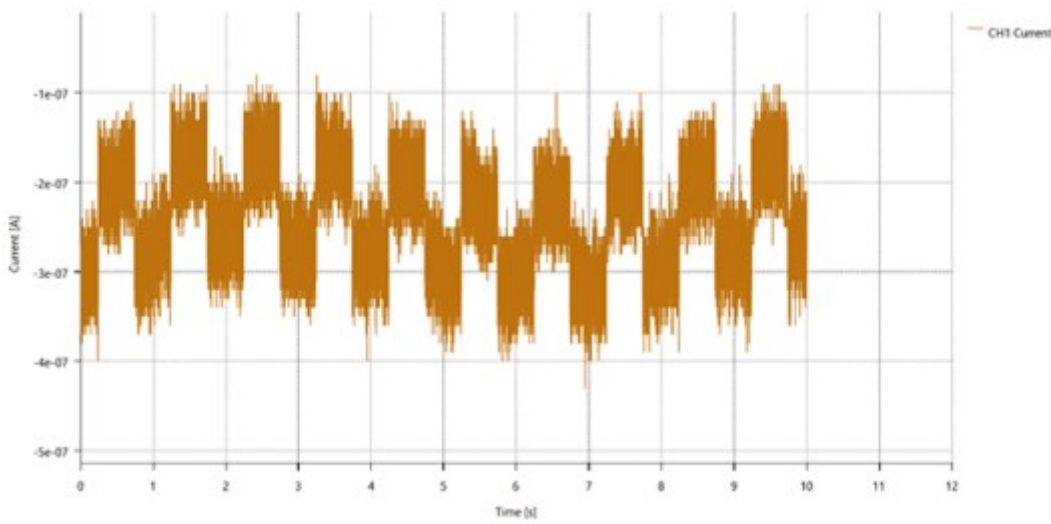


Figure 4-47: The organic photodiode responded to a flashing green inorganic LED which had an intensity greater than that of the green OLED. This test at least proved that the organic photodiode can respond to green wavelengths and the selection of chemicals were responsive if the intensity was high enough.

The response was then checked with a commercial red inorganic LED. The response can be seen in Figure 4-48, indicating the selection of chemicals could respond to red wavelengths.

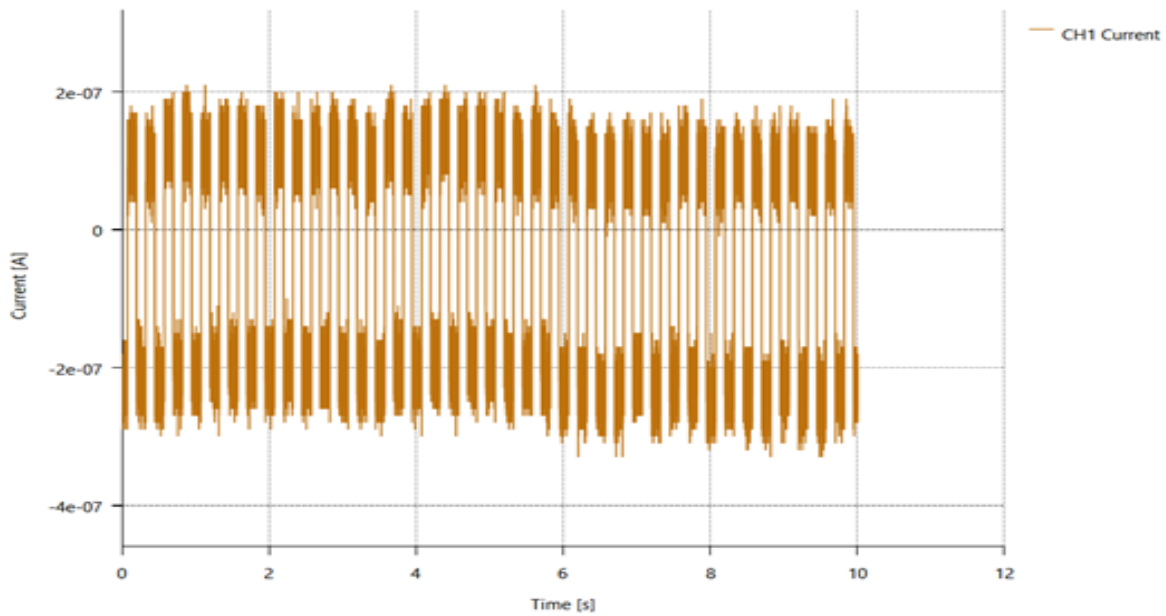


Figure 4-48: Direct measurement of current for OPD responding to a red inorganic LED flashing. The response indicates the selection of chemicals for the organic photodiode can respond to red wavelengths as long as the intensity is high enough.

The fluorescent white room light and fluorescent white room glovebox light response of the organic photodiode were also recorded. The organic photodiode did respond to the changing light conditions of the room as shown in Figure 4-49.

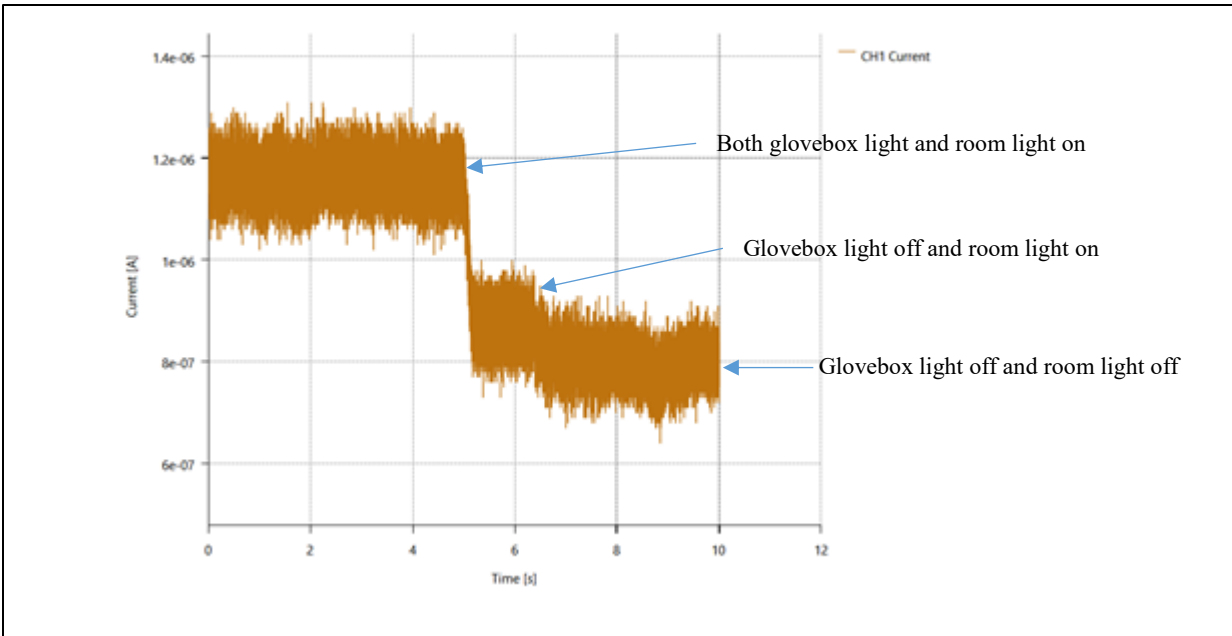


Figure 4-49: Organic photodiode could also be made to respond to the fluorescent lights of both the room and the glovebox.

Since the organic photodiode could respond to the room light, a dark and light current measurement was taken as a function of applied voltage. This can be seen in Figure 4-50.

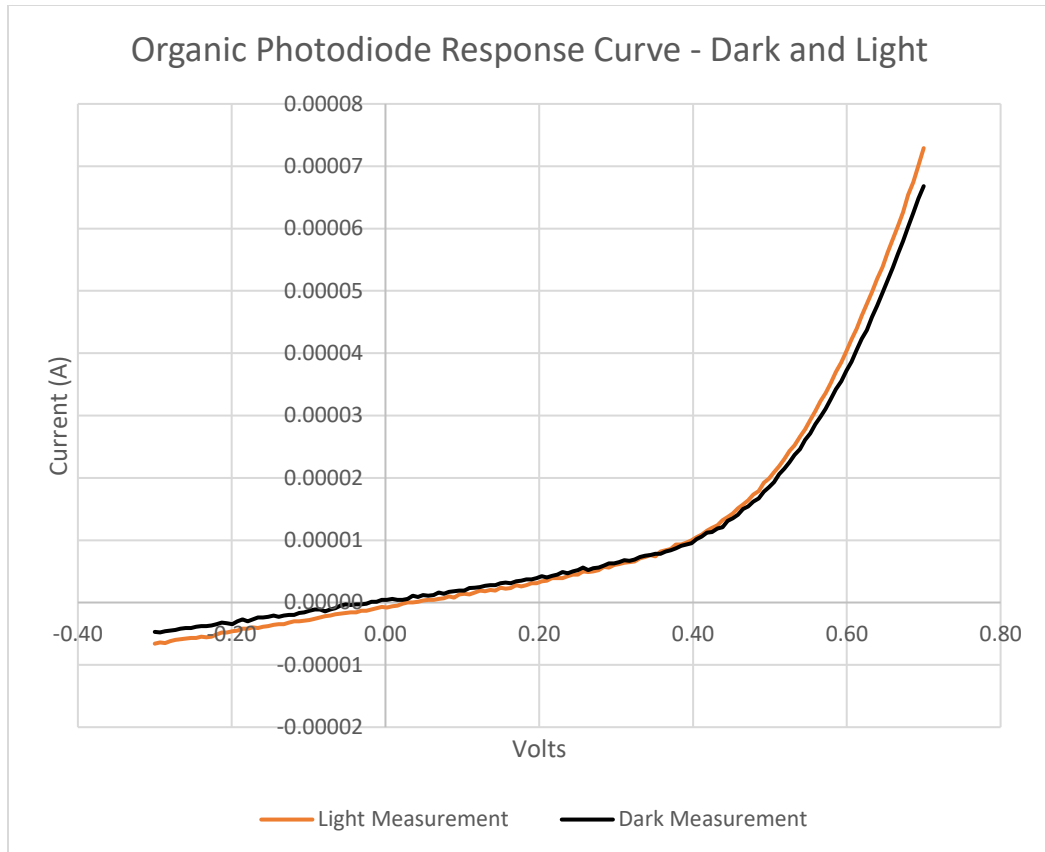


Figure 4-50: The dark and light current measurement was taken as a function of applied voltage for the organic photodiode response curve. The short circuit current was 8×10^{-7} A (0V intercept) and the open circuit voltage was 0.029V (0 Current intercept).

Since the organic photodiode did not respond to the OLED, but could be made to respond to the higher intensity of the room lights and inorganic LEDs, the conclusion was to make both the OLED and OPD devices have a larger surface area. A new mask was cut increasing the device sizes from approximately 10 mm^2 to 49 mm^2 .

The larger green OLED was then tested for coupling with the larger organic photodiode. They were mounted 5 mm apart as shown in Figure 4-51.

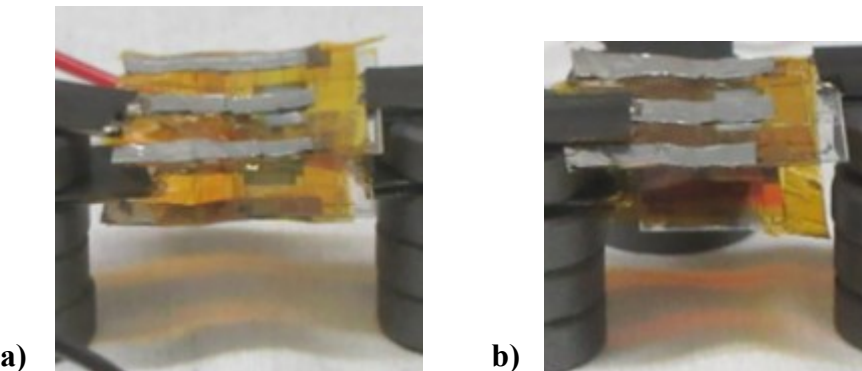


Figure 4-51: The larger sized devices were tested for coupling with the a) green OLED and b) red OLED mounted with the organic photodiode.

When the green OLED with larger surface area was flashed on the larger organic photodiode, the current response could be seen in the organic photodiode as shown in Figure 4-52.

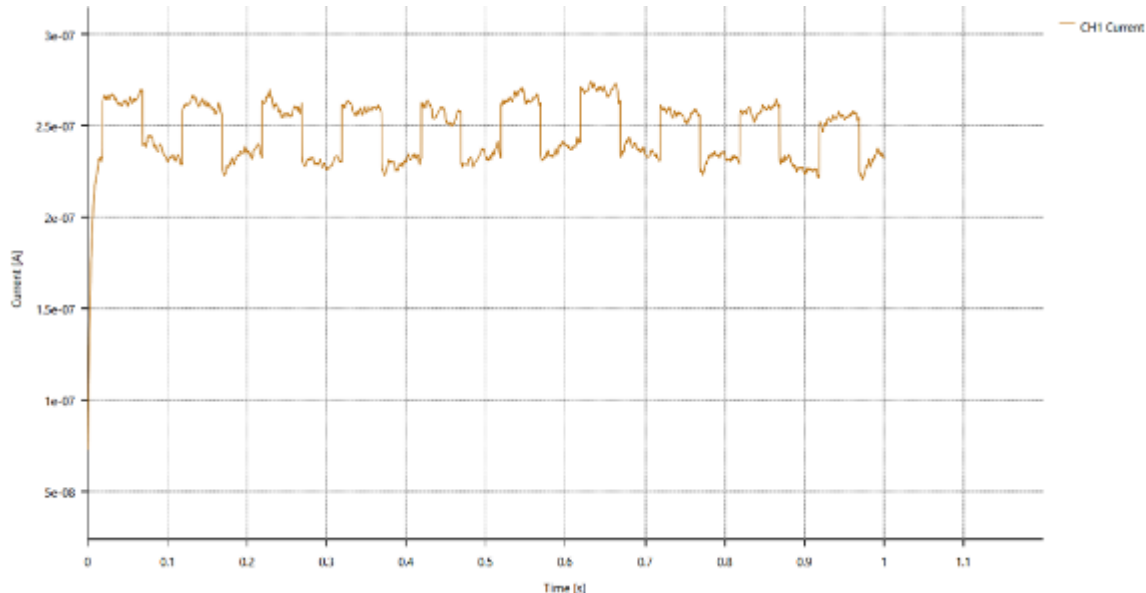


Figure 4-52: The larger green OLED response in the organic photodiode OPD could be seen, but had noise in it.

However, the same was not true with the red OLED. When the organic photodiode was tested with the red OLED, a visible signal could not be seen. It could be made to respond to a red inorganic LED, but the signal was noisy. A possible reason for this is that the green

polymer emission spectra is more centrally located to the response curve of the organic photodiode and the response is better as a result. To verify that the organic photodiode was working, an inorganic red LED was used and a response could be seen, however it was noisy even when the LED was operated brightly, indicating that perhaps the overall response to red wavelengths is weak for this fabricated photodiode. At this point it was decided to use the SiPM as a different light detector. That is discussed more in section 4.7 where it is shown how the SiPM had a response to the fabricated red and green OLEDs.

4.6 Interconnects for flexible devices

For any device to operate outside of a lab bench top experiment, it needs to have connections, also called interconnects. For the PPG and pulse oximetry purposes of this work, these kinds of interconnects needed to be developed and several methods were attempted.

4.6.1 Z-Axis Tape Interconnect

Z-axis tape was the first connection type attempted since previously connections with it to silicon devices were successful [81]. First wire connections with Z-axis tape covered devices. The wires tended to come off and not adhere to the Z-axis tape. The next attempt involved taking copper coated polyimide sheets (Pyralux) and cutting them into narrow strips to be used as leads. Figure 4-53 shows interconnects with the copper coated polyimide with Z-axis tape.

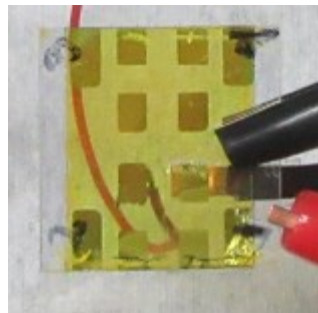


Figure 4-53: Z-axis tape used to create a flexible interconnect to the green OLED with a copper coated polyimide lead (in black, above red alligator clip).

A green OLED device that illuminated well and had a proper IV curve (Figure 4-54a) , was used to create a Z-axis-copper-polyimide interconnect. However, as can be seen from Figure 4-54a to Figure 4-54b these attempts were not successful.

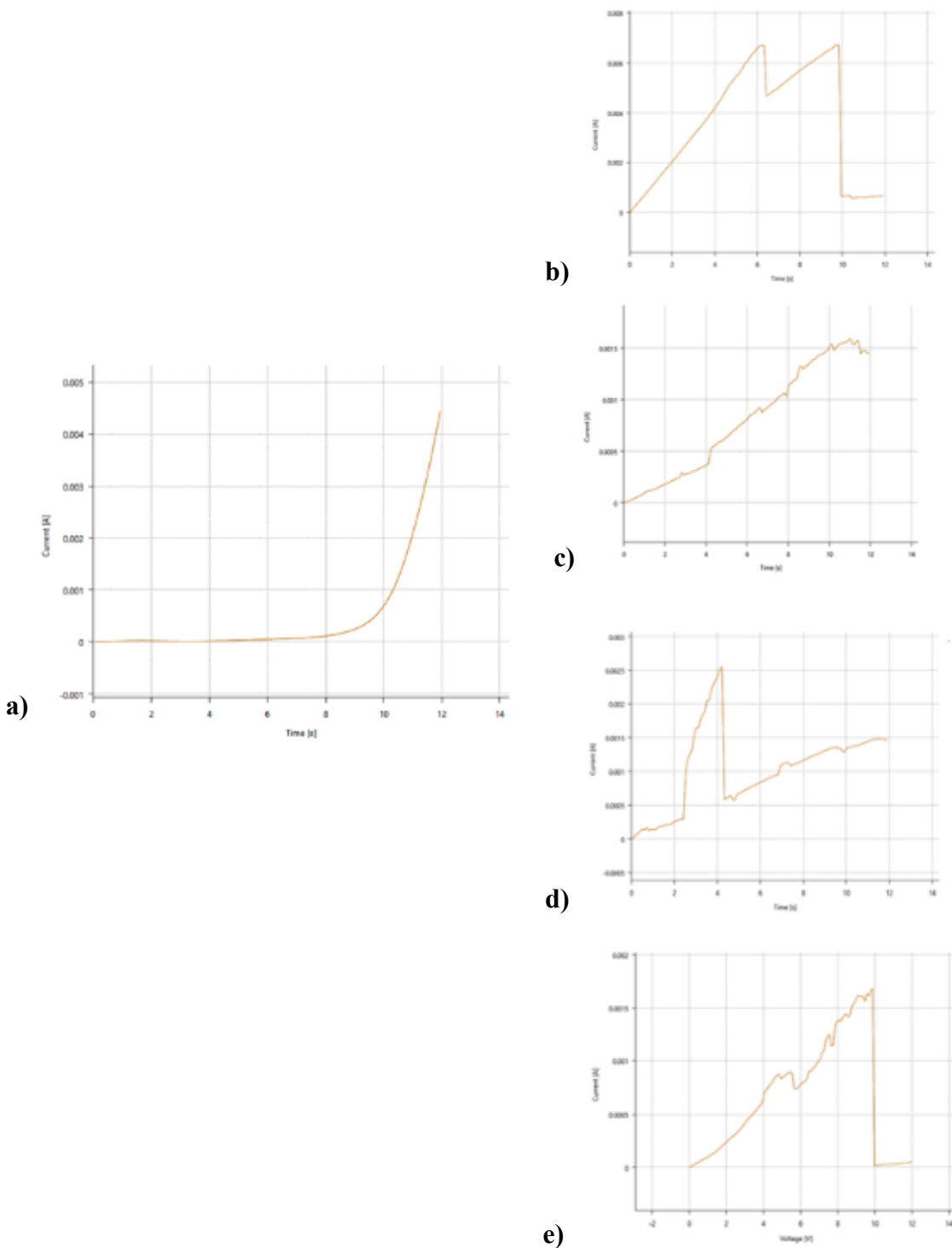


Figure 4-54: Green OLED IV curve before and after Z-axis interconnect. Before interconnect OLED was lighting up, but afterwards b)-e) it did not light up. A light press was done for c) but that did not produce illumination in c) through e). The conclusion was that Z-axis tape requiring a pressure resulted in malfunctioning devices.

The attempt to connect with Z-axis tape was not only detrimental to the device being tested, but the pressure used to apply the tape also affected neighboring devices on the same substrate.



Figure 4-55: This is the OLED neighbor to the Z-axis device interconnected in Figure 4-53. Even though this device was not connected with the Z-axis tape, it was affected by the pressure put on nearby region of the flexible substrate and consequently fractured. This is the device being touched by the curving red wire in Figure 4-53. The metal electrode didn't seem to have any marks that matched up with the fractures observed during illumination.

Figure 4-55 shows how a previously working device was negatively affected by the application of the Z-axis tape and copper polyimide interconnect.

4.6.2 Flexible silver epoxy Interconnect

Prior work had used silver traces to make connections to flexible devices [2]. However, the application of the conductive and flexible silver epoxy was done with screen printing. In this work, various formulations of flexible silver epoxy and techniques were tried to see if similar flexible conductive interconnects could be made.

The first set of experiments were done in applying heat cured silver epoxy (MG Chemical) with stencils made of paper and plastic sheets. Figure 4-56 shows an example of this method using a plastic stencil.

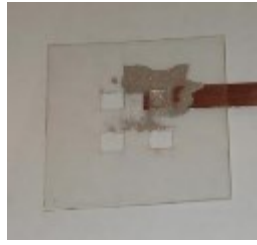


Figure 4-56: Stencil used for first silver epoxy application attempts.

An immediate issue that occurred with using a stencil was that the silver epoxy smeared outside of the stencil box area. Conductive carbon epoxy was also attempted and it did the same.

Resistivity measurement tests of the epoxies were done with small strips of conductive foil with overlaps of approximately 9 square millimeters. The carbon epoxy resistivity ranged from ohms to megaohms in value. The resistance varied with flexing and with pressure, usually applied by finger. The silver epoxy was much more conductive, generally ranging from under 1 ohm to a few tens of ohms. Since the silver epoxy was better with electrical resistance, work continued with it and it was taken to the glovebox.

At the glovebox another issue became apparent that it was more difficult to handle the stencil with the heavy gloves of the glovebox inside the enclosure. Figure 4-57 shows the substrate with devices and applied silver epoxy. Out of four connected OLEDs, three OLEDs did not turn on. One did manage to turn on once, but it would not illuminate a second time. The leads in these experiments came off easily, sometimes taking the underlayer of stacked polymer layers with it as shown in Figure 4-57c. An additional difficulty at this stage was also the selection of epoxy because it had a 10 minute working time, and it would have been better to have more time to align the leads.

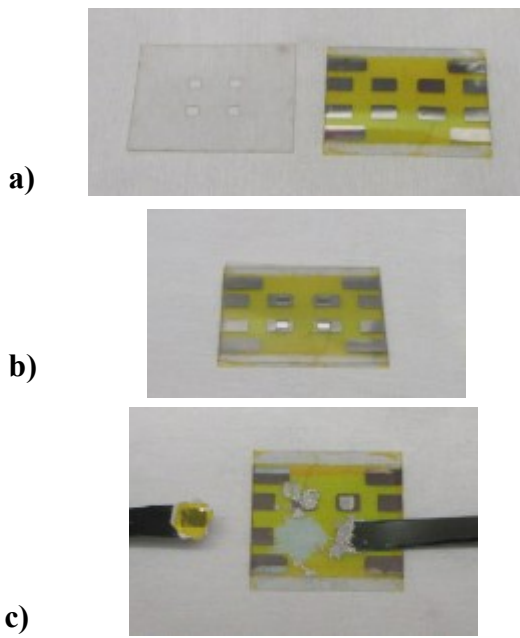


Figure 4-57: Silver epoxy interconnect attempted with green OLED. A stencil a) was laser cut out of a transparency, which allowed the silver epoxy to be b) patterned. When the leads were attached, the epoxy would smear and the leads could detach from the polymer surface, sometimes taking parts of the polymer layer with it.

The next experiments were accomplished with epoxy (MG Chemical) with a longer working time of 4 hours. This was done with newly fabricated red OLEDs. The silver epoxy trace was carefully applied and patterned as seen in Figure 4-58.

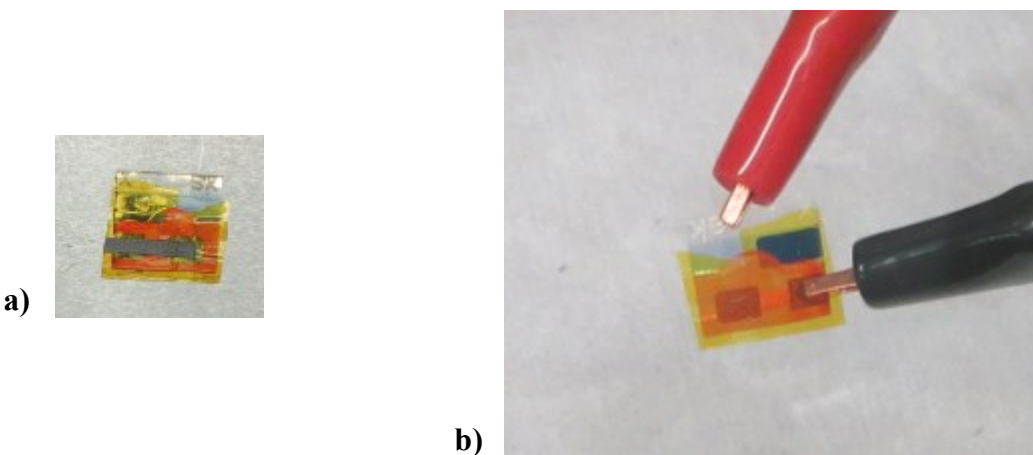
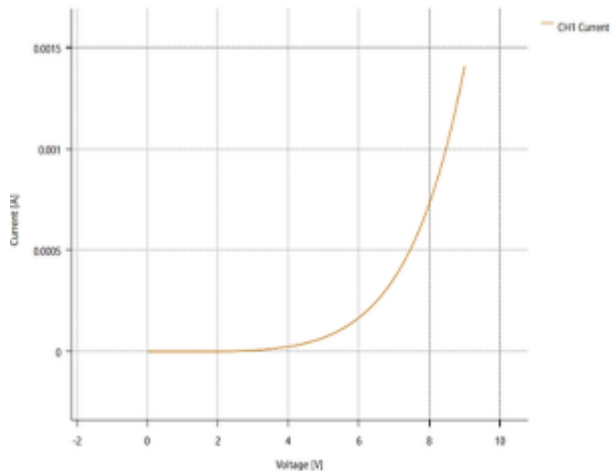


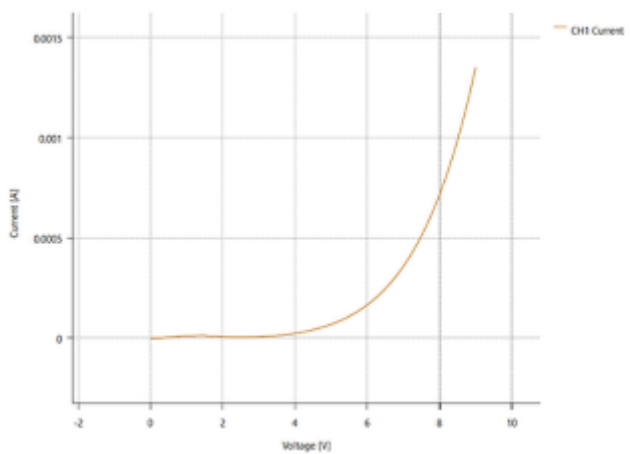
Figure 4-58: Silver epoxy interconnect attempted with red OLED. The device was patterned with silver epoxy on the a) deposited electrode side. The other side of device in a) is seen in b) and the silver interconnect pathway can be seen through the plastic substrate.

Measurements were then taken of the red OLED's IV curve to be sure it responded and illuminated correctly while it was still on the substrate on which it was fabricated (Figure 4-59a). Then the red OLED was cut from the substrate and again the IV curve was taken to be sure the act of excising the OLED from the substrate did not ruin the device (Figure 4-59b). When it was verified the device continued working properly after being removed from the main substrate, the device was then patterned with the silver epoxy. After the silver epoxy was cured, the current-voltage measurements were taken again (Figure 4-59c). It was at this point the response was measured again, and it was found that the device no longer operated properly. It would not illuminate and functioned like a resistive load. The conclusion was that the 4 hour working time silver epoxy will ruin the devices.

a) Red OLED IV Curve before cut out of full substrate



b) Red OLED after cut out of full substrate , but before silver epoxy.



c) Red OLED IV curve after cut out of full substrate and with cured silver epoxy.

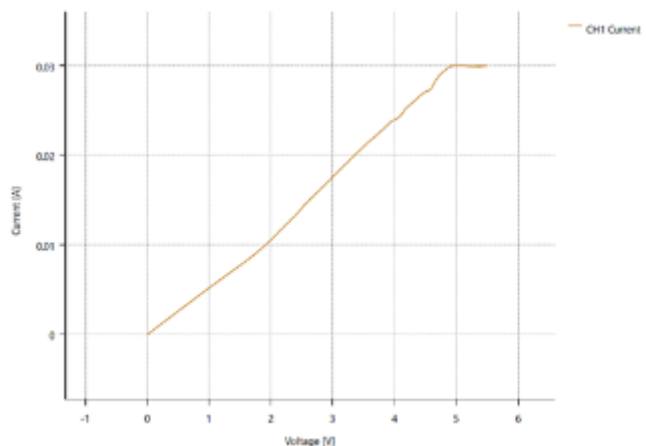


Figure 4-59: Red OLED IV curves a) after fabrication, b) after excising from the substrate and c) after the second type of silver epoxy interconnect application.

It was believed that the solvents or chemistries of the prior silver epoxies could be responsible for ruining the devices. Therefore, another brand of silver epoxy was chosen with a 2 day working time which was also suitable for medical applications. Again the device was patterned with silver epoxy as shown in Figure 4-60a)-b).

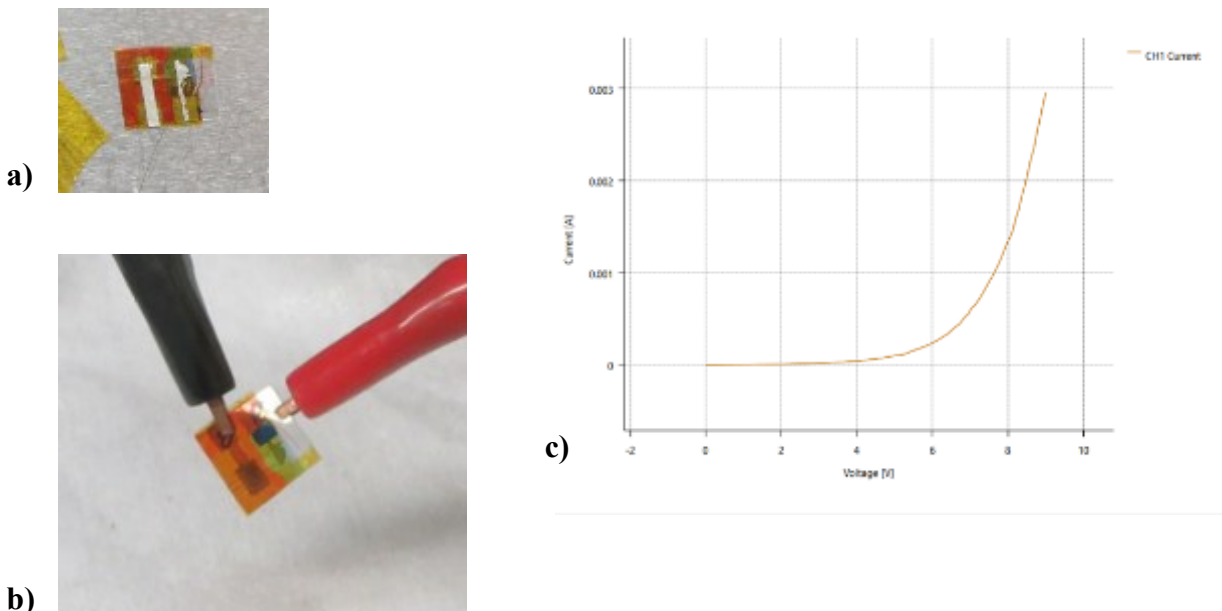


Figure 4-60: A third silver epoxy was attempted, this one with a 2 day working time and suitable for medical applications. The patterned epoxy can be seen in a) on the deposited electrode and b) reverse sides, respectively. The IV curve of the OLED resembles a normal diode curve after it was removed from the fabrication substrate and had silver epoxy applied and cured. However, these devices did not turn on and illuminate.

The conclusion was that this epoxy may also be preventing the device from working correctly. The next step was to increase the layer of the deposited aluminum to act as a barrier to any of the chemicals of the silver epoxy that may degas or release during curing. These devices are represented in Figure 4-61.

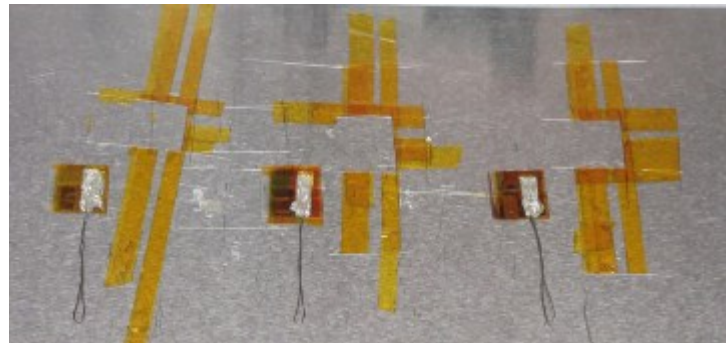


Figure 4-61: Devices made with extra aluminum being deposited on the metal electrode for the fourth variation of silver epoxy interconnects.

The devices with thickened layers of deposited aluminum in Figure 4-61 had the unfortunate tendency of developing pinholes as shown in Figure 4-62. These would be tiny sparks of light that would appear when the device was activated.

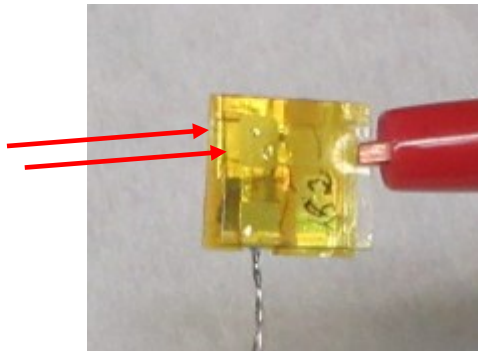


Figure 4-62: Pinholes formed where the arrows are indicating for the devices from Figure 4-61.

4.6.3 Flexible conductive tape.

Another option was attempted to make interconnects with a flexible conductive tape. The static conditions inside the glovebox made the tape difficult to handle.

The tape was first used with the red OLED shown in Figure 4-63 it worked well. There was slight damage to this OLED during the handling and attachment process, but otherwise it had the expected performance of a diode as shown in Figure 4-64.



Figure 4-63: Fabricated red OLED with conductive tape.

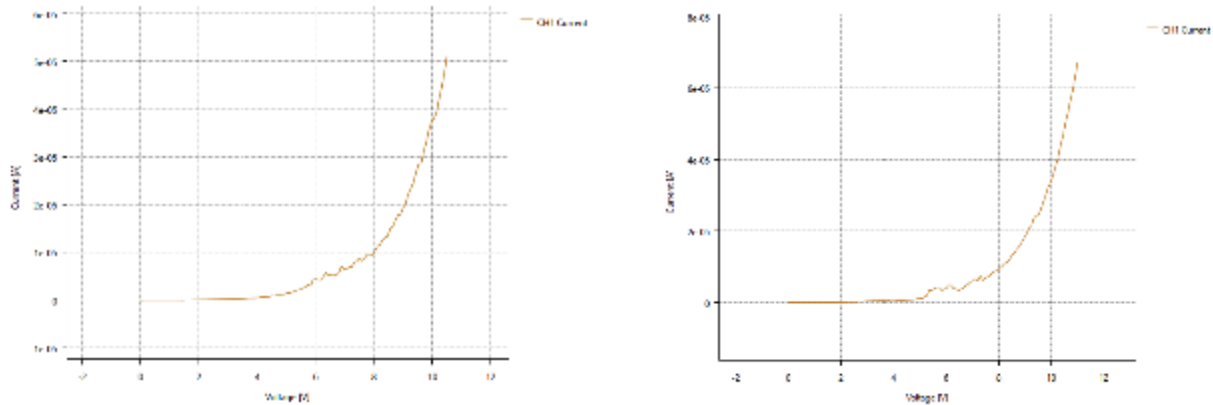


Figure 4-64: This measurement was the proof of concept that conductive tape could work to connect an OLED, as shown by IV curve of devices. Illumination was seen.

Next a test was done with an organic photodiode to validate the tape would work with it.

Measurements were taken of the First OPD before and after conductive tape application and device performance was not modified with the application of the tape as shown in Figure 4-65.

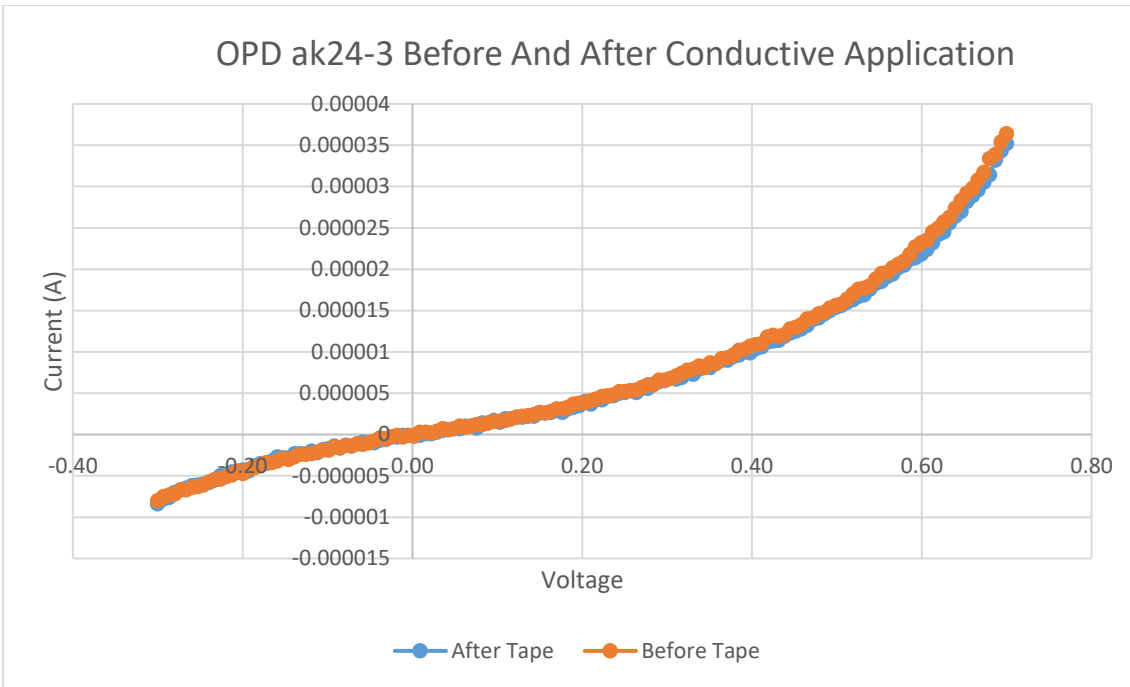


Figure 4-65: OPD testing before and after conductive tape application. The response was essentially identical.

As a final test of the viability and compatibility of the conductive tape with the organic devices, the conductive tape was attempted with the green OLEDs. In this case the OLED was fabricated and had the leads attached and then mounted inside of a testing box. The response of the OLED was repeatable even after testing with a square wave.

From this result it was determined that now all three devices could use this conductive tape interconnect approach.

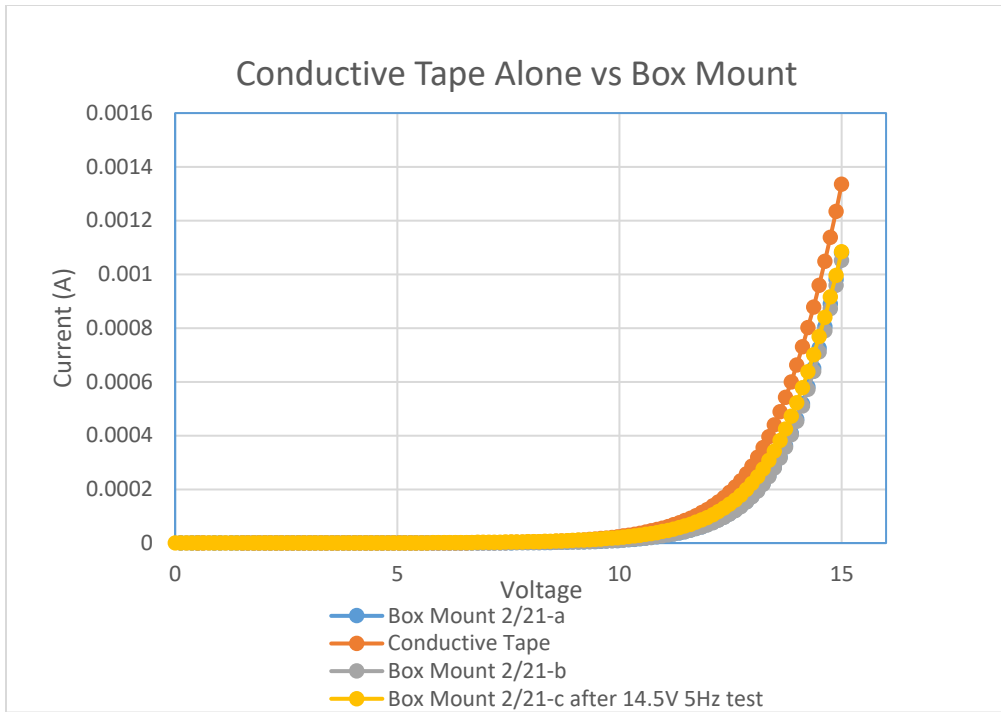


Figure 4-66: Green OLED testing with the conductive tape and mounting.

The first step in applying the conductive tape to the metal deposited electrode was cutting a substrate into two pieces to spate the large devices that were made. Then kapton (polyimide) tape was added to the device to act as a platform for the conductive tape while maintaining the device's flexibility. The conductive tape became the negative electrode.

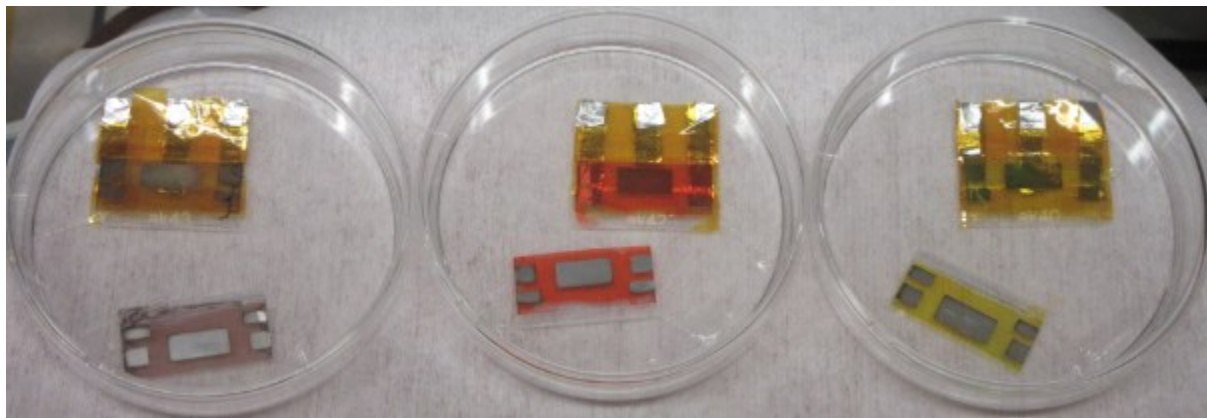


Figure 4-67: Device pairs that were fabricated on the same substrate were separated by cutting and then kapton tape and conductive tape were applied. Pairs of device are shown here that were made on the substrate with one of the pair had the kapton tape added and ready for testing.

4.7 OLED Human PPG Signal with Silicon Photomultiplier (SiPM)

Since the response of the organic photodetector were not robust, another light detector was chosen to work with the OLEDs. This detector was an SiPM (sensL MicroFC-30035). The SiPM acronym means “Silicon Photomultiplier” and is a device that operates like an avalanche photodiode and has mechanical robustness and strong response [82]. If it could be shown that the SiPM could respond to the green and red OLEDs then there was the possibility of using the OLEDs with the SiPM for either PPG or pulse oximetry.

The first step was to have the SiPM attached to a circuit board in a reflow oven, and then begin putting black tape around the device to minimize reflection from the board’s surface.

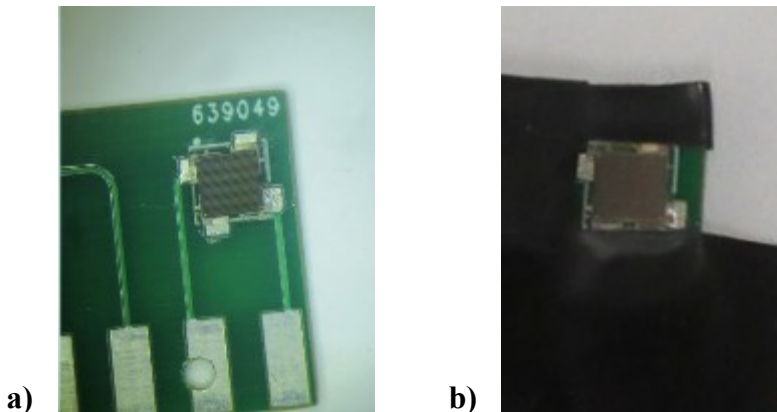


Figure 4-68: A solder oven a) was used to attach the SiPM to a printed circuit board and then b) black tape was put around it to minimize reflection from the circuit board. The circuit board section that is visible was covered as well.

The green and red OLEDs were mounted in parallel with the SiPM, approximately 5 mm apart, Figure 4-69.

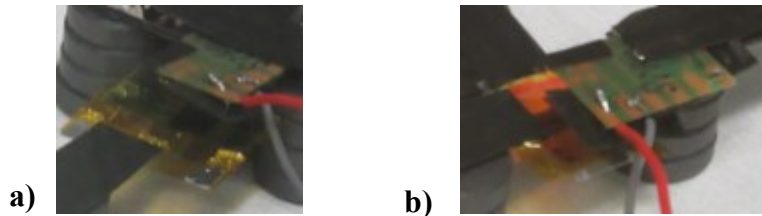


Figure 4-69: The a) green OLED and b) red OLED mounted with the SiPM to measure response.

The OLEDs were driven with a 10 Hz signal. The response of the SiPM to the Green OLED being operated at 11V, 12V and 12.5V can be seen in Figure 4-70. The SiPM used has a response time measured in nanoseconds, specifically 0.6 ns, so the response time of the SiPM is negligible. This indicates that in Figure 4-70 it is the OLED that is taking different lengths of time to reach peak luminosity based upon the driving voltage. At 11V it took 0.05s, at 12V, 0.03s and at 12.5 V 0.01s to reach the maximum SMU setting of 10 mA. The most relevant detail was that the SiPM could detect the OLED's light.

SiPM response of Green OLED driven by Different Square Wave Voltages

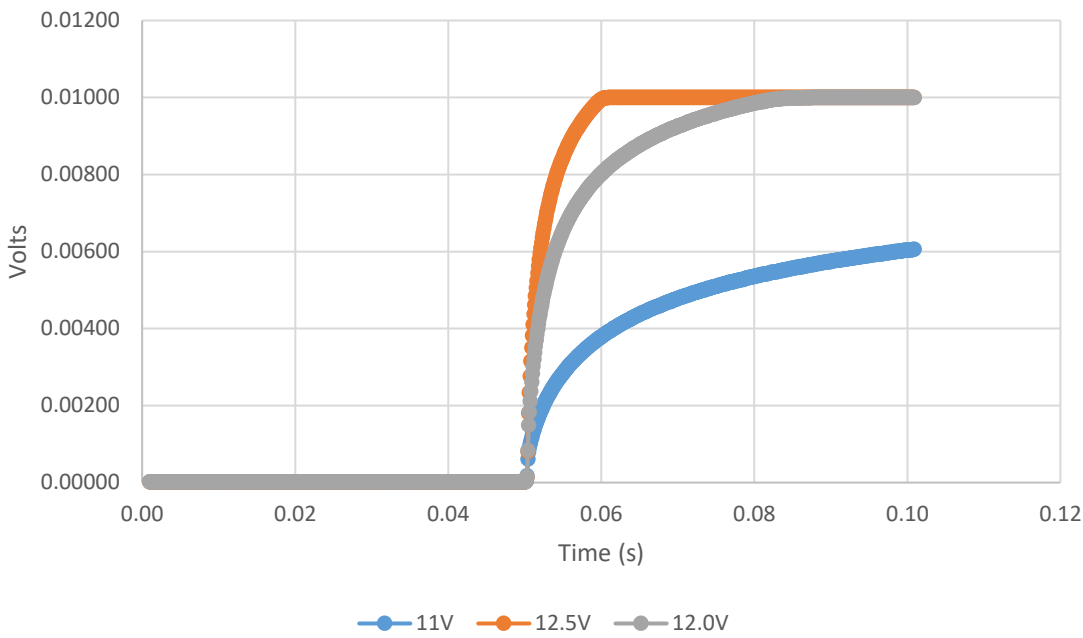


Figure 4-70: The SiPM response curve to the green OLED being driven with a 10Hz, 50% duty cycle signal at different voltages. The peak luminosity of the green OLED was reached at 0.05s at 11V, 0.03s at 12V and 0.01s at 12.5 V. The 12.5V case reached the maximum current setting.

This measurement was repeated for the red OLED at different voltages. Here again a square wave was used, this time at 6V and 9V. The lower voltage did not attain the same luminosity as in the green OLED case. The response can be seen in Figure 4-71. Again, the most important point was that the SiPM could detect the OLED's light output.

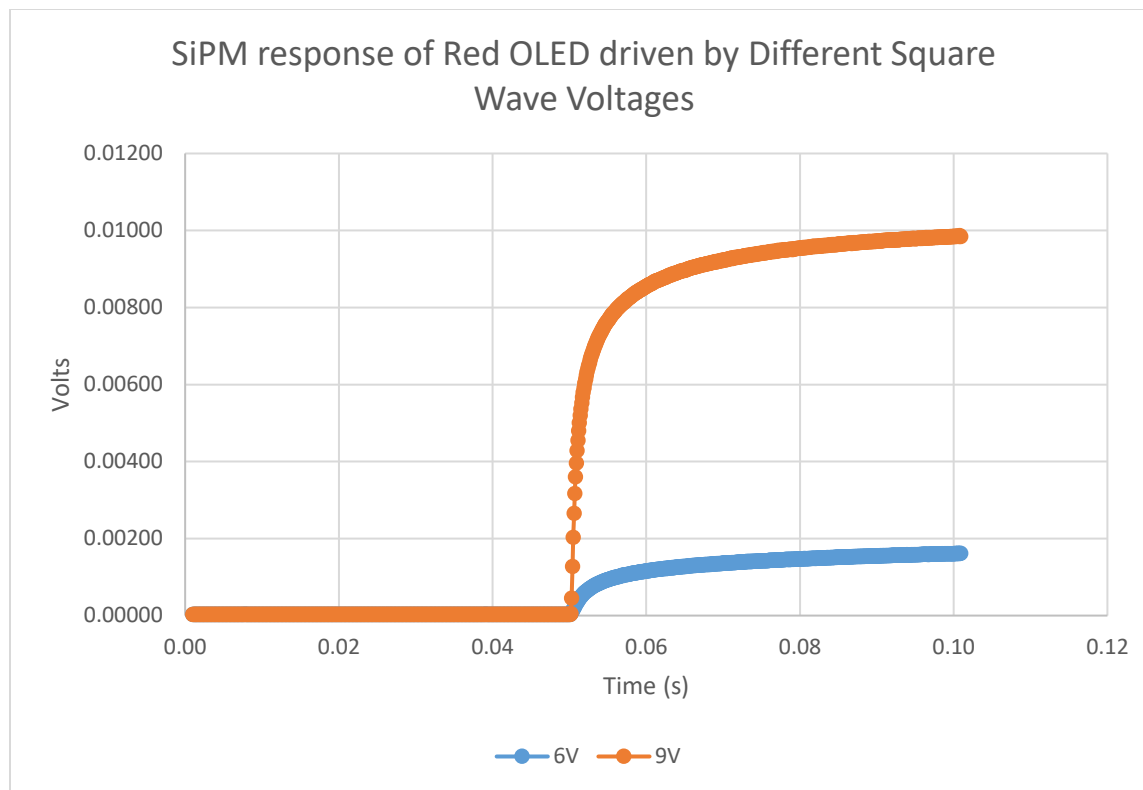


Figure 4-71: The SiPM response curve to the red OLED being driven with a 10Hz, 50% duty cycle signal at different voltages.

Since the green OLED and SiPM were verified as being capable of working together, the next step was to prepare the OLED to be taken out of the glovebox and prove that it is of appropriate wavelength for a human PPG measurement. In order to accomplish this, the OLED needed to be encapsulated to protect it from the ambient oxygen and moisture in the air outside the glovebox.

Other literature has used epoxy to encapsulate their devices [5][2]. However, considering that epoxy has solvents in it and the UV lamp may not cure it fast enough, those solvents could negatively impact the device. Also it was not clear how much stiffness would be added to the device with the addition of the epoxy. As a result of these concerns and a desire to maintain the flexibility of the device, it was decided to use kapton (polyimide) tape as the encapsulation.

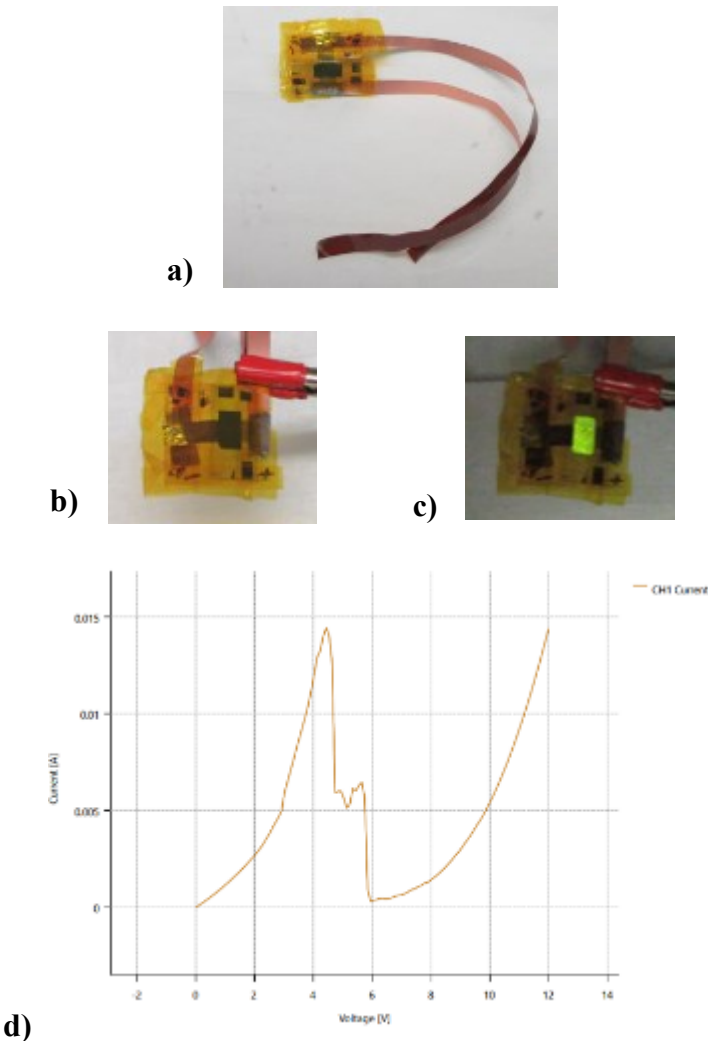


Figure 4-72: Leads were a) attached to the green OLED and it was encapsulated with b) kapton tape and could be made to c) illuminate. Encapsulation with tape sometimes introduced momentary d) shorts during initial IV curve measurements, but after the momentary short, the OLED could be made to operate normally and also have a normal IV curve.

A piece of rectangular plastic was 3D printed with a window for the OLED to illuminate through. The kapton encapsulated device was attached to this as shown in Figure 4-73a and it was confirmed it still functioned properly by activating it and making sure it illuminated as demonstrated in Figure 4-73b.

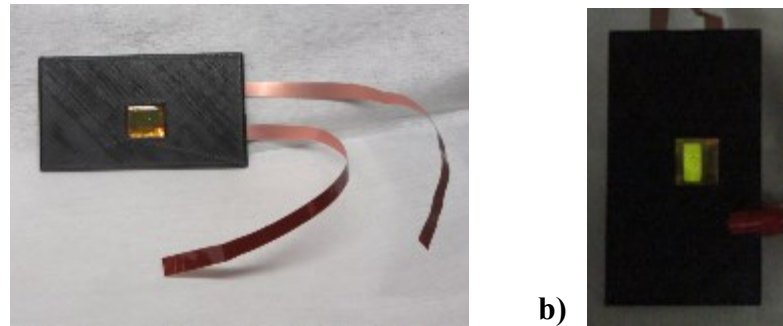


Figure 4-73: The green OLED was encapsulated and a) attached to leads and the 3D printed holder and b) could be made to activate.

At this stage, the OLED and its holder was taken out of the glovebox and attached to a plate that had the SiPM mounted on it as diagrammed in Figure 4-74.

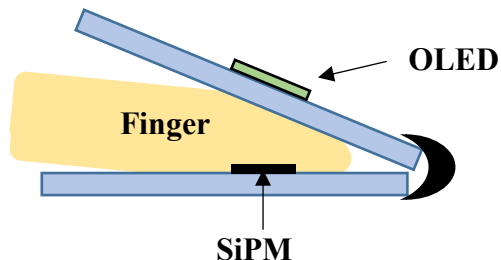


Figure 4-74: The human PPG was obtained with the OLED mounted on a 3D printed plastic plate OLED that was hinged with a second plate that had the SiPM mounted.

In the configuration of Figure 4-74, the human PPG was obtained. PPGs were able to be collected for over an hour demonstrating that the kapton tape encapsulation method worked at least for that duration of time. The PPGs can be found in Figure 4-75 and Figure 4-76.

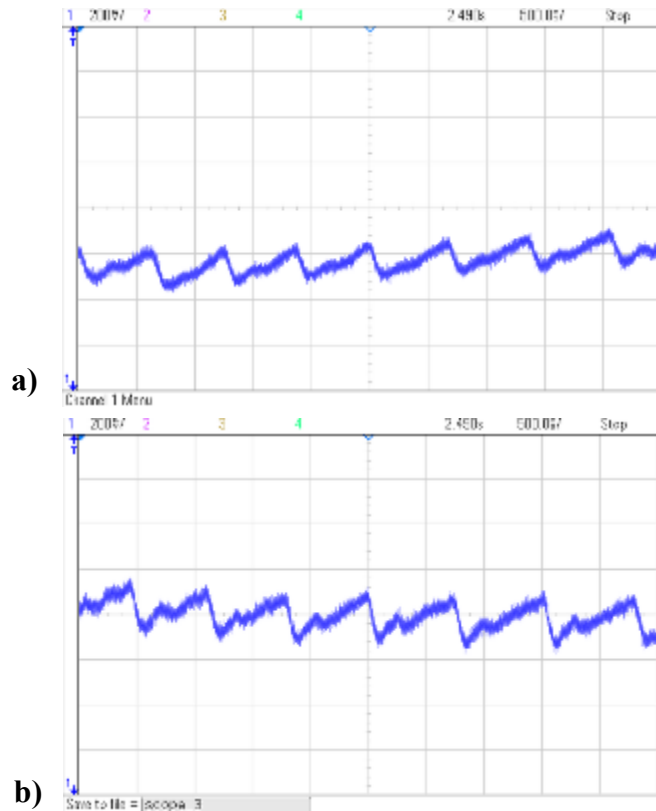


Figure 4-75: Two PPG's obtained with the OLED and SiPM within 10 minutes of glovebox withdrawal of the OLED.

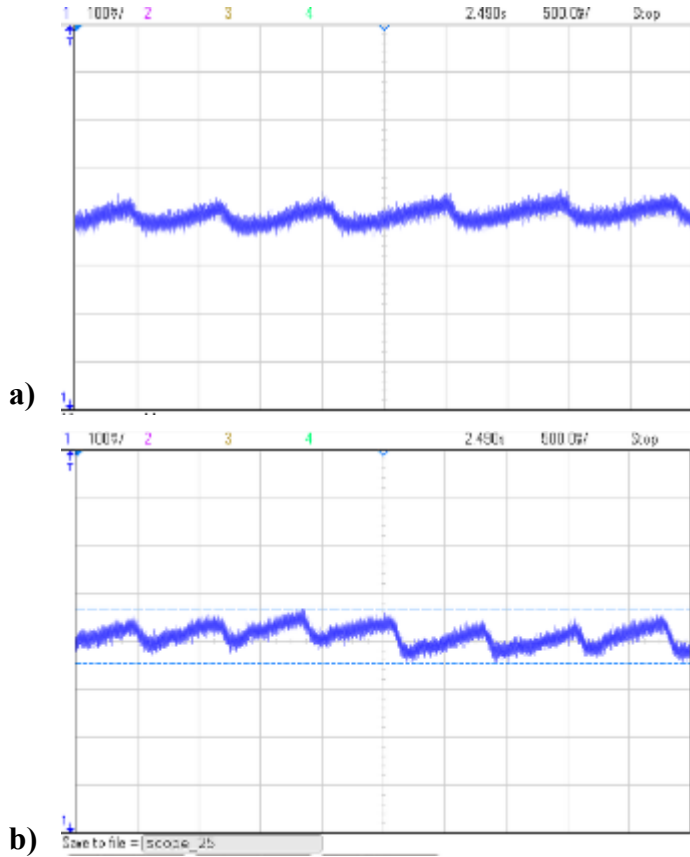


Figure 4-76: The encapsulation with kapton tape worked and additional PPGs could be obtained even at a) 1 hour 9 minutes outside the glovebox and, b) 1 hour 40 minutes.

4.8 Additional Encapsulation Trials

The next encapsulation method tried to avoid touching the tape directly to the surface of the OLED by putting a layer of tape around the perimeter of the OLED. On top of this was put a layer of flexible plastic. Out of 4 new devices made this way, one was not active at all disconnected, one had defect (Figure 4-77a) and two appeared to illuminate properly (Figure 4-77b-c).

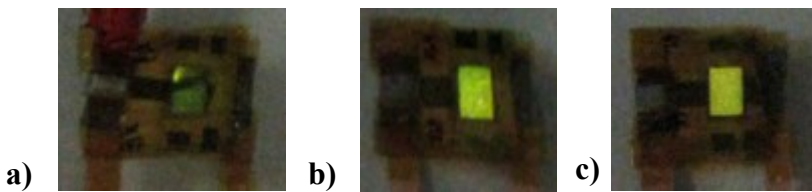


Figure 4-77: Out of 4 devices made with another encapsulation method, 1 did not work, a) had a defect from the process, while b) and c) did illuminate properly.

Chapter 5: Nanostructure Fabrication in Silicon

5.1 Introduction

The steps of nanosphere lithography are explained in the next couple of sections in terms of how the experiments and results progressed together and what decisions were made along the way to the final experimental results. For an explanation that bypasses the incremental steps, a complete description of the final experimental setup are given in section 5.6 of this chapter, “Biomimetic Nanostructure Fabrication to Increase Light Transmission Efficiency in Optoelectronic Devices”.

5.2 Fabrication and Nanosphere Lithography

Nanosphere lithography has low cost for device , feasible for large volume production, however is sensitive to fabrication conditions and has defect issues [83]. But it is less expensive than FIB milling which operates in a serial manner, instead of a wide spread self assembly fashion [83]. Nanosphere lithography also allows for large areas to be patterned which was a useful aspect for the purposes of this work.

Nanosphere lithography can be accomplished with different methods and for this work aspects of these various methods were attempted to see which was best suited for the local equipment and conditions. Some of the necessary tools to begin this work can be seen in Figure 5-1.

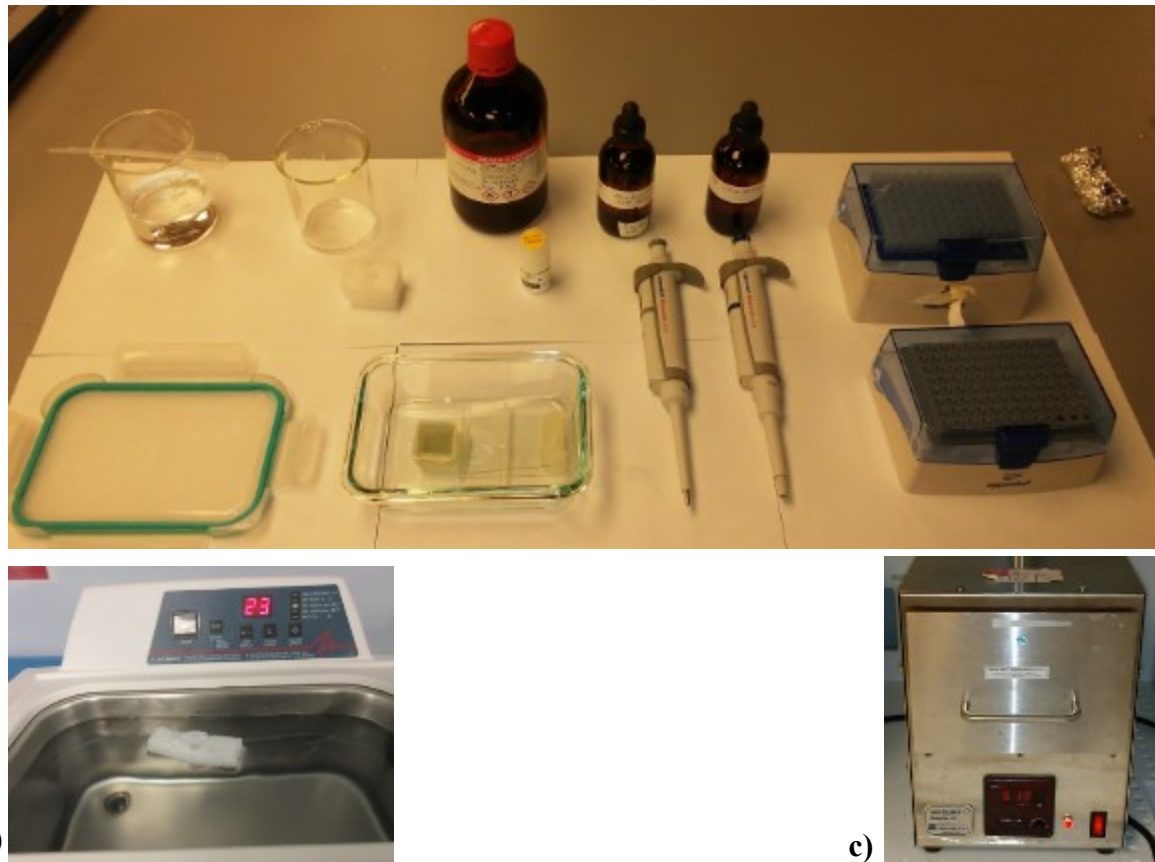


Figure 5-1: Some necessary tools for nanosphere lithography include a) beakers, pipettes, pipetters, glass bowls, solvents like ethanol, solutions of different SDS concentrations, a solution of nanospheres, b) a sonicator and c) a UVO cleaner.

Examples of the nanospheres used in this work can be found in Figure 5-2. Here they were imaged on an aluminum surface by a scanning electron microscope (SEM).

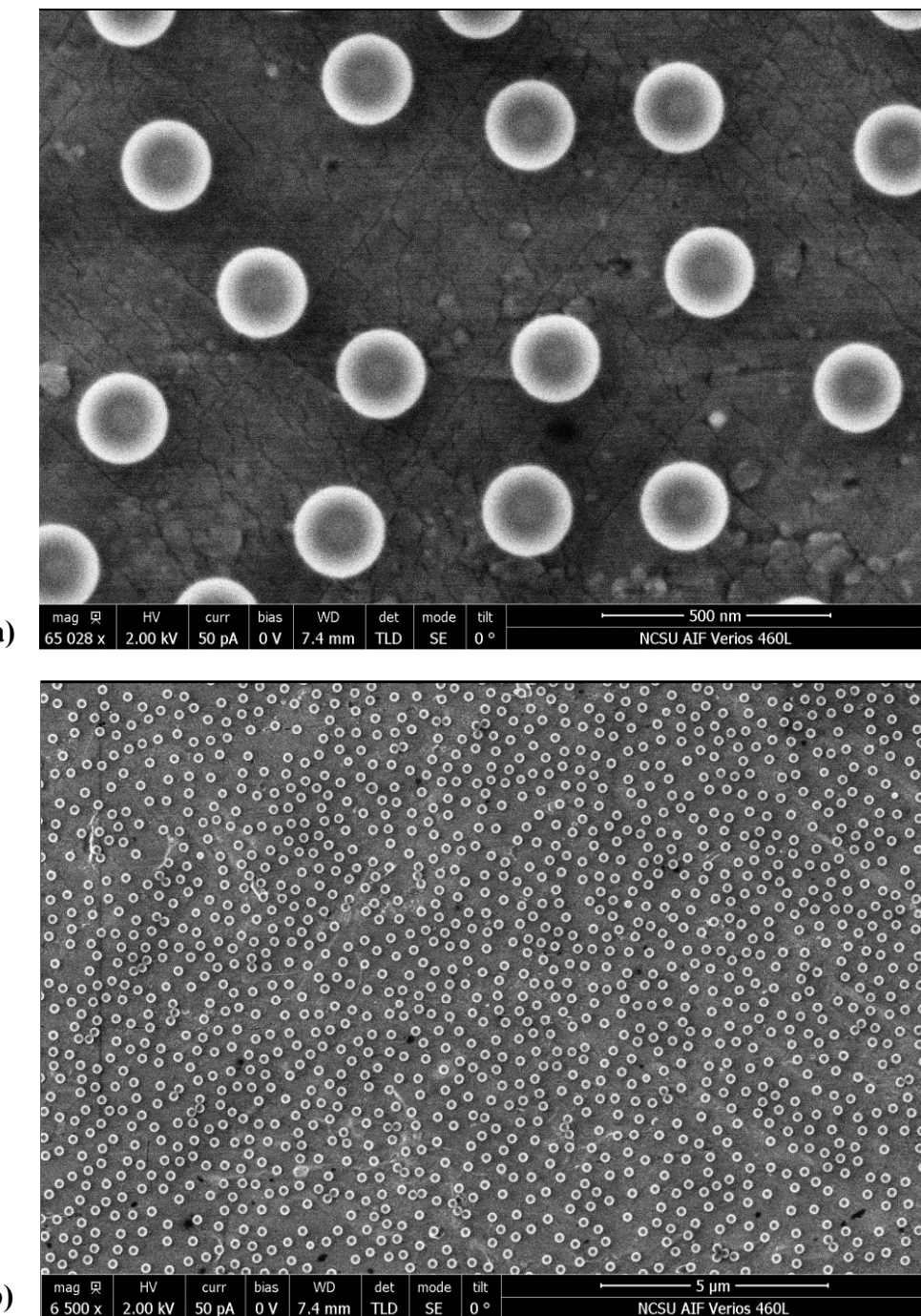


Figure 5-2: SEM image of the monodisperse polystyrene nanospheres used in this work on an aluminum surface in a non-compact distribution.

The first attempt at making nanospheres deposition was simple and resembled prior work found in literature. A stack of glass slides were glued together and put in a bowl with a tilted glass slide as shown in Figure 5-3a. On the tilted slide was put a piece of silicon that had

been cleaned in solvents. Deionized (DI) water level was added to the bowl to form a meniscus with the glass slide stack. Then a suspension of nanobeads mixed with alcohol and deionized water were released on the stack, whereas they spread out and then went on the water's surface. Sodium dodecyl sulfate (SDS) was added to the water surface to compact the nanospheres in the direction of the silicon piece. The water then was pipetted out, leaving a layer of beads on the silicon to me SEM imaged. This concept was derived from Su et al [84].

A very similar approach is shown in Figure 5-3b, except that the nanospheres suspension is not released on the stack of glass slides but on a cleaned glass slide that goes into the DI water.

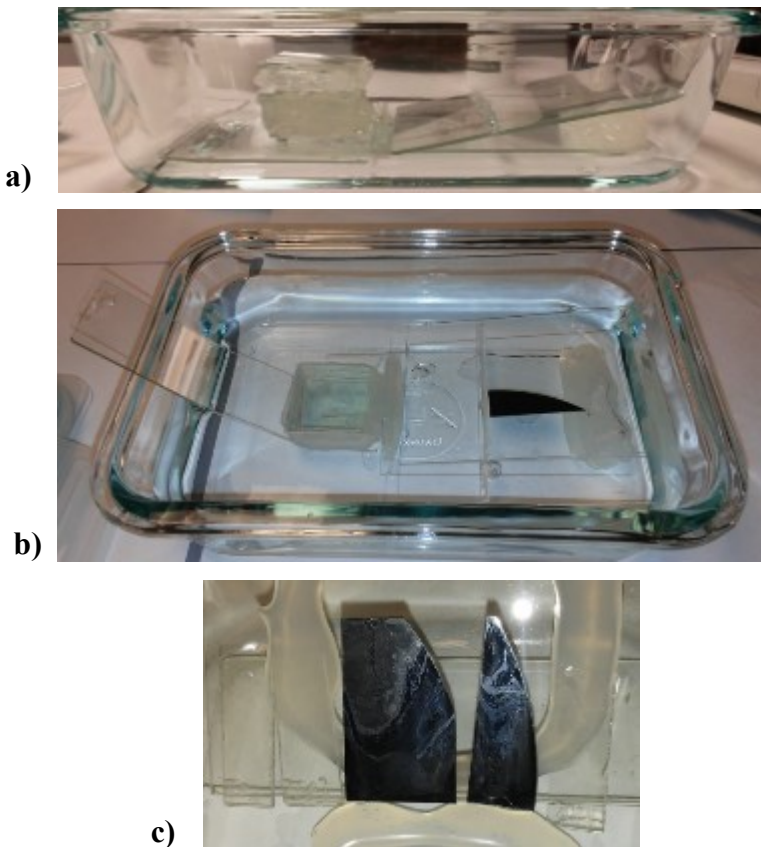


Figure 5-3: Early methods for nanosphere colloidal crystal deposition.

Both the methods of Figure 5-3a)-b) created results like those seen in Figure 5-3c with some silicon pieces being covered with non-uniform patterns.

The theory is that as the water level descends a surface, there is a convective assembly driving the self-assembly of monospheres into a crystal as shown in Figure 5-10.

Since the patterns were not uniform in the methods from Figure 5-3a-b), spinning on the nanospheres on clean glass slides were attempted as done by Kiraly et al [85] but this did not produce uniform deposition in the local conditions as shown in Figure 5-4.

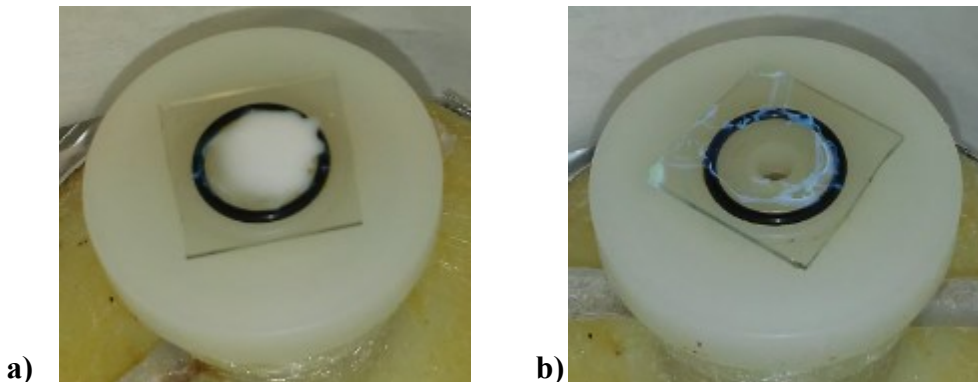


Figure 5-4: Spinning on the nanospheres to a glass slide was also attempted but did not produce consistent nor uniform results.

At this stage, several problems quickly started unfolding in this work. The first was that the collection of glass slides were not a good arrangement to use for consistent results because the glass could slide past one another and the exact placement for each experiment was likely not the same. As a result a metal ramp was used for deposition as seen in Figure 5-5a. This was an improvement in stability and repeatability but results were similar to those seen in of Figure 5-3c. Other issues lingered and needed to be solved.

Another issue was that the correct etching parameters for a newly installed plasma etcher needed to be found and this required the creation of many samples. Working on one large piece at a time as shown in literature would not be beneficial in this work. To address this problem, silicon was diced into smaller pieces than earlier. Instead of depositing onto a few

pieces at a time, many pieces would be deposited on simultaneously. The new smaller dimensions of the silicon can be seen in Figure 5-5d.

A third issue was that there needed to be a different approach to depositing the nanospheres layer which would establish the layer in a consistent way. The layer needed to be widespread and even. Using a bowl with a large surface area was not ideal for this and was wasteful in the use of these expensive nanospheres.

The solution came with designing and 3D printing a ramp that would be weighed down and submerged under water. The weight was required because the plastic was a buoyant in water. The ramp was designed with a sliding arm that could go up and down on the inclined surface to hold silicon pieces of different lengths. The ramp also had holes designed into it to help drain water off its surface or release water that was behind the silicon pieces as the water level descended. The ramp and silicon pieces can be seen in Figure 5-5b.

A noticeable difference between this and prior attempts was that the nanospheres solution was no longer allowed to spread all over the surface of the water. The range of movement for it was physically restricted by the introduction of an aluminum foil skirt held in place by strong wire as shown in Figure 5-5b)-c). DI water would be added to this configuration and the nanospheres would be allowed onto the water surface with a glass slide.

A problem that was in the prior designs was the use of the pipette to drain the water introduced disturbances and miniature waves to the water that were not useful for the deposition of the colloidal crystal of nanospheres. To make the withdrawal of water smoother, a siphon was employed as indicated by the tube in Figure 5-5c. Other work had made use of drains to accomplish the same removal of the underlying water [86].

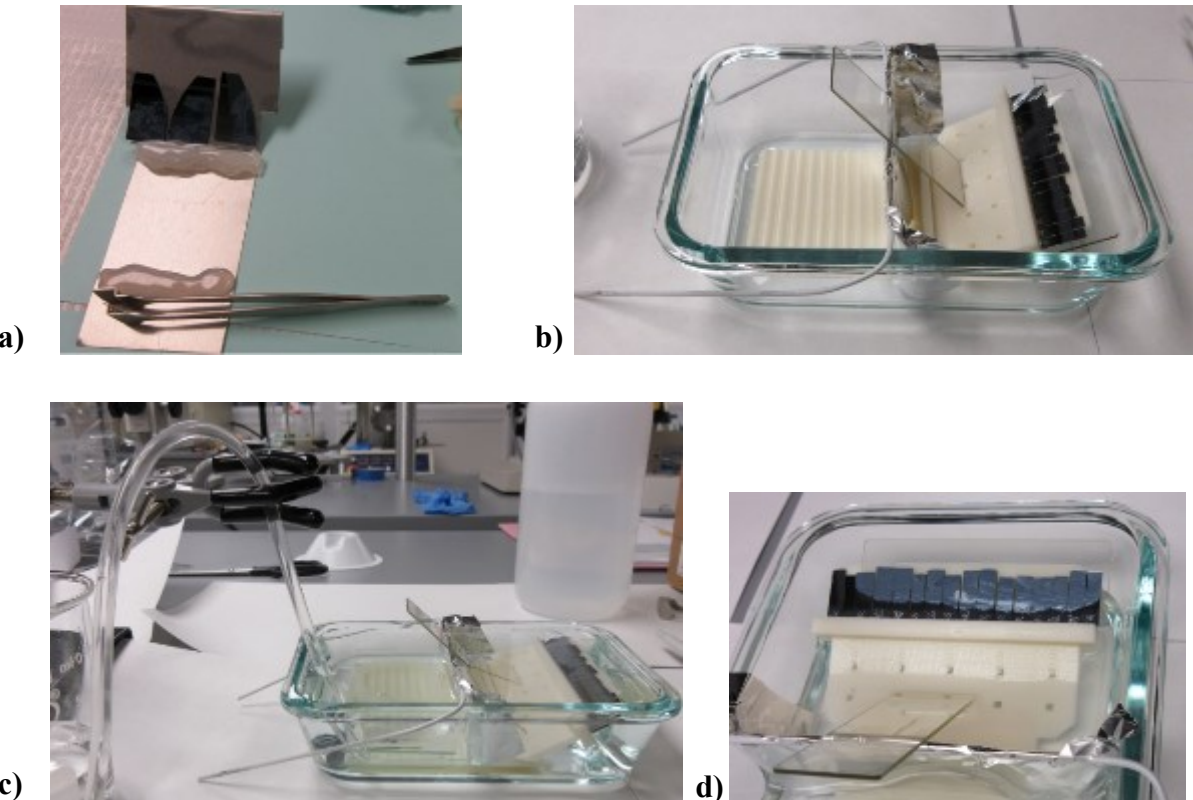


Figure 5-5: Attempted deposition techniques. The use of small silicon samples allowed for many pieces to be coated simultaneously, helping to provide the number of samples needed to explore the parameter space of the plasma etcher.

The rate of the water withdrawal was slowed to ensure a smooth movement of the water across the surface of the silicon pieces. A whiteish deposit was left on the pieces as shown in Figure 5-5d. These pieces were dried, stored and then taken to the plasma etcher to be processed.

After plasma processing, the samples were taken to the scanning electron microscope (SEM) to be examined.

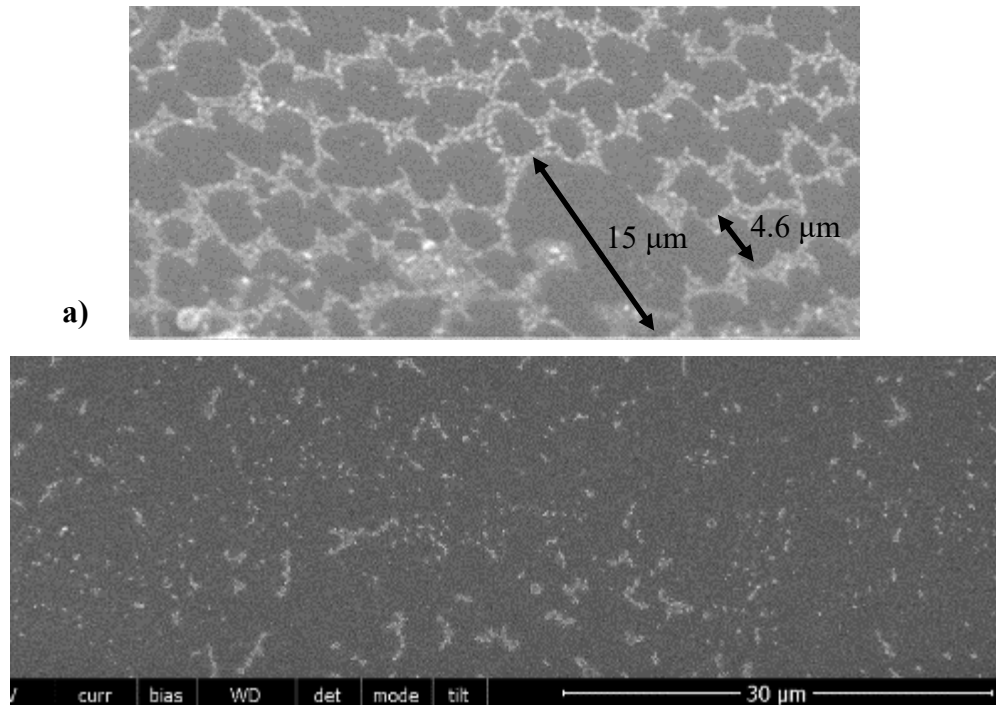


Figure 5-6: The initial samples had unexpected features large scale where a) elliptical patterns or b) sparse coverage.

Features that were not expected are seen in Figure 5-6a)-b) where elliptical patterns were seen and as well as areas of sparse coverage. The elliptical features were judged to be artifacts from dissolved gas in the water producing bubbles pushing the nanospheres on the surface to their perimeter. The slope of the drying silicon substrate likely caused the bubble circle to become elliptical. The water used for the experiment was allowed to degas before usage and the density of coverage would be worked on as the experiments progressed as detailed later.

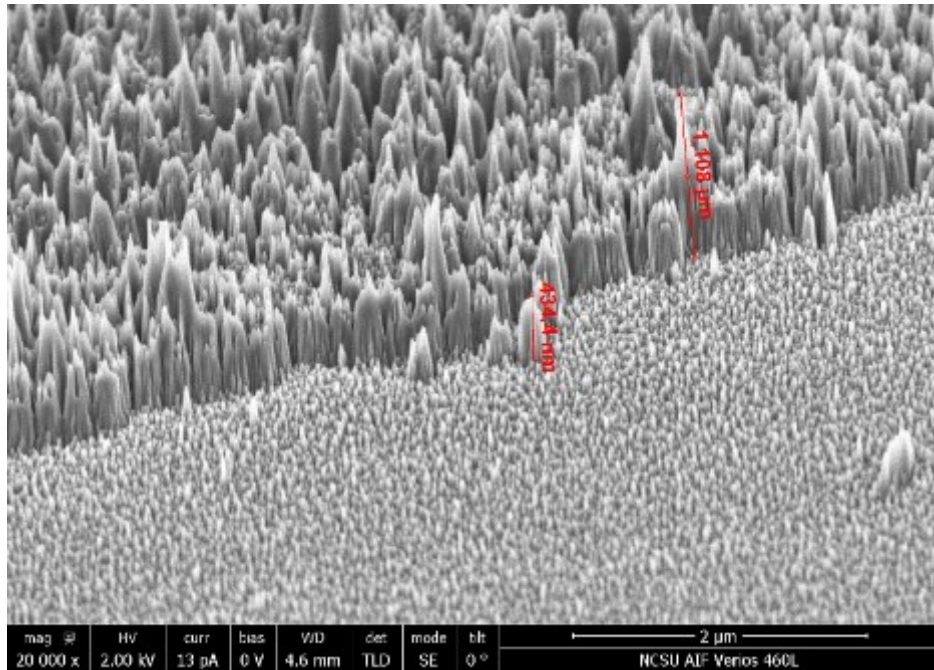


Figure 5-7: Close resolution of one of the first attempts at etching silicon with a nanosphere mask lacked any distinct indication of correct patterning or what step to take next. Features in this SEM image range from nanometers to microns.

Upon closer examination, the smaller scale features were not expected either. Figure 5-7 shows one of the first results in imaging a silicon surface that had nanospheres applied to it and then plasma etched. The features ranged in sizes from nanometers to microns and there wasn't a clear indication of how to proceed after these results.

The only step that could be taken was to go forward with making more silicon pieces, deposit nanospheres on them, and explore the parameter space of the plasma etcher to unveil the necessary conditions to produce the desired moth-eye biomimetic features.

A subset of the etch results can be seen in Figure 5-8 showing wide range of results from the indistinct to well patterned, and many form types in-between.

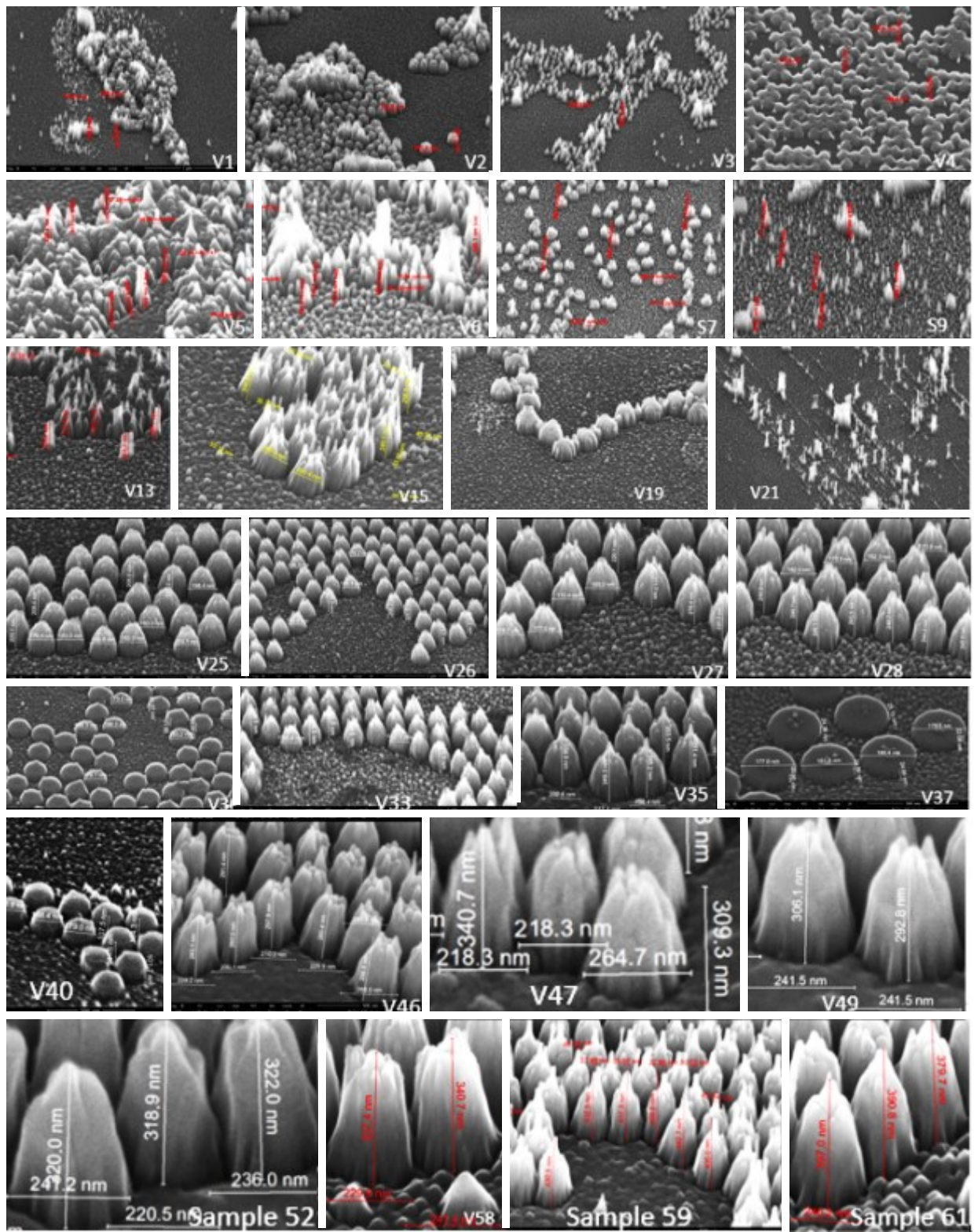


Figure 5-8: Images showing the results of different silicon etch conditions.

The results from the plasma etcher's parameter experimenting slowly yielded results that were helping to arrive at the desired outcome. With each experiment the features grew taller and more distinct. However, as also indicated by Figure 5-8, the problem that persisted was the lack of the nanosphere mask being distributed evenly across the surface of the silicon. The images from Figure 5-8 represented small areas where the nanobeads were randomly located. More control of the nanospheres' deposition was required to make them be uniformly distributed. The solution was not immediately clear and required some attempts to discover the method to use.

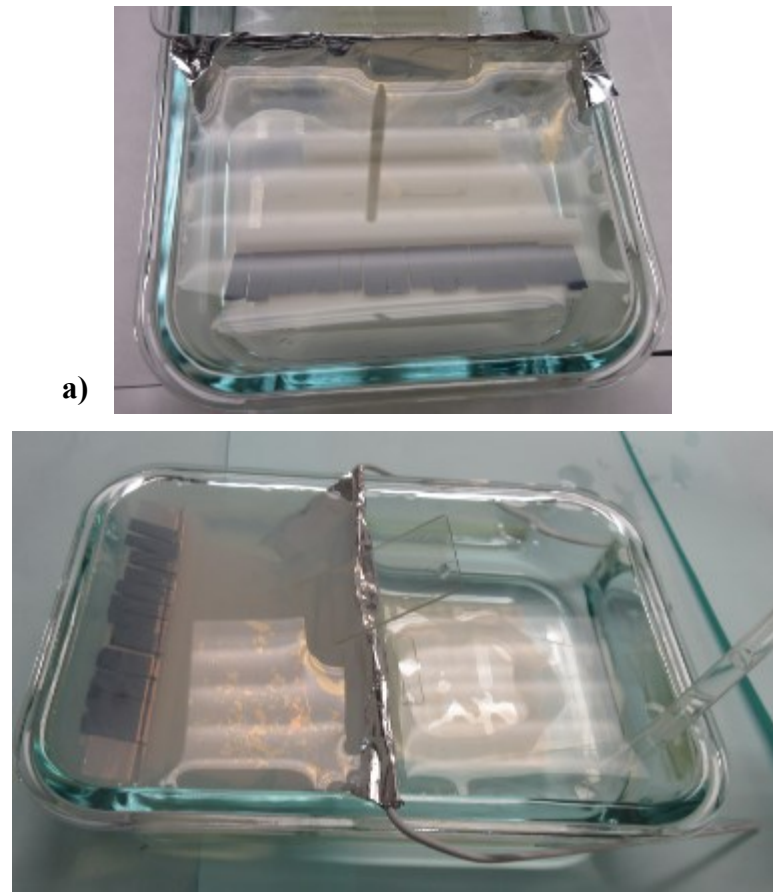


Figure 5-9: Results of the application of the nanosphere suspension to the DI water surface hinted at the next procedure to attempt.

The strategy that was next tried hinged on an observation of what happened during the application of the nanospheres suspension to the DI water surface. Literature had mentioned that the 200 nm nanospheres were too small to interact with light and would be invisible in visible light. As a result, when small golden colored islands appeared on the water's surface it was assumed that these were areas where the nanobeads were not monodispersed and formed rafts, clumps, or multi-layers several beads thick, leading to the yellowish hue. Toward the upper area of the water surface in Figure 5-9a illustrates this observation.

Not having the proper coverage could also mean there aren't enough beads to make the colloidal mask. For this reason it was decided to try to increase the density of the beads by increasing the concentration. The consequence of this is seen in Figure 5-9b. Here, the golden islands multiplied and became more prevalent on the water's surface.

At the same time, it was reasoned that the beads need to be more constrained in order to increase their coverage density on the silicon. Smaller bowls were not available, so a new method needed to be devised. Additionally, it was becoming more apparent that a way to establish even more accurate control could be useful. These two needs helped drive the setup that was created Figure 5-11.

The arrangement in Figure 5-11 shows the bowl from previous figures, but also new items of a syringe pump, and a sample being suspended on a sample holder above the bowl. Over several iterations of design, a blue cantilever arm was 3D printed with each revision making the custom design more sturdy and better fitting. Wire was chosen to hold the sample holder since it has a thin diameter and would impact the colloidal crystal the least.

The concept driving the deposition is similar to the case as the water level dropping.

Instead of the water surface going past the substrate, now the substrate goes past the water surface. The idea is illustrated in Figure 5-10.

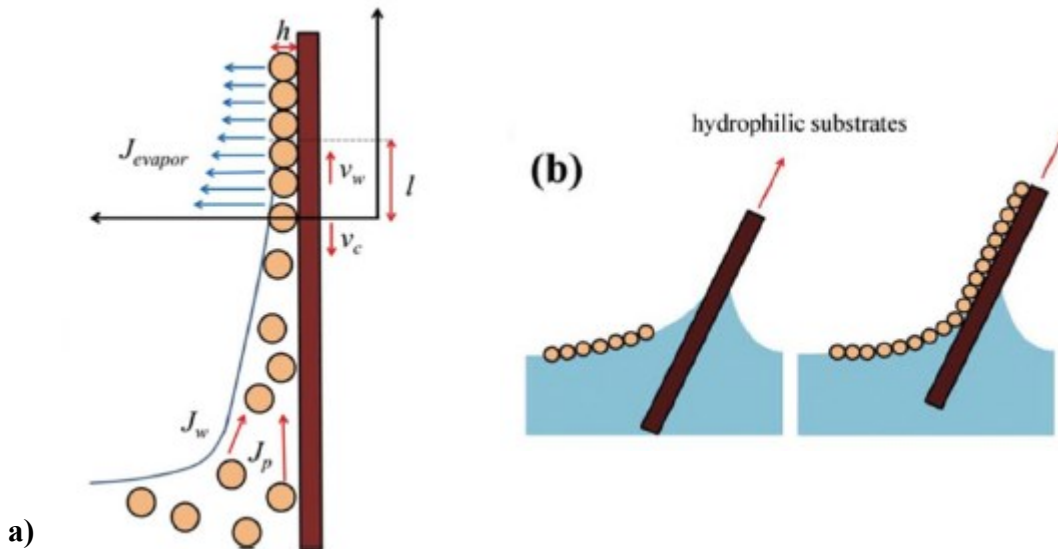


Figure 5-10: The diagram a) shows convective assembly drives self-assembly of the colloidal crystal [87][88]. Here 'h' is the particle layer that develops as water is evaporating from a surface with a meniscus. In b) a simplified version is illustrated. The concept for a dropping water level with a colloidal crystal on its surface is similar to both a) and b). Images reprinted from "Advances in Colloid and Interface Science", vol. 246, Lotito et al, "Approaches to self-assembly of colloidal monolayers: A guide for nanotechnologists", pp. 217–274, Copyright (2017), with permission from Elsevier.

Eventually it was discovered that the golden areas were desirable and represented the kind of self-assembled colloidal crystal that would adhere to the silicon as a compact nanospheres mask and efforts were focused on making more of the water have a yellow sheen.

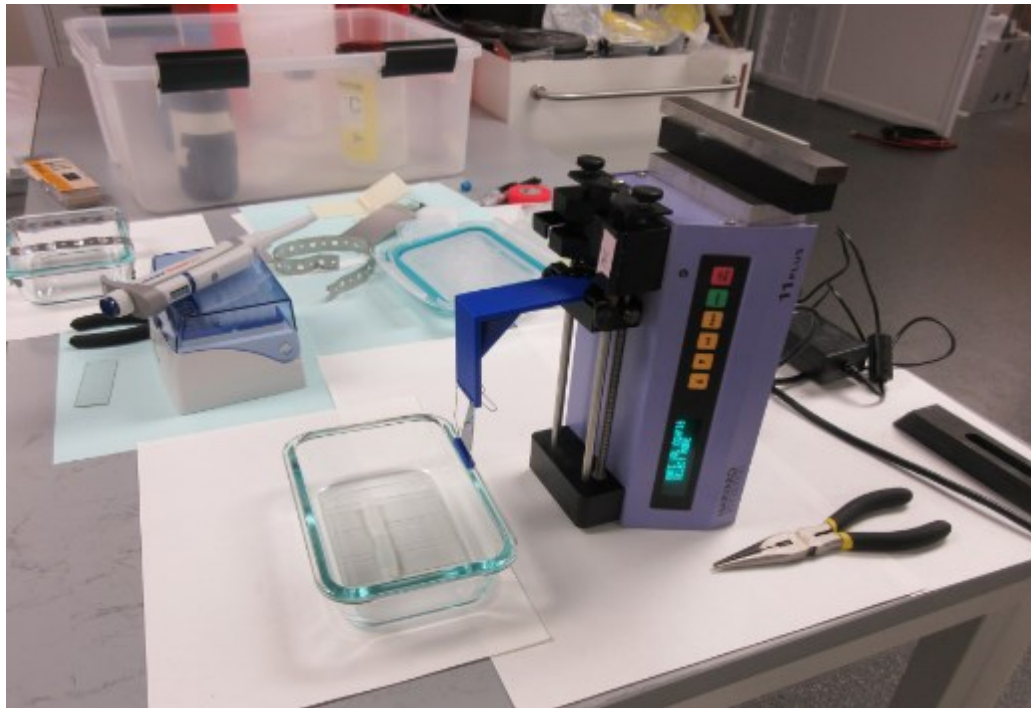


Figure 5-11: The improved setup included the bowl, sample, sample holder and most importantly, the syringe pump. Metal weights were put on the pump too to make it more secure.

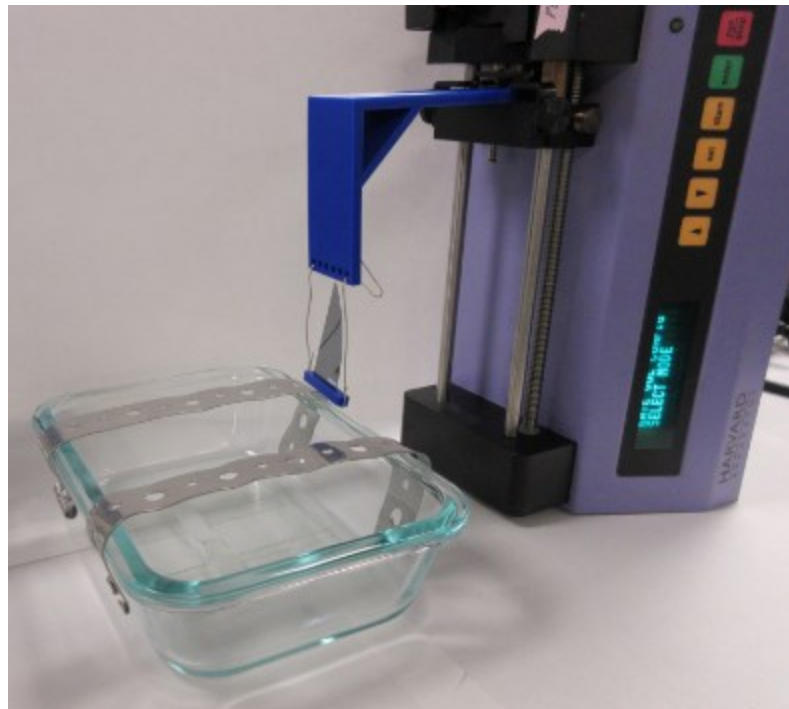


Figure 5-12: A sideways view of the setup showing how the metal strips were put in place defining where the reduced area for the nanospheres dispersal would be.



Figure 5-13: An aluminum foil barrier was added to the metal bars to create a smaller channel and limit the water's surface area. The nanospheres suspension was then introduced creating a greater amount of yellow areas.

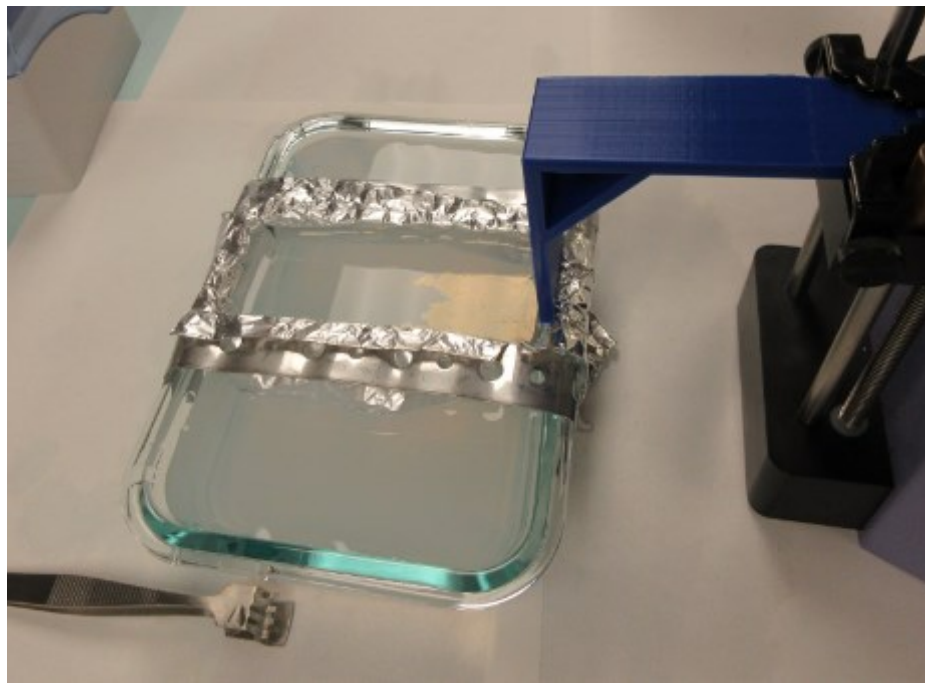


Figure 5-14: By adding a solution of SDS a compacted layer of monodisperse nanospheres was created. The silicon was hoisted through this layer and SDS was continually applied to maintain the pressure.

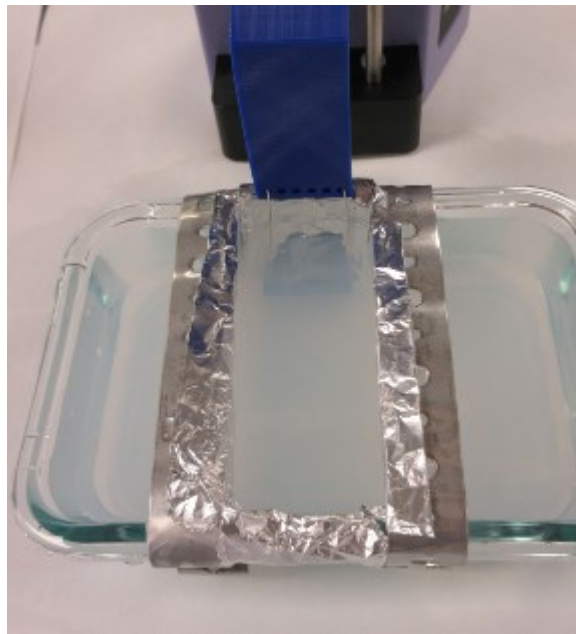


Figure 5-15: When viewed from another angle, the same colloidal monolayer of nanobeads from the prior figure was not visible.

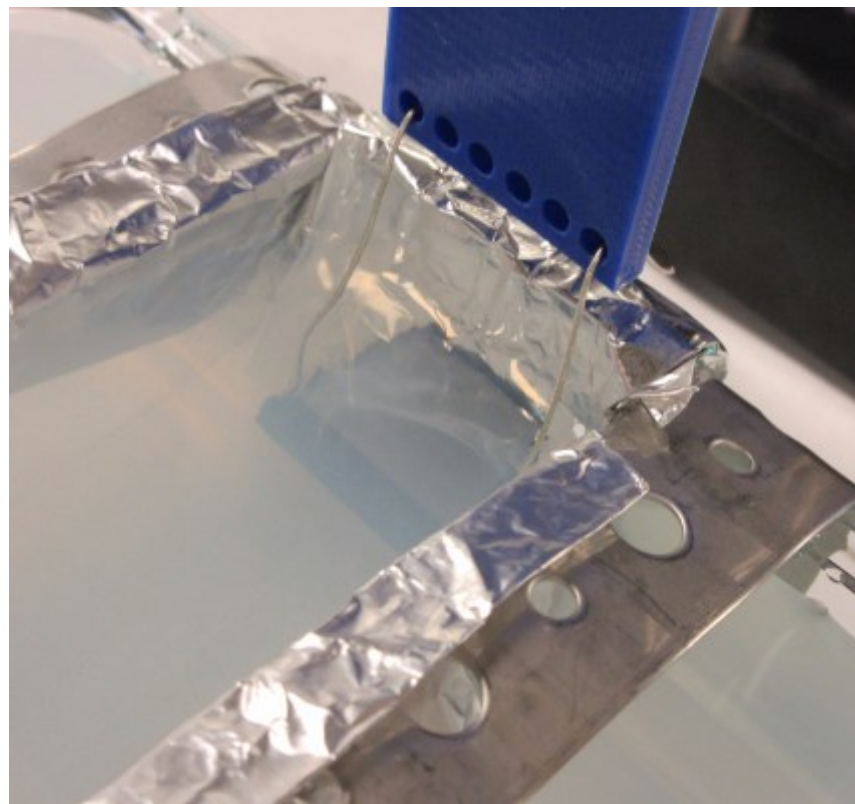


Figure 5-16: Even up close, the monolayer cannot be seen from the incorrect angle.

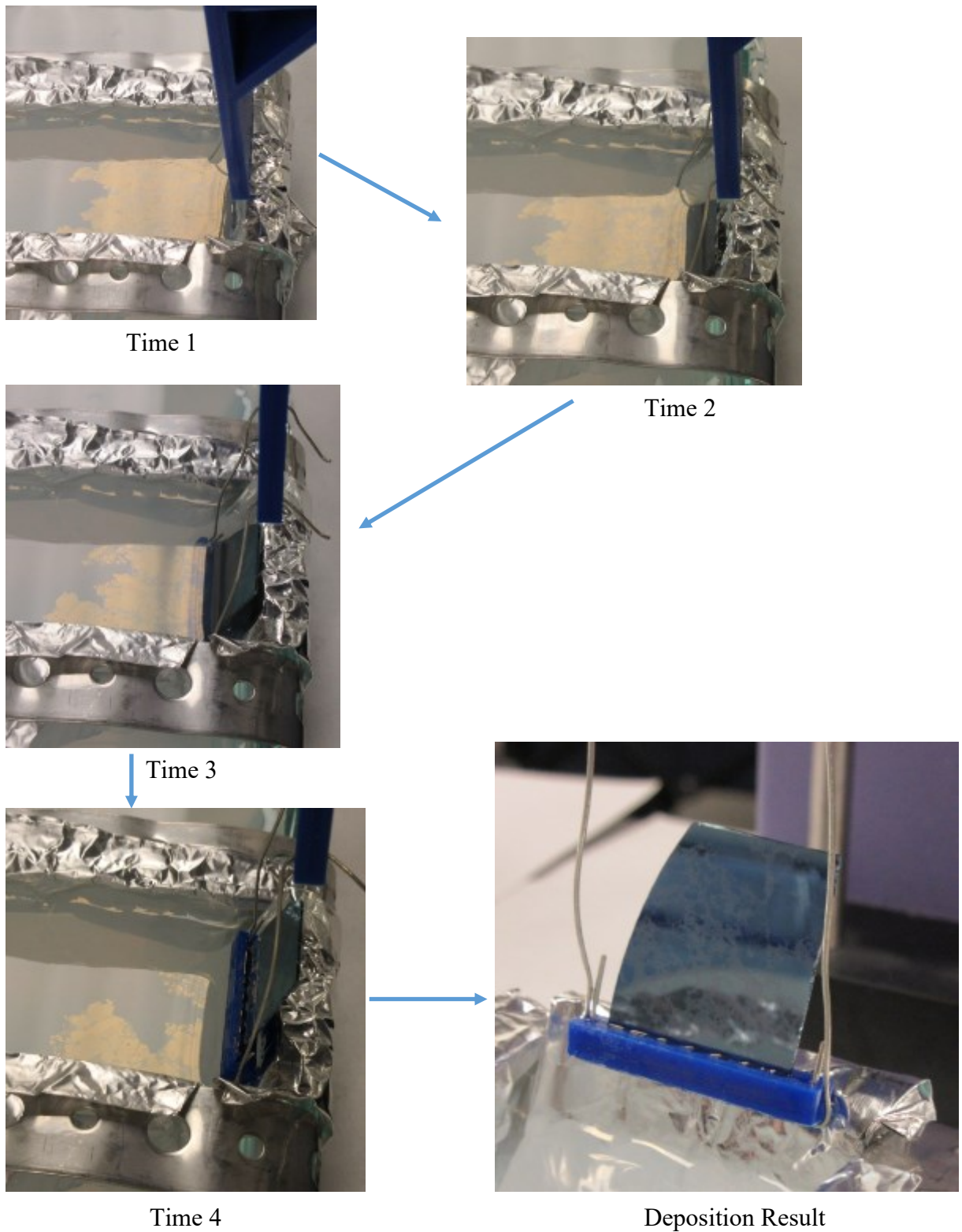


Figure 5-17: A time series of the deposition of the self-assembled nanosphere colloidal crystal on silicon that is slowly hoisted upwards from underneath the water with the monolayer on it.

With the changes in the experiment design, long range structure started becoming visible to the naked eye. The RIE treatment of the silicon produces black area because light is not being reflected in those regions as shown in Figure 5-18.

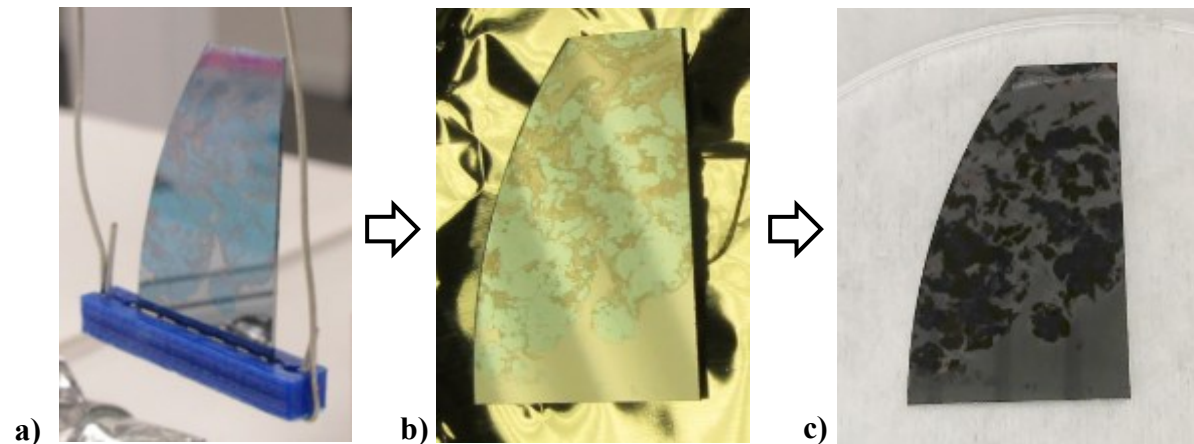


Figure 5-18: With the adjustments in experiments features become large enough to see and start becoming areas measured in square millimeters. The silicon piece here is about 2 cm long in height. In a) the substrate can be seen after nanosphere deposition and before reactive ion etching (RIE). In b) the same substrate can be seen when it is removed from the blue holder of the previous picture, dried, and still before RIE. In c) the substrate is shown after RIE. The dark areas indicate where the moth-eye features have formed on a large scale.

Rate of movement was investigated as well. Changes in concentration and rate of movement are shown in Figure 5-19.

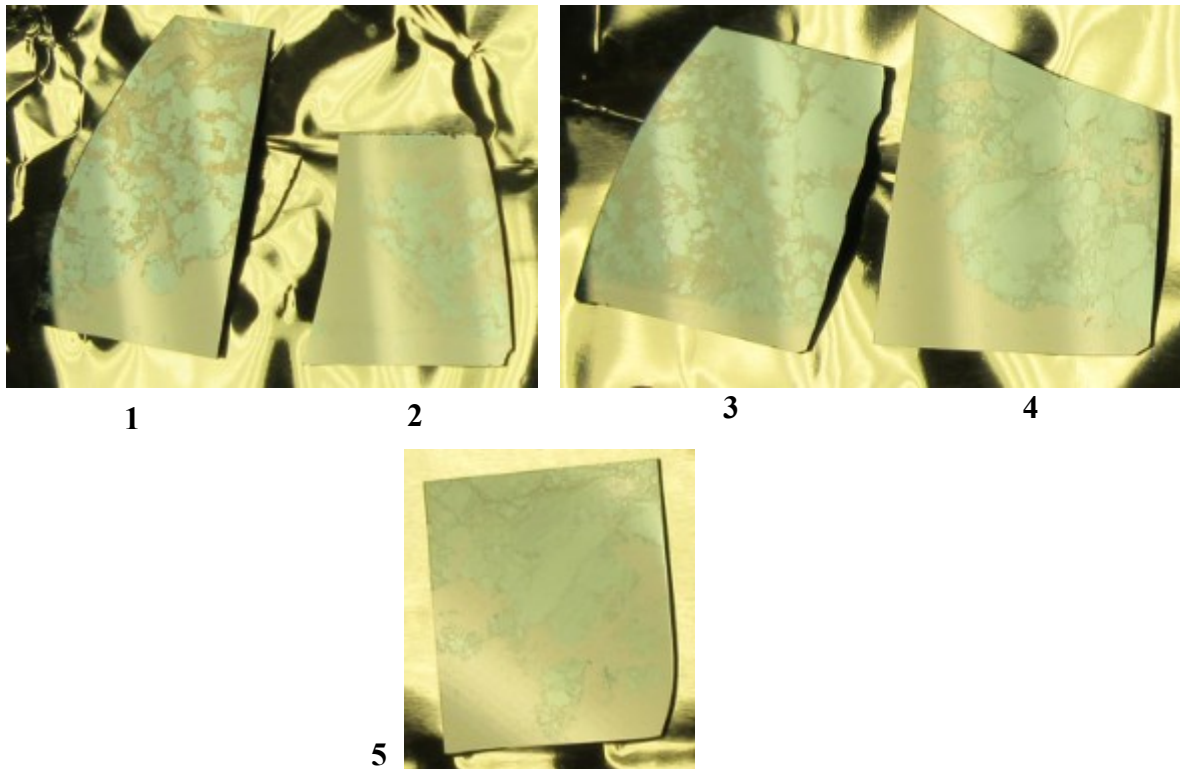


Figure 5-19: The results of concentrations and rate of movement were compared too. The concentration of samples 3 and 4 are double of 1 and 2. Samples 3 and 4 also were withdrawn from the water at 1/3 the speed of samples 1 and 2. The concentration of sample 5 is also double the concentration of samples 1 and 2, but the speed was reduced even further to be 1/10 the speed of samples 1 and 2. Higher concentration and slower movement seemed to help make a larger nanosphere crystal deposit. Under the right lighting conditions, the blueish tint areas can be seen where the nanospheres were deposited as a colloidal crystal and the moth-eye biomimetic nanostructures with long range order would appear after etching. The patches of monolayer crystals here are approaching centimeter scales.

With constant improvement and adaptation, the problems of creating the colloidal crystal were overcome and large areas of the water surface were covered by the monolayer as shown in Figure 5-20.

The addition of the SDS solution to cause compaction sometimes had the unfortunate effect of introducing a pressure that split and broke apart the colloidal crystal as illustrated in Figure 5-21. It was found that there were ways the gaps could be minimized making the crystal more complete looking and subsequently leaving less gaps on the silicon.

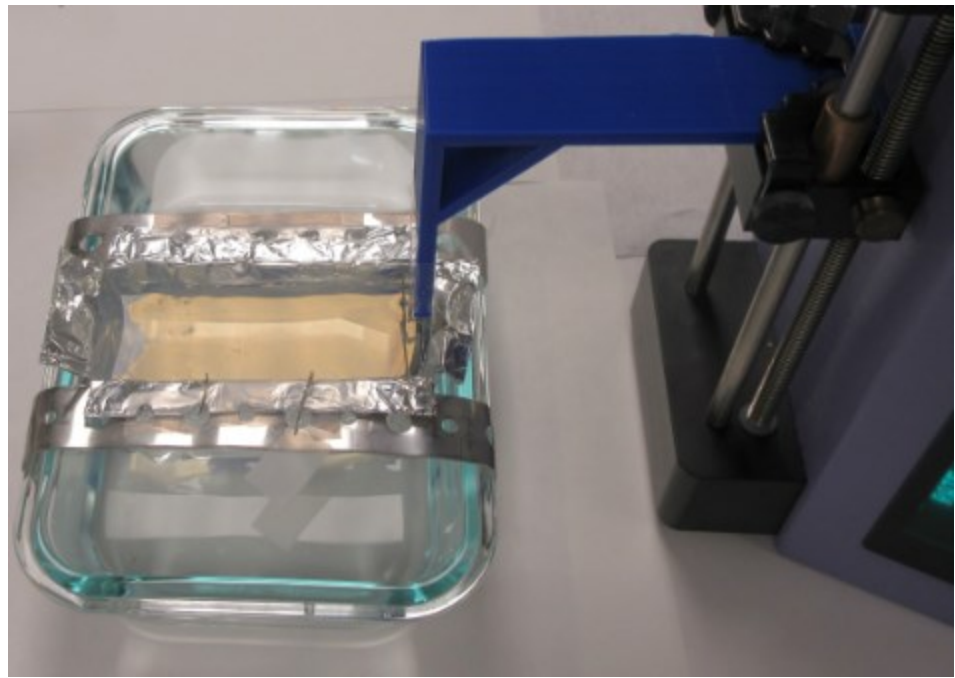


Figure 5-20: An excellent compacted monolayer crystal ready to be transferred to a silicon piece.

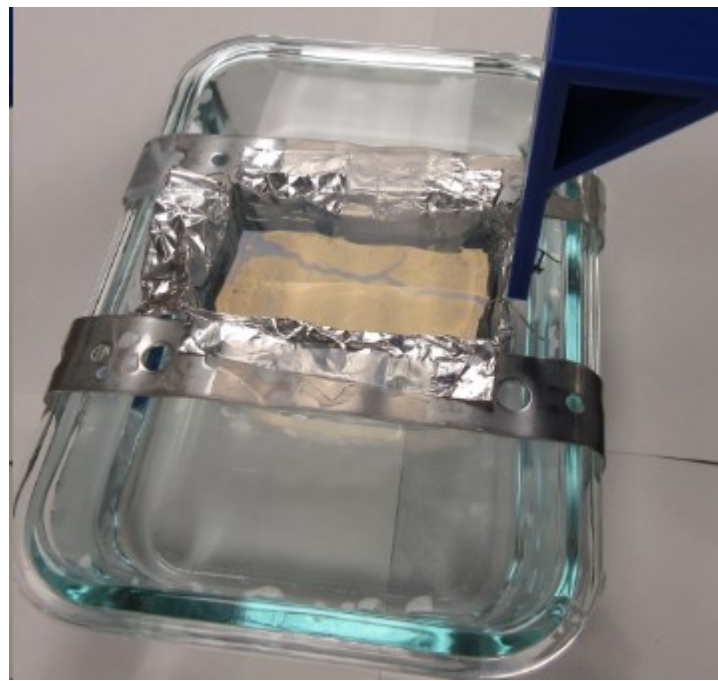


Figure 5-21: Compaction could sometimes lead to fracturing of the crystal from the pressure of the SDS.

After the silicon pieces were coated with the self-assembled layer of nanospheres, they were taken to the cleanroom plasma etcher. The samples underwent a 3 step etching process. The first was an oxygen plasma to reduce the diameter of the nanospheres, the second was a chlorine plasma to etch the silicon, and the third was another oxygen plasma treatment to remove any excess polystyrene from the nanospheres. Through the plasma etcher's portal, the plasma could be seen for oxygen, chlorine, and oxygen again. This is more completely explained in the later in this chapter in the section called "Biomimetic Nanostructure Fabrication to Increase Light Transmission Efficiency in Optoelectronic Devices".

The samples underwent a visual transformation from the plasma etching process. When put on the sample platter to go into the machine, the samples had the characteristic blue tint of a deposited colloidal crystal. After the process was completed and the samples reemerged, they were now black where the crystal worked as an etching mask. The biomimetic moth-eye nanostructures were created in these areas over centimeter scale samples. Light was not being reflected from these areas since the structures were helping to absorb light. The before and after processing look of the samples are seen in Figure 5-22a-b).

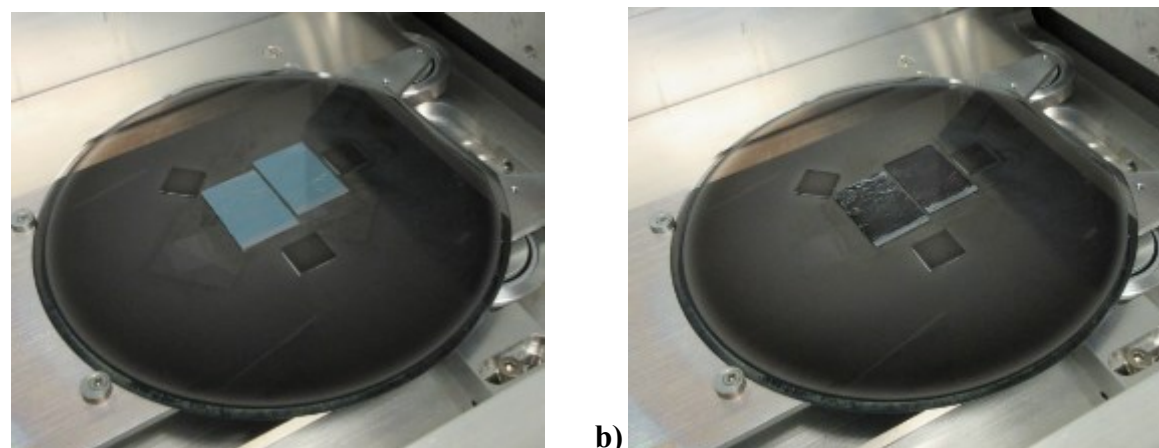


Figure 5-22: Before and after plasma etching of silicon samples coated with the colloidal nanosphere mask. In b) the biomimetic nanostructures have been fabricated, causing light to be absorbed and the surface to turn black. The samples here are approximately 1.5 cm by 2 cm in size.

With the proper etching parameters identified, along with the refinement of the colloidal crystal deposition technique, larger samples could be created with the nanostructures across their surface, with some of them being shown in Figure 5-23.

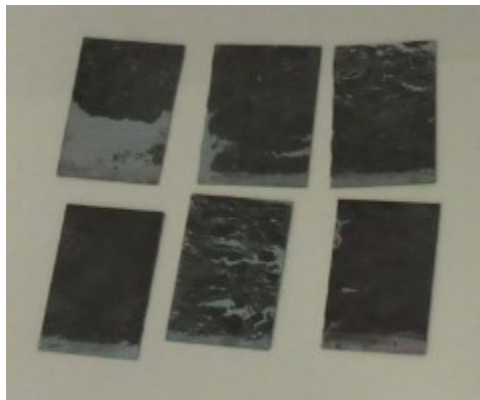


Figure 5-23: Samples that were now on the centimeter scale could be made with a refined colloidal crystal deposition process and appropriate plasma etching parameters. These samples are approximately 1.5 cm by 2 cm long and much larger than the samples of the Figure 5-5 setup that only produced microscopic sized dense coverage moth-eye patterns on one silicon sample.

5.3 Transferring the Nanostructure from Silicon to Other Surfaces (Nanoimprint Lithography)

Following the establishment of a protocol that could provide features of a correct morphology and adequate coverage on the silicon substrate, the next step was to develop a technique transfer those features to another surface with the eventual goal of being able to transfer them to an optoelectronic device. Figure 5-24 shows the features of the etched silicon substrate that was used for the initial PDMS molds.

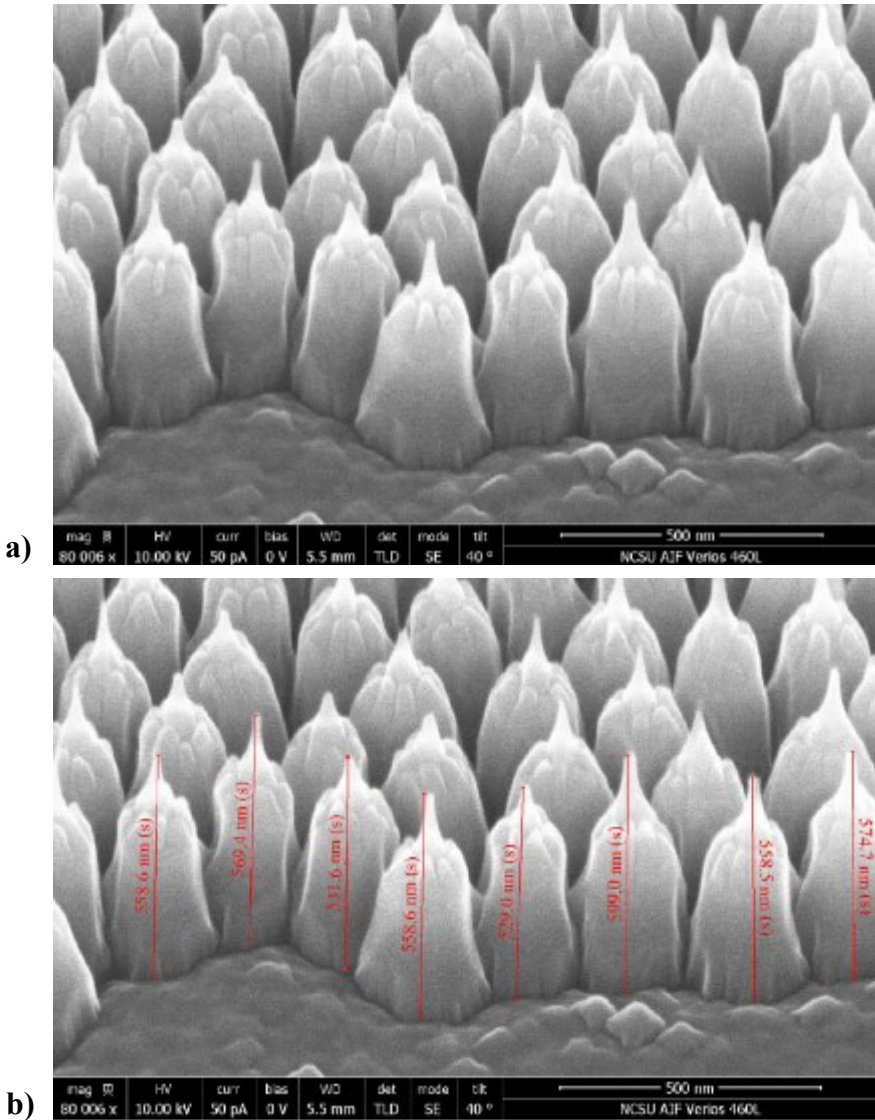


Figure 5-24: A patterned silicon substrate that was used to create a PDMS stamp to pattern heat cured glue, UV cured glue, standard epoxies and medical epoxy. The specifics of fabricating the PDMS stamp are diagrammed later in this chapter.

The view from above for these features can be seen in Figure 5-25 showing the close packed arrangement of the structures.

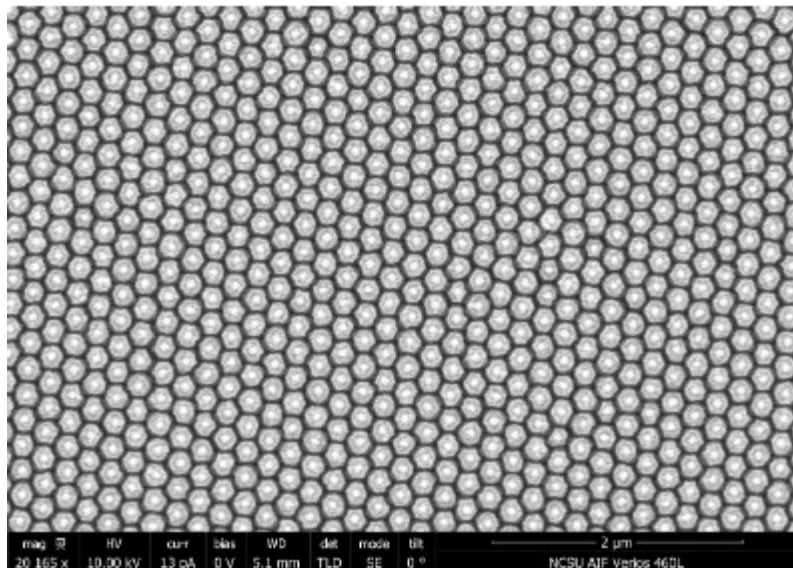


Figure 5-25: The features of Figure 5-24 were close packed as seen in this SEM image from above.

The creation of the mold involved several steps, with the first being the silanization of the surface. The nanostructures and the silanization created a hydrophobic surface. A drop of water was released onto the substrate in Figure 5-26 and it did not adhere to the surface, but promptly rolled off.

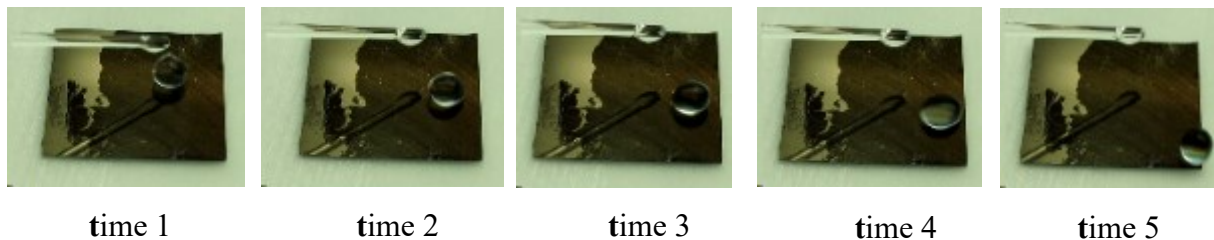


Figure 5-26: Time series showing the hydrophobic surface of the silanized nanostructured silicon substrate.

Contact angle measurement showed the angle made by the water droplet touching the surface was 135 degrees. For the same silanization reagent, references say that the contact angle on a bare piece of silanized flat silicon wafer to be approximately 104 degrees [89]. The additional angle size measured in Figure 5-27 likely occurs because it is a hydrophobic

nanostructured surface[90]. For reference, the water contact angle on silicon dioxide is 48 degrees and on silicon, 89 degrees [91].

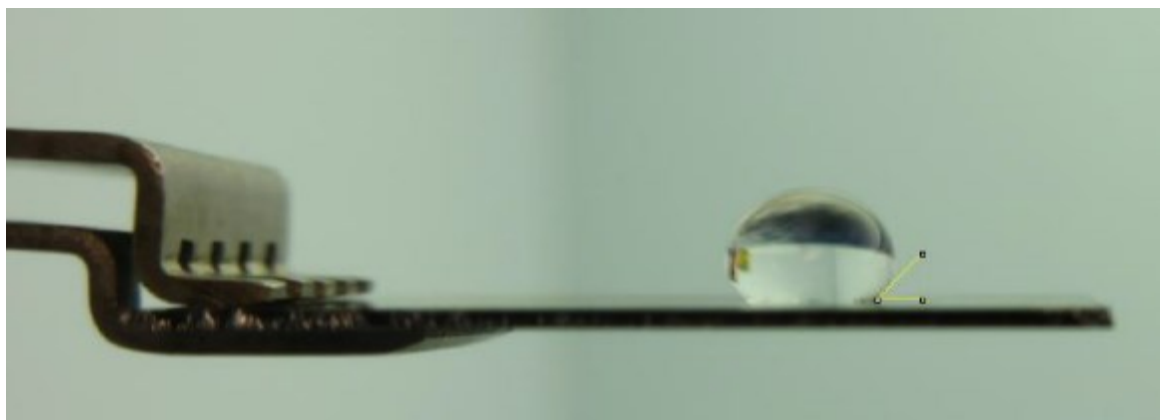


Figure 5-27: The nanostructured silicon surface was treated with a silane to produce a hydrophobic surface. The contact angle of a water droplet was found to be 135 degrees.

The silanization was a required first step in the PDMS mold making process to prevent the PDMS mold from adhering strongly to the surface. The detailed mold making steps are described in the next chapter.

After the mold was made, it was diced. Some UV curable epoxy was spread on a transparency and then the mold was pushed into the glue surface. The assembly was placed under a UV lamp to cure for the appropriate amount of time. Then stamp was removed, and the area under the stamp was cut out to be prepared for imaging with the scanning electron microscope. Being a non-conductor, the glue surface was difficult to image as they were. The samples were taken to be sputtered with gold palladium. The sputtering apparatus is shown in Figure 5-28.

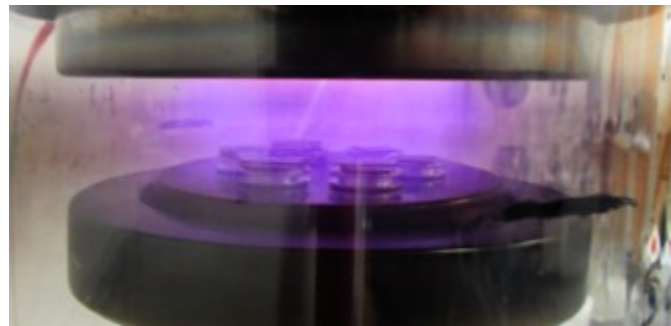


Figure 5-28: The nanostructures transferred to glue were sputtered with gold-palladium to be observable in the SEM.

Once the samples were sputtered they were ready to be imaged. One of the early imaging results can be seen in Figure 5-29. This was not using the sample from Figure 5-24, but an earlier patterned silicon piece in order to start working out the mechanics of the mold process.

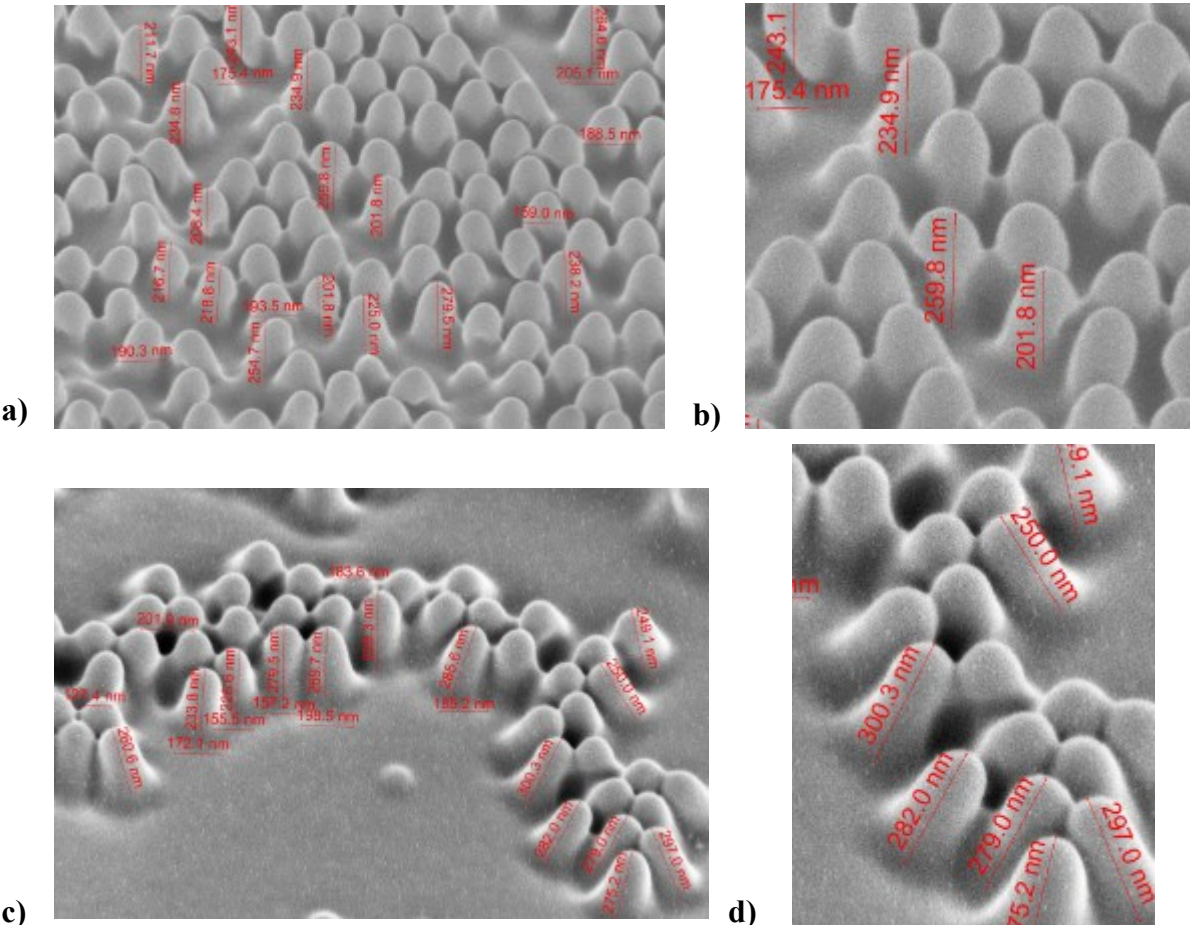


Figure 5-29: The first transfer attempts had feature collapse and possible static effects. When enlarging the images of a) and c), the contact and leaning of the features are easily seen in b) and d) respectively.

Despite the features not being ideal in Figure 5-29, the result was an overall positive outcome since it did show that the silicon features had made their way into the mold and the mold could pattern the glue on a secondary surface.

Eventually, from repeated trials, the structures started remaining upright. However, the next issue was that their height was not close to the original scale of the silicon features that towered in excess of 530 nm in Figure 5-24b above the plane of the planar silicon surface. There was a problem, but it was unclear where the problem was. One possible reason was that the features of Figure 5-24 were too close-packed, preventing the mold material from

penetrating to the bottom of the patterned nanostructures. The next concept tried was to do modify the etching to open up the space between pillars. The results of this are shown in Figure 5-30. The wider spacing between the cones came at a cost of the pillar height being slightly reduced to be closer to 500 nm tall.

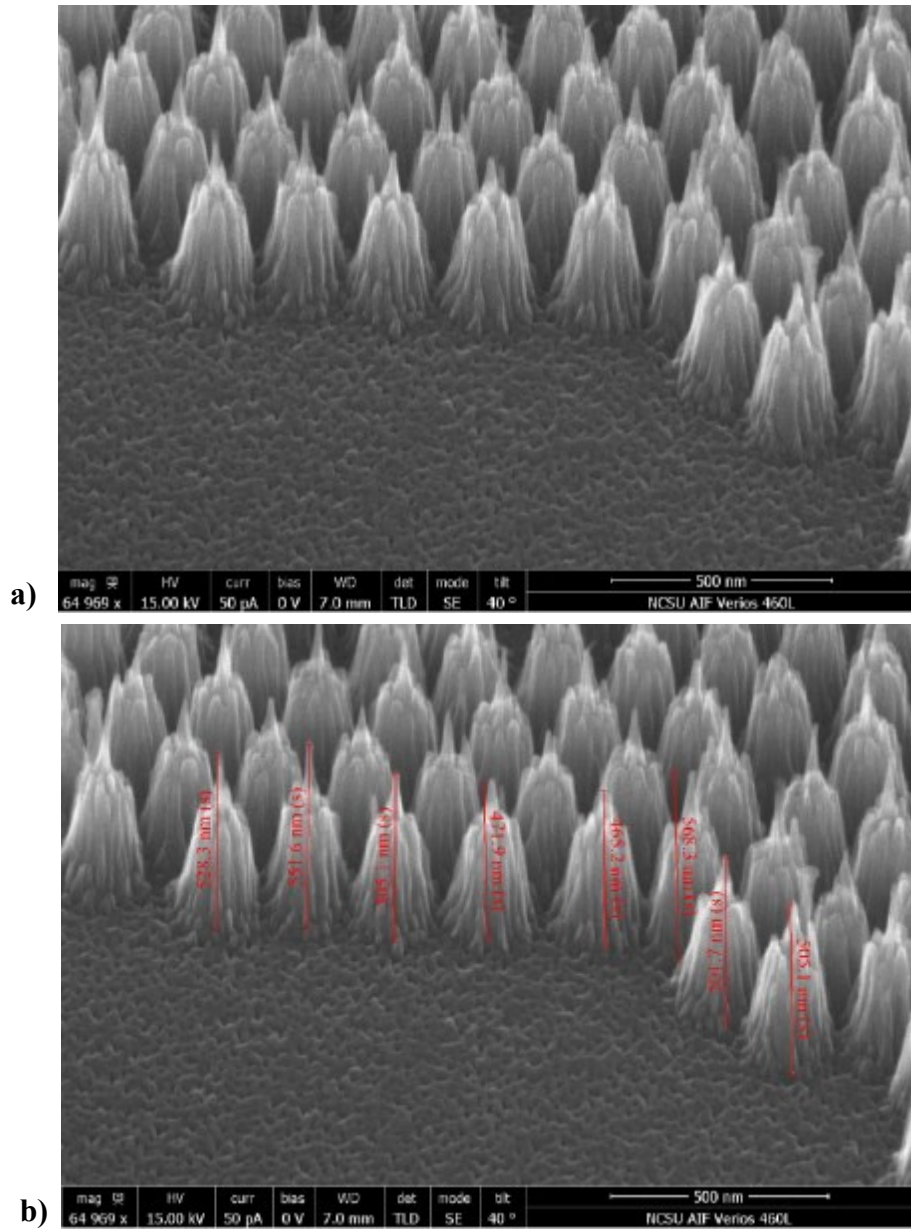


Figure 5-30: A different silicon sample with more etch done and more space between the cones became the next candidate for PDMS mold and stamp fabrication.

The extra spacing between the silicon substrates of Figure 5-24 and Figure 5-30 are more observable from above as shown in Figure 5-31. This was done in an effort to allow the PDMS spaces silicon 15 seconds different

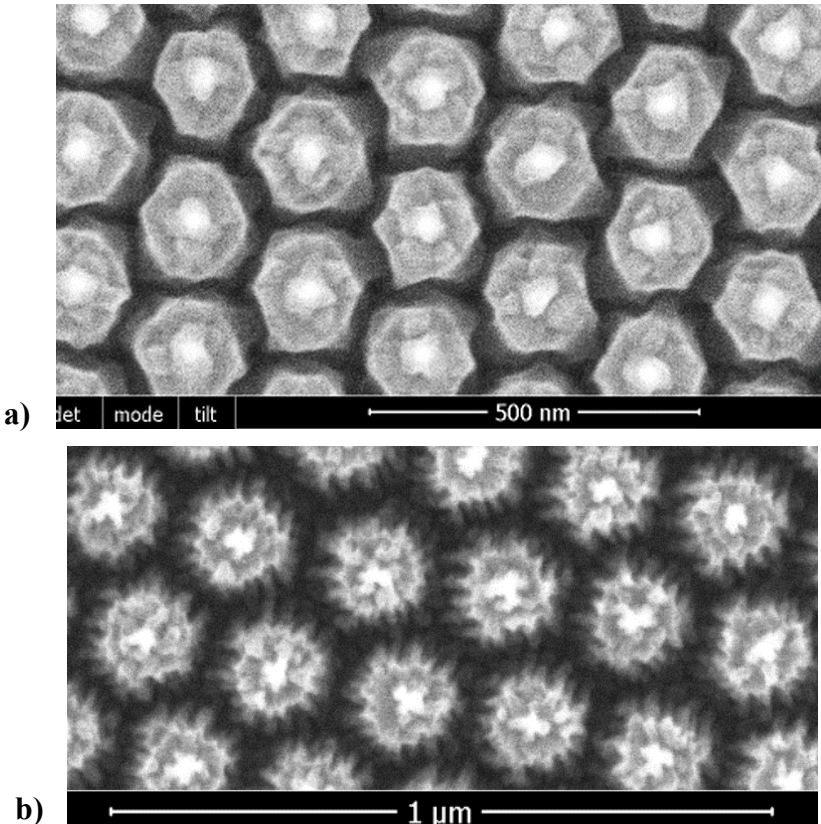


Figure 5-31: The spacing differences of the nanostructured silicon from Figure 5-24 and Figure 5-30 are best seen when comparing the samples from above.

To achieve the results of Figure 5-30 and Figure 5-31 the conditions of the etching were adjusted very carefully. Variations of etch time, gas flow and chamber power could very easily change the sample feature outcome. Conditions not that much different than those for Figure 5-30 and Figure 5-31 caused the peaks to become sharper.

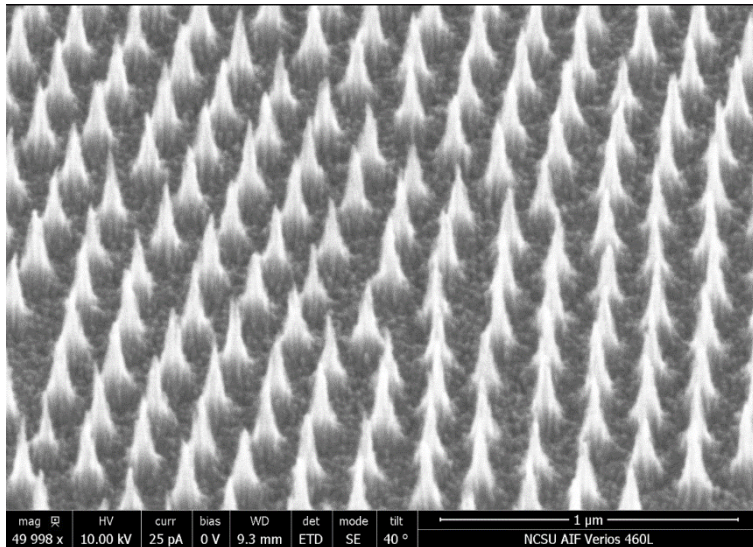


Figure 5-32: Small variation in process can change feature outcome. In this image the parameters that produced Figure 5-30 and Figure 5-31 were slightly adjusted, producing sharper features.

At this point, the silicon structure fabrication conditions that produced of Figure 5-30 and Figure 5-31 were held constant and more substrates and molds were made. There was still a question of how to make the transferred structures in glue taller because they were not close to the height of the original silicon pattern. This started an investigation of different glues and different ways of applying them. The following are results of the different trials.

One of the glues attempted was a heat cured glue. There was an additional reason for checking this type of glue and that was because the glovebox had a hotplate in it. If the pattern could be transferred and cured by heat then the hotplate in the glovebox could be used to help transfer the pattern to the organic devices in the glovebox.

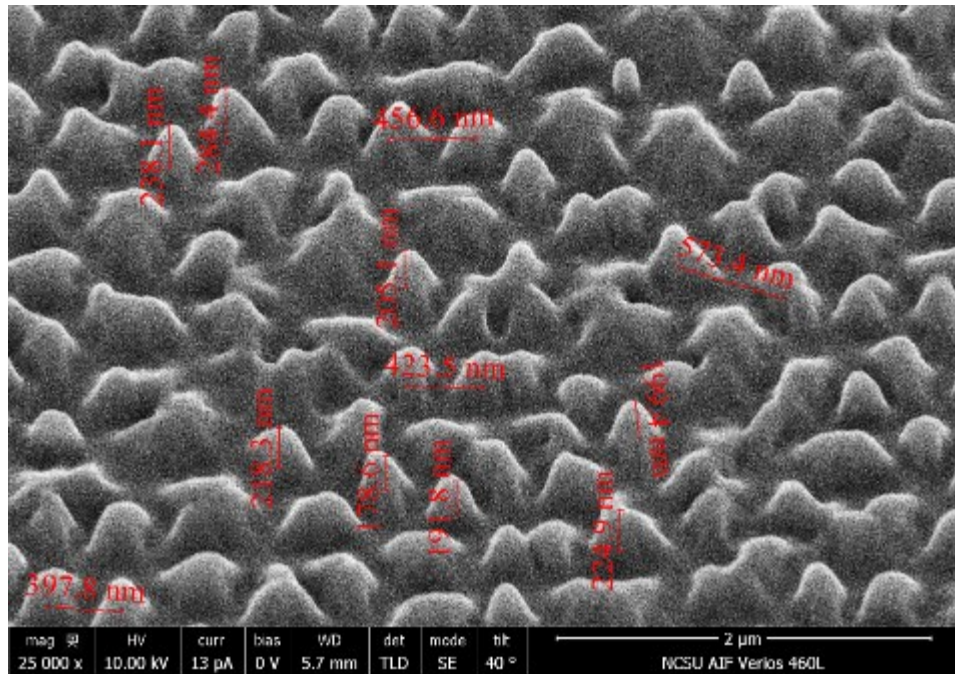


Figure 5-33: One variety of heat cured glue patterning produced results that were incorrectly shaped. This glue had a high viscosity and was not pursued further.

The glue of Figure 5-33 had a high viscosity. It was thought the viscosity prevented the glue from flowing into the molds properly and that is why the final product was misshapen.

Another variety of heat cured glue was also selected that had a viscosity 100 times less than Figure 5-33. The next series of figures demonstrates how the lowered viscosity was helpful in creating the structures to some extent.

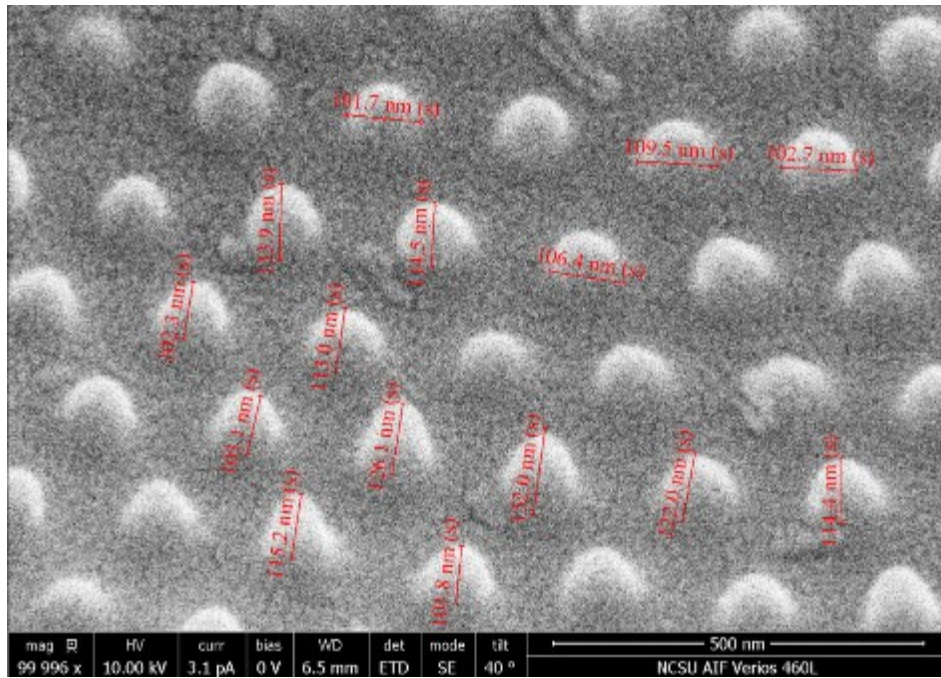


Figure 5-34: The next heat cured glue results. Some moth-eye like nanostructures are visible, but the pattern is small.

The heat cured glue did not produce structures that were sufficiently high, but the long range patterning was uniform as shown in Figure 5-35.

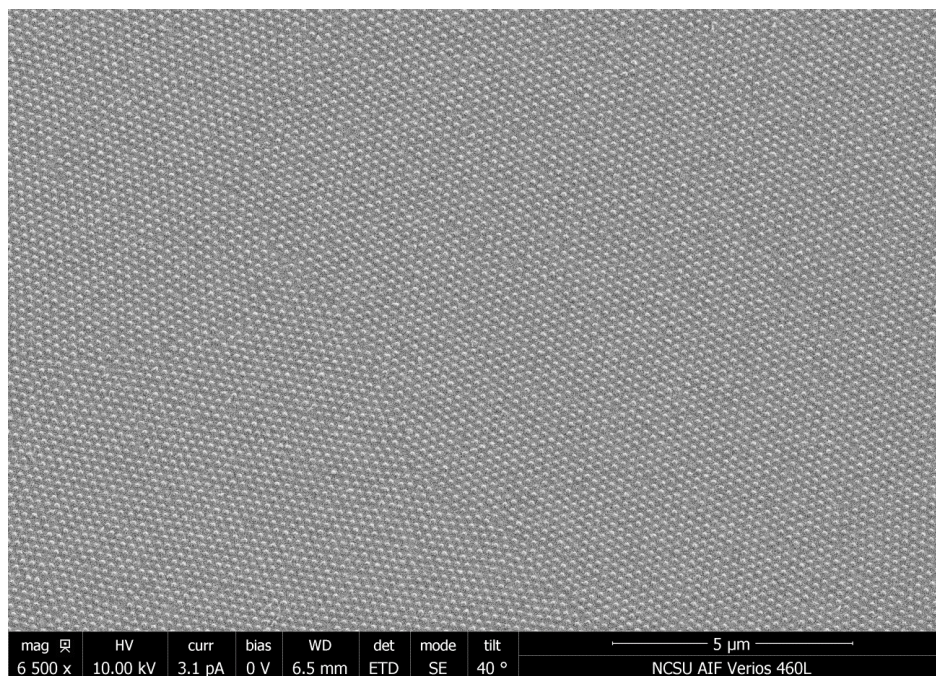


Figure 5-35: Large scale of heat cured glue showed good uniformity.

It was noticed that the PDMS stamp of the first heat cured glue had a slant to it and another sample was tried, with the results seen in Figure 5-36.

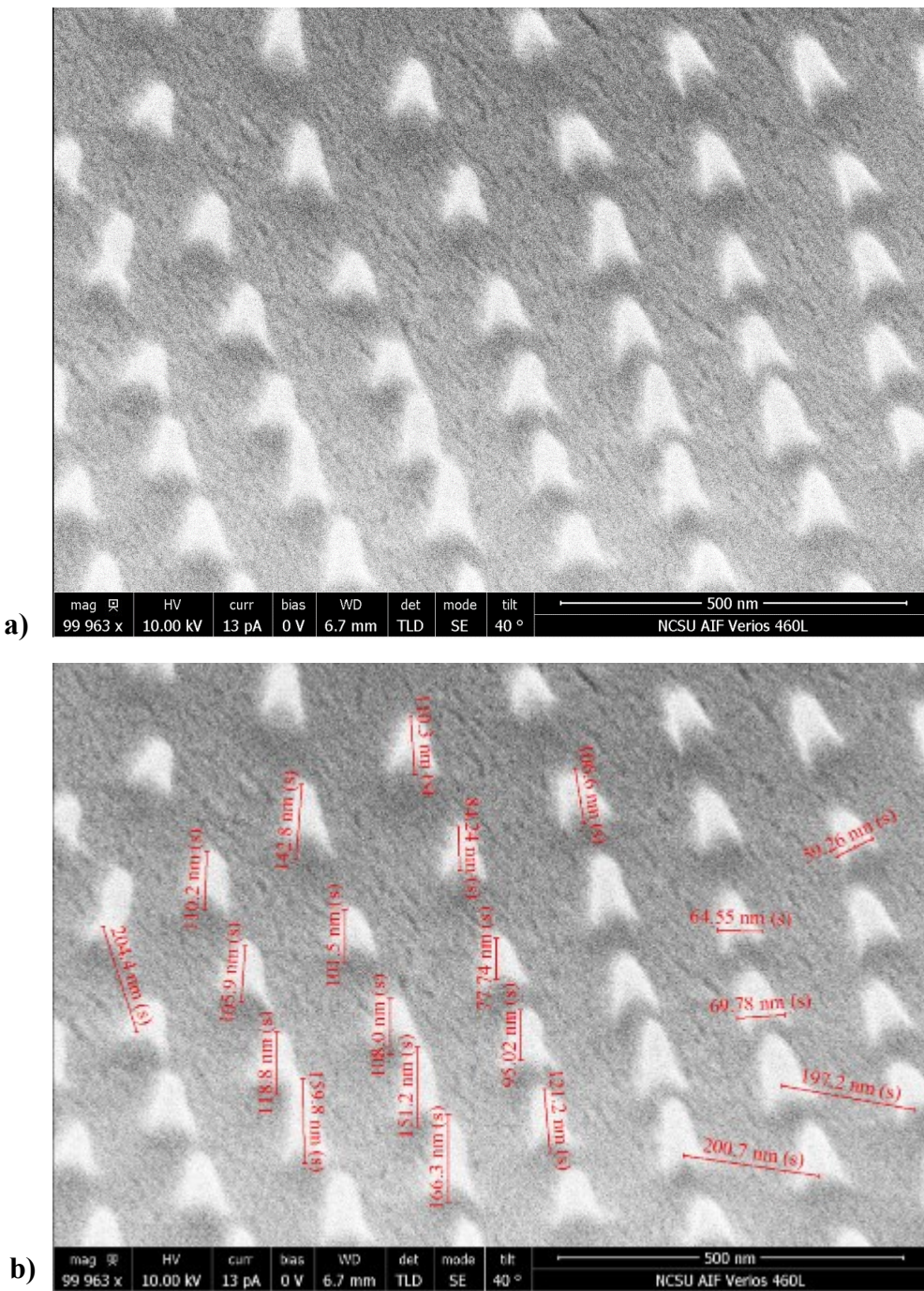


Figure 5-36: Different heat cure sample. This PDMS stamp did not have slight slope in the stamp as previous.

The UV cured glue showed better results with the next set of measurements as shown in Figure 5-37.

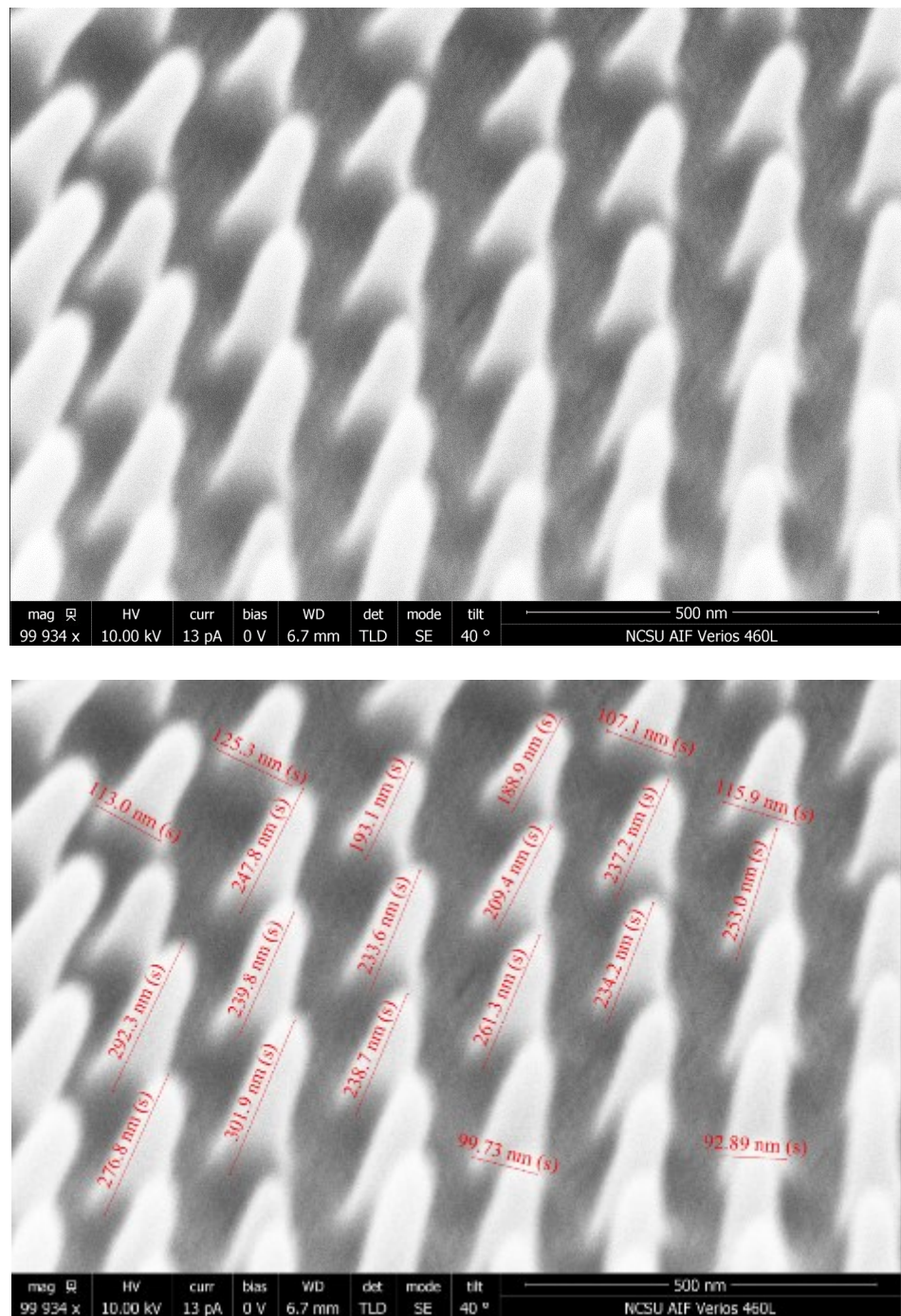


Figure 5-37: UV cure glue results were again not in the desired size range. Both a) and b) are the same image, but b) has measurements.

However, like the heat cure glue, the UV cure glue could show large scale uniformity as shown in Figure 5-38.

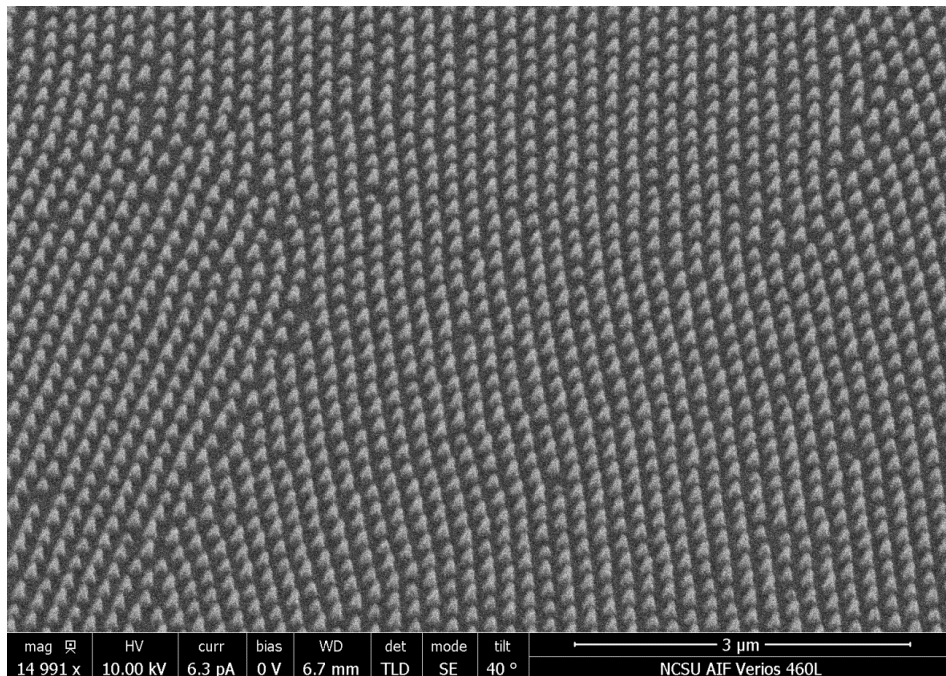


Figure 5-38: Large scale UV glue showed good uniformity.

Scanning electron microscope images needed to be collected within a prescribed about of time, otherwise the energy of the beam could impact the samples as shown in Figure 5-39.

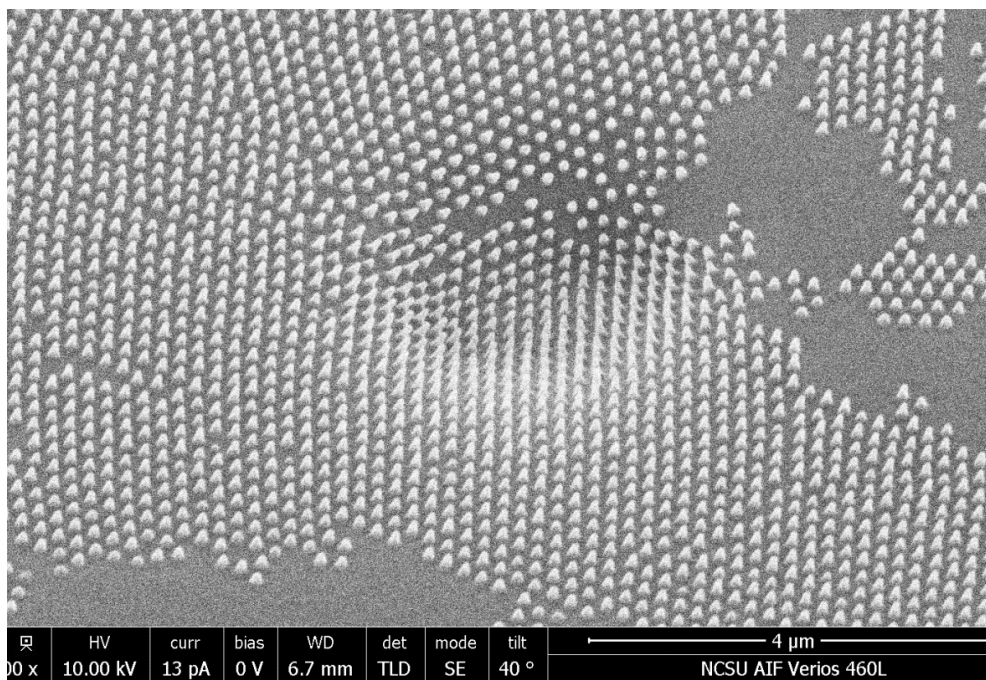


Figure 5-39: The scanning electron beam can wear down the epoxy samples over time if the beam is focused too long on a single area.

As the long term goal of this project was to make a medical device, medical epoxy was attempted as well and the results follow in Figure 5-40, Figure 5-41, and Figure 5-42.

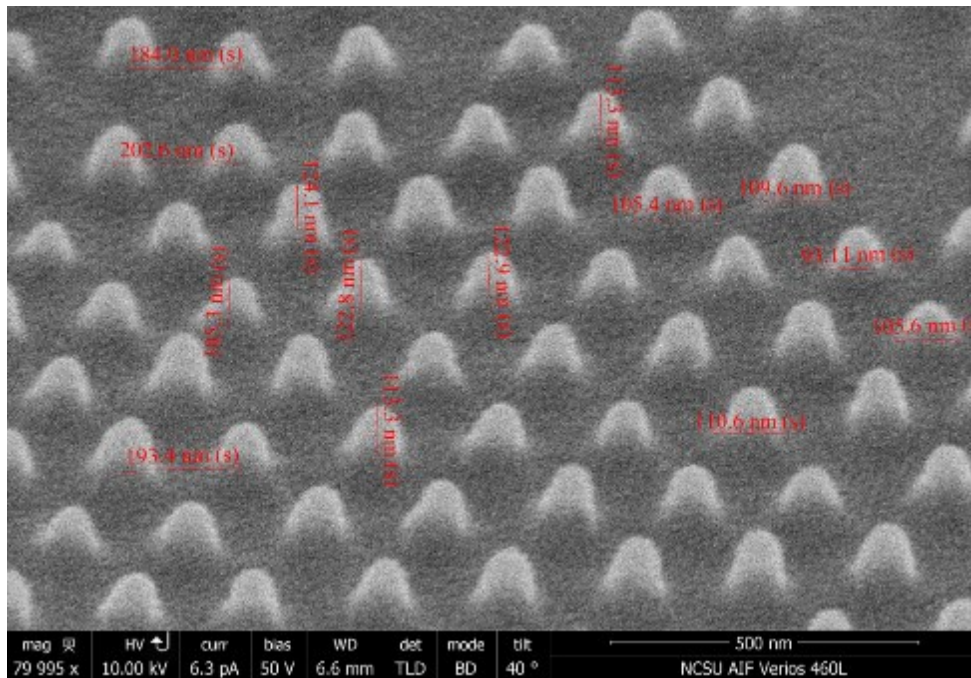


Figure 5-40: Medical epoxy nanostructure patterning were short as well.

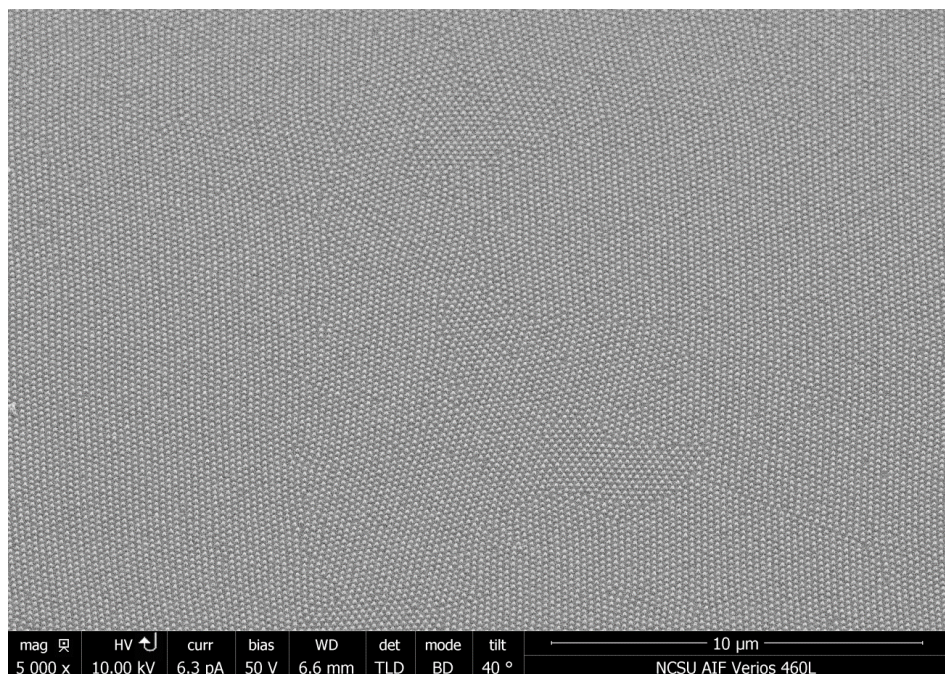


Figure 5-41: The medical epoxy large scale nanostructure patterning was uniform as seen with a tilt.

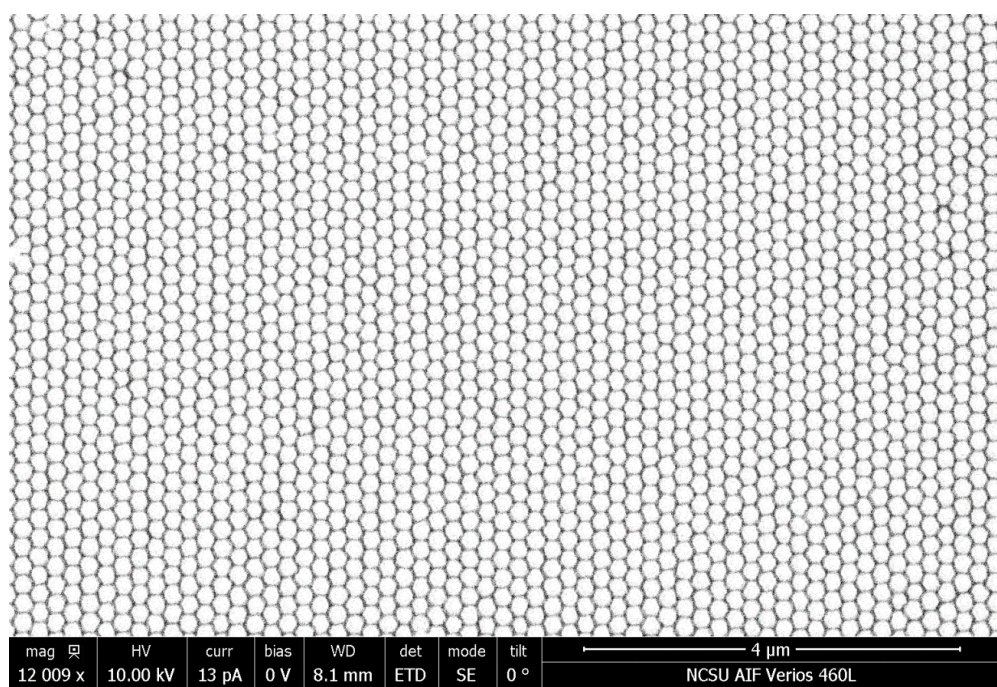


Figure 5-42: A closer look at the medical epoxy from above without a tilt shows nice feature spacing.

5.4 Patterning with Low Viscosity UV Curable Glue

Since the UV curable glue was giving the best results, it was decided to use it to further develop nanostructures with greater height.

The first item to be examined was if the mold looked like as it should. Under the scanning electron microscope the mold looked adequate and there was nothing unusual about it to cause the smaller than expected stature of the nanocones. The mold is shown in Figure 5-43.

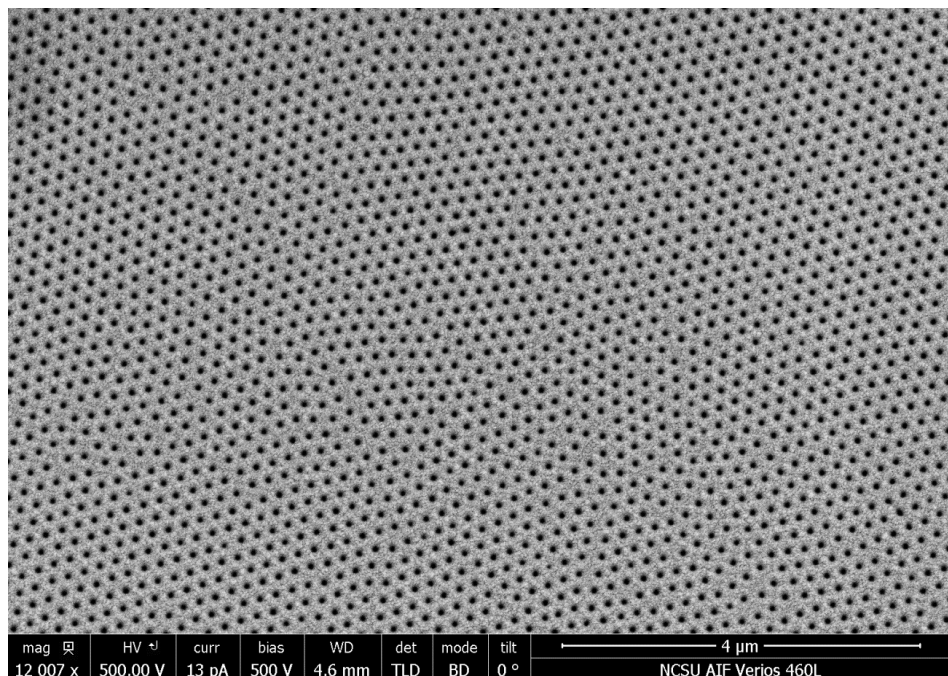


Figure 5-43: Large scale hole pattern in the PDMS stamp looked normal upon inspection.

Heat is known to make liquids flow more easily by lowering their viscosity, so the UV curable glue was heated and then the mold applied. The results are in Figure 5-44.

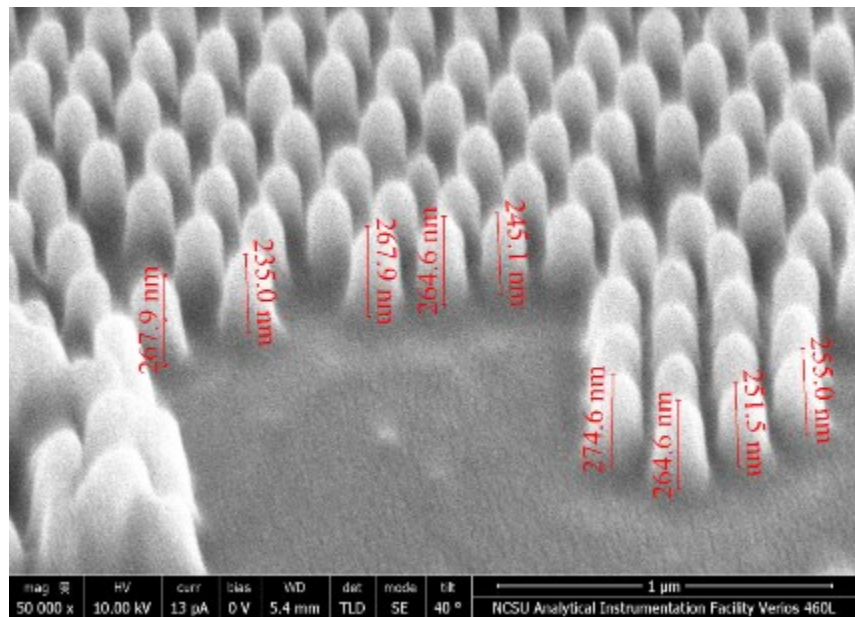


Figure 5-44: Results of UV glue that was heated before the mold was applied.

Air was thought to maybe create a layer on the bottom of the silicon substrate pattern that prevented the mold from going down into the patterned substrate. The next trial had the glue applied in a vacuum to prevent air from being an issue. The results are shown in Figure 5-45.

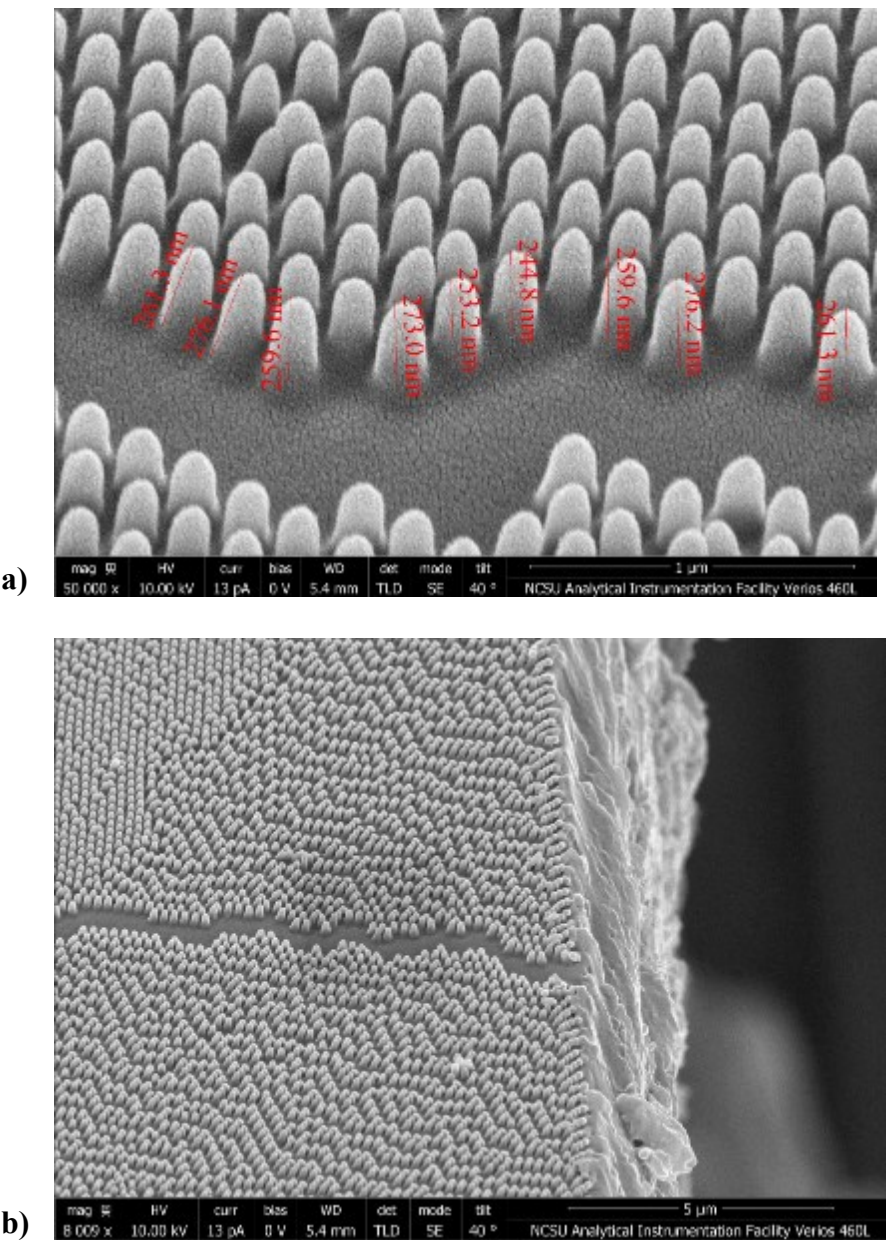


Figure 5-45: Results of UV glue applied in a vacuum. Long term b) ordering looked good , here seen at the edge of a sample where the sample was warped from the cutting pressure of a razor.

It was not clear if a longer pressure was needed to increase feature size to get the UV glue to go into the mold more effectively. It was investigated if a prolonged pressure for a minute helped make the glue go into the mold better to create taller features. The results can be seen in Figure 5-46.

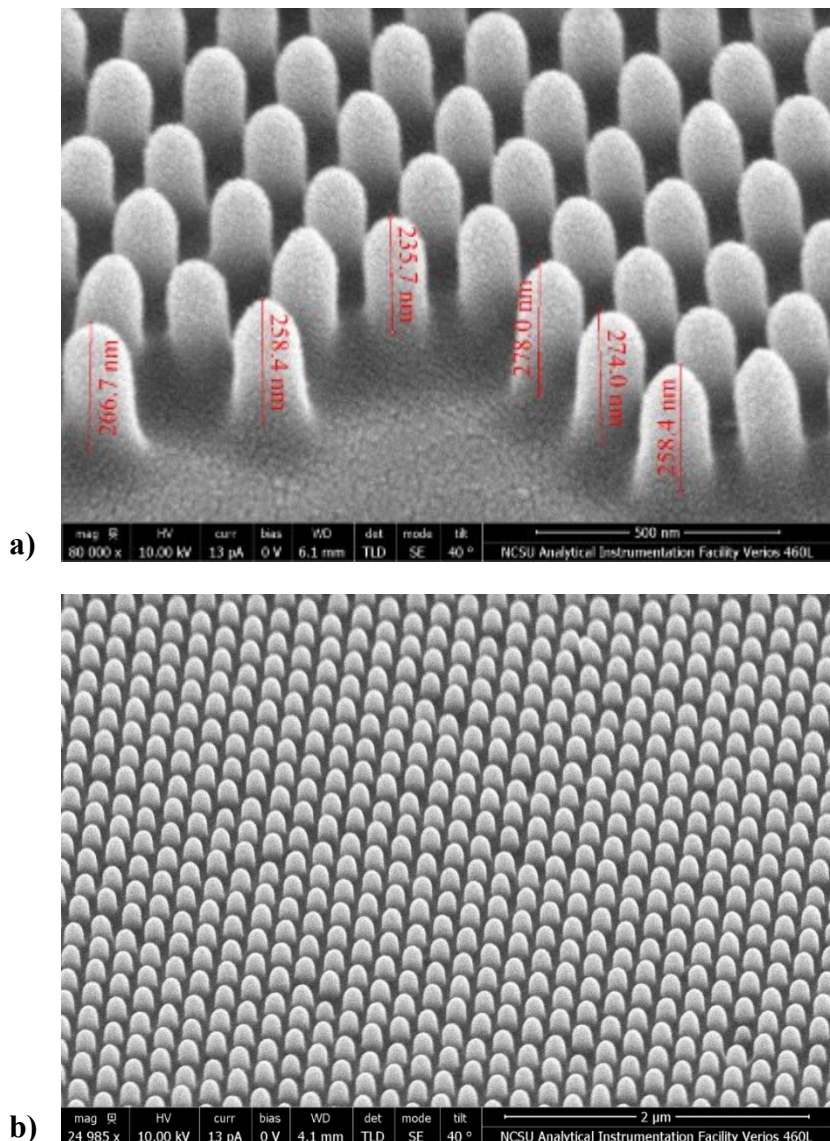


Figure 5-46: Samples of UV glue being pushed for 1 minute by the mold showed good feature form and long range order.

A summary of the methods and the results of the feature heights are given in Table 5-1 showing how the methods attempted still created features less tall than the original silicon by over 100 nm.

Table 5-1: Mold application technique and nanocone height

Method	Average Nanocone Height
UV glue hard press on stamp	263 nm
Hotplate heated UV glue	264 nm
UV glue applied in vacuum	264 nm
UV glue with one minute push on stamp	236 nm

It was difficult to determine why the features were not in the range of the etched silicon wafer nanocone heights. Some experiments were done to modify the creation of the PDMS mixture. The favorable consequence of this technique adjustment were features that were now in the 320-370 nm range and averaging 356 nm tall. This was the technique used going forward.

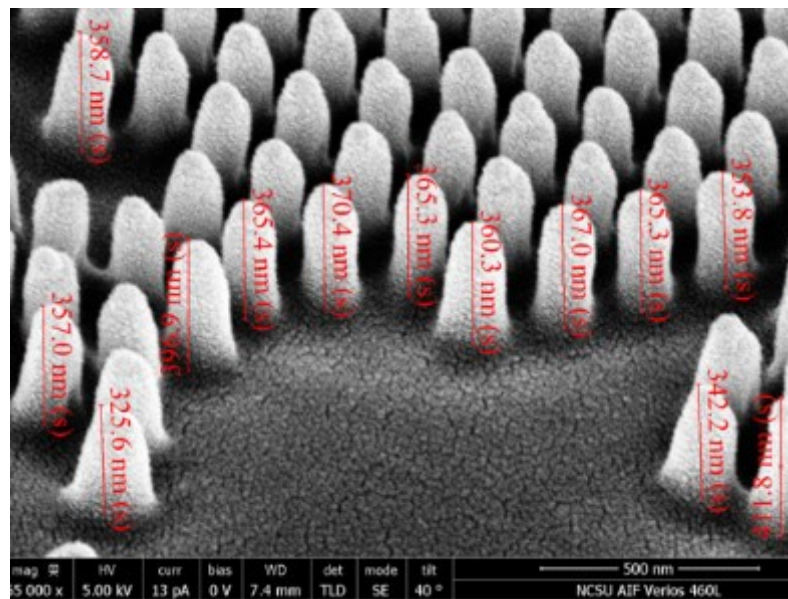


Figure 5-47: Modifying the mold making technique was advantageous for creating taller features.

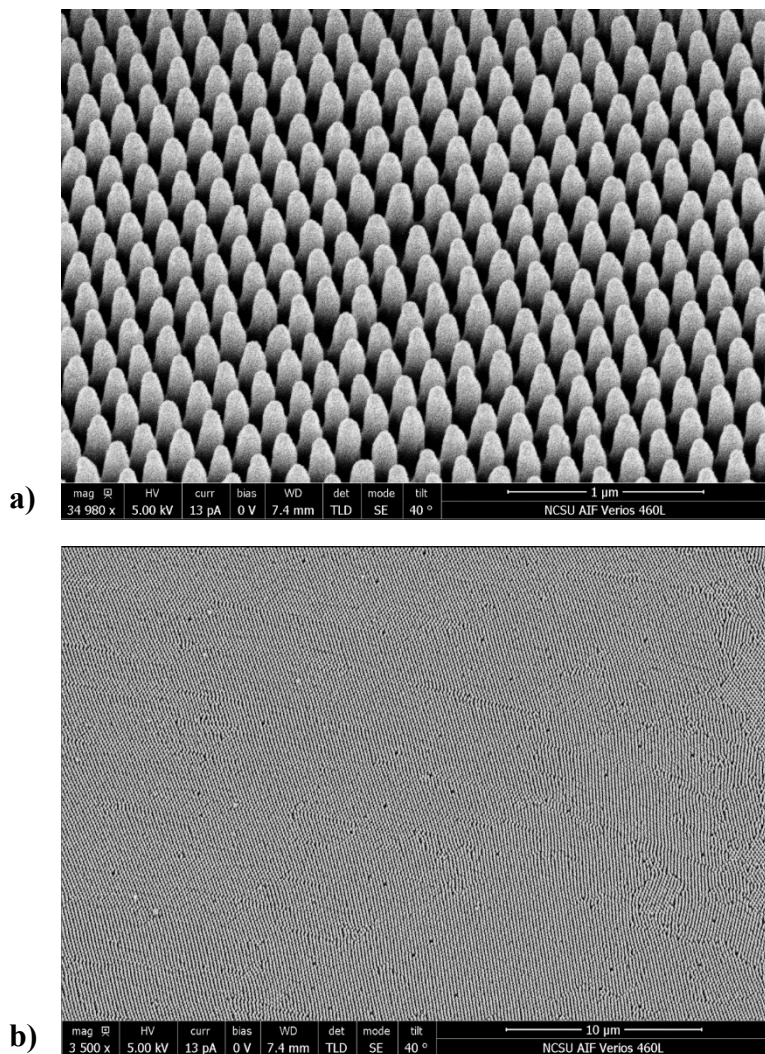


Figure 5-48: The taller structures were also close packed with good long range order.

5.5 Characterizing Nanostructures to Inorganic Devices

Characterizing the inorganic devices with nanostructures first began with making secure backing for the devices. The LEDs and photodiodes were soldered to wires and secured to one inch square glass slides to lie as flat with the glass as possible. The SiPMs were attached to circuit boards with a solder oven and wires connected afterwards. All devices were made as level as possible.

UV curable glue, NOA 61, was put on the surface of the optoelectronic device. Then a sliced sections of the PDMS mold was put on top of the device. For this step it was help to make the mold as thin as possible. The mold was usually approximately 4 mm thick and needed to be shaved down to be in the range of about 1.5 mm thick as shown in Figure 5-49.

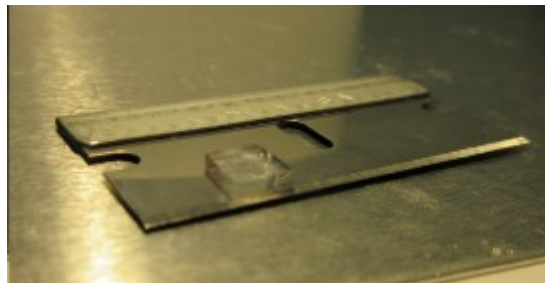


Figure 5-49: Cutting the molds for nanoimprint lithography required the mold to be cut to be approximately 1.5 mm thicker. If it was much thicker, there was a chance the UV glue would not cure since the PDMS could absorb some of the light.

By making the mold this thin, the UV glue could cure in 3 hours in the UV lightbox. If the mold was much thicker there was a chance that the ultraviolet light would be absorbed by the PDMS, preventing full curing of the glue and also causing the mold to be ripped upon removal. This bilayer mold has its chemicals and fabrication explained in the later section “Biomimetic Nanostructure Fabrication to Increase Light Transmission Efficiency in Optoelectronic Devices”.

In this way, the nanostructures were transferred to 631 nm LEDs (LTST-C230KRKT, Lite-On Inc., Tapei, Taiwan), photodiodes c and silicon photomultipliers (SiPMs, sensL MicroFC-30035). The light detectors were characterized in the setup of Figure 5-50.

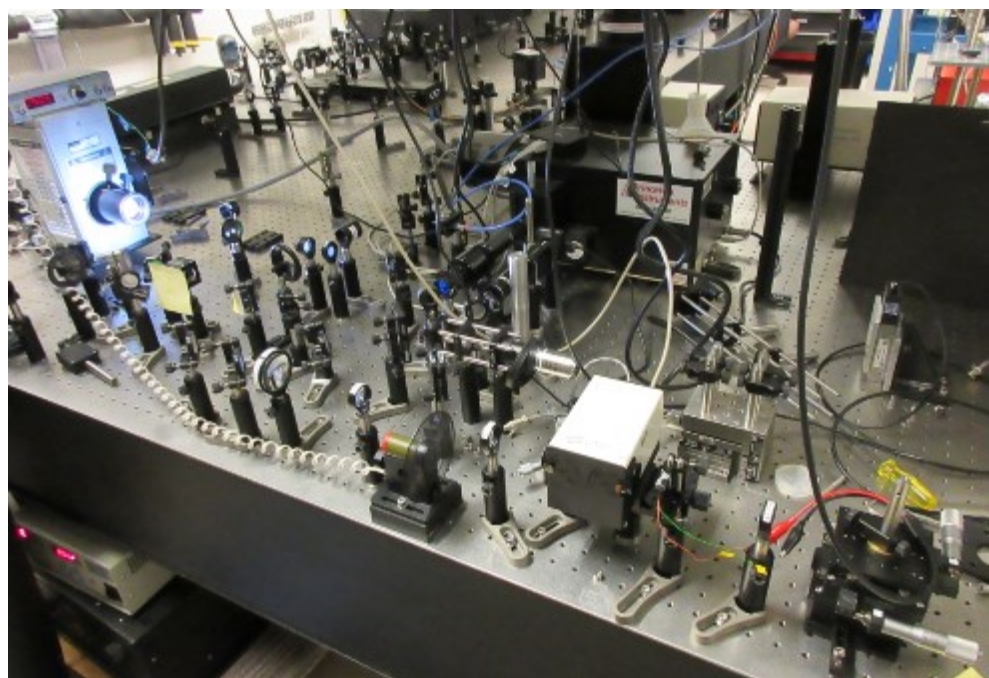


Figure 5-50: Xenon lamp source, Digikrom monochromator and platform for characterizing the photodiode and SiPM detectors.

The response for patterned versus unpatterned photodiodes can be seen in Figure 5-51.

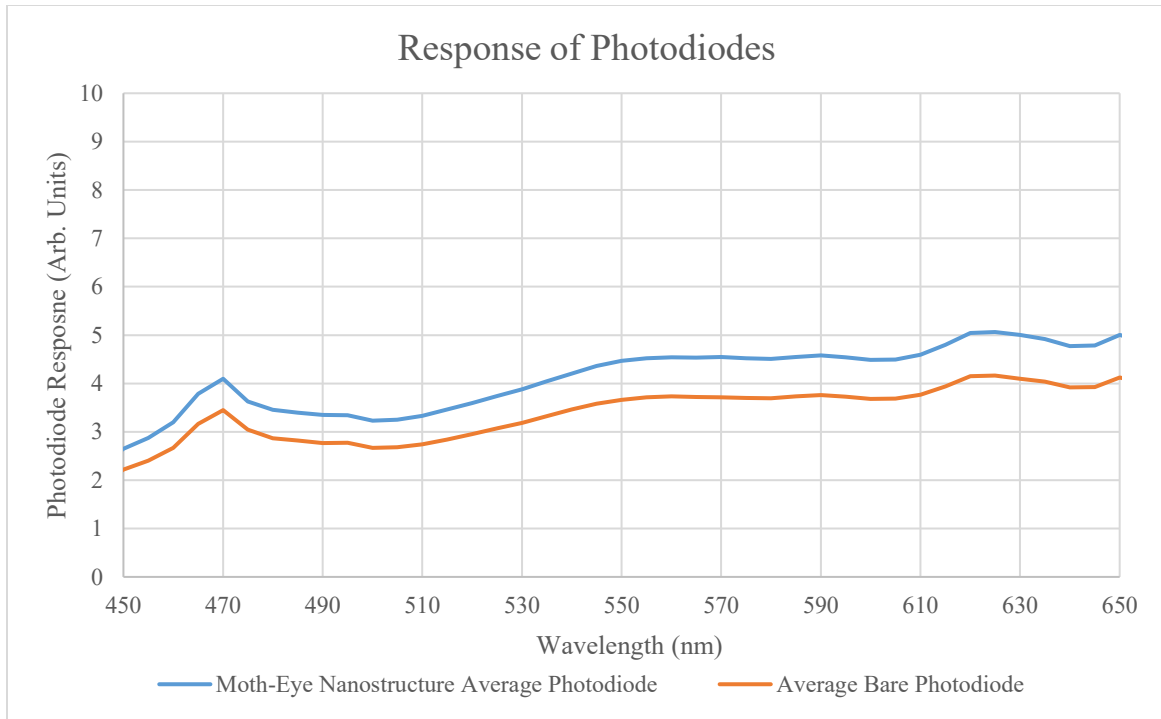


Figure 5-51: Photodiode response with and without nanostructures from 450 nm to 650 nm.

It is clear that the nanostructures aid in the absorption of light and the response of the photodiode from 450 nm to 650 nm.

Table 5-2: Photodiode (PD) gain based on wavelength.

λ (nm)	500	520	530	540	580	600	620	630	640	650
Moth Eye Nanostructure PD	3.23	3.59	3.88	4.21	4.51	4.49	5.04	5.00	4.77	5.01
Unpatterned Bare PD	2.67	2.95	3.19	3.46	3.70	3.68	4.15	4.10	3.92	4.12
Percent Increase (given λ)	20.89	21.67	21.78	21.53	22.00	21.89	21.49	22.03	21.91	21.42
Average Percent Gain (select λ above) = 21.66										
Average Percent Gain (450 to 650 nm at 5 nm steps) = 21.31										

For select wavelengths and across the 450 to 650 nm, the average percent increase for the photodiode response was over 21% as shown in Table 5-2 .

An expanded spectrum for the photodiode response of additional wavelengths are seen in Figure 5-52.

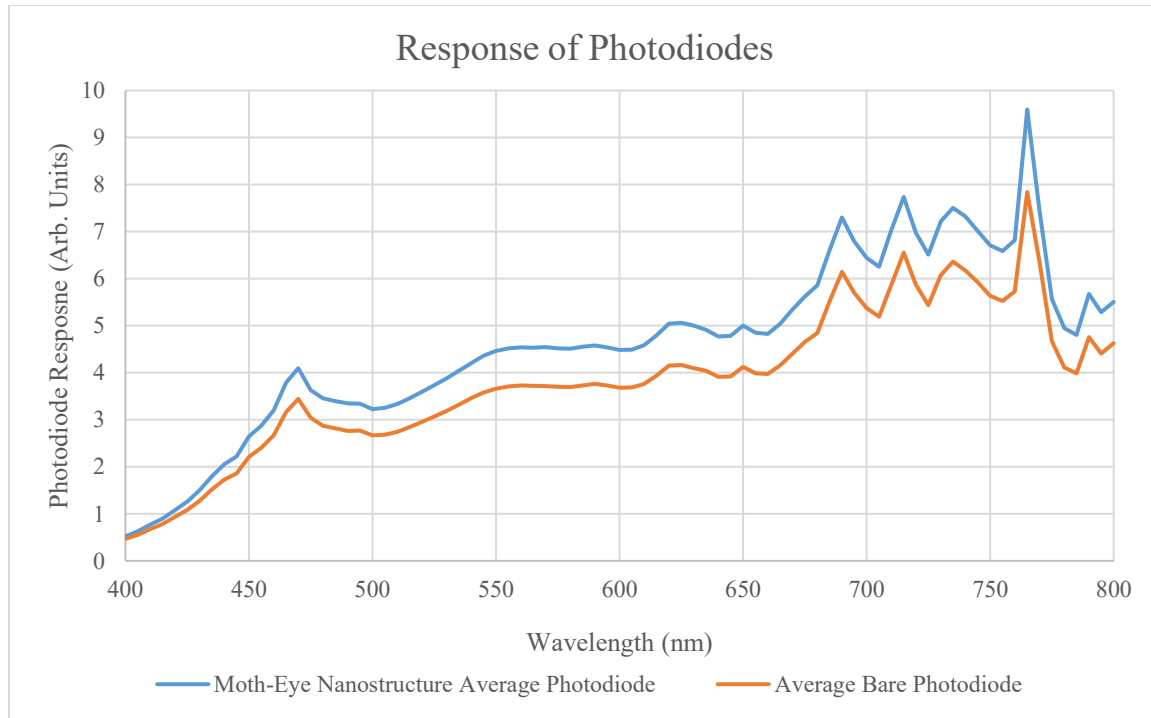


Figure 5-52: Photodiode response with and without nanostructures from 400 nm to 800 nm.

The response of the SiPMs were also compared with and without nanostructures. The enhanced output can be seen in Figure 5-53.

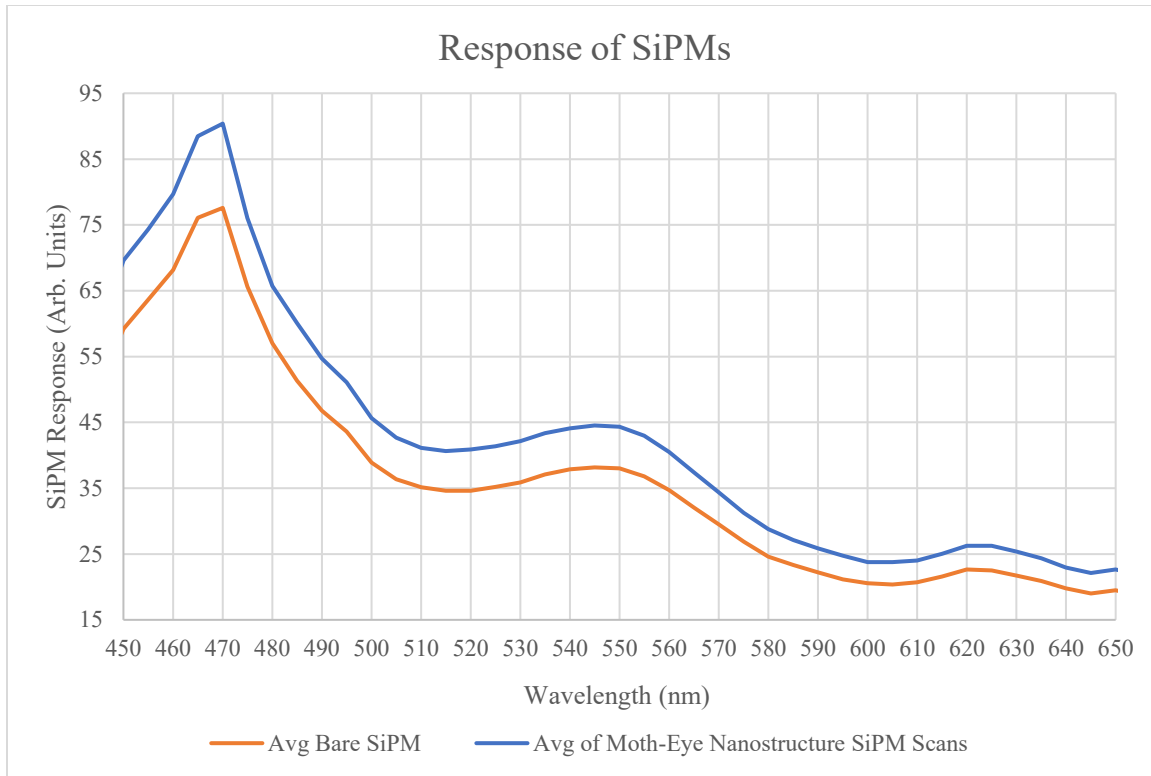


Figure 5-53: SiPM response with and without nanostructures from 450 nm to 650 nm.

For select wavelengths and across the 450 to 650 nm, the average percent increase for the SiPM response was over 16% as shown in Table 5-3.

Table 5-3: SiPM gain based on wavelength.

λ (nm)	500	520	530	540	580	600	620	630	640	650
Moth Eye Nanostructure SiPM	45.64	40.87	42.13	44.09	28.76	23.80	26.24	25.37	22.94	22.65
Unpatterned Bare SiPM	38.88	34.62	35.89	37.86	24.62	20.57	22.64	21.72	19.77	19.48
Percent Increase (given λ)	17.38	18.05	17.38	16.44	16.79	15.66	15.87	16.83	16.07	16.26
Average Percent Gain (select λ above) =	16.67									
Average Percent Gain (450 to 650 nm at 5 nm steps) =	16.67									

An expanded spectrum for the photodiode response of additional wavelengths are seen in Figure 5-54.

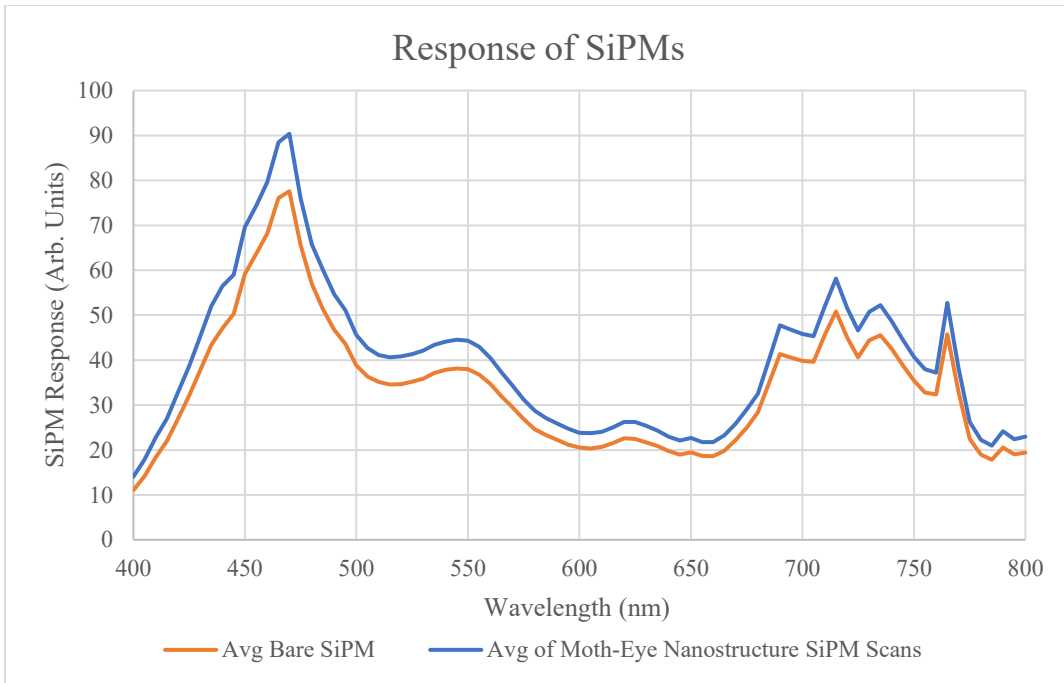


Figure 5-54: SiPM response with and without nanostructures from 400 nm to 800 nm.

Next, the patterned and unpatterned LEDs were characterized with the use of an integrating sphere (IS6, Stellarnet) and spectrometer as shown in Figure 5-55.

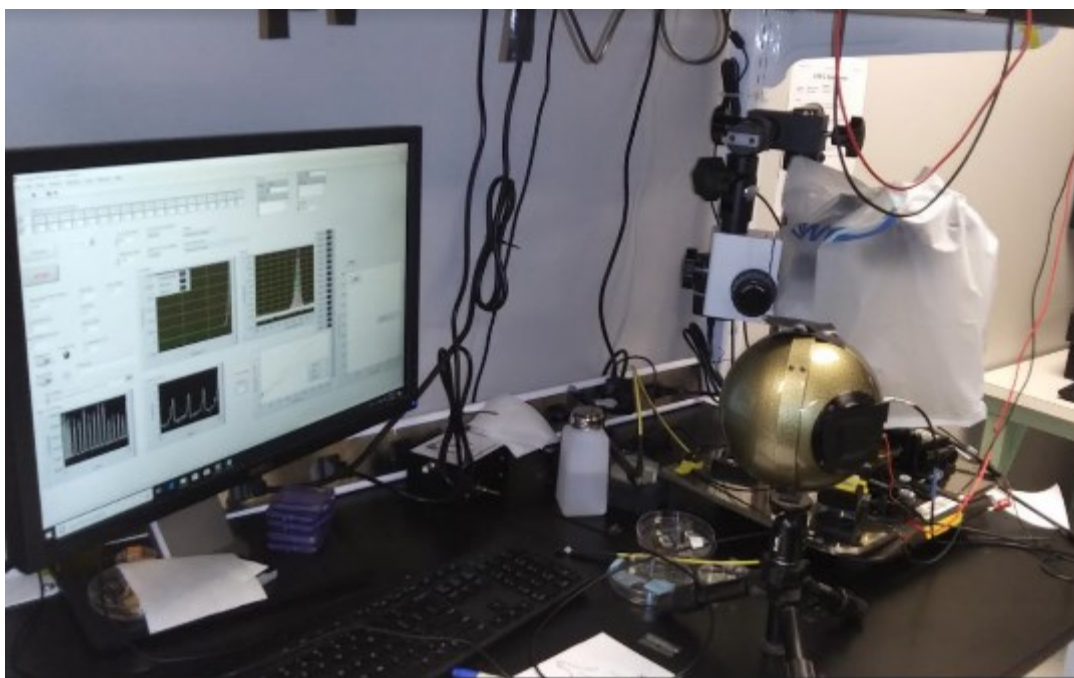


Figure 5-55: A StellarNet integrating sphere setup with ASEQ spectrometer for LED characterization.

Figure 5-56 shows that with the nanostructures, there was a peak increase with the presence of the nanostructures. The output peak went from $0.0338 \mu\text{W}/\text{cm}^2$ to $0.0209 \mu\text{W}/\text{cm}^2$, an approximate 61% increase.

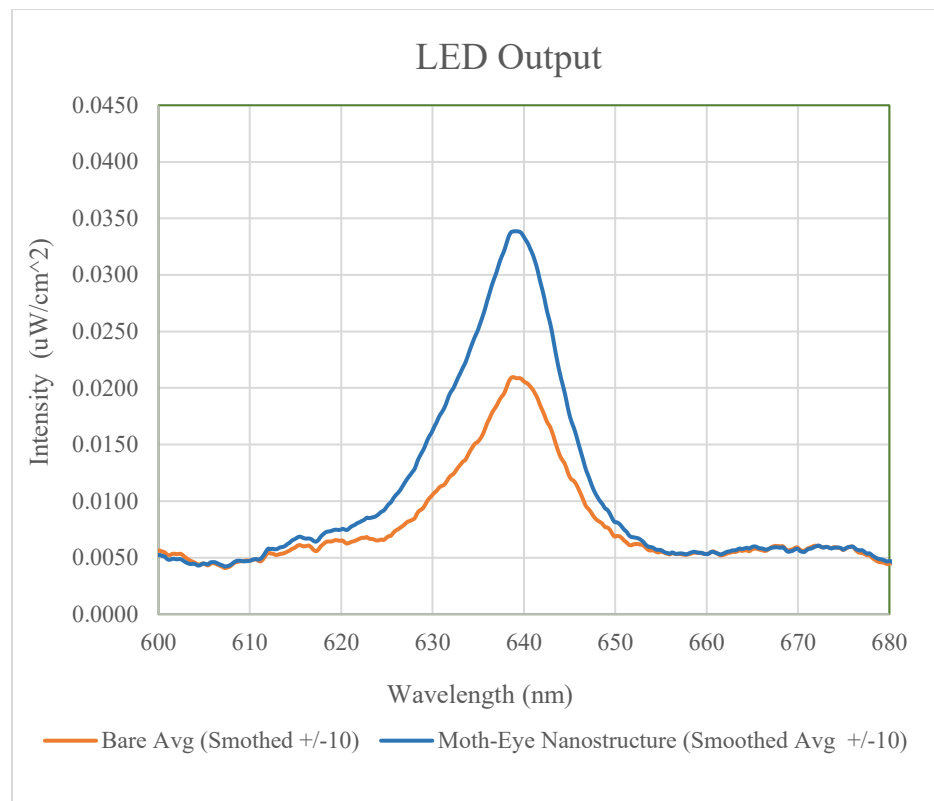


Figure 5-56: LED output with and without nanostructures.

5.6 Biomimetic Nanostructure Fabrication to Increase Light Transmission Efficiency in Optoelectronic Devices

© 2019 IEEE. Reprinted (adapted), with permission, P. Sotory and A. Bozkurt, "Biomimetic Nanostructure Fabrication to Increase Light Transmission Efficiency in Optoelectronic Devices," 2019 IEEE SENSORS, Montreal, QC, Canada, 2019, pp. 1-4, doi: 10.1109/SENSORS43011.2019.8956604.

In reference to IEEE copyrighted material which is used with permission in this thesis, the IEEE does not endorse any of North Carolina State University's or University of North Carolina Chapel Hill's products or services. Internal or personal use of this material is permitted. If interested in reprinting/republishing IEEE copyrighted material for advertising or promotional purposes or for creating new collective works for resale or redistribution, please go to http://www.ieee.org/publications_standards/publications/rights/rights_link.html to learn how to obtain a License from RightsLink.

5.6.1 Polystyrene Mask on Silicon Substrate Preparation

The fabrication began by dicing silicon <100> wafers (University Wafer Inc., Boston, MA, USA) into approximately 1.5 cm by 2 cm rectangles. Along with a glass slide, these silicon substrates were ultrasonically cleaned in baths of acetone, isopropyl alcohol and deionized water for 10 minutes each to clean them and increase their hydrophilicity. This was followed by approximately 30 minutes of ultraviolet-ozone (UVO) cleaning (Model 342 from Jelight Company Inc, Irvine, CA, USA) for these items. A solution was then made of 330 µL of 200 nm polystyrene nanospheres (Bang Laboratories, Fishers, IN, USA), 633 µL ethanol (Sigma-Aldrich Corporation, St. Louis, MO, USA) and 633 µL deionized water inside of an Eppendorf tube. This was set floating in a water bath while being ultrasonicated.

Deionized water was then used to fill a rectangular dish deep enough to completely immerse the 2 cm long silicon substrate. At the end of the dish, one of the cleaned silicon substrates was immersed underwater and suspended vertically while connected to a cantilever arm attached to a syringe pump as shown in Figure 5-57a.

When the ultrasonication of the Eppendorf tube solution was completed, the contents of the tube were transferred to a syringe. The aforementioned cleaned glass slide was placed at an angle with the water surface at the opposite end from the submerged silicon piece. The syringe solution was slowly drip-cast onto the angled slide and allowed to spread down the slide onto the surface of the deionized water. A 5% solution of sodium dodecyl sulfate (purchased from Sigma-Aldrich Corporation, St. Louis, MO, USA) was then delivered with a dropper which compressed the random dispersion of nanospheres, as shown in Figure 5-57d, into a close-packed self-assembled monolayer colloidal crystal, as shown in Figure 5-57e, on the water surface. The syringe pump was then activated to slowly bring the submerged silicon substrate upwards as shown in Figure 5-57 a-c. The sodium dodecyl sulfate provides a pressure on the nanospheres that causes the colloidal crystal to be deposited on the emerging silicon substrate. Essentially this is a kind of Langmuir-Blodgett dip coating method [49]. Once fully withdrawn, the silicon is covered with an highly ordered array of polystyrene nanospheres, as shown in Figure 5-57f. The substrates were then removed from the syringe pump and allowed to air dry at a 45 degree angle for 10 minutes.

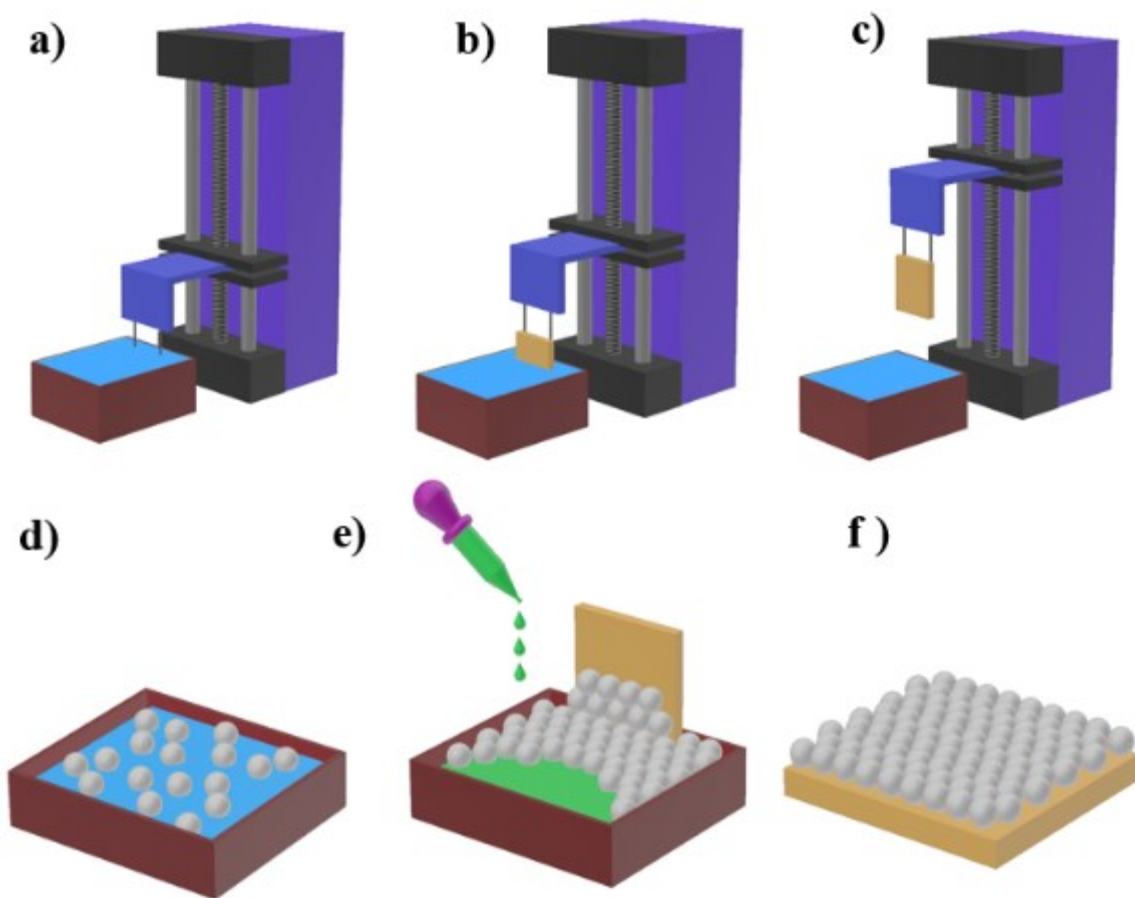


Figure 5-57: A schematic illustration (a-c) showing the syringe pump with the cantilever arm slowly lifting the silicon substrate out of the water with the polystyrene nanosphere monolayer. d) The nanospheres are initially distributed across the water surface in an unordered monolayer. e) A dropper introduces a 5% solution of sodium dodecyl sulfate (SDS) that compacts the monolayer to form a highly ordered colloidal crystal that is deposited on the silicon while it is withdrawn from the water. f) The silicon becomes covered with the polystyrene nanosphere monolayer and set aside to dry.

5.6.2 Reactive Ion Etching, Mold Casting, and Pattern Transfer

Several steps of reactive ion etching (RIE) were next used to pattern the silicon as shown in Figure 5-58. First, the close-packed polystyrene nanosphere templates were exposed to oxygen plasma to reduce their diameter with an Oxford Plasmalab 100 Inductively Coupled Plasma (ICP) Etcher. The oxygen etch RF power was 30 W, ICP Power of 500 W, with a gas flow of 20 sccm, at a 50 mTorr base pressure, with an etch time of 90 seconds. This was followed by a chlorine gas etch to pattern the silicon using the reduced diameter polystyrene

spheres as a mask. The RF power was 90 W, ICP Power 500W, with a gas flow of 50 sccm, base pressure of 50 mTorr, with an etch time of 11 minutes. This was followed by another oxygen etch to remove any remaining traces of polystyrene. This final etch had an RF power of 200 W, ICP Power of 1000W, a gas flow of 50 sccm, a base pressure of 50 mTorr, with an etch time of 3 minutes.

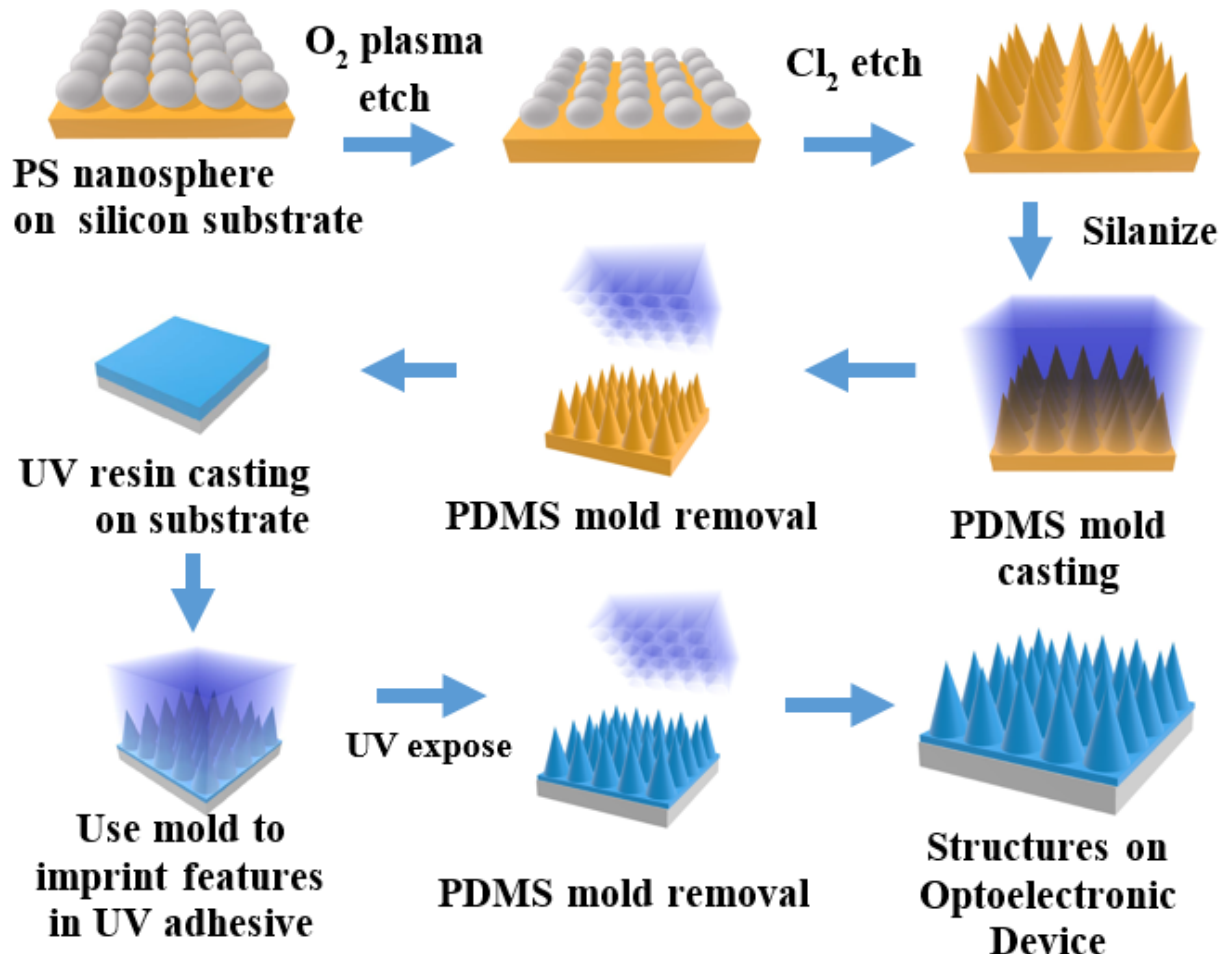


Figure 5-58: Steps to fabricate the moth-eye like structure include a polystyrene (PS) mask deposition on silicon, reactive ion etching (RIE), mold making, and stamping the pattern into UV curable adhesive on an optoelectronic device.

The next step was to silanize the silicon surface to make it non-adhering. This was done by placing a glass petri dish with several drops of (tridecafluoro-1,1,2,2-tetrahydrooctyl) trichlorosilane (Gelest, Inc., Morrisville, PA, USA) in a vacuum chamber along with the silicon

substrate set away from the petri dish. The vacuum was maintained for approximately half an hour to give the silane in the petri dish time to evaporate and coat the sample via siloxane bonding. The surface was then ready to be used for mold making to transfer the etched silicon pattern to the desired substrate.

The mold making process started with creating a bilayer mold composed of a hard polydimethylsiloxane (PDMS), h-PDMS, and soft-PDMS, s-PDMS, layer. The h-PDMS was made by mixing the co-polymers 25%-35% methylhydro-siloxane-dimethylsiloxane (HMS-301, Gelest, Inc., Morrisville, PA, USA) and 7-8% vinylmethylsiloxane-dimethylsiloxane (VDT-731, Gelest, Inc., Morrisville, PA, USA). Added to this mixture was 1,3,5,7 tetravinyl 1,3,5,7- tetramethylcyclotetra-siloxane and platinum-divinyltetramethyldisiloxane complex (Gelest, Inc., Morrisville, PA, USA).

The combination was then spin-coated onto the silanized silicon and allowed to cure a sufficient amount of time. The sample was then put in a petri dish and had Sylgard 184 (Dow Inc, Midland, MI) dispensed on it and oven cured. This bilayer PDMS was later diced into stamps to imprint the pattern into an ultraviolet curable adhesive (NOA61 purchased from Norland Product, Cranbury, NJ, USA).

5.6.3 Nanostructure Characterization

To evaluate the nanostructures created by the described imprinting process, the PDMS molds were diced into small square stamps a few millimeters in size. Optical adhesive was dispensed on piece of flexible plastic polypropylene sheet (the transparency sheet typically used for laser copiers). The diced PDMS stamp then had its patterned side pushed into the glue and allowed to cure under an ultraviolet lamp.

After curing, the stamp was removed, and the patterned area in the glue was cut out with a razor and prepared for examination with a FEI Verios 460L (Thermo Fisher Scientific,

Waltham, MA, USA) scanning electron microscope (SEM) to determine the height, width and period of the moth-eye like nanostructures.

The obtained results are presented in Table 5-4. Examples of the nanostructures and their long range ordering as acquired in the SEM can be seen in Figure 5-59.

5.6.4 Electrical and Coupling Characterization

The coupling test was done by using commercially available 631 nm LEDs (LTST-C230KRKT, Lite-On Inc., Tapei, Taiwan) and photodiodes (QSB34CGR, ON Semiconductor, Phoenix, AZ). We modified the surface of these by adding the nanostructures in optical adhesive as described earlier.

The coupling was assessed and compared by measuring the current generated by the photodiode when illuminated by the LED. The two devices were placed approximately 5 cm apart facing one another inside an optically insulated enclosure. Different pairs of devices were examined. The pairs were either a) bare with no modification of their surfaces, b) had the moth-eye like nanostructures fabricated on them in optical adhesive, or c) had a thin layer of optical adhesive not patterned but pressed flat with an unpatterned piece of PDMS as a control to assess the effect of nanopatterning. This last case was to illustrate that the glue alone did not have a coupling enhancing property.

In this set up the LED was made to illuminate with the application of a 4 Hz 1.76 V square wave signal by using a function generator (33250A, Agilent Technologies, Santa Clara, CA, USA). The resulting photodiode currents were measured with a precision source / measure unit (SMU) (B2902A, Agilent Technologies, Santa Clara, CA, USA). The averaged peak current results of the SMU measurements of the photodiode output for the different conditions can be seen in Table 5-5.

Table 5-4: Nanostructure measurements

	N	Mean (nm)	Standard Dev.
Height	84	356	17.6
Width	17	151	10.3
Period	14	198	5.1

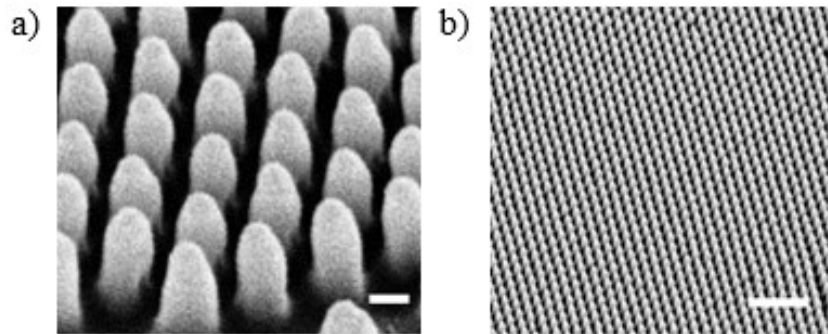


Figure 5-59: Examples of the a) biomimetic moth-eye nanostructures (scale bar 100 nm) and b) their long range order (scale bar 1 micron) as fabricated in optical adhesive.

Table 5-5: Coupling Results Under different Conditions

Pair Type	N (device pairs)	Photodiode Mean Current (nA)	Standard Dev.	Percent Difference Relative to Bare Device Pair
Bare LED/PD	3	15.9	0.3	-
Flat Glue on LED/PD	2	14.6	-	-7.7%
Moth-Eye Patterned on LED/PD	3	19.3	3.5	+21.4%

The results indicated that there was a stronger coupling with the moth-eye mimicking nanostructures being present on the devices. We observed that the flat glue condition without the nanopatterning actually degraded the coupling because it introduces a layer that can reflect or absorb some of the light.

5.7 Results for Simulated and Actual PPG Measurements

5.7.1 Simulated PPG Measurement and Coupling

Measuring the coupling of the surface modified devices versus unmodified surface devices were done with a phantom finger (FingerSim, BC Biomedical, 97% SPO₂) and a human finger.

Each method had the devices mounted on glass plates which were subsequently mounted on 3D printed plastic holders. The glass plate part was covered in black electrical tape to prevent interaction with light. The 3D printed plastic holders were designed to be versatile and be able to accommodate both inorganic and organic devices testing on phantom and real fingers. The devices had locations where they could be mounted either approximately 8 mm or 5 mm from the surface and be used for either transmission or reflectance mode PPG or pulse oximetry operation. For these experiments, the devices were mounted 8 mm from the surface of the phantom finger.

This distance was incorporated into the holder design because during the course of this work the graph in Figure 5-60 was found, which indicates the residue of a human finger may hamper the transmission through a nanostructured surface and needs to be cleaned off after being touched. It was unclear if the UV resin on the devices with the nanostructures on them could be cleaned without damage. For this reason, it was judged best to introduce a non-contact test. This still maintains the concept that air can be between the device and the skin either from the skin not being a smooth surface or due to the intentional design of some optoelectronic devices with air under the device.

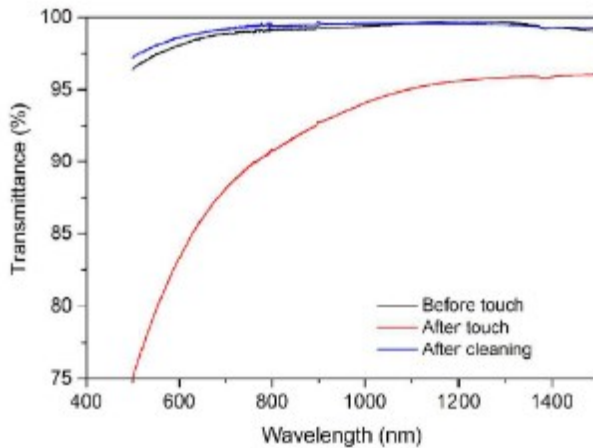


Figure 5-60: During the course of this work, it was found that fingerprint residue can have an effect and as a result, the non-contact holders were designed and 3D printed [92]. Reprinted with permission from "Nanostructured Stealth Surfaces for Visible and Near-Infrared Light", Ref [92], retrieved from <https://pubs.acs.org/doi/abs/10.1021/acs.nanolett.6b03308>, © 2016 American Chemical Society. Further permissions related to this excerpted material should be directed to the American Chemical Society.

The inorganic devices were mounted on the holders and then tested in pairs in transmission mode on either side of the finger. Figure 5-61 illustrates the setup.

For the phantom finger, the pair of devices and phantom finger were placed on a mount inside an optically isolated metal enclosure which also helped reduced the electrical noise and interference of the testing environment. A simulated PPG signal was programmed into the Agilent 33250A Signal Generator and fed into the LED with a peak voltage of 2.2 V at 1 Hz.

The photodiode (PD) was connected to the Agilent B2902A Precision Source / Measure Unit (SMU) and the current was measured with the Keysight software.

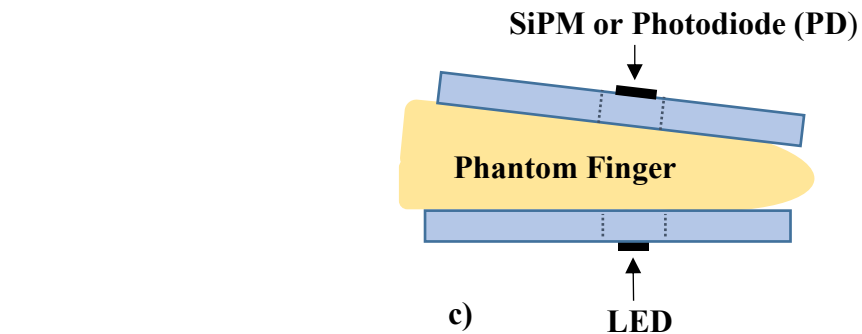
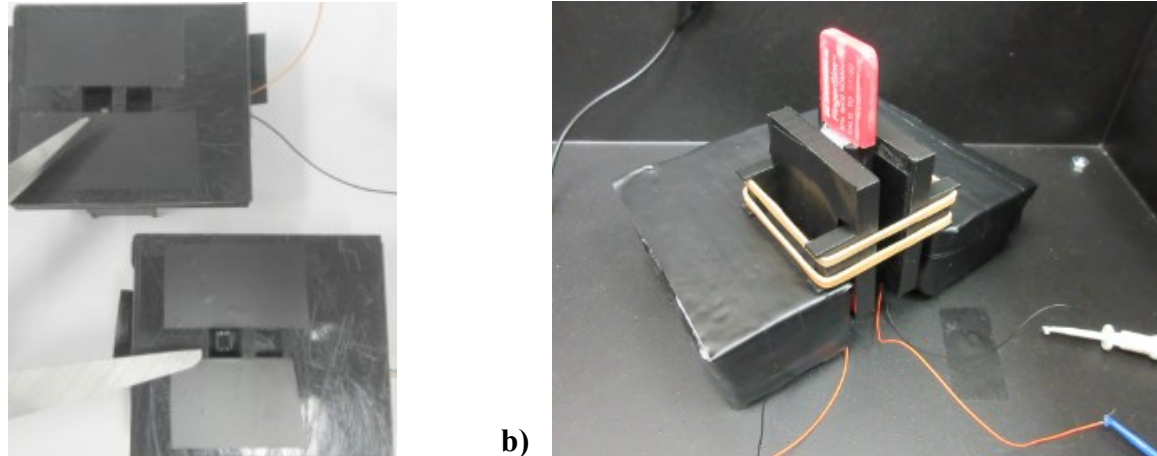


Figure 5-61: The patterned and unpatterned a) devices were each mounted in their individual 3D printed holders. The b) phantom finger was placed between two device holders inside of an enclosure. An c) illustration showing how the device holders held the devices.

The signal output was recorded and compared between device pairs. The device pairs were moth-eye LED and moth-eye photodiode, moth-eye LED and bare PD, bare LED and moth-eye PD, and bare LED and bare photodiode. The first device pairs examined were the LED and photodiode sets.

The results for the photodiode current for the different pairings are shown in Figure 5-62.

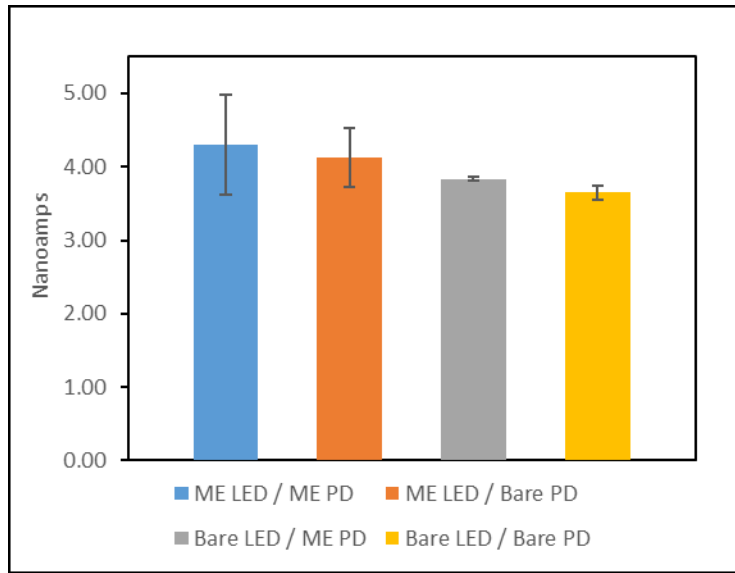


Figure 5-62: Comparison of LED-PD (photodiode) coupling produced from combinations of moth-eye (ME) patterned and unpatterned (bare) LED and PD.

In Figure 5-62 it can be seen that the highest current produced was when the pair of devices were both patterned with the nanostructures. This increased coupling is due to the improved outcoupling of light from the LED and incoupling into the photodiode creating an overall larger electrical coupling effect.

To further investigate how the coupling varied with the pairing combination, the maximum values of the resulting PPG photocurrent were compared in relation to each other and are shown in Table 5-6.

Table 5-6: LED – Photodiode Nanoamp (nA) Coupling for Simulated PPG

	Average Maximum Photodiode Current (nA)	Percent Increase from Bare/Bare
ME LED / ME PD	4.30	18
ME LED / Bare PD	4.13	13.3
Bare LED / ME PD	3.83	5.1
Bare LED / Bare PD	3.65	-

The corresponding normalized PPG photocurrent response scaled to the maximum value and percentages found in Table 5-6 can be seen in Figure 5-63.

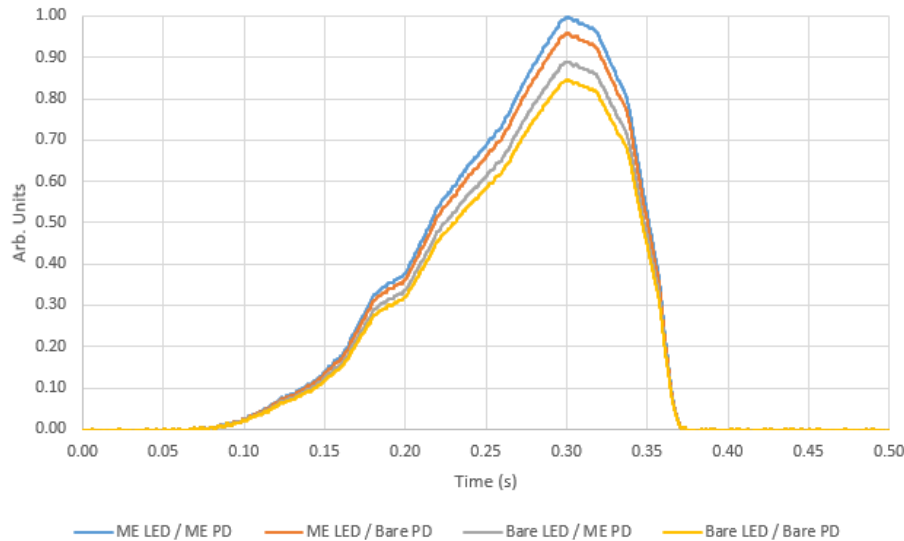


Figure 5-63: A normalized photodiode current response from a simulated PPG for patterned and bare LED/PD combinations scaled to the results from Table 5-6.

Besides Table 5-6 indicating how a pair of patterned devices produce more current than a pair of unpatterned devices, the intermediate combinations of a single patterned devices matched with unpatterned devices were also examined. In these cases, it was found that the moth-eye patterned LED and bare photodiode pair, produced a stronger coupling than the bare LED and the moth-eye patterned photodiode. This can be interpreted as the moth-eye pattern has having a more significant effect on the LED than on photodiode. When the percent increase is added from these two scenarios (5% and 13.3%), it approximately equals the percent increase seen by the ME/ME combination (18%) over the bare/bare combination.

An identical set of simulated PPG experiments were also done with combinations of patterned and unpatterned LEDs and silicon photomultipliers (SiPM).

The PPG signal that was programmed into the Agilent 33250A Signal Generator was used to drive the LED with a peak voltage of 2.2 V at 1 Hz.

Unlike the photodiode, where the light detector device could be directly connected to the Agilent B2902A Precision Source / Measure Unit (SMU), the operation of the SiPM

required a different arrangement. Here the SiPM was biased with a 28V Keysight E3631A Power Supply and a 51 ohm resistor was put in series with the SiPM's negative lead. Across the resistor was connected the SMU. This configuration was effectively like a voltage divider where the changes in voltage could be measured across the resistor. These voltage fluctuations due to the amount of light being detected were measured with the Keysight software.

The signal output was recorded and compared between device pairs. The device pairs were moth-eye LED and moth-eye SiPM, moth-eye LED and bare SiPM, bare LED and moth-eye SiPM, and bare LED and bare SiPM.

The results for the LED-SiPM coupling for the different pairings are shown in Figure 5-64.

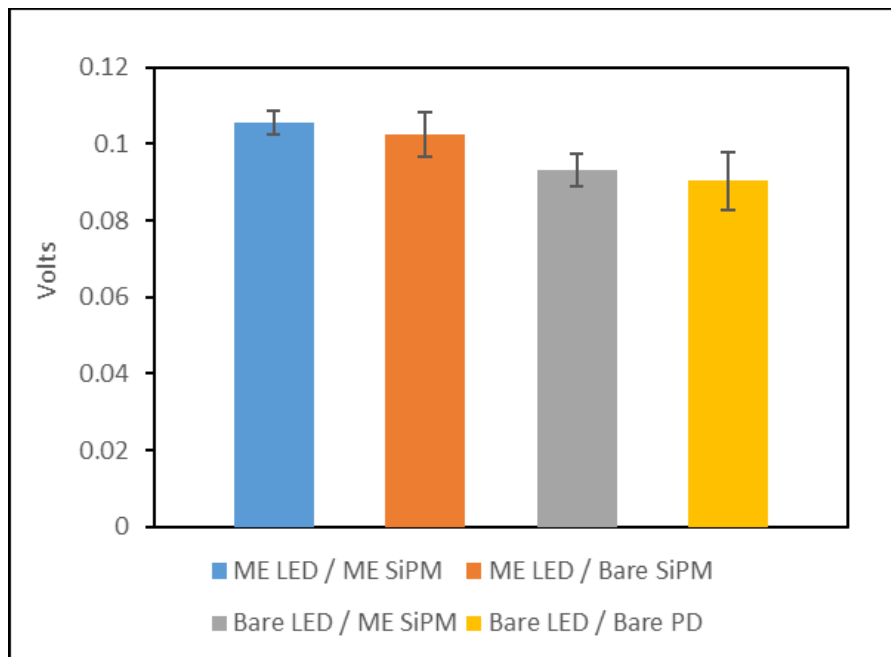


Figure 5-64: Comparison of LED-SiPM coupling produced from combinations of moth-eye (ME) patterned and unpatterned (bare) LED and SiPM.

As in Figure 5-62 with the LED-PD, the data for the LED-SiPM combinations in Figure 5-64 it can be seen that the highest coupling was produced was when the pair of devices were both patterned with the nanostructures on their surfaces. As before, this increased coupling is

due to the improved outcoupling of light from the LED and incoupling into the light detector creating an overall larger electrical coupling effect.

Table 5-7 shows the maximum value of the coupled simulated PPG signal for different pairing combinations.

Table 5-7: LED – SiPM Coupling for Simulated PPG

	Average Maximum Voltage Across Series Resistor	Percent Increase from Bare/Bare
ME LED / ME SiPM	0.105530833	16.9
ME LED / Bare SiPM	0.102327267	13.3
Bare LED / ME SiPM	0.093238567	3.3
Bare LED / Bare SiPM	0.090289333	-

The corresponding normalized PPG photocurrent response scaled to the maximum value and percentages found in Table 5-7 can be seen in Figure 5-65.

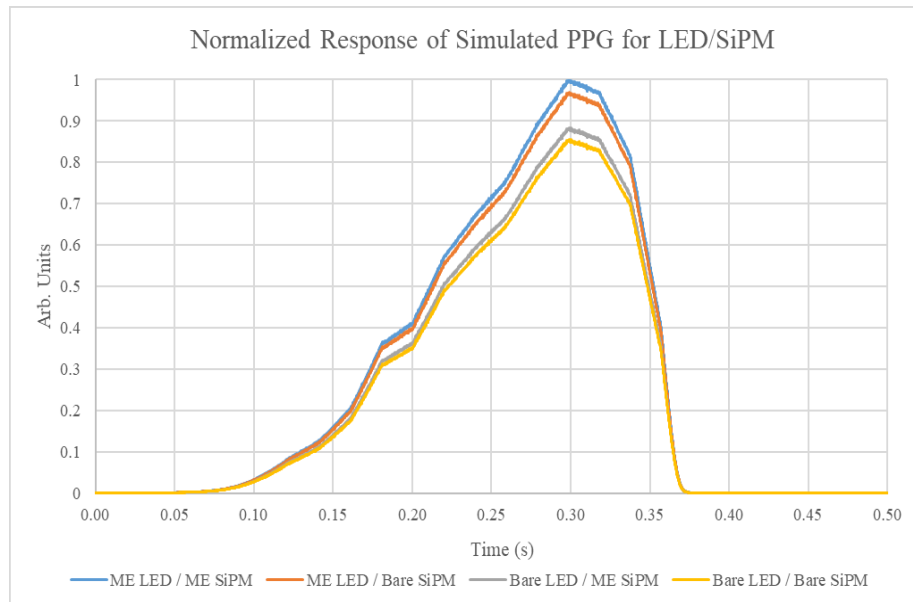


Figure 5-65: A normalized photodiode current response from a simulated PPG for patterned and bare LED/SiPM combinations scaled according to the results of Table 5-7.

Similar results are found in Table 5-7 for the LED/SiPM combinations as in Table 5-6 for the LED/PD combinations. The bare pairs had the least coupling, while the devices that

had both of the pair patterned had the most coupling. The intermediate combinations of a single patterned devices matched with unpatterned devices showed that the moth-eye patterned LED and bare SiPM pair, produced a stronger coupling than the bare LED and the moth-eye patterned SiPM. For these devices, it shows that the moth-eye pattern as having a more significant effect on the LED for the coupling. When the percent increase is added from these two scenarios (3.3% and 13.3%), it approximately equals the percent increase seen by the ME/ME combination over the bare/bare combination (16.6 % vs 16.9%).

5.7.2 Human PPG Measurements

The next step was to investigate if the signal gains seen with the phantom finger experiments could also be seen with a biological PPG. Here a human finger was substituted for the phantom finger and devices were mounted across the finger to operate in transmission mode with the LED on one side of the fingertip and the photodiode on the other. The devices were held approximately 8mm from the surface of the finger and placed on the finger in 3D printed holders as depicted in the diagram in Figure 5-66.

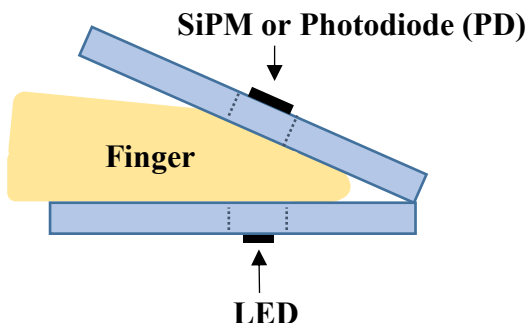


Figure 5-66: An illustration showing how the pairs of patterned and unpatterned LEDs, photodiodes and SiPM were held with a holder to take the human PPG measurement a few millimeters away from the skin.

When the test was conducted the lights of the room were turned off and the LED was operated at constant illumination of 2V from the Keysight power supply. The SMU collected the current generated by the photodiode with Keysight software as the finger and arm were kept

as still as possible. An example of a collected PPG can be seen in Figure 5-67. The collected signal was done several times with each measurement session lasting approximately 10 seconds.

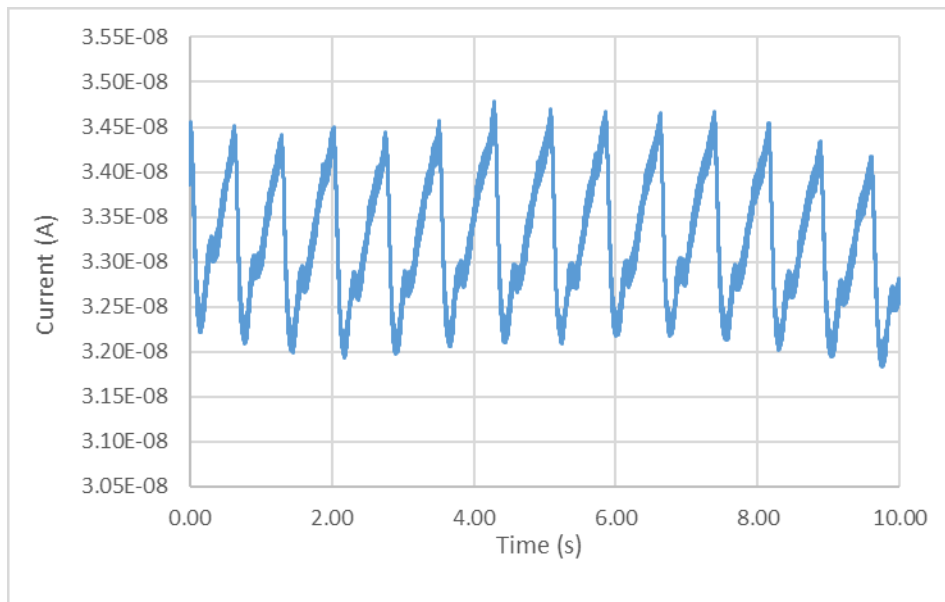


Figure 5-67: Example of a collected human PPG signal using the LED at constant voltage and photodiode. Signal height was measured peak to peak.

The amplitude of the PPG was measured from peak to peak. Table 5-8 below shows the results of the bare LEDs and bare photodiodes.

Table 5-8: Unmodified LED with Unmodified Photodiode PPG Measurement Results

Number of Samples	Average PPG Amplitude (nA)	PPG Standard Deviation
55	1.712	0.27
61	1.752	0.35
47	1.381	0.193
Total: 165	Total Average: 1.631	Total STD : 0.324

The three sets of bare LED and photodiodes had an average PPG amplitude of 1.631 nanoamps (nA).

The same kind of human finger PPG experiments were conducted with pairs of LEDs and photodiodes modified to have moth-eye surfaces. Table 5-9 shows the results for these devices.

Table 5-9: Moth-Eye LED with Moth-Eye Photodiode PPG Measurement Results

Number of Samples	Average PPG Amplitude (nA)	PPG Standard Deviation
61	2.266	0.367
54	2.181	0.233
63	1.84	0.162
Total: 178	Total Average : 2.054	Total STD : 0.255

The results of the moth-eye LED and moth-eye photodiode pairing show that the signal strength is greater than in the bare devices case. The next table, Table 5-10, compares the mean values for both the unmodified pairs versus the surface structure modified devices.

Table 5-10: Coupling Gains Seen in Modified vs Unmodified LED/PD Device Pairs

	Average PPG Amplitude (nA)
Bare LED-Bare Photodiode	Total Average: 1.631
Moth-eye LED – Moth-eye Photodiode	Total Average : 2.054
Gain	ME vs Bare: 26% increase

There is some variation in the pairs as seen in Table 5-9. If the top 2 unmodified bare pairs are compared to the ME pairs, then the gains drop but are probably more reflective of the actual gains between more consistently made devices.

In this comparison, Table 5-11 shows the gain is 18.6%.

Table 5-11: Top 2 Bare Pair vs ME Sets for LED/Photodiode

	Average PPG Amplitude (nA)
Top 2 Bare LED-Bare Photodiode	Total Average: 1.732
Moth-eye LED – Moth-eye Photodiode	Total Average : 2.054
Gain	ME vs Bare: 18.6% increase

Regardless of which comparison is made, Table 5-10 or Table 5-11, what is clear is that there is a gain in the average PPG amplitude measurement when the moth-eye structures are utilized on both the LED and photodiode.

The same kind of human PPG measurements were made with pairs of LED and SiPMs. In this situation, the Keysight E3631A Power Supply was used to bias the SiPM with 28V. The LED was biased with 1.95V with an Agilent E3620A power supply. There was a 51 ohm resistor connected to the SiPM and the Agilent B2902A Precision Source / Measure Unit (SMU) was used to measure the voltage across the resistor. The results of the bare device pairs can be seen in Table 5-12. Measurements were again done peak to peak.

Table 5-12: Unmodified LED with unmodified SiPM Human PPG Measurement Results

Number of Samples	Average PPG Amplitude (mV)	PPG Standard Deviation
84	8.691	1.216
120	9.816	1.391
158	8.582	1.303
Total: 362	Total Average: 9.021	Total STD : 1.384

The same setup was used to take PPG measurements from a human finger. The results can be seen in Table 5-13.

Table 5-13: Moth-Eye LED with Moth-Eye SiPM PPG Measurement Results

Number of Samples	Average PPG Amplitude (mV)	PPG Standard Deviation
70	10.86	1.061
85	11.06	0.988
74	11.12	0.762
Total: 229	Total Average: 11.018	Total STD : 0.924

The device pairs with the nanostructures had a stronger coupling than the bare devices.

A comparison of the bare devices to the patterned devices can be seen in Table 5-14.

Table 5-14: Coupling Gains Seen in Modified vs Unmodified LED/SiPM Device Pairs

	Average PPG Amplitude (mV)
Bare LED-Bare SiPM	Total Average: 9.021
Moth-eye LED – Moth-eye SiPM	Total Average : 11.018
Gain	ME vs Bare: 22% increase

The average PPG amplitude showed a 22% increase with the presence of the nanostructures in voltage or converted to current. Table 5-15 shows a comparison of the gains for the patterned LED/PD and LED/SiPM. If the values of Table 5-11 are considered, then the LED/PD pair increase is 18.6% for Table 5-15. Despite some variation being seen, the relevant point is that there is an overall coupling gain trend with the usage of the nanostructures.

Table 5-15: Comparison of Coupling Gains on LED/PD versus LED/SiPM

	Average PPG Amplitude
Moth-eye LED – Moth-eye Photodiode	ME vs Bare: 26% increase *18.6%
Moth-eye LED – Moth-eye SiPM	ME vs Bare: 22% increase

Chapter 6: Conclusion and Future Work

The result of this work can be grouped into different categories of effort. The organic devices are one area. Green and red OLEDs with the layers of PET/ITO/PEDOT:PSS/Active Polymer/Ca/Al and different active polymers were successfully fabricated and could be made to illuminate. The green and red OLEDs were based on the F8BT and MDMO-PPV polymers, respectively. Photodiode light detectors were also fabricated successfully with the layers PET/ITO/PEDOT:PSS/ICBA:P3HT/Ca/Al. These light detectors could be made to respond to different sources of light but did not have a strong enough response.

Each type of organic device had a specific recipe developed for dissolving and applying its active layer, which became more refined over time, yielding more consistent devices. All the devices were made to be flexible. The challenge of creating rigid carriers for holding flexible devices during their processing that could later release the flexible devices was also addressed. The issue of how to eliminate the carbon contamination from the mineral oil packaging in which the calcium arrived in, was successfully resolved as well. The device sizes were also increased by almost five times from 10 mm^2 to 0.49 cm^2 . An encapsulation method was additionally devised to take these devices out of their nitrogen atmosphere environment where they were fabricated. The encapsulation allowed the PPG to be taken with the green OLED.

Another significant area of effort was the creation of the biomimetic structures on silicon. This required taking diced pieces of silicon wafers and making their surfaces very clean with the use of solvents and UV light. This was important to prepare the surface for the deposition of nanospheres in order to use them as a mask in reactive ion etching in a process known as nanosphere lithography. The local plasma etching machine had not been used for this

procedure before, and repeated attempts were accomplished to discover the parameters that would appropriately etch and pattern the silicon. Simultaneously a related issue was also solved of how to deposit the nanospheres in large areas to cover the majority of the silicon pieces. Different methods were attempted to make the nanosphere colloidal crystal have a greater surface area and achieve increasingly better coverage on larger pieces of silicon. The next step that was worked on was transferring the pattern from the silicon to another surface by means of a PDMS created stamp that functioned as a mold.

The PDMS mold needed to have a special bilayer design for the nanoimprint lithography to work. There were several approaches that were attempted before this method was perfected. Changes to the chemical formulations and application technique allowed the height of the transferred biomimetic moth-eye nanostructure pattern to be maximized in UV curable optical resin. This was a successful step to create the final structures which allowed the nanostructures to be successfully transferred in UV resin to LEDs, photodiodes and SiPMs. Following this, the device types were also characterized to evaluate their performance enhancement.

A testing platform was also successfully developed to measure if there was additional coupling between light emitting and light detecting devices with nanostructures. The testing platform was later expanded to take human finger PPG measurements. With this final accomplishment, the majority of the research objectives were met.

The testing of these light emitter and light detector pair devices with nanostructures translated to several beneficial conclusions. First, the overall response current and associated signal strength can be improved for a sensor pair without needing to add extra power to the system. Second, the sensitivity of the system could be improved by merely modifying the

surfaces of photonic devices. Third, a system's power level could potentially be reduced while still maintaining its existing sensitivity level. Fourth, the application of the nanostructures are useful for self-powered battery operated sensor systems where power conservation can be important. Fifth, this is a promising application not just for PPG measurements, but also useful for the broader application of sensing systems that requires pairs of light emitters and detectors where there is an index of refraction change that causes reflection or light loss.

6.1 Future work

There are several possibilities that could expand this work and develop it further in the future. In terms of the organic devices, there could be a relatively quick attempt to take the materials that worked in producing this project and see if another method could be established locally that would be more conservative of the reagents such as blade coating instead of the existing spin coating method. After it is learned how to make devices of equal or better quality than what was produced in this work with the existing reagents, then there is the potential to re-examine the choice of materials for the active matrix and pick other types that were previously cost prohibitive due to spincoating, such as high performing reagents or polymers that can be chemically synthesized specifically for their emission spectra or absorption.

Additionally, future work with the organic devices could be to change their plastic substrate, resulting in better thermal cycling and mechanical properties, and preferably without ITO, which can limit curvature. Encapsulation and interconnect methodologies could be examined in future work as well, where better chemical and mechanical compatibility with the devices could be investigated.

The work created here also could be developed in terms of the physiological measurements for future work. The experiments could be expanded to have a fabricated pulse

oximeter device take measurements at the same time as a commercial device. The measurement could be on the same hand or the same finger on different hands. A baseline comparison between the two could be established and the fabricated device could also be calibrated against the commercial device. Then the nanostructures could be introduced to the fabricated device, the signal improvement could be analyzed and another comparison could be made of how much improvement could be possible on the commercial device. The analysis could include how much power savings the commercial device could have or improved sensitivity if it used these structures on the surface of their light emitters and light detectors.

Another aspect for future work could be the expansion of the concept to other sensor designs other than PPG or pulse oximetry. For other devices that require pairs of light emitters and detectors, the design improvement of incorporating the nanostructures could be examined qualitatively. Possible immediate devices to experiment with could include proximity detectors and light based assays (e.g. fluorescence/phosphorescence or other). In the broader scope, many other sensor devices could be tested. As long as there is a light emitter and light detector and a significant enough change in the index of refraction between the two device types to cause light loss in a unmodified system, the concept of modifying the system to include nanostructures to couple the light out of the light emitter and to couple the light into the light detector should have beneficial results.

REFERENCES

- [1] Han, Donggeon, Khan, Yasser, Ting, Jonathan, King, Simon M., Yaacobi-Gross, Nir, Humphries, Martin J. Newsome, Christopher J., Arias A., “Flexible Blade-Coated Multicolor Polymer Light-Emitting Diodes for Optoelectronic Sensors,” *Adv. Mater.*, p. 1606206, 2017.
- [2] Y. Khan *et al.*, “A flexible organic reflectance oximeter array,” *Proc. Natl. Acad. Sci.*, vol. 115, no. 47, pp. E11015–E11024, 2018.
- [3] W. Yokota, Tomoyuki, Zalar, Peter, Kaltenbrunner, Martin, Jinno, Hiroaki, Matsuhisa, Najo, Kitanosako, Hiroki, Tachibana, Yutaro, Yukita and T. Koizumi, Mari, Someya, “Ultra-flexible Organic Photonic Skin,” *Sci. Adv.*, no. April, pp. 1–9, 2016.
- [4] H. Lee *et al.*, “Toward all-day wearable health monitoring: An ultralow-power, reflective organic pulse oximetry sensing patch,” *Sci. Adv.*, vol. 4, no. 11, pp. 1–9, 2018.
- [5] C. M. Lochner, Y. Khan, A. Pierre, and A. Arias, “All-organic optoelectronic sensor for pulse oximetry.,” *Nat. Commun.*, vol. 5, p. 5745, 2014.
- [6] J. G. Webster, *Design of Pulse Oximeters*. 1997.
- [7] P. Silverston, “Pulse oximetry in primary care,” *InnovAiT*, vol. 9, no. 4, pp. 202–207, 2016.
- [8] W. R. Mower, G. Myers, E. L. Nicklin, K. T. Kearin, L. J. Baraff, and C. Sachs, “Pulse oximetry as a fifth vital sign in emergency geriatric assessment.,” *Acad. Emerg. Med.*, vol. 5, no. 9, pp. 858–865, 1998.
- [9] D. Evans, B. Hodgkinson, and J. Berry, “Vital signs in hospital patients: A systematic review,” *Ijns*, vol. 38, no. 6, pp. 643–650, 2001.
- [10] S. Martin, J. Martin, and T. Seigler, “Evidence-Based Protocols to Guide Pulse Oximetry and Oxygen Weaning in Inpatient Children with Asthma and Bronchiolitis: A Pilot Project,” *J. Pediatr. Nurs.*, vol. 30, no. 6, pp. 888–895, 2015.
- [11] Y. Sun and N. Thakor, “Photoplethysmography Revisited: From Contact to Noncontact, from Point to Imaging,” *IEEE Trans. Biomed. Eng.*, vol. 63, no. 3, pp. 463–477, 2016.
- [12] Y. Khan, A. E. Ostfeld, C. M. Lochner, A. Pierre, and A. C. Arias, “Monitoring of Vital Signs with Flexible and Wearable Medical Devices,” *Adv. Mater.*, vol. 28, no. 22, pp. 4373–4395, 2016.
- [13] S. Prahl, “Optical Absorption of Hemoglobin,” 1999. [Online]. Available: <https://omlc.org/spectra/hemoglobin/>.
- [14] P. A. Haigh *et al.*, “Wavelength-Multiplexed Polymer LEDs: Towards 55 Mb/s Organic

Visible Light Communications," *IEEE J. Sel. Areas Commun.*, vol. 33, no. 9, pp. 1819–1828, 2015.

- [15] X. Guo, M. Zhang, C. Cui, J. Hou, and Y. Li, "Efficient polymer solar cells based on poly(3-hexylthiophene) and indene-C₆₀ bisadduct fabricated with non-halogenated solvents.," *ACS Appl. Mater. Interfaces*, vol. 6, no. 11, pp. 8190–8, 2014.
- [16] V. C. Bender, T. B. Marchesan, and J. M. Alonso, "Solid-State Lighting: A Concise Review of the State of the Art on LED and OLED Modeling," *IEEE Ind. Electron. Mag.*, vol. 9, no. 2, pp. 6–16, 2015.
- [17] P. 2 Committee on Assessment of Solid-State Lighting and C. Kassakian, John, Hu, Evelyn, Black, Iain, Clanton, Nancy, Davis, Wendy, Ettenberg , Michael, Hakkarainen, Pekka, Narendran, Nadarajah, Savitz, Maxine, Spencer, Michael, and Tang, *Assessment of Solid State Lighting, Phase Two*. 2017.
- [18] E. J. Culurciello, Eugenio, Tang, Wei, Park, *Biomedical Circuits and Systems*. Lulu.com.
- [19] A. Fernandez, "How a Solar Cell Works by the American Chemical Society," 2013. [Online]. Available: <https://www.acs.org/content/acs/en/education/resources/highschool/chemmatters/past-issues/archive-2013-2014/how-a-solar-cell-works.html>.
- [20] R. Meerheim, B. Lüssem, and K. Leo, "Efficiency and stability of p-i-n type organic light emitting diodes for display and lighting applications," *Proc. IEEE*, vol. 97, no. 9, pp. 1606–1626, 2009.
- [21] W. Brütting, J. Frischeisen, T. D. Schmidt, B. J. Scholz, and C. Mayr, "Device efficiency of organic light-emitting diodes: Progress by improved light outcoupling," *Phys. Status Solidi Appl. Mater. Sci.*, vol. 210, no. 1, pp. 44–65, 2013.
- [22] Y. Karzazi, "Organic Light Emitting Diodes: Devices and applications," *Environ. Sci.*, vol. 5, no. 1, pp. 1–12, 2014.
- [23] O. V. Mikhnenko, P. W. M. Blom, and T.-Q. Nguyen, "Exciton diffusion in organic semiconductors," *Energy Environ. Sci.*, vol. 8, no. 7, pp. 1867–1888, 2015.
- [24] G. L. Ingram and Z.-H. Lu, "Design principles for highly efficient organic light-emitting diodes," *J. Photonics Energy*, vol. 4, no. 1, pp. 040993–040993, 2014.
- [25] A. Opitz, "Energy level alignment at planar organic heterojunctions: influence of contact doping and molecular orientation," *J. Phys. Condens. Matter*, vol. 29, no. 13, p. 133001, 2017.
- [26] B. Sim, C.-K. Moon, K.-H. Kim, and J.-J. Kim, "Quantitative Analysis of the Efficiency of OLEDs," *ACS Appl. Mater. Interfaces*, vol. 8, no. 48, pp. 33010–33018, 2016.
- [27] F. Zhao and D. Ma, "Approaches to high performance white organic light-emitting

diodes for general lighting,” *Mater. Chem. Front.*, vol. 1, pp. 1933–1950, 2017.

- [28] A. Opitz *et al.*, “Charge Separation at Molecular Donor – Acceptor Interfaces : Correlation Between Morphology and Solar Cell Performance,” *IEEE J. Sel. Top. Quantum Electron.*, vol. 16, no. 6, pp. 1707–1717, 2010.
- [29] K. Nakano and K. Tajima, “Organic Planar Heterojunctions: From Models for Interfaces in Bulk Heterojunctions to High-Performance Solar Cells,” *Adv. Mater.*, 2016.
- [30] K. M. Pelzer and S. B. Darling, “Charge generation in organic photovoltaics: a review of theory and computation,” *Mol. Syst. Des. Eng.*, vol. 1, no. 1, pp. 10–24, 2016.
- [31] K. A. Mazzio and C. K. Luscombe, “The future of organic photovoltaics,” *Chem. Soc. Rev.*, vol. 44, no. 1, pp. 78–90, 2014.
- [32] N. S. Dennler, G., Lungenschmied, C., Sariciftci, “Flexible conjugated polymer fullerene based bulk heterojunction solar cells basic encapsulation and integration,” *J. Mater. Res.*, vol. 20, no. 12, pp. 3224–3233, 2005.
- [33] J. D. Servaites, M. A. Ratner, and T. J. Marks, “Practical efficiency limits in organic photovoltaic cells: Functional dependence of fill factor and external quantum efficiency,” *Appl. Phys. Lett.*, vol. 95, no. 16, pp. 1–4, 2009.
- [34] B. Qi and J. Wang, “Fill factor in organic solar cells,” *Phys. Chem. Chem. Phys.*, vol. 15, no. 23, p. 8972, 2013.
- [35] G. J. Hedley, A. Ruseckas, and I. D. W. Samuel, “Light Harvesting for Organic Photovoltaics,” *Chem. Rev.*, vol. 117, no. 2, pp. 796–837, 2017.
- [36] W. Cao and J. Xue, “Recent progress in organic photovoltaics: device architecture and optical design,” *Energy Environ. Sci.*, vol. 7, no. 7, pp. 2123–2144, 2014.
- [37] C. K. Nien and H. H. Yu, “The applications of biomimetic cicada-wing structure on the organic light-emitting diodes,” *Mater. Chem. Phys.*, vol. 227, no. January, pp. 191–199, 2019.
- [38] R. P. Xu, Y. Q. Li, and J. X. Tang, “Recent advances in flexible organic light-emitting diodes,” *J. Mater. Chem. C*, vol. 4, no. 39, pp. 9116–9142, 2016.
- [39] S. A. Boden and D. M. Bagnall, “Nanostructured biomimetic moth-eye arrays in silicon by nanoimprint lithography,” p. 74010J, 2009.
- [40] E. J. Hong *et al.*, “Fabrication of moth-eye structure on p-GaN layer of GaN-based LEDs for improvement of light extraction,” *Mater. Sci. Eng. B Solid-State Mater. Adv. Technol.*, vol. 163, no. 3, pp. 170–173, 2009.
- [41] H. Sakurai *et al.*, “Fabrication of high-efficiency LED using moth-eye structure,” *Gall. Nitride Mater. Devices VI*, vol. 7939, no. March 2011, p. 79391V, 2011.

- [42] S. M. Kang *et al.*, “Moth-Eye TiO₂ Layer for Improving Light Harvesting Efficiency in Perovskite Solar Cells,” *Small*, vol. 12, no. 18, pp. 2443–2449, 2016.
- [43] L. Zhou *et al.*, “Light manipulation for organic optoelectronics using bio-inspired moth’s eye nanostructures,” *Sci. Rep.*, vol. 4, p. 4040, 2014.
- [44] W. Lan, Y. Cui, Q. Yang, M. F. Lo, C. S. Lee, and F. Zhu, “Broadband light absorption enhancement in moth’s eye nanostructured organic solar cells,” *AIP Adv.*, vol. 5, no. 5, 2015.
- [45] J. De Chen *et al.*, “Single-junction polymer solar cells exceeding 10% power conversion efficiency,” *Adv. Mater.*, vol. 27, no. 6, pp. 1035–1041, 2015.
- [46] Q. D. Ou *et al.*, “Extremely efficient white organic light-emitting diodes for general lighting,” *Adv. Funct. Mater.*, vol. 24, no. 46, pp. 7249–7256, 2014.
- [47] D. G. Stavenga, S. Foletti, G. Palasantzas, and K. Arikawa, “Light on the moth-eye corneal nipple array of butterflies,” *Proc. R. Soc. B Biol. Sci.*, vol. 273, no. 1587, pp. 661–667, 2006.
- [48] G. Tan *et al.*, “Broadband antireflection film with moth-eye-like structure for flexible display applications,” *Optica*, vol. 4, no. 7, p. 678, 2017.
- [49] L. W. Chan, D. E. Morse, and M. J. Gordon, “Moth eye-inspired anti-reflective surfaces for improved IR optical systems & visible LEDs fabricated with colloidal lithography and etching,” *Bioinspiration and Biomimetics*, vol. 13, no. 4, 2018.
- [50] D. Boden, S., Bagnall, “Moth-Eye Antireflective Structures,” in *Encyclopedia of Nanotechnology*, Springer Science, 2015.
- [51] Q. Yang, “Antireflection property of a periodic nanocine structured solid-solid interface,” *Thesis*, 2012.
- [52] H. Ding, J. Q. Lu, W. A. Wooden, P. J. Kragel, and X. H. Hu, “Refractive indices of human skin tissues at eight wavelengths and estimated dispersion relations between 300 and 1600 nm,” *Phys. Med. Biol.*, vol. 51, no. 6, pp. 1479–1489, 2006.
- [53] E. Manna, T. Xiao, J. Shinar, and R. Shinar, *Organic Photodetectors in Analytical Applications*, vol. 4. 2015.
- [54] H. Zheng *et al.*, “All-solution processed polymer light-emitting diode displays.,” *Nat. Commun.*, vol. 4, no. May, p. 1971, 2013.
- [55] S. Rehg, James, Murphy, Susan, Kumar, *Mobile Health: Sensors, Analytic Methods, and Applications*, 1st ed. Springer, 2017.
- [56] C. Honrado and T. Dong, “Development and optimization of an integrated capillary-based opto-microfluidic device for chemiluminescence quantitative detection,” *J.*

Micromechanics Microengineering, vol. 24, no. 12, p. 125023, Dec. 2014.

- [57] N. M. M. Pires, T. Dong, U. Hanke, and N. Hoivik, “Integrated optical microfluidic biosensor using a polycarbazole photodetector for point-of-care detection of hormonal compounds.,” *J. Biomed. Opt.*, vol. 18, no. 9, p. 097001, 2013.
- [58] N. M. M. Pires and T. Dong, “Measurement of salivary cortisol by a chemiluminescent organic-based immunosensor,” *Biomed. Mater. Eng.*, vol. 24, no. 1, pp. 15–20, 2014.
- [59] N. M. Matos Pires and T. Dong, “Microfluidic biosensor array with integrated poly(2,7-carbazole)/fullerene-based photodiodes for rapid multiplexed detection of pathogens.,” *Sensors (Basel).*, vol. 13, no. 12, pp. 15898–15911, 2013.
- [60] G. Williams, C. Backhouse, and H. Aziz, “Integration of Organic Light Emitting Diodes and Organic Photodetectors for Lab-on-a-Chip Bio-Detection Systems,” *Electronics*, vol. 3, no. 1, pp. 43–75, 2014.
- [61] A. K. Bansal, S. Hou, O. Kulyk, E. M. Bowman, and I. D. W. Samuel, “Wearable organic optoelectronic sensors for medicine,” *Adv. Mater.*, pp. 7638–7644, 2014.
- [62] Y. Chuo, B. Omrane, C. Landrock, J. N. Patel, and B. Kaminska, “Platform for All-Polymer-Based Pulse-Oximetry Sensor,” pp. 155–159, 2010.
- [63] M. Kramer, A. Lobbestael, E. Barten, J. Eian, and G. Rausch, “Wearable Pulse Oximetry Measurements on the Torso, Arms, and Legs: A Proof of Concept,” *Mil. Med.*, vol. 182, no. S1, pp. 92–98, 2017.
- [64] T. Tamura, Y. Maeda, M. Sekine, and M. Yoshida, “Wearable Photoplethysmographic Sensors—Past and Present,” *Electronics*, vol. 3, no. 2, pp. 282–302, 2014.
- [65] D. Y. Kang, Y. S. Kim, G. Ornelas, M. Sinha, K. Naidu, and T. P. Coleman, “Scalable microfabrication procedures for adhesive-integrated flexible and stretchable electronic sensors,” *Sensors (Switzerland)*, vol. 15, no. 9, pp. 23459–23476, 2015.
- [66] W. H. Yeo *et al.*, “Multifunctional epidermal electronics printed directly onto the skin,” *Adv. Mater.*, vol. 25, no. 20, pp. 2773–2778, 2013.
- [67] J. A. Rogers, R. Ghaffari, and D.-H. Kim, *Stretchable Bioelectronics for Medical Devices and Systems*. 2016.
- [68] M. Koetse *et al.*, “In plane optical sensor based on organic electronic devices,” *Proc. SPIE Vol. 7054 70541I-1*, vol. 7054, pp. 70541I--70541I, 2008.
- [69] F. P. Wieringa, G. T. Van Heck, P. Rensing, M. M. Koetse, S. S. Kalisingh, and H. Schoo, “Systems in foil - Opening new perspectives in medical technology,” *IFMBE Proc.*, vol. 22, pp. 2292–2295, 2008.
- [70] J. Nevrela *et al.*, “Secondary doping in poly(3,4-ethylenedioxythiophene):Poly(4-

styrenesulfonate) thin films,” *J. Polym. Sci. Part B Polym. Phys.*, vol. 53, no. 16, pp. 1139–1146, 2015.

- [71] M. Weis, T. Otsuka, D. Taguchi, T. Manaka, and M. Iwamoto, “Charge injection and accumulation in organic light-emitting diode with PEDOT:PSS anode,” *J. Appl. Phys.*, vol. 117, no. 15, 2015.
- [72] M. S. White *et al.*, “Ultrathin, highly flexible and stretchable PLEDs,” *Nat. Photonics*, vol. 7, no. 10, pp. 811–816, 2013.
- [73] V. Zardetto, T. M. Brown, A. Reale, and A. Di Carlo, “Substrates for flexible electronics: A practical investigation on the electrical, film flexibility, optical, temperature, and solvent resistance properties,” *J. Polym. Sci. Part B Polym. Phys.*, vol. 49, no. 9, pp. 638–648, 2011.
- [74] B. Demirel, A. Yaraş, and H. Elçiçek, “Crystallization Behavior of PET Materials,” *BAÜ Fen Bil. Enst. Derg. Cilt*, vol. 13, no. 1, pp. 26–35, 2011.
- [75] C. Scott, “PEN @ [www.polymerprocessing.com.](http://www.polymerprocessing.com/)” [Online]. Available: <http://www.polymerprocessing.com/polymers/PEN.html>.
- [76] G. J. Zhao, Y. J. He, and Y. Li, “6.5% efficiency of polymer solar cells based on poly(3-hexylthiophene) and indene-C60 bisadduct by device optimization,” *Adv. Mater.*, vol. 22, no. 39, pp. 4355–4358, 2010.
- [77] M. U. Hassan, Y. C. Liu, K. U. Hasan, H. Butt, J. F. Chang, and R. H. Friend, “Highly efficient PLEDs based on poly(9,9-diethylfluorene) and Super Yellow blend with Cs₂CO₃ modified cathode,” *Appl. Mater. Today*, vol. 1, no. 1, pp. 45–51, 2015.
- [78] Q. An *et al.*, “Enhanced performance of polymer solar cells by employing a ternary cascade energy structure,” *Sol. Energy Mater. Sol. Cells*, vol. 16, pp. 16103–16109, 2014.
- [79] D. Gao, B. Djukic, W. Shi, C. R. Bridges, L. M. Kozycz, and D. S. Seferos, “Evolution of the electron mobility in polymer solar cells with different fullerene acceptors,” *ACS Appl. Mater. Interfaces*, vol. 5, no. 16, pp. 8038–8043, 2013.
- [80] H. A. Méndez-Pinzón, D. R. Pardo-Pardo, J. P. Cuéllar-Alvarado, J. C. Salcedo-Reyes, R. Vera, and B. A. Páez-Sierra, “Analysis of the current-voltage characteristics of polymer-based organic light-emitting diodes (OLEDs) deposited by spin coating TT - Análise da característica corrente-voltagem de diodos orgânicos emissores de luz (OLEDs) baseados em polímeros depositad,” *Univ. Sci.*, vol. 15, no. 1, pp. 68–76, 2010.
- [81] V. A. Pozdin, M. A. Yokus, P. Sotory, N. Wisniewski, A. Bozkurt, and M. A. Daniele, “Low-cost flexible inorganic optical devices for flexible sensors,” *Proc. IEEE Sensors*, vol. 2017-Decem, pp. 1–3, 2017.
- [82] ON Semincoductor/sensL Light, “An Introduction to the Silicon Photomultiplier

Introduction to SiPM,” *Tech. note*, pp. 1–16, 2011.

- [83] B. Brady, P. H. Wang, V. Steenhoff, and A. G. Brolo, *Nanostructuring solar cells using metallic nanoparticles*. Elsevier Ltd., 2018.
- [84] S. Su, L. Lin, Z. Li, J. Feng, and Z. Zhang, “The fabrication of large-scale sub-10-nm core-shell silicon nanowire arrays,” *Nanoscale Res. Lett.*, vol. 8, no. 1, p. 405, 2013.
- [85] B. Kiraly, S. Yang, and T. J. Huang, “Multifunctional porous silicon nanopillar arrays: Antireflection, superhydrophobicity, photoluminescence, and surface-enhanced Raman scattering,” *Nanotechnology*, vol. 24, no. 24, 2013.
- [86] J. T. Zhang, L. Wang, D. N. Lamont, S. S. Velankar, and S. A. Asher, “Fabrication of large-area two-dimensional colloidal crystals,” *Angew. Chemie - Int. Ed.*, vol. 51, no. 25, pp. 6117–6120, 2012.
- [87] V. Lotito and T. Zambelli, “Approaches to self-assembly of colloidal monolayers: A guide for nanotechnologists,” *Adv. Colloid Interface Sci.*, vol. 246, no. April, pp. 217–274, 2017.
- [88] A. S. Dimitrov and K. Nagayama, “Continuous convective assembling of fine particles into two-dimensional arrays on solid surfaces,” *Langmuir*, vol. 12, no. 5, pp. 1303–1311, 1996.
- [89] J. Zhong, J. Chinn, C. B. Roberts, and W. R. Ashurst, “Vapor-Phase Deposited Chlorosilane-Based Self-Assembled Monolayers on Various Substrates for Thermal Stability Analysis,” *Ind. Eng. Chem. Res.*, vol. 56, no. 18, pp. 5239–5252, 2017.
- [90] S. S. Latthe, C. Terashima, K. Nakata, and A. Fujishima, “Superhydrophobic surfaces developed by mimicking hierarchical surface morphology of lotus leaf,” *Molecules*, vol. 19, no. 4, pp. 4256–4283, 2014.
- [91] M. Barisik and A. Beskok, “Wetting characterisation of silicon (1,0,0) surface,” *Mol. Simul.*, vol. 39, no. 9, pp. 700–709, 2013.
- [92] Z. Diao, M. Kraus, R. Brunner, J. H. Dirks, and J. P. Spatz, “Nanostructured Stealth Surfaces for Visible and Near-Infrared Light,” *Nano Lett.*, vol. 16, no. 10, pp. 6610–6616, 2016.